Electroactive polyoxometalate-based molecular layers for nano-electronics

Raphaël Salles

Sorbonne Université

Nanyang Technological University

École doctorale de Chimie Moléculaire de Paris Centre - ED 406

Institut Parisien de Chimie Moléculaire / Équipe Édifices PolyMétalliques

School of Materials Science and Engineering

Pr Lee Pooi See's group

Electroactive polyoxometalate-based molecular layers for nano-electronics

By Raphaël Salles

Thesis submitted for the degree of Doctor of Philosophy in Chemistry

Supervised by Anna Proust, Pooi See Lee and Guillaume Izzet

Presented and publicly defended on December 13th, 2021

In front of a jury composed of:

Jean-Christophe LACROIX, Professor	Reviewer
Lixin WU, Professor	Reviewer
Zhili DONG, Professor	Examiner
Rodrigue LESCOUEZEC, Professor	Examiner
Pooi See LEE, Professor	Supervisor
Anna PROUST, Professor	Supervisor
Guillaume IZZET, Researcher	Supervisor (invited)

Sois toujours très imprudent, mon petit, c'est la seule façon d'avoir un peu de plaisir à vivre dans notre époque de manufactures. […] Tu peux être tout ce que tu veux et fou en surplus, mais il faut être fou, mon enfant. Regarde autour de toi le monde sans cesse grandissant de gens qui se prennent au sérieux.

Jean Giono, Le Hussard sur le toit

Always be very foolhardy, my dear, it's the only way of getting a little pleasure out of life in this factory age of ours. […] You can be anything you like and crazy into the bargain, but it's essential to be crazy, my child. Look around you at the ever-increasing number of people who take themselves seriously.

Jean Giono, The Horseman on the roof

TABLE OF CONTENTS

ABREVIATIONS LIST

AFM: Atomic Force Microscopy

CV: Cyclic Voltammetry

DOSY: Diffusion Ordered Spectroscopy

EDX: Energy-dispersive X-ray spectroscopy

IR: Infrared spectroscopy

ITO: Indium Tin Oxide

KPFM: Kelvin Probe Force Microscopy

NMR: Nuclear Magnetic Resonance

POM: Polyoxometalate

RRAM: Resistive Random-Access Memory

SEM-FEG: Scanning Electron Microscopy – Field Emission Gun

SSRM: Scanning Spread Resistance Microscopy

TBA: Tetrabutylammonium

XPS: X-ray Photoelectron Spectrometry

PART I – GENERAL INTRODUCTION

1. POLYOXOMETALATES

1.1. HISTORICAL INTRODUCTION

As a way to enter history, the Swedish scientist Jöns Jacobs Berzelius didn't want to wait 1864 (one of the reasons being his human nature that led him to die 16 years before, 1779-1848) when his name was given to an unforgettable albeit rather small street of Paris 17th district. A safer and easier way for him to make it to school books was to multiply the discoveries and achievements in his predilection field: chemistry. His major accomplishment, regarding this thesis, was obtained in 1826 when he reported the first synthesis of a polyoxometalate, $(NH_4)_3$ $[PMo_{12}O_{40}]_{aq}$ as it happens. This yellow precipitate obtained in a laboratory in Stockholm opened a new field of chemistry which is still nowadays under investigation because of their promises for modern technological progress. Jean-Charles Galissard de Marignac (who discovered and characterized the first heteropolytungstate), Arthur Rosenheim, Linus Pauling and many others talented and renowned scientists participated in this adventure.

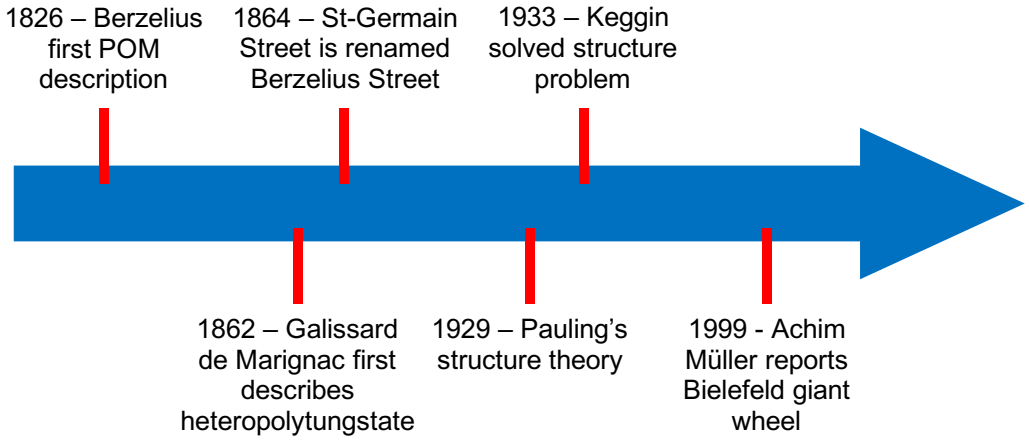

Figure 1 - Timeline of some major POMs achievements

It is James F. Keggin who first solved the problem of the complex octahedral structure of the polyoxometalates in 1933[1] by suggesting that the octahedral units were linked by both corners and edges, in rectification of Pauling's system,[2] when he suggested in 1929 that only corners were linkers. In more recent days, scientists like Pierre Souchay, Michael T. Pope or Achim Müller[3–5] brought the subject at a next step,

deepening (better comprehension on synthesis key parameters, isomers study…)[6] and extending (discovery of the giant wheel structure,[7] nano hedgehog structure…)[8] the knowledge in the domain.

1.2. OVERVIEW

1.2.1. PRESENTATION

Polyoxometalates, or POMs, are nano-scaled early transition metal oxides cluster anions. As explained previously, their structure relies on polyhedral units, with a metallic atom at its center and oxygens around, that share edges and corners.

As they always need to control, weigh, measure and classify things - otherwise they would have been poets - scientists indexed POMs in category and sub-category. The two big families representing the first level of classification are isopolyoxometalates and heteropolyoxometalates. The first one concerns POMs with only metallic elements ($[M_pO_y]^{n-}$, where M = Mo (VI), W(VI), V(V), Nb(V)…), one example being the Lindqvist series (*Fig.* 2); the second one concerns POMs that contain one or multiple heteroatoms at the core of their structure ($[X_xM_pO_y]^{n-}$, where X = P, Si… and M = Mo (VI),), W(VI), V(V), Nb(V)…).

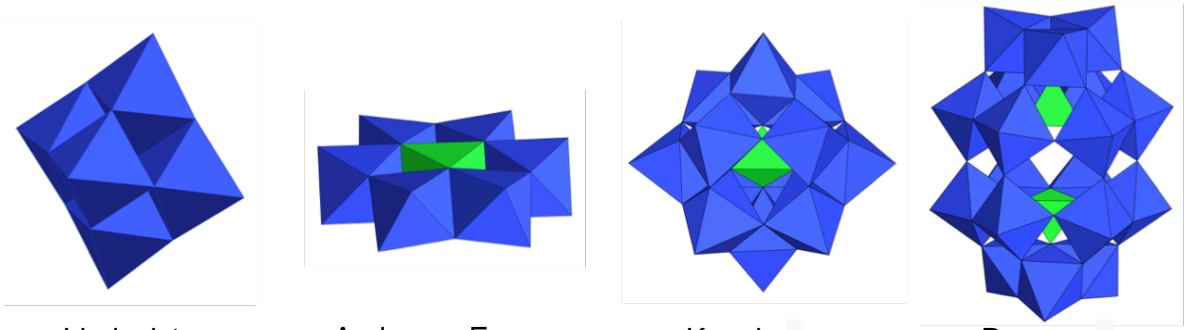

Lindqvist $[M_6O_{19}]^{n-}$ | Anderson-Evans $[XM_6O_{24}]^{n-}$ | Keggin α- $[XM_{12}O_{40}]^{n-}$ | Dawson α- $[X_2M_{18}O_{62}]^{n-}$

Figure 2 - Some of the most popular POMs structures

For this thesis we will focus on heteropolyoxometalates and more specifically on Keggin and Dawson types, but it is worth noticing that other compounds can lead to over nanometer-scaled structures.[9] It is also noteworthy that many structures have isomers (for instance, the Dawson one has 6 isomers). The Keggin structure is based on twelve metal atoms surrounding one heteroatom, each metal is linked to six

oxygens and the heteroatom to four. More precisely, it is composed of four "M_3O_{13}" (three edge-sharing octahedra) groups each one of them being connected to others and to the heteroatom. This complex structure has symmetry axes fitting with the tetrahedron group, giving hence rise to multiple possibilities of rotation and isomers. In case of the Dawson anion, its structure is actually based on two lacunary (a POM formally lacking one or many of its metallic centers) Keggin, $[XM_9O_{34}]^{n-}$, merging in a dimer with eighteen metals and two heteroatoms.

POMs synthesis has been refined for nearly two centuries but in the end the basic principle itself is well-known and quite easy to sum up. It is based on the addition of acids to an aqueous solution of oxide metallic salt. A polycondensation – olation/oxolation processes occur when precursors are turned into hydroxides and then oxides, as schematized in *Fig.* 3. Due to their anionic profile, polyoxometalates are surrounded by cations (potassium, sodium, tetrabutylammonium…). POM synthesis is thus governed by pH control and continues to be studied by scientific community.[10]

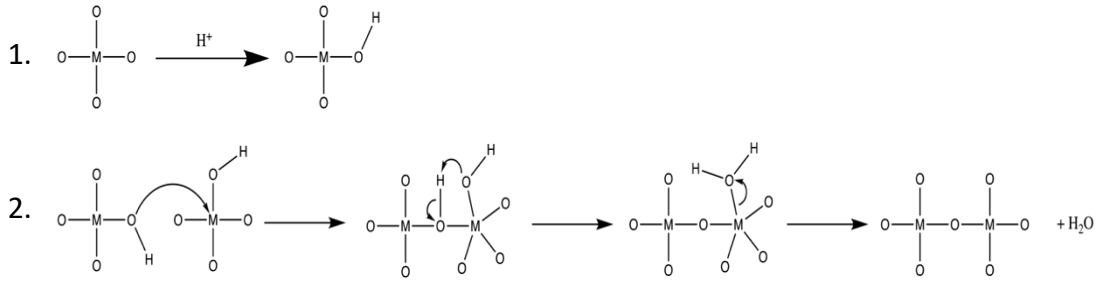

Figure 3 - POM synthesis; 1. Acidic catalysis; 2. Oxolation

1.2.2. CHARACTERISATION

Once it has been synthesized, POMs displays various properties that can be investigated through a wide variety of analytical techniques. While IR spectroscopy can be an interesting way to distinguish isomers (among others information),[11] NMR (^{183}W, ^{95}Mo, ^{51}V)[12] or mass spectrometry[13] can also give information on the structure of synthesized in solution. At the solid-state, scanning tunneling microscopy (STM)[14]

is able to provide insightful information (*Fig.* 4) – even if reproducibility of this technique is questionable.

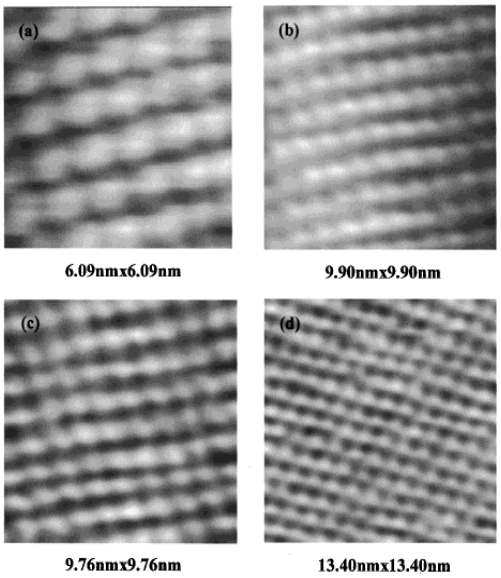

Figure 4 – STM images of (a) $H_3PW_{12}O_{40}$, (b) $H_4SiW_{12}O_{40}$, (c) $H_5BW_{12}O_{40}$, (d) $H_6CoW_{12}O_{40}$ freshly deposited on graphite. I. K. Song et al.; Inorg. Chem., 2002, 41, 5, 1292-1298.

1.2.3. REDOX PROPERTIES

As oxidized forms of POMs are composed of metals in their highest oxidation state, these compounds often display fascinating redox properties. Among the different seires, the Keggin and Dawson ones stand out. A famous example in Keggin is the metatungstate ion $[H_2W_{12}O_{40}]^{6-}$ that can be reduced 24 times, by Prof. J.-P. Launay, in a fully reversible process;[15] but Dawson reversible multi-redox experiment was also observed (*Fig.* 5).[16] In both cases, the added electrons are located on the metallic

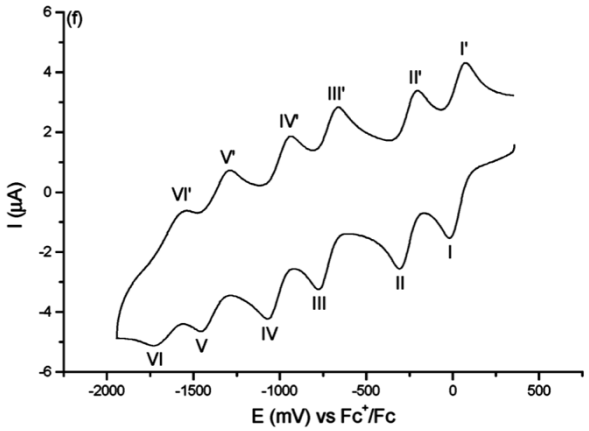

Figure 5 – Cycling voltammograms (0.1 $V.s^{-1}$) obtained in 1-n-butyl-3-methylimidazolium hexafluorophosphate, with glassy carbon working electrode, POM being $(TBA)_4[S_2W_{18}O_{62}]$ (5 mM). J. Zhang et al.; Inorg. Chem., 2005, 44, 5123.

atoms in d orbital with a non-binding character, leading to very limited nuclear reorganization, facilitating the reversibility of the redox properties.

1.2.4. APPLICATION

Not only thanks to their vast versatility in composition, structure, dimension or charge, but also because of their stability and non-toxicity, POMs offer a wide range of applications, which has, most of the time, for only limitation the imagination of researchers around the world. The most historical application field for them is catalysis. They have been indeed highly for their catalytic activities, in both homogeneous[17] and heterogeneous[18,19] situations and many reviews where published on potential applications, such as the one from Prof. Ronny Neumann and coll. enlightening electron transfer oxidation for catalysis.[20] POMs exhibit both multi-electron redox potentials and fast reversible charge transfer properties, this combination makes them

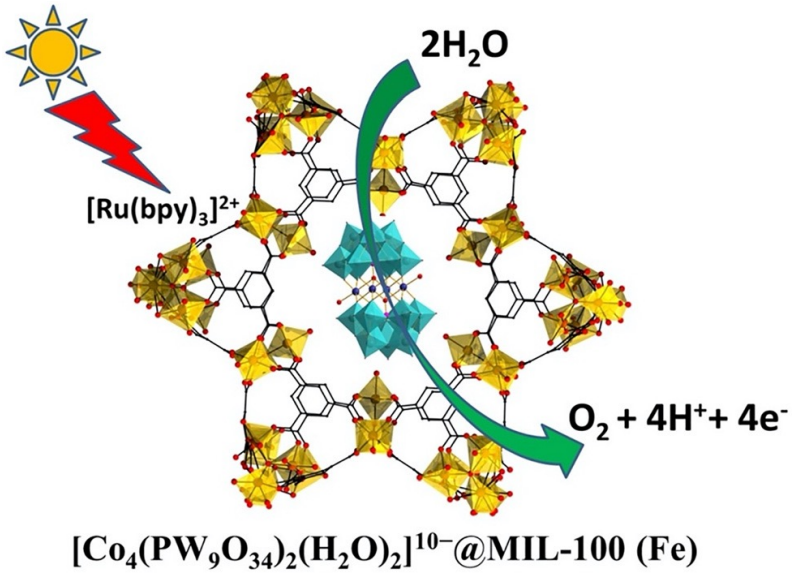

Figure 6 – Encapsulation of cobalt-based POMs in the cavities of iron-based PMOF (MIL-100) for photocatalytic OER (Oxygen Evolution Reaction) process. W. A. Shah et al.; Appl. Catal. Gen., 2018, 567, 132-138.

highly relevant in the quest of solar induced water splitting and their encapsulation in large MOFs-based or COFs-based frameworks is under vigorous study.[21,22]

Furthermore, POMs are also used for other applications thanks to their redox properties.[23] For instance they have been used studied for batteries,[24] electro- and photochromic[25] and memory[26] devices. A notable example in POM-based lithium-ion batteries was reported by Prof. Kunio Awaga and coll. with the case of carbon

nanotubes for electrode.[27] To solve the problem concerning slow charging/discharging rate and insufficient cyclability, they developed a nanohybridization between POMs ($(TBA)_3[PMo_{12}O_{40}]$) and carbon nanotubes. This new system presented a higher battery capacity and faster charging/discharging in comparison with precedent systems. The goal being to improve both electron transport and Li^+ dispersion in batteries. A recent review from Prof. Jia-Jia Chen and coll. presents in details this POMs application topic involving their intrinsic charge carriers characteristic in various situations (memory, solar and thermal driven system, energy storage…).[28]

2. POLYOXOMETALATE-BASED HYBRIDS

2.1. HYBRIDS: PRESENTATION & SYNTHESIS

POMs can be covalently associated to one or several organic arms giving rise to so-called polyoxometalates-based hybrids. While the term POM hybrid is also used

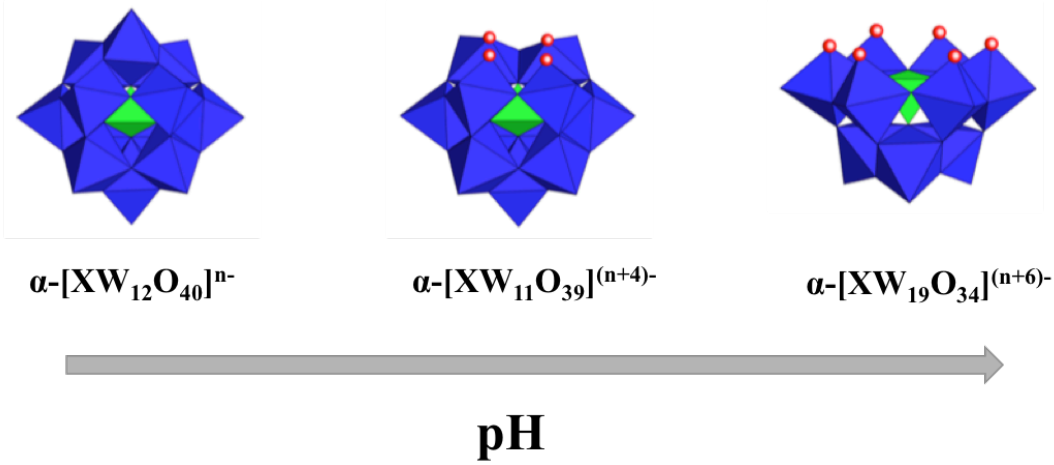

Figure 7 - Keggin dismemberment under basic conditions

for species resulting from the electrostatic association of a POM with an organic cation, in this thesis we define POM-based hybrids as compounds in which one or several organic moieties are covalently grafted onto the polyoxometalate framework. The science of attaching organic moieties to these oxo-clusters requires a certain degree of finesse in execution but allows to multiply the possibilities of application.[29]

It often starts with the obtention of a lacunary species, which is the name given to a polyoxometalate that formally lacks one metallic center. To do so, the POM needs to be dismembered in a basic aqueous solution, the key parameter being a very precise control of the pH (*Fig.* 7).

For the next step, its reaction with an organometalloid is realized under, again, closely controlled acidic pH. After purification, the final product is an organic/inorganic hybrid compound in which the polyoxometalate has exchanged one (or several) metallic center for an organometalloid. Among the most frequently utilised organic groups for POM hybrids are organotin,[30] organosilicates (*Fig.* 8) and organophosphonates.

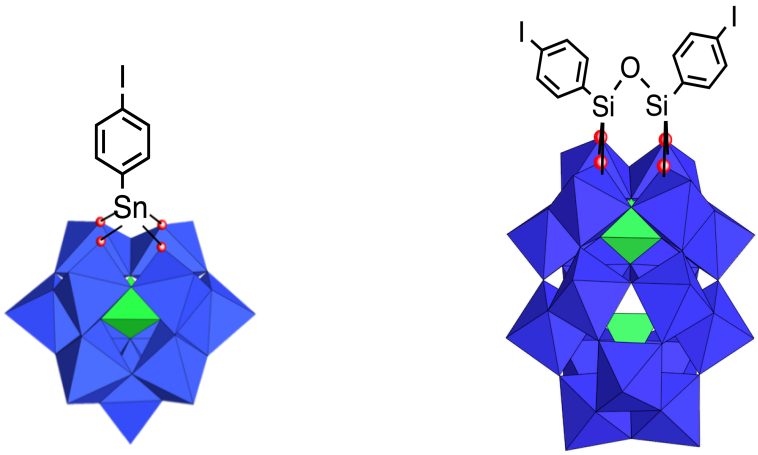

Figure 8 - Examples of POM hybrids used in this thesis; Keggin-type $[PW_{11}O_{39}SnC_6H_4I]^{4-}$ (left); Dawson-type $[P_2W_{17}O_{62}Si_2C_{12}H_8I_2]^{6-}$ (right)

Now that an organic arm is attached to the POM, the final step is to post-functionalize it to obtain the desired platform. In this thesis used Sonogashira cross-coupling reactions (*Fig.* 9), but other processes can be used like peptide bond formation have also been reported (with amino-terminated POM-based platforms). Named after Kenkichi Sonogashira, who first reported this reaction in 1975 with Nobue Hagihara, it is based on two cycles with two different catalysts (palladium and copper). This reaction allows to substitute the halogen termination of the arm with a triple carbon-carbon bond. Practically, this reaction can be applied to an almost unlimited

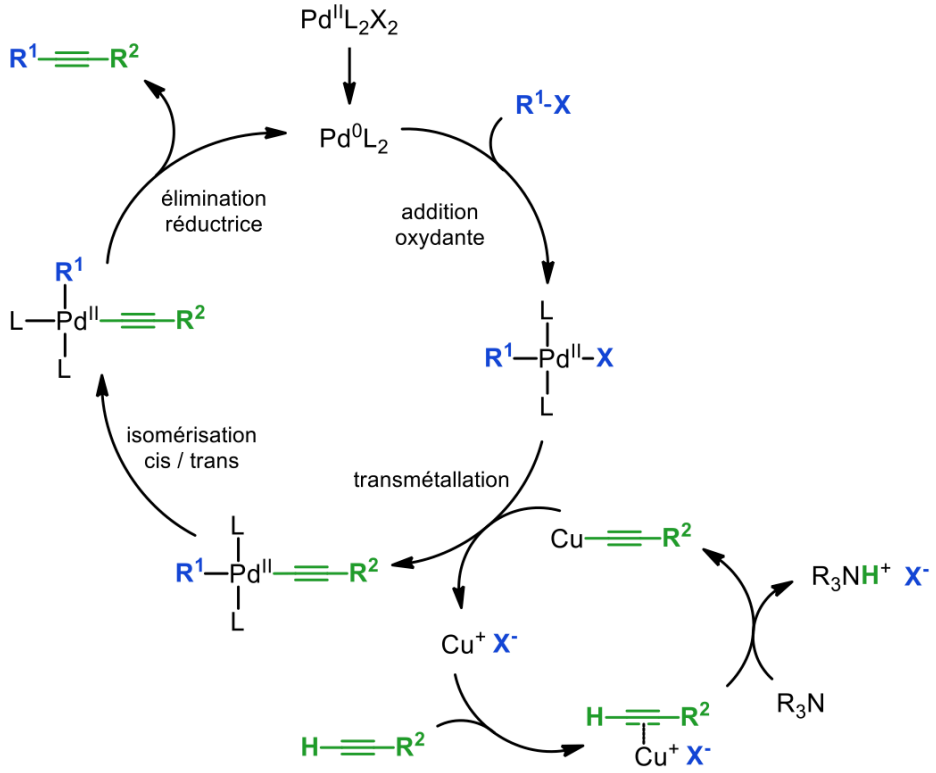

Figure 9 - Scheme of Sonogashira cross-coupling

number of compounds bearing a terminal alkyne function and thus allows the elaboration of a large variety of hybrid POMs starting from a limited number of hybrid POM-based platforms.

2.2. SELECTED EXAMPLES

Hybridization of POMs can aim at a gain in structuration, allowing a POM-based architecture deposition or a new deposition possibility, or in properties. Since the domain of POM-based hybrids is too vast to be summarize here, it was necessary to determine some limits. Thus, this part will mostly focus on the expertise of our group, i.e. POM hybrids, and self-assembled POM-based systems as this will constitute a part of the work developed in this thesis.

In the properties enhancement's area, in 2018, Dr. Elizabeth A. Gibson and Dr. Guillaume Izzet and coll. studied the photoactive character of POMs hybridized with bodipy sensitizers. They evaluated the kinetic of the electron transfer (forward and backward), when the compound was light irradiated.[31] This study successfully revealed the occurrence of photoinduced electron transfer, from the bodipy to the POM, opening the door for future applications in solar energy conversion.

If POM hybridization can be seen as a way to add supplementary properties to the polyoxometalate itself, it is frequently the opposite that is aimed: enhancement of the organic moiety or of a third compound characteristics by the addition of the polyoxometalate. In a paper from 2013, Prof. Pierre Mialane and coll. reported a very interesting case of property enhancement induced by the attachment of a POM.[32] Spiropyran derivatives (SPR) are renowned for the photochromic property in solution, but not in solid-state. However, when covalently bonded to a lacunary polyoxometalate, the system revealed the appearance of a large absorption peak in the visible domain (*Fig.* 10).

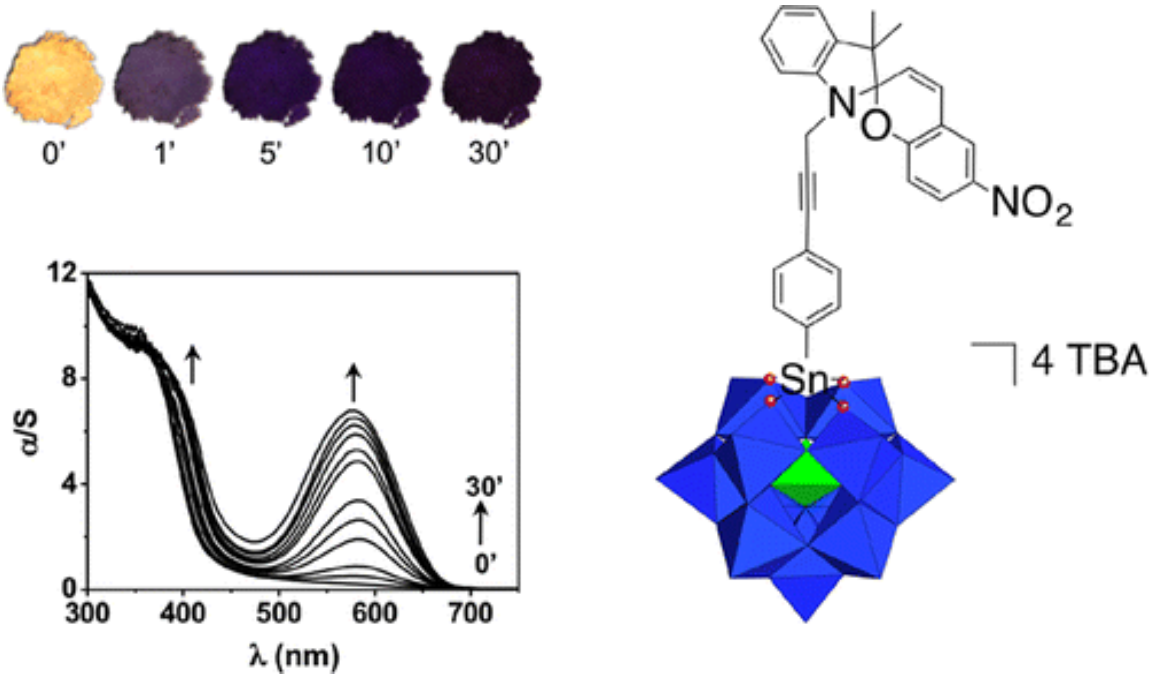

Figure 8 - (right) TBA.K_{Sn}[SPR]; (upper left) photographs of powders of TBA.K_{Sn}[SPR] after different 365 nm UV irradiation times (in min); (bottom left) evolution of the photogenerated absorption in TBA.K_{Sn}[SPR] after 0, 0.166, 0.5, 1, 1.5, 2, 3, 4, 5, 8, 15 and 30 min of UV irradiation (365 nm). A. Parrot et al.; Inorg. Chem., 2013, 52, 11156-11163.

However, POMs hybridization can be realized, not to obtain new properties but in order to deposit the POM on new surfaces, or to structure the deposition. In a paper from 2014, Prof. Anna Proust, Prof. Eugenio Coronado and coll. enlightened the case of POM hybrids ($[P_2W_{17}O_{61}\{O(Si\text{-}phenyl\text{-}ethynyl\text{-}pyrene)_2\}]^{6-}$) utilized to enhance single-walled carbon nanotubes (SWCNT), turning it into a potential electron reservoir thanks to POM capacity to play the electron acceptor role and SWCNT the electron donor role (when it is usually an electron acceptor).[33] Polyoxometalate hybrids cover around 10 % of the total nanotube surface thank to π – π stacking between sidewalls and π – conjugated pyrenes.

In another domain but still with the objective of gaining more control and understanding on POM hybrid and their organization, Prof. Anna Proust and coll. published in 2016 an article about surface organization on POM hybrids immobilized on gold surface.[34] Here a lacunary Keggin is functionalized by a remote acid group to allow S-Au covalent bond, but the key of the system is a two-dimensions honeycomb structure obtained by self-assembly of melamine and PTCDI (perylene-3-4-9-10-tetracarboxylic acid diimide) (*Fig.* 11). This network allowed to obtain an ordered structure from the bonded POM hybrids.

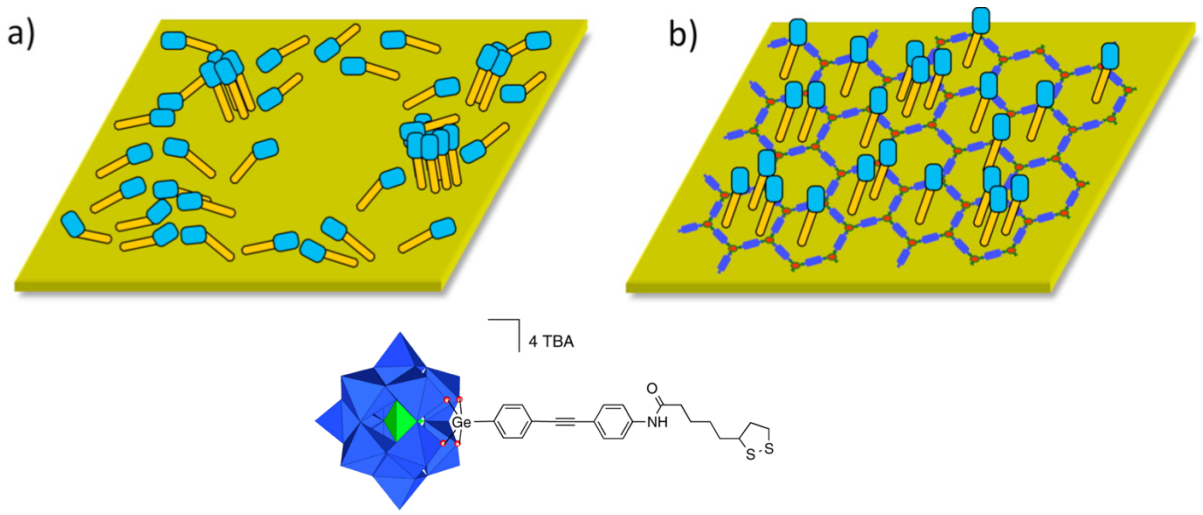

Figure 9 – Representation of the level of organization of (a) $TBA_4[PW_{11}O_{39}\{Ge(C_6H_4)C{\equiv}C(C_6H_4)NHCO(C_7H_{13}S_2)\}]$ on bare Au (111); (b) $TBA_4[PW_{11}O_{39}\{Ge(C_6H_4)C{\equiv}C(C_6H_4)NHCO(C_7H_{13}S_2)\}]$ on the PTCDI/Melamine templated Au(111) surface; (bottom) scheme representation of the concerned POM. A. Lombana, et al. ; J. Phys. Chem. C, 2016, 120, 2837-2845

In 2019 Prof. Tianbo Liu and Prof. Leroy Cronin investigated the driving forces ruling a POM hybrids-based macrostructure.[35] The idea being to ally nature's building blocks, aka peptides, with the inorganic building blocks that are POMs. The hybrid developed was based on the Anderson-Evans structure hybridized by the addition of two peptides. While the hybrid behaves as discrete species in acetonitrile, oligomerization process will occur when water is poured to the solution, to finally reach a single-layered blackberry structure formation (*Fig.* 12). This study concluded that the self-assembly structure is ruled by strong electrostatic interaction and weak hydrogen bonding.

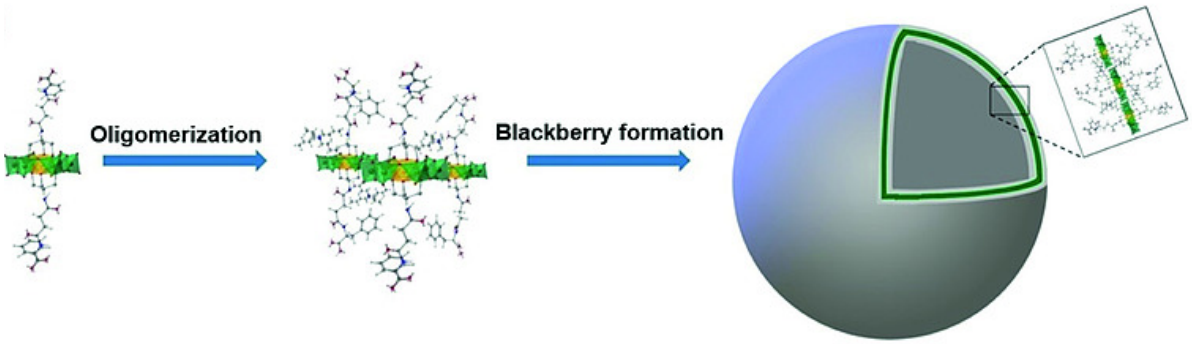

Figure 10 – Illustration of single-layer blackberry-like formation process. J. Luo et al.; Eur. J. Inorg. Chem., 2019, 380-386

By definition, POM hybrids can easily be tuned to be amphiphilic species. Indeed, the polyoxometalate will be water soluble (if the correct counter-ion is selected), so the addition of an alkyl chain (which has a tendency to hydrophobia) will reveal the amphiphilic potential of the compound. This is quite interesting since it means possibility to interact with two different phases, it generally leads to self-assembled highly ordered structures.[36] Furthermore, in 2003 Prof. R. Carlisle Chambers reported mono and multilayers reversible films obtained from Keggin hybrids with alkyl chains, using the Langmuir-Blodgett technique to synthesize it at the air-water interface.[37]

Finally, it is worth noticing that sometimes, hybridization of POMs can lead to both of the possibilities detailed previously. One recent example is from Dr Guillaume Izzet and coll., where a lacunary POM was functionalized by the addition of bis(thiophene)thienothiophene (BTTT) units (*Fig.* 13).[38] These organic functional groups allowed the apparition of a smectic-like multi-layered structure and at the same time brang an electron donor property, complementary with the intrinsic electron acceptor character of the POM.

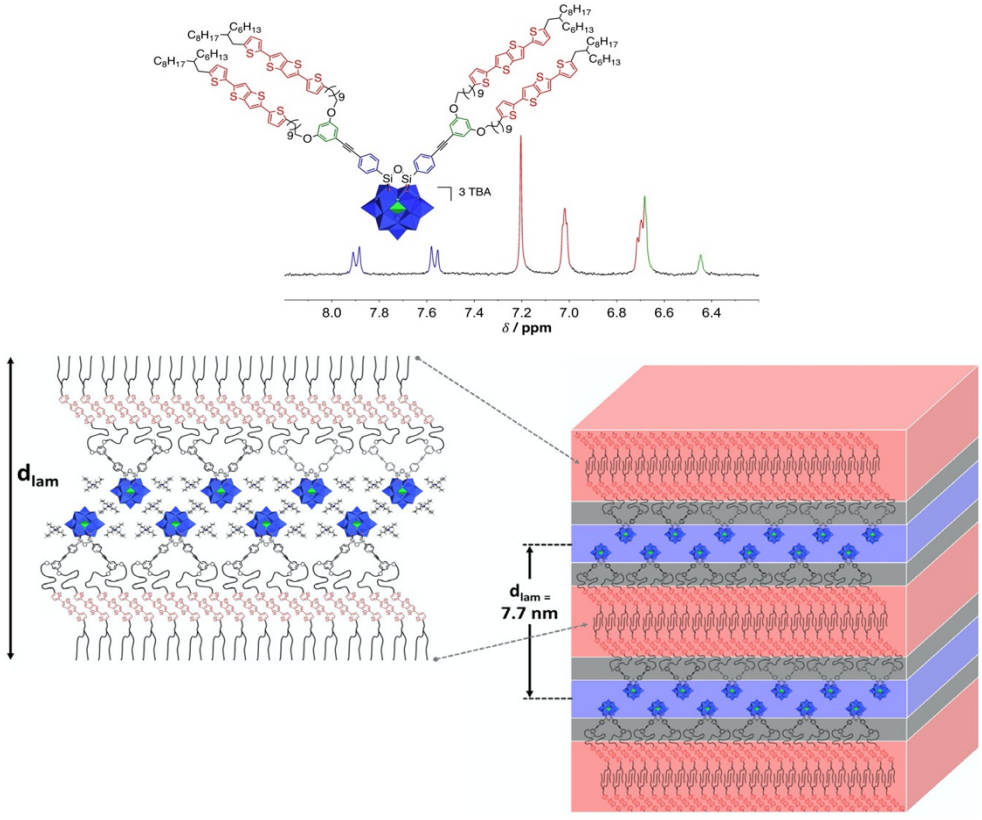

Figure 11 – (top) Molecular representation and elargement of the aromatic ppm region of the ^1H NMR of K_{Si}[BTTT-2] in CD_2Cl_2. (down) 3D schematic representation of K_{Si}[BTTT-2] arrangement. X. Zhu et al.; Angew. Chem. Int. Ed., 2021, 60, 8419-8424.

3. PROBLEM-STATEMENT AND OBJECTIVES

As previously discussed, polyoxometalates are promising compounds in many aspects of cutting-edge science as well as daily life issues like energy production. Being a co-tutelle, this thesis aims to leverage the strengths of two different groups, universities and scientific cultures and approaches in view of making one step further in the direction of inserting POM hybrids in soft materials for nano-electronics devices. Allying expertise of the Prof. Proust group at Sorbonne Université on turning POMs in platforms for multiple applications, with the application aspect offered by Prof. Lee group at Nanyang Technological University. Two fields were chosen for this work, auto-assemblies and memory devices, where the goal was to obtain a stable POM-based system without the classical issues encountered in memory such as volatility.

In this thesis, the work will be detailed in two parts. On one hand, polyoxometalates hybrids-based self-assemblies, in both discrete and macro structures, looking for applications as soft materials (described in Part II). On the other hand, grafting of POMs hybrids to substrates, reaching for memory devices applications in nano-electronics (described in Part III). The hypothesis relying on the unique feature that the redox behavior of the POMs hybrids could provide in the electrical performance of the bistable memory states with the aid of the self-assembly structures on conductive surfaces.

4. REFERENCES

(1) Keggin, J. F. Structure of the Molecule of 12-Phosphotungstic Acid. *Nature* **1933**, *131* (3321), 908–909. https://doi.org/10.1038/131908b0.
(2) Pauling, L. The Molecular of the Tungstosilicates and Related Compounds. *J. Am. Chem. Soc.* **1929**, *51* (10), 2868–2880. https://doi.org/10.1021/ja01385a002.
(3) Chauveau, F.; Souchay, P. Nouveaux composes a structure d'heteropolyanions, renfermant du fluor. *J. Inorg. Nucl. Chem.* **1974**, *36* (8), 1761–1770. https://doi.org/10.1016/0022-1902(74)80508-7.
(4) Lamache, M.; Souchay, P. Mécanisme de réduction du molybdène (VI) dans l'acide chlorhydrique peu concentré, sur électrode de mercure. *J. Chim. Phys.* **1973**, *70*, 384–391. https://doi.org/10.1051/jcp/1973700384.
(5) Pope, M. T.; Müller, A. Polyoxometalate Chemistry: An Old Field with New Dimensions in Several Disciplines. *Angew. Chem. Int. Ed. Engl.* **1991**, *30* (1), 34–48. https://doi.org/10.1002/anie.199100341.
(6) Hervé, G.; Tézé, A. Study of Alpha- and Beta.-Enneatungstosilicates and -Germanates | Inorganic Chemistry. *Rev. Inorg. Chem.* **2002**, *22*, 63–111.
(7) Müller, A.; Kögerler, P.; Kuhlmann, C. A Variety of Combinatorially Linkable Units as Disposition:† from a Giant Icosahedral Keplerate to Multi-Functional Metal–Oxide Based Network Structures. *Chem. Commun.* **1999**, No. 15, 1347–1358. https://doi.org/10.1039/a901436e.
(8) Müller, A.; Das, S. K.; Kögerler, P.; Bögge, H.; Schmidtmann, M.; Trautwein, A. X.; Schünemann, V.; Krickemeyer, E.; Preetz, W. A New Type of Supramolecular Compound: Molybdenum-Oxide-Based Composites Consisting of Magnetic Nanocapsules with Encapsulated Keggin-Ion Electron Reservoirs Cross-Linked to a Two-Dimensional Network. *Angew. Chem. Int. Ed.* **2000**, *39* (19), 3413–3417. https://doi.org/10.1002/1521-3773(20001002)39:19<3413::AID-ANIE3413>3.0.CO;2-Q.
(9) Müller, A.; Beckmann, E.; Bögge, H.; Schmidtmann, M.; Dress, A. Inorganic Chemistry Goes Protein Size: A Mo368 Nano-Hedgehog Initiating Nanochemistry by Symmetry Breaking. *Angew. Chem. Int. Ed.* **2002**, *41* (7), 1162–1167. https://doi.org/10.1002/1521-3773(20020402)41:7<1162::AID-ANIE1162>3.0.CO;2-8.
(10) Gumerova, N. I.; Rompel, A. Polyoxometalates in Solution: Speciation under Spotlight. *Chem. Soc. Rev.* **2020**, *49* (21), 7568–7601. https://doi.org/10.1039/D0CS00392A.
(11) Fournier, M.; Franck, R.; Rocchiccioli-Deltcheff, C. Vibrational Investigations of Polyoxometalates. 3. Isomerism in Molybdenum(VI) and Tungsten(VI) Compounds Related to the Keggin Structure. *Inorg. Chem. 23* (5), 598–605.
(12) Fedotov, M.; Maksimovskaya, R. NMR Structural Aspects of the Chemistry of V, Mo, W Polyoxometalates. *J. Struct. Chem.* **2006**, *47*, 952–978. https://doi.org/10.1007/s10947-006-0413-6.
(13) Song, Y.-F.; Long, D.-L.; Kelly, S. E.; Cronin, L. Sorting the Assemblies of Unsymmetrically Covalently Functionalized Mn-Anderson Polyoxometalate Clusters with Mass Spectrometry. *Inorg. Chem.* **2008**, *47* (20), 9137–9139. https://doi.org/10.1021/ic801366r.
(14) Song, I. K.; Shnitser, R. B.; Cowan, J. J.; Hill, C. L.; Barteau, M. A. Nanoscale Characterization of Redox and Acid Properties of Keggin-Type Heteropolyacids by Scanning Tunneling Microscopy and Tunneling Spectroscopy: Effect of Heteroatom Substitution. *Inorg. Chem.* **2002**, *41* (5), 1292–1298. https://doi.org/10.1021/ic010832d.
(15) Launay, J. P. Réduction de l'ion métatungstate: stades élevés de réduction de $H_2W_{12}O_{40}^{6-}$, dérivés de l'ion HW12O407- et discussion générale. 10.
(16) Zhang, J.; Bond, A. M.; MacFarlane, D. R.; Forsyth, S. A.; Pringle, J. M.; Mariotti, A.

W. A.; Glowinski, A. F.; Wedd, A. G. Voltammetric Studies on the Reduction of Polyoxometalate Anions in Ionic Liquids. *Inorg. Chem.* **2005**, *44* (14), 5123–5132. https://doi.org/10.1021/ic050032t.
(17) Hill, C. L.; Prosser-McCartha, C. M. Homogeneous Catalysis by Transition Metal Oxygen Anion Clusters. *Coord. Chem. Rev.* **1995**, *143*, 407–455. https://doi.org/10.1016/0010-8545(95)01141-B.
(18) Zhou, Y.; Chen, G.; Long, Z.; Wang, J. Recent Advances in Polyoxometalate-Based Heterogeneous Catalytic Materials for Liquid-Phase Organic Transformations. *RSC Adv.* **2014**, *4* (79), 42092–42113. https://doi.org/10.1039/C4RA05175K.
(19) Samaniyan, M.; Mirzaei, M.; Khajavian, R.; Eshtiagh-Hosseini, H.; Streb, C. Heterogeneous Catalysis by Polyoxometalates in Metal–Organic Frameworks. *ACS Catal.* **2019**, *9* (11), 10174–10191. https://doi.org/10.1021/acscatal.9b03439.
(20) Weinstock, I. A.; Schreiber, R. E.; Neumann, R. Dioxygen in Polyoxometalate Mediated Reactions. *Chem. Rev.* **2018**, *118* (5), 2680–2717. https://doi.org/10.1021/acs.chemrev.7b00444.
(21) Ullah, I.; Munir, A.; Haider, A.; Ullah, N.; Hussain, I. Supported Polyoxometalates as Emerging Nanohybrid Materials for Photochemical and Photoelectrochemical Water Splitting. *Nanophotonics* **2021**, *10* (6), 1595–1620. https://doi.org/10.1515/nanoph-2020-0542.
(22) Shah, W. A.; Waseem, A.; Nadeem, M. A.; Kögerler, P. Leaching-Free Encapsulation of Cobalt-Polyoxotungstates in MIL-100 (Fe) for Highly Reproducible Photocatalytic Water Oxidation. *Appl. Catal. Gen.* **2018**, *567*, 132–138. https://doi.org/10.1016/j.apcata.2018.08.002.
(23) Ueda, T. Electrochemistry of Polyoxometalates: From Fundamental Aspects to Applications. *ChemElectroChem* **2018**, *5* (6), 823–838. https://doi.org/10.1002/celc.201701170.
(24) Huang, B.; Yang, D.-H.; Han, B.-H. Application of Polyoxometalate Derivatives in Rechargeable Batteries. *J. Mater. Chem. A* **2020**, *8* (9), 4593–4628. https://doi.org/10.1039/C9TA12679A.
(25) Liu, S.; Möhwald, H.; Volkmer, D.; Kurth, D. G. Polyoxometalate-Based Electro- and Photochromic Dual-Mode Devices. *Langmuir* **2006**, *22* (5), 1949–1951. https://doi.org/10.1021/la0523863.
(26) Busche, C.; Vilà-Nadal, L.; Yan, J.; Miras, H. N.; Long, D.-L.; Georgiev, V. P.; Asenov, A.; Pedersen, R. H.; Gadegaard, N.; Mirza, M. M.; Paul, D. J.; Poblet, J. M.; Cronin, L. Design and Fabrication of Memory Devices Based on Nanoscale Polyoxometalate Clusters. *Nature* **2014**, *515* (7528), 545–549. https://doi.org/10.1038/nature13951.
(27) Kawasaki, N.; Wang, H.; Nakanishi, R.; Hamanaka, S.; Kitaura, R.; Shinohara, H.; Yokoyama, T.; Yoshikawa, H.; Awaga, K. Nanohybridization of Polyoxometalate Clusters and SingleWall Carbon Nanotubes: Applications in Molecular Cluster Batteries. *Angew Chem Int Ed* **2011**, 4.
(28) Yang, L.; Lei, J.; Fan, J.; Yuan, R.; Zheng, M.; Chen, J.; Dong, Q. The Intrinsic Charge Carrier Behaviors and Applications of Polyoxometalate Clusters Based Materials. *Adv. Mater.* **2021**, 2005019. https://doi.org/10.1002/adma.202005019.
(29) Anyushin, A. V.; Kondinski, A.; Parac-Vogt, T. N. Hybrid Polyoxometalates as Post-Functionalization Platforms: From Fundamentals to Emerging Applications. *Chem. Soc. Rev.* **2020**, *49* (2), 382–432. https://doi.org/10.1039/C8CS00854J.
(30) Bareyt, S.; Piligkos, S.; Hasenknopf, B.; Gouzerh, P.; Lacôte, E.; Thorimbert, S.; Malacria, M. Efficient Preparation of Functionalized Hybrid Organic/Inorganic Wells−Dawson-Type Polyoxotungstates. *J. Am. Chem. Soc.* **2005**, *127* (18), 6788–6794. https://doi.org/10.1021/ja050397c.

(31) Black, F. A.; Jacquart, A.; Toupalas, G.; Alves, S.; Proust, A.; Clark, I. P.; Gibson, E. A.; Izzet, G. Rapid Photoinduced Charge Injection into Covalent Polyoxometalate–Bodipy Conjugates. *Chem. Sci.* **2018**, *9* (25), 5578–5584. https://doi.org/10.1039/C8SC00862K.
(32) Parrot, A.; Izzet, G.; Chamoreau, L.-M.; Proust, A.; Oms, O.; Dolbecq, A.; Hakouk, K.; El Bekkachi, H.; Deniard, P.; Dessapt, R.; Mialane, P. Photochromic Properties of Polyoxotungstates with Grafted Spiropyran Molecules. *Inorg. Chem.* **2013**, *52* (19), 11156–11163. https://doi.org/10.1021/ic401380a.
(33) Bosch-Navarro, C.; Matt, B.; Izzet, G.; Romero-Nieto, C.; Dirian, K.; Raya, A.; Molina, S. I.; Proust, A.; Guldi, D. M.; Martí-Gastaldo, C.; Coronado, E. Charge Transfer Interactions in Self-Assembled Single Walled Carbon Nanotubes/Dawson–Wells Polyoxometalate Hybrids. *Chem Sci* **2014**, *5* (11), 4346–4354. https://doi.org/10.1039/C4SC01335B.
(34) Lombana, A.; Rinfray, C.; Volatron, F.; Izzet, G.; Battaglini, N.; Alves, S.; Decorse, P.; Lang, P.; Proust, A. Surface Organization of Polyoxometalate Hybrids Steered by a 2D Supramolecular PTCDI/Melamine Network. *J. Phys. Chem. C* **2016**, *120* (5), 2837–2845. https://doi.org/10.1021/acs.jpcc.5b11945.
(35) Luo, J.; Zhang, B.; Yvon, C.; Hutin, M.; Gerislioglu, S.; Wesdemiotis, C.; Cronin, L.; Liu, T. Self-Assembly of Polyoxometalate–Peptide Hybrids in Solution: Elucidating the Contributions of Multiple Possible Driving Forces. *Eur. J. Inorg. Chem.* **2019**, *2019* (3–4), 380–386. https://doi.org/10.1002/ejic.201800158.
(36) Li, D.; Yin, P.; Liu, T. Supramolecular Architectures Assembled from Amphiphilic Hybrid Polyoxometalates. *Dalton Trans.* **2012**, *41* (10), 2853–2861. https://doi.org/10.1039/C2DT11882C.
(37) Chambers, R. C.; Atkinson, E. J. O.; McAdams, D.; Hayden, E. J.; Brown, D. J. A. Creating Monolayers and Thin Films of a Novel Bis(Alkyl) Substituted Asymmetrical Polyoxotungstate, {[CH3(CH2)11Si]2OSiW11O39}4− Using the Langmuir–Blodgett Technique. *Chem. Commun.* **2003**, No. 19, 2456–2457. https://doi.org/10.1039/B307808F.
(38) Zhu, X.; Hessin, C.; Salamé, A.; Sosa-Vargas, L.; Kreher, D.; Adachi, C.; Proust, A.; Mialane, P.; Marrot, J.; Bouchet, A.; Sliwa, M.; Méry, S.; Heinrich, B.; Mathevet, F.; Izzet, G. Photoactive Organic/Inorganic Hybrid Materials with Nanosegregated Donor–Acceptor Arrays. *Angew. Chem. Int. Ed.* **2021**, *60* (15), 8419–8424. https://doi.org/10.1002/anie.202014319.

PART II – MACROMOLECULAR AUTO-ASSEMBLIES

1. INTRODUCTION

1.1. AUTO-ASSEMBLIES OVERVIEW

Auto-assembly corresponds to the auto-induced aggregation of tuned molecules in larger concretion. The formation can be governed by different interactions covalent or not (π- π stacking, Van der Waals interaction, electrostatic interaction, polarity, hydrogen bonding, metal-ligand interaction…). Self-assembled systems, if not well prepared upstream, can lead to various unexpected structures. To avoid this issue, a solution can be to proceed to a selection when it comes to the building block and the bonding type. Metal-ligand bond, being directional and selective can be seen as a solution. Indeed, the preferential geometry of many metallic ions is well-known, high predictability of the obtained discrete structure can then be expected.

The impact on the synthesis conditions and the final product, of the variation from both the ligand and the metallic complex, has been studied to obtain better understanding on this kind of system. When it comes to self-assembly architecture, the competition between the enthalpy and the entropy is a keystone. When enthalpy will try to preserve the original structure of the components, entropy will prefer to constrain it to form the smaller discrete species.

One famous example of metal-ligand based auto-assembled structures in a previously determined geometry has been reported by Prof. Fujita and its group.[1] They presented a square-shape nanostructure born from the interaction between palladium (II) clusters and pyridine moieties (*Fig.* 1).

After confirming that the resulting species was square-shaped as expected, they investigated the impact of a metallic variation by comparing it with an analogue platinum (II) complex. While the square shape is easily obtained at ambient temperature in the first case, modification of the metallic center into platinum requires heating of the solution for several weeks to override the natural inertia of platinum complexes.

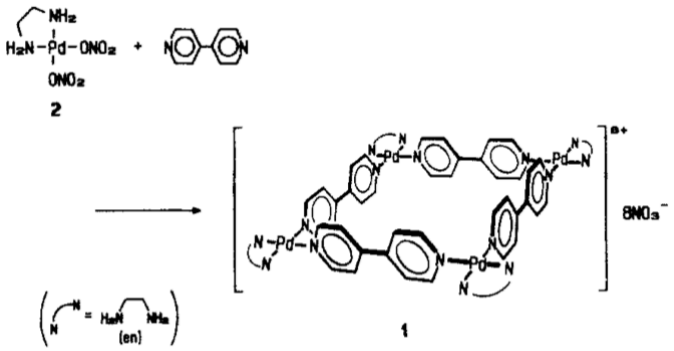

Figure 12 – Synthesis of a square-planar Pd(II) complex [(en)Pd(4,4'-bpy)]$_4$(NO$_3$)$_8$. M. Fujita et al.; J. Am. Chem. Soc., 1990, 112, 14, 5645-5647.

Still on the subject of variation impact, but of the ligand too this time, Prof. Severin *et al.* published a study where the ratio length/thickness of the ligand was studied.[2] To do so, they compared the different auto-assembled systems obtained from the interaction of clathrochelate ligand with metallic centers. Their work revealed that if the final geometry is dependent of the metal, it also relies on the characteristic of the ligand as shown by *Fig.* 2. Indeed, different species were observed when the ligand is elongated, shortened or thickened.

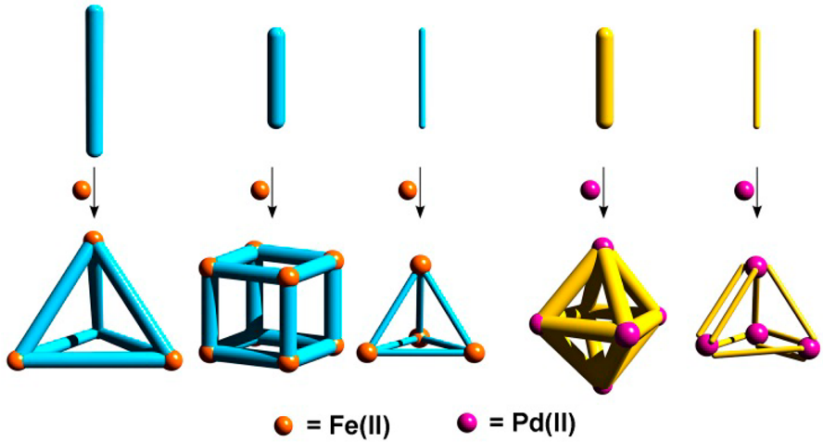

Figure 13 – Rigid rod-type ligands with different aspect ratios give rise to different coordination cages. K. Severin et al.; J. Am. Chem. Soc., 2016, 138, 6, 2046-2054.

When it comes to polyoxometalates, since they are charged structures, electrostatic interactions become key components for POM-based discrete self-assemblies. In many examples, the amphiphilic character that can be present in such species is exploited to form larger aggregates.

Prof. Wu and his group reported a study where Lindquist-type POMs ($[Mo_6O_{19}]^{2-}$) form a self-assembled structure by switching its counter-ions, tetrabutylammonium (TBA), for cationic surfactants (dioctadecyldimethylammonium, DODA).[3] If the system will first form a helical structure when the discrete species are in dichloromethane/propanol solution (4:1), it can be turned into spherical shape by the reduction of the POM (induced by light irradiation), as shown in *Fig.* 3. This process is reversible since a re-oxidation, by the addition of H_2O_2, turns the system back to its helical structure. Since the aggregation of the discrete species is governed by electrostatic interactions, modification of the POM charge induced a change in the macro structure. In another study from 2013, the same group reported another structure where POMs (Anderson type with two azobenzene grafted arms) will react with quaternary ammonium-ionized β-cyclodextrins to form a discrete self-assembled system, then the aggregation was based once again on light-induced reversibility.[4] This time, light irradiation was used to switch between *cis*- et *trans*- forms of the grafted azobenzene-derivated organic arms, allowing a control of the aggregation of the discrete species.

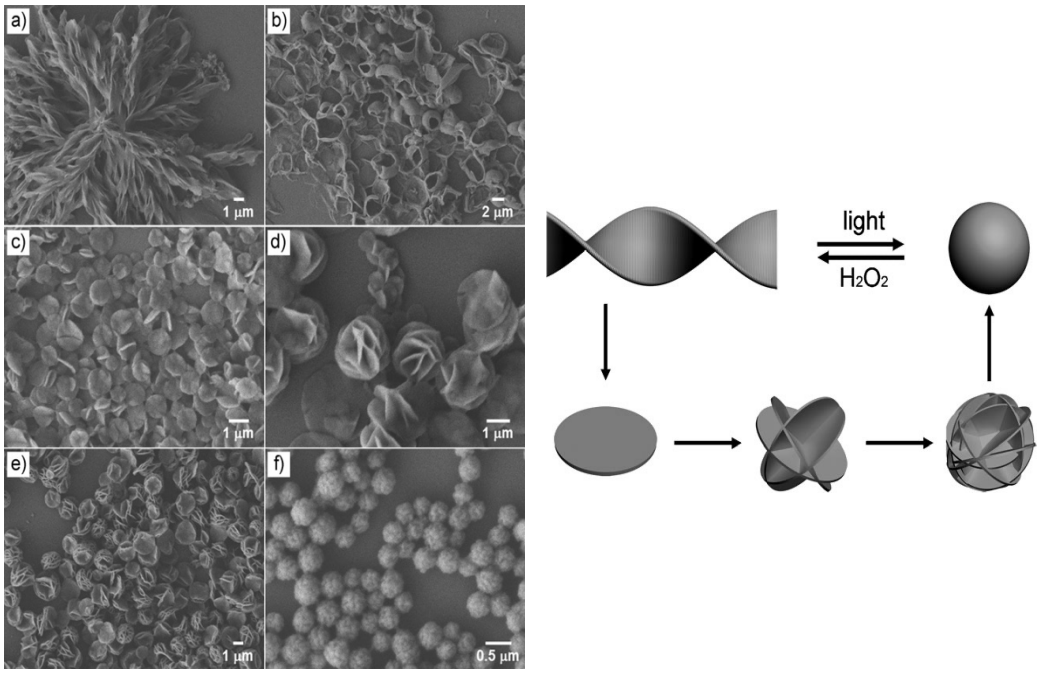

Figure 14 – (left) SEM images of a 1 mg.mL^{-1} solution of $(DODA)_2[Mo_6O_{19}]$ in dichloromethane/propanol (4:1) at 30 °C after UV irradiation for a) 0.5, b) 1.0, c) 1.5, d) 2.0, e) 3.0 and f) 4.0 min; (right) schematic evolution of the assembly of $(DODA)_2[Mo_6O_{19}]$ from helical strips to spherical structures under UV irradiation. L. Wu et al.; Chem. Eur. J., 2013, 19, 25, 8129-8135.

This switch between *cis*- and *trans*- forms was also used by Prof. Cronin *et al.* for a Dawson POM hybrid, grafted with bipyridine units, to obtain a vesicle shape (*Fig.* 4). The discrete species are aggregated thanks to the amphiphilic character gained when the organic part is in its correct *cis*- form.[5] The difference here is that the switch is not induced by light but relies on the presence or not of Zn ions (allowing rotation of the C3-C4 bond).

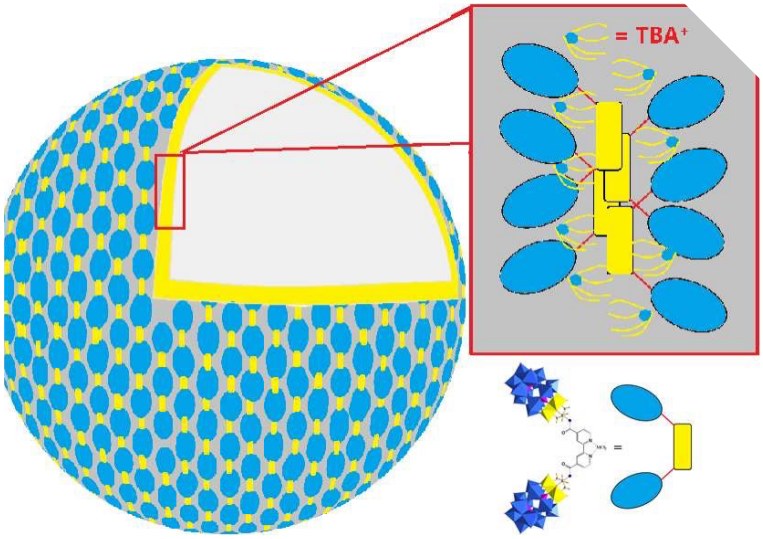

Figure 15 - Bilayer model for the vesicle structure. L. Cronin et al.; J. Am. Chem. Soc., 2013, 135, 36, 13425-13432.

However, POM-based self-assemblies relying on electrostatic interactions lack directionality. To gain control on the structure and form more complex architectures, the metal-ligand bond can be privileged, since it is selective and directional. Thus, it is worth noticing two more papers, from B. Hasenknopf and coll.[6,7] In the first one a discrete triangle was obtained by the self-assembly of a POM-based hybrid with *trans*-$[PdCl_2(CH_3CN)_2]$ (*Fig.* 5). This publication is even more interesting when read in parallel of the other one where a linear dimer was obtained. This dimer turns into a gel when the correct solvent (methanol) is added to the solution (a technic that will be detailed in part 3. of this chapter).

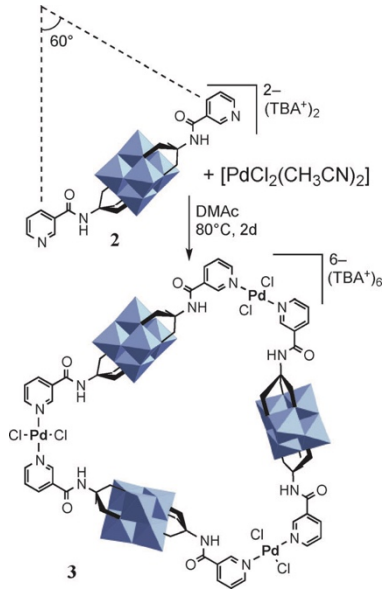

Figure 16 – Synthesis of discrete triangle from functionalized POM derivative and $PdCl_2(CH_3CN)_2$. B. Hasenknopf et al.; Chem. Commun., 2012, 48, 200-202.

1.2. APPLICATIONS

After all these fundamental studies investigating the discrete species formation, the aggregation process in large nanostructure and the variation impact of the different components, the next logical step was to consider applications. In this part some examples will be detailed to show the great potential of polyoxometalate auto-assembled macromolecular structures in human health and environment.

When it comes to human health it is not difficult to find a more harmful and global disease than cancer. This is why it is under immense attention for all scientists. In this domain, an advanced progress was made thanks to polyoxometalate. In a paper published in 2014, Prof. Li and coll. presented a hierarchical nanostructure (flower-like, *Fig.* 6) constituted of a self-assembly of dopamine and phosphotungstatic acid (PTA, $H_4[PW_{12}O_{40}]^{4-}$) used for oral drug delivery.[8]

The chosen drug for the test, doxorubicin hydrochloride (a widely used anticancer drug in chemotherapy), was loaded in the structure, the aim being to deliver it at will. Interestingly, a pH gap between stomach acidic conditions (pH 1-3) and intestine neutral conditions (pH 5-8) can be observed and thus used for delivery

conditions. As shown by *Fig.* 7, the release of the drug is succesfully realised at pH 7.4 while it is still loaded inside the nanostructure at pH 2.8.

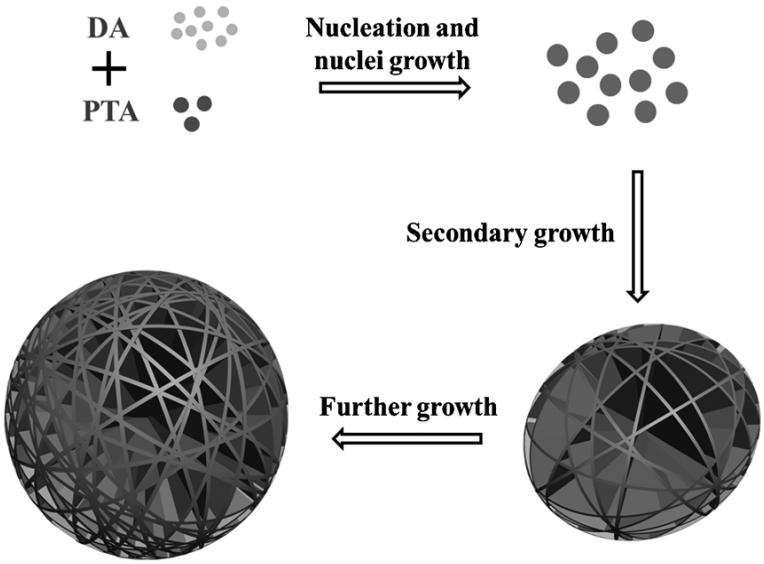

Figure 17 - Schematic illustration of the morphological evolution of flower-like hierarchical nanostructures. DA = Dopamine, PTA = $H_4[PW_{12}O_{40}]^{4-}$. Li et al.; Chem. Eur. J., 2014, 20, 499-504.

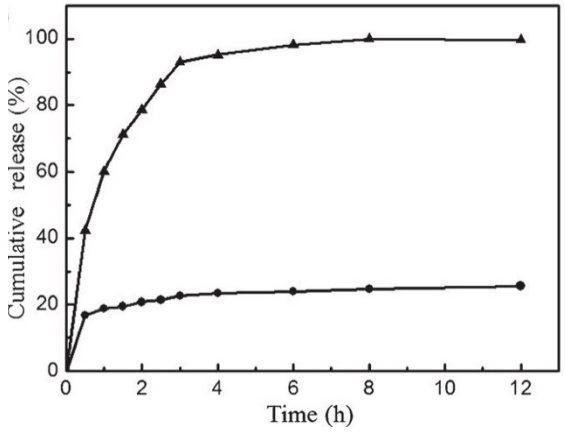

Figure 18 – Drug release profiles of doxorubicin-loaded flowerlike microspheres in pH 2.8 glycine-HCl buffer solution (●) and pH 7.4 phosphate buffered saline (PBS) solution (▲).Li et al.; Chem. Eur. J., 2014, 20, 499-504.

Treatments of the dyes found in waste water is of primordial aspect from an ecological point of view. It has been studied through the prism of POM-based auto-assemblies. Prof. Gröhn and coll. reported the case of selective photocatalytic activities resulting from the association of Keggin type POM ($[SiW_{12}O_{40}]^{4-}$) with cationic dendrimers by electrostatic self-assembly.[9] Discrete species were aggregated in supramolecular structures in aqueous solution revealing high potential for application

in photodegradation of dyes (methyl red here) degradation via the formation of radicals (*Fig.* 8).

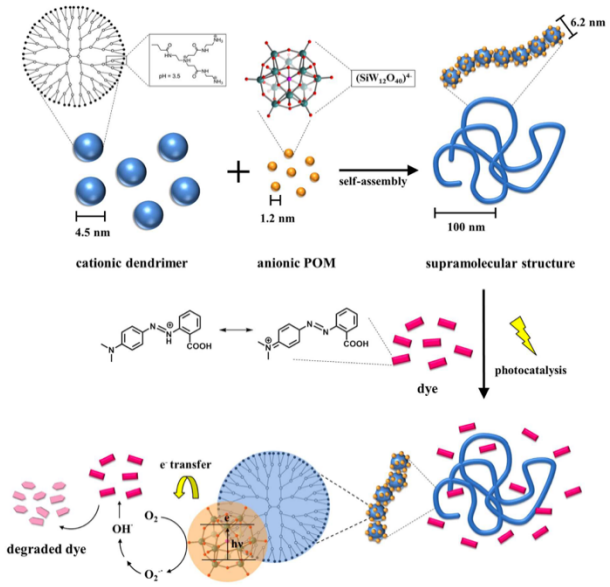

Figure 19 – Schematic representation of POM-dendrimer self-assembly and photocatalysis in aqueous solution. Catalyzed model reaction is the photo-degradation of the dye methyl red. F. Gröhn et al.; Nanoscale, 2018, 10, 3, 914-920.

Another example of dye degradation induced by POM-based self-assembled system is was presented recently by Prof. Edler *et al.*, in this case the dye being rhodamine B (RhB).[10] In this study, they used organosilyl derivatives of Dawson-type POM ($[P_2W_{17}O_{61}]^{6-}$) associated to hydrophobic organic tails (with three different lengths) and displaying amphiphilic properties. In aqueous solution, this compound formed micelles that were used for templating nanostructured TiO_2 formation (*Fig.* 9). The ability of this hybrid material to photodegrade RhB was studied. The authors found that the system was five times superior to sodium dodecyl sulfate templated TiO_2, a

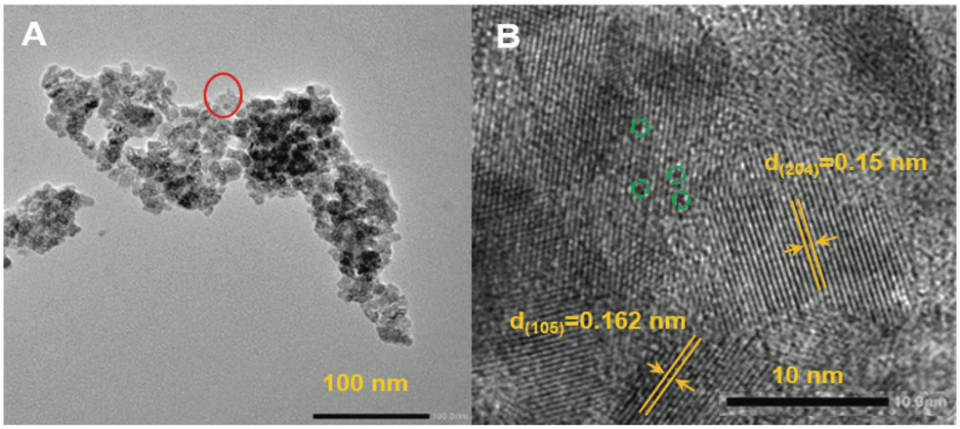

Figure 20 – (A) TEM and (B) HRTEM micrographs of the POM-TiO_2 material. HRTEM micrograph in (B) is a zoom from the region indicated with a red circle in (A). Dashed green circles in (B) are the possible locations of POM in the material. Di et al.; Nanoscale, 2020, 12, 43, 22245-22257.

traditional well-known material for RhB degradation. It is worth noticing that methylene blue degradation was also studied with other POM-based auto-assembled systems.[11]

2. METALLOMACROCYCLES

2.1. PREVIOUS WORK

Our group has important experience in the elaboration of geometrically-shaped self-assembled structures. In 2015, the E-POM team presented a new system where an auto-assembly process lead to the formation of a triangle-shaped (*Fig.* 10) supramolecular structure, characterized by DOSY NMR and SAXS measurements. In this system they used an organosilyl Dawson-type polyoxometalate hybrid, associated to two organic arms ending by pyridyl moieties and *trans*-[$PdCl_2(MeCN)_2$] in 1:1 stoichiometry.[12]

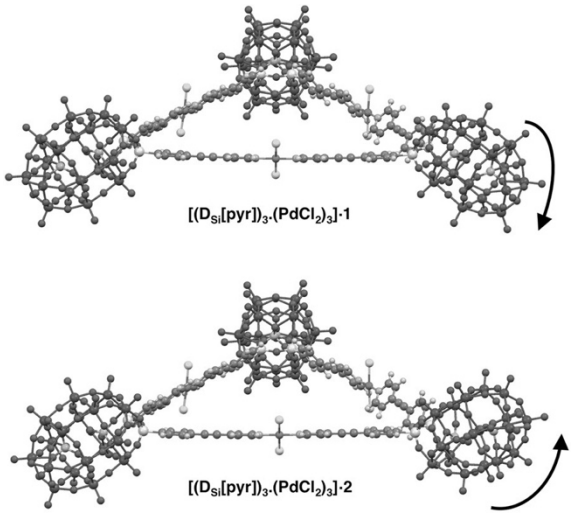

Figure 21 - Optimized structures of the two molecular triangle. G. Izzet et al.; Chem. Eur. J., 2015, 21, 19010-19015.

Next year, the remote ligands were changed for a terpyridine units and the palladium complex for Fe(II).[13] The idea behind this modification was to use a cationic metal linker (by contrast to the formal "$PdCl_2$" linker) to obtain a reversible aggregation of the discrete species when dropped in the correct solvent. Indeed, as shown by *Fig.* 11 (a), in acetonitrile the discrete triangles assembled in dense monodisperse

nanostructures, due to a lower solvation. This was confirmed by combination of SAXS and TEM measurements.

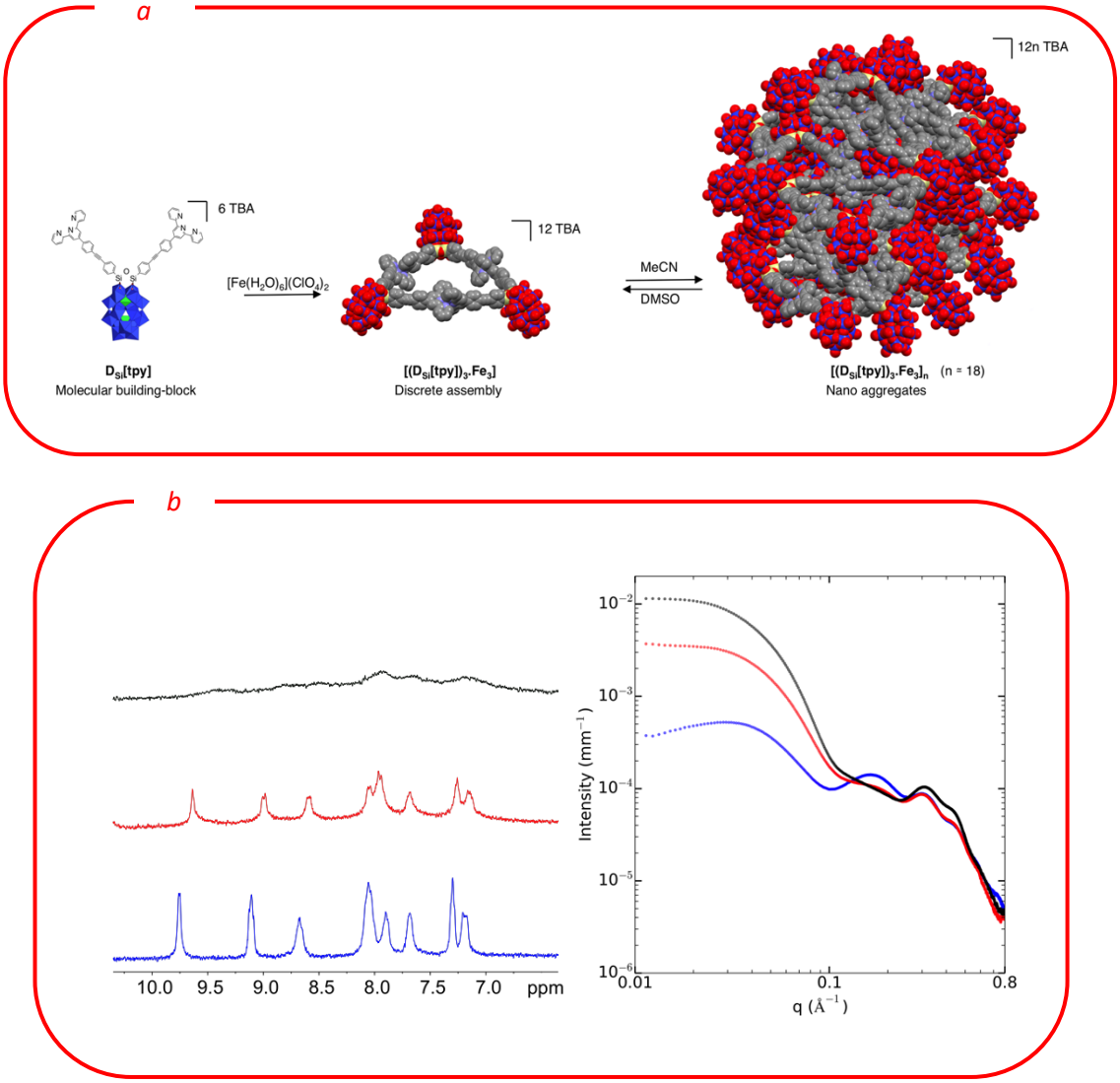

Figure 22 – (a) Schematic representation of the formation of the nanosized aggregates by hierarchical self-assembly of D_{Si}[tpy] upon complexation with Fe^{2+}. (b) ^{1}H NMR spectra and (left) and SAXS curves (right) of solutions of D_{Si}[tpy] (1 mM) in the presence of 1 equiv. of $[Fe(H_2O)_6](ClO_4)_2$ in DMSO-d_6 (blue), DMSO-d_6/CD_3CN (1/1) (red), and DMSO-d_6/CD_3CN (1/4) (black). G. Izzet et al.; J. Am. Chem. Soc., 2016, 138, 5093-5099.

In 2017, the group published the case of a Keggin hybrid, displaying two remote pyridyl-units, self-assembled with *trans*-$[PdCl_2(MeCN)_2]$.[14] In this study, they showed that owing to the lower charge of the building block, a mixture of square-shaped and triangle-shaped assemblies in the supramolecular discrete species was observed (*Fig.*

12). It can be explained by the entahlpy/entropy competition, the entropy favorized the smaller triangles while enthalpy prefered the non-constraining squares.

This study outlined the decisive effect of the charge of the POM disfavoring the formation of large asssemblies probably owing to an important entropic contribution.

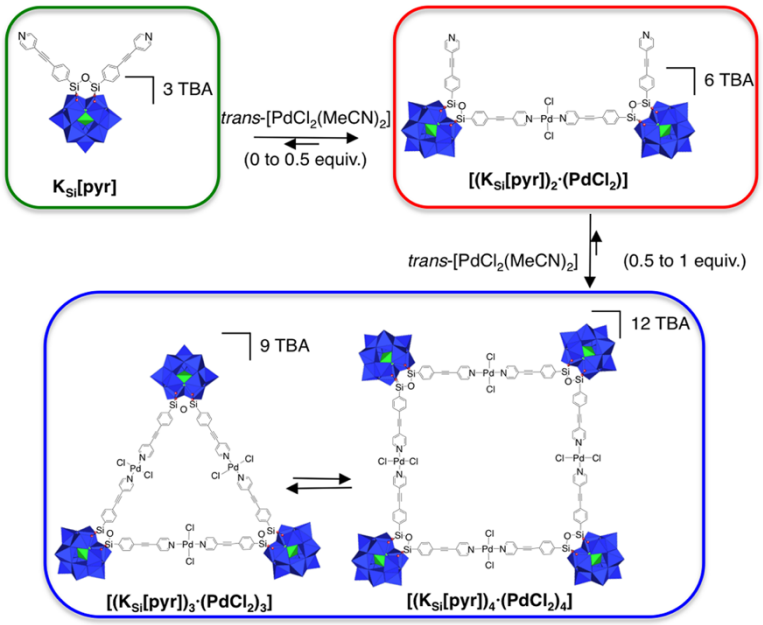

Figure 23 – Metal-driven formation of the molecular triangle and square from the POM hybrid K_{Si}[pyr]. M. Piot et al.; Inorg. Chem., 2017, 56, 8490-8496.

They also observed that while the POM-based molecular building block and related coordination oligomers displayed different shapes, a power law between the diffusion coefficient D and the molecular mass M was applicable to this series of hybrids, indicating that the diffusion coefficient of these compounds was mainly determined by their occupied volume rather than by their shape.

Finally the next year, a Dawson hybrid with a remote pyridine was auto-assembled with $[Co(H_2O)_6](NO_3)_2$ and formed both squares and triangles in DMSO (*Fig.* 13).[15] In a DMSO/MeCN (1:4) solution, the discrete species aggregate in a dense nanoparticle shape as with Fe(II) linker. In this study they evaluated the effect of the charge of the metal linker to see if this could affect the shape and size of the aggregate. Indeed, if the Co(II) complex is oxidized upon the addition of $TBABR_3$ in DMSO (prior the aggregation) the nanostructure will not be a nanoparticle but a more elongated worm-like structure as a consequence of stronger electrostatic interactions between the metallomacrocycles.

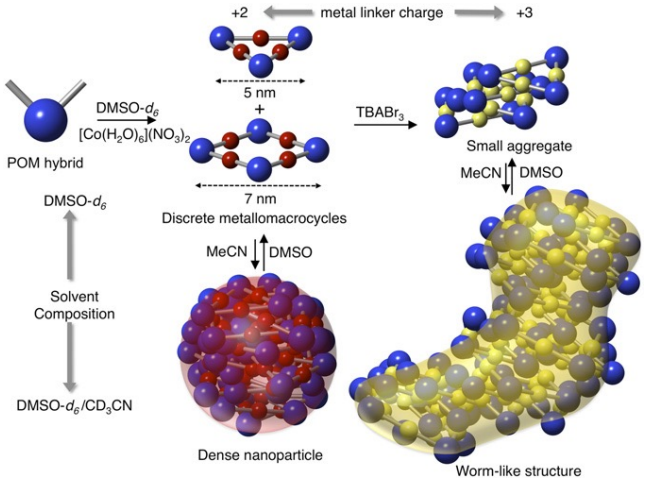

Figure 24 – Schematic representation of the formation of the nanosized aggregates by hierarchical metal-driven self-assembly of POM (1) according to the solvent composition (DMSO-d_6/CD_3CN mixtures) and the metal linker charge. M. Piot et al.; PNAS, 115, 36, 8895-8900.

2.2. SOLUTION TO TRIANGLE ISSUE: NEW METALLIC CENTER

As previously detailed in the latter part, a way to have discrete POM-based metallomacrocyles from self-assembly of hybrid POMs with metallic complex was developed. However, in most cases, a mixture between triangles and squares was unavoidably obtained, as a result of the high entropy cost for the association of highly charged species. To prevent the attainment of different discrete supramolecular species, a new method is needed to be developped. In the previous structures, metallic complexes used were linear and POM on the corners, determining the angles and thus the geometry of the structures. However, the flexibility of the organic arms attached to the POM allowed a wide variety of angles, leading to the square/triangle mixture formation.

In this thesis, a new system based on a new metallic complex was prepared, $[Pd(en)\text{-}(MeCN)_2](BF_4)_2$, this node is well-known and the ethylenediamine (en) ligand assurates the rigidity of the coordination sites, leading to a less modular angle. In this structure, squares are composed of only two polyoxometalates and two metallic complexes (*Fig.* 14) when the precedent structure had the double of both. To perform the discrete structure synthesis, Keggin-type POM with pyridine-ending organic arms

($(TBA)_3[PW_{11}O_{39}\{O(SiC_{13}H_8N)_2\}]$, K_{Si}[pyr]) was put in presence of [Pd(en)-$(MeCN)_2](BF_4)_2$, 1.2 equivalents, in DMSO-d_6.

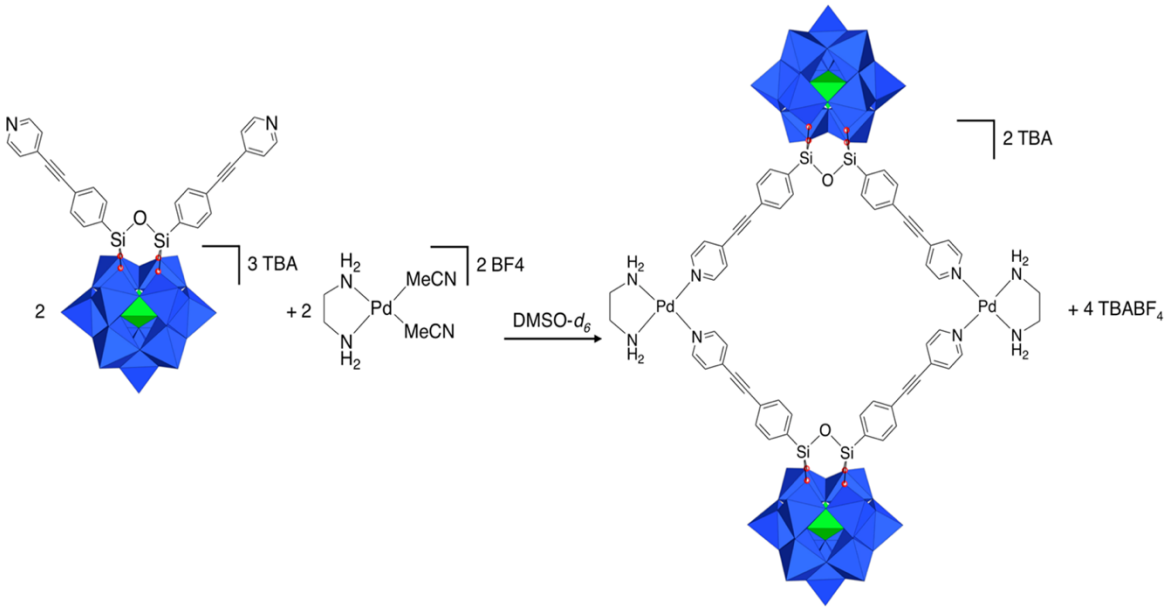

Figure 25 – Metal-driven formation of the molecular square from the POM hybrid K_{Si}[pyr]. R. Salles et al.; Inorg. Chem., 2020, 59, 2458-2463.

2.3. POST-SYNTHESIS ANALYSIS

Formation of the discrete square species ($K_{Si}[pyr]_2$•$[Pd(en)]_2$) was observed by NMR. As revealed by *Fig*. 15, reaction requires 1.2 equivalents of [Pd(en)-$(MeCN)_2](BF_4)_2$ to have a 1:1 stoichiometry in the final metallomacrocycle. The little excess of metal node, observable at 5.5 ppm, is independent from the square but necessary to complete the reaction with the pyridyl ligands, as shown by DOSY NMR, still *Fig.* 15, revealing a unique diffusion coefficient of 7.7 x 10^{-11} $m^2.s^{-1}$ for the auto-assembly.

As previously mentioned, with the K_{Si}[pyr] hybrid, a correlation between the diffusion coefficient and nuclearity of the species was found.[14] For instance in the case of the formation of a dimer, the ratio between the diffusion coefficient of the monomer and the dimer was found to be 1.7[14]. In the present case, the $D_1/D_2 \approx 1.6$ (D_1 = 1.2 x 10^{-10} $m^2.s^{-1}$ and D_2 = 7.7 x 10^{-11} $m^2.s^{-1}$), confirming the dimeric POM structure of the macrocyclic species.

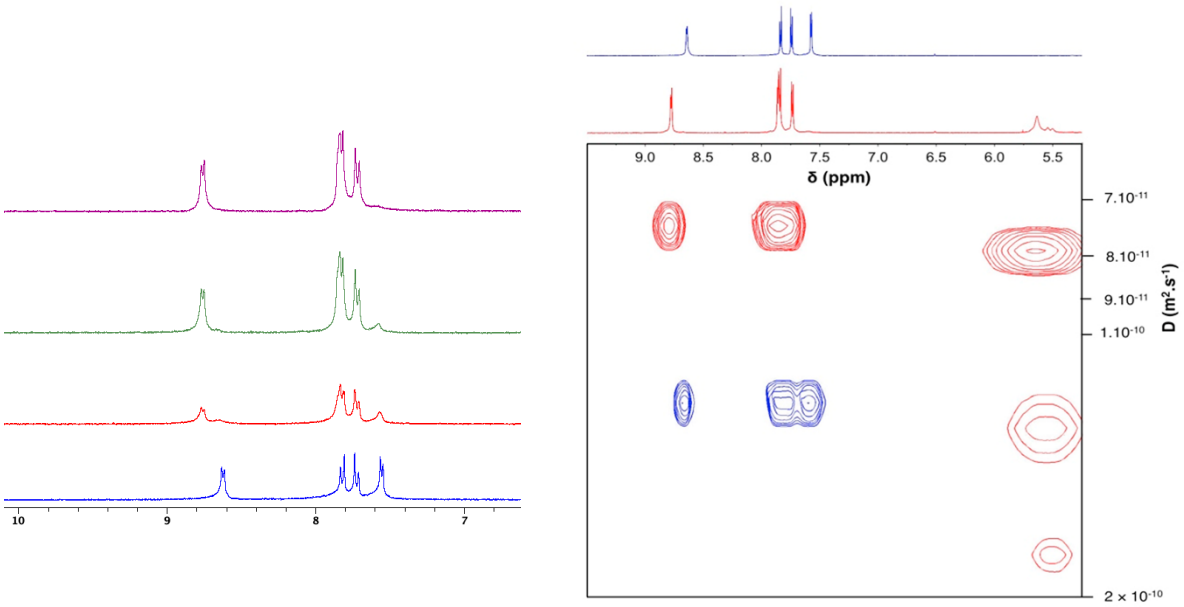

Figure 26 – (left) ^{1}H NMR of K_{Si}[pyr] (5 mM) in DMSO-d_6 with addition of $[Pd(en)(MeCN)_2](BF_4)_2$: 0 equiv. (blue), 0.5 equiv. (red), 1 equiv. (green), 1.2 equiv. (purple). (right) ^{1}H NMR in DMSO-d_6 of K_{Si}[pyr] (5 mM, blue) with corresponding DOSY and its resulting supramolecular assembly in the presence of 1.2 equiv. of $[Pd(en)(MeCN)_2](BF_4)_2$ (red).

In the same time, an optimized computational structure, obtained by density-functional tight-binding (DFTB) method, was developed by Dr. E. Derat from Sorbonne Université (*Fig.* 16). It helped us to understand the most likely structure of our system, with an estimated distance POM-POM of 14.7 Å and a Pd-Pd distance of 24.0 Å.

Small angle X-ray scattering (SAXS) is frequently used to characterize nanosized objects under 100 nm. It allows to have insight on the internal architecture of such compounds. In this case, we computed the theoretical SAXS patterns of the dimer using CRYSOL software and compared it to the experimental SAXS pattern of the dimer in DMSO solution. As shown by *Fig.* 17, the estimated SAXS spectrum fits well with the experimental one for both small q value and first oscillation.

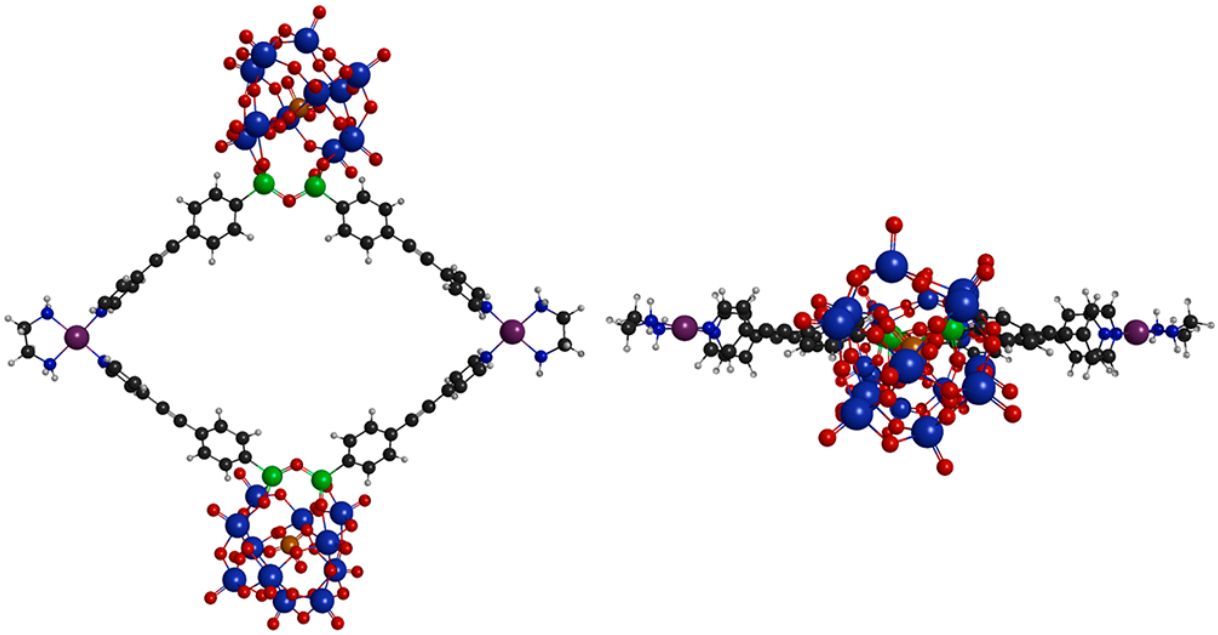

Figure 16 – Optimized structure (left: top view; right: side view) of $K_{Si}[pyr]_2$•$[Pd(en)]_2$. R.Salles et al.; Inorg. Chem., 2020, 59, 2458-2463.

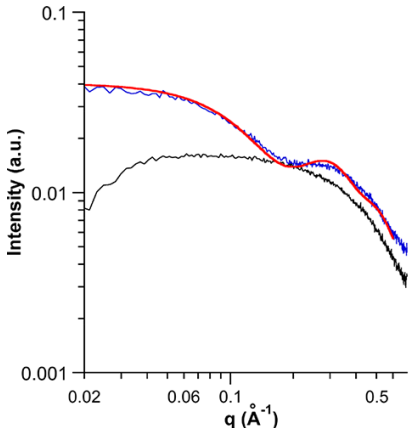

Figure 17 – Experimental SAXS pattern of a solution of $K_{Si}[pyr]$ (0.5 mM in DMSO-d6, black), the resulting supramolecular assembly in the presence of 1.2 equiv. of $[Pd(en)\text{-}(MeCN)_2](BF_4)_2$ (blue) and the computed SAXS pattern (CRYSOL) of the optimized structure of $K_{Si}[pyr]_2$•$[Pd(en)]_2$ (red). R.Salles et al.; Inorg. Chem., 2020, 59, 2458-2463.

2.4. SOLVENT IMPACT: AGGREGATION

In previous papers, it has been shown that in solvent other than pure DMSO-d_6, because they are protic or less dissociative, discrete species will tend to aggregate by electrostatic interactions (thanks to positively and negatively charges areas in the structure). Thus, DMSO-d_6/CD_3CN: 1/4 and DMSO-d_6/D_2O: 1/1 were tested.

In SAXS analysis (*Fig. 18*), the CD_3CN-induced aggregation revealed a peak at that can be deconvoluted for a mono-q value, q = 0.436 $Å^{-1}$, corresponding to a distance of 1.44 nm. For the D_2O case, the peak is deconvoluted in two q values, q_1 = 0.376 Å (d_1 = 1.67 nm) and q_2 = 0.490 Å (d_2 = 1.28 nm), the second one being the main one. This results revealed a shorter POM-POM distance in water than in acetonitrile.

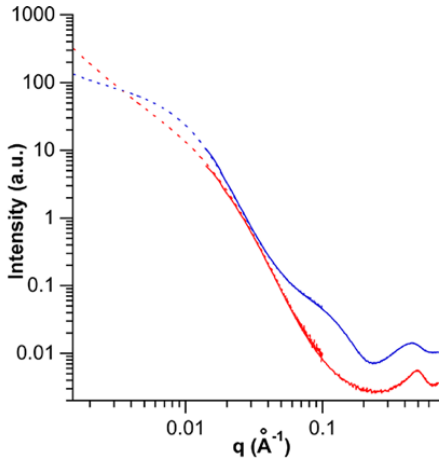

Figure 27 - Experimental SAXS pattern of a solution of the POM-Pd supramolecular assembly in DMSO-d_6/D_2O: 1/1 (red) and DMSO-d_6/CD_3CN: ¼ (blue). R.Salles et al.; Inorg. Chem., 2020, 59, 2458-2463.

Various models were tested to fit with the experimental data, to understand the structure of the resulting aggregates. In the case of D_2O, the closest one was a nearly infinite flexible cylinder, with 5.4 nm radius, a polydispersity of 50% and a Kuhn length (basically the average size of straight segment) of 15 nm. TEM results (*Fig.* 19) confirmed this result, revealing a ramified flexible cylinders system, apparented to cherry-branch design in ukiyo-e, with a segment size of around 8-10 nm.

In DMSO/CD_3CN, TEM images shown isotropic polydisperse round aggregates with a diameter range of 15-55 nm. Even if polydispersity made it harder to fit with SAXS analysis, the closest system found is a multishell vesicle model (1.5, half/half mixtures of single and double layers, one layer being 2.3 nm thick).

The shape variation between the solvents (cherry-branches versus vesicles) is explained by the solvation of the charged species and some hydrophobic effect. Indeed, the vesicles have thin layers leading to a surface-to-volume ratio larger than in the case of cherry-branches, meaning that the number of POMs pointing toward solvent is greater in comparison with the elongated structure in water, a solvent in which all the components are individually insoluble (POM when counter-ions are TBA and Pd(en)

complex). This better packing in water and shorter POM-POM distance is due to less solvated POM, because of their hydrophobic character.

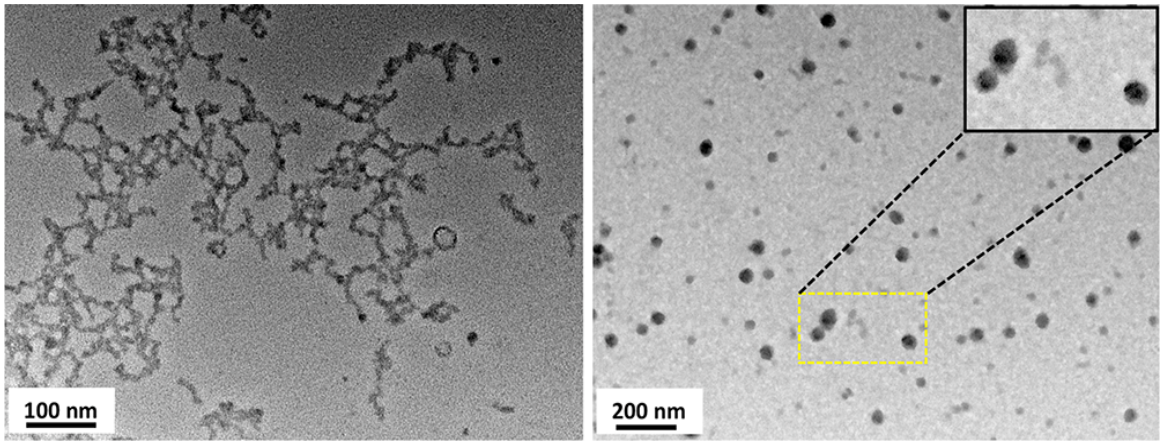

Figure 28 – TEM micrograph of the POM-Pd assemblies in DMSO/D_2O 1:1 (left) and DMSO-d_6/CD_3CN 1:4 (right, magnification of three vesicles in the upper right corner) mixtures. R.Salles et al.; Inorg. Chem., 2020, 59, 2458-2463.

2.5. SUMMARY

This work was presented in a paper published in 2020.[16] It sums up the synthesis and characterization of the discrete structure, square-shaped, auto-assembled from K_{Si}[pyr] and $[Pd(en)(MeCN)_2](BF_4)_2$. This was allowed by the addition of a new metallic complex with more rigid arms, limiting the architecture possibilities. Squares were aggregated in different macrostructures according to the solvent, it is explained by solvation process and hydrophobic effect. Next step for this work would be to think about application. In particular, cherry-branches could be interesting for semiconductor device in neuromorphic networks.

3. GELS

3.1. PREVIOUS WORK

In the self-assembly domain, polyoxometalate-based gel is a not so developed area yet. However, thanks to their redox properties and color swap possibilities, they could be relevant candidates for many applications like photochromic and electrochromic devices which are currently under interest.[17]

As mentioned in the introductory part of this chapter, at the beginning of the century B. Hasenknopf and coll. presented a system where an Anderson-type polyoxomolybdate hybrid with pyridine-ending organic arms ($[MnMo_6O_{18}\{(OCH_2)_3CNHCO(4\text{-}C_5H_4N)\}]^{3-}$) formed a gel in the presence of a Pd complex ($[PdCl_2(PhCN)_2]$)[7]. The addition of the latter in CD_3CN and the subsequent formation of macrostructure was followed by NMR. Gel formation is generally induced by the addition of the right solvent. In this case, methanol is the key (and patience too since it requires ageing for a few days). It finally turned in an orange transparent gel, revealing a birefringent character, proving its anisotropic arrangement, when observed under crossed polarized light (*Fig.* 20*)*.

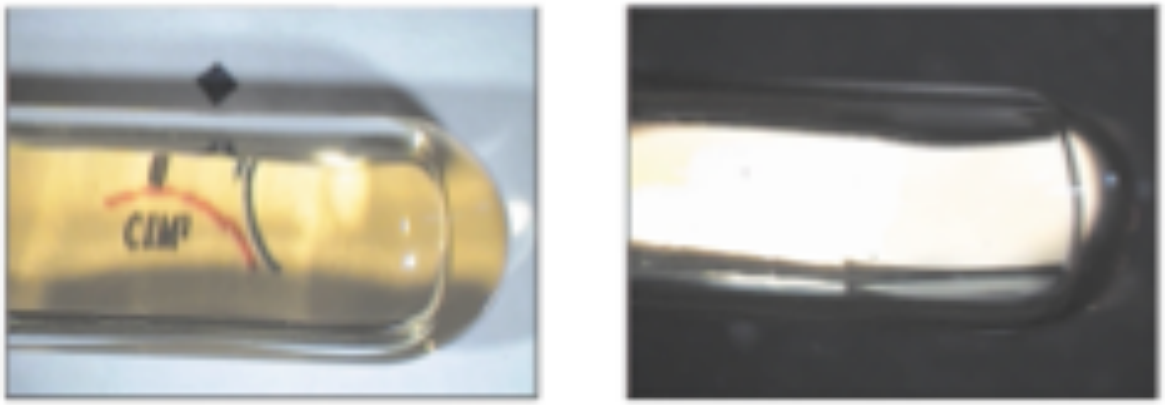

Figure 29 – Two photographs of the gel in a test tube of 1 cm in diameter. Left : taken under ambient light to show the transparency of the gel; right: taken through crossed polarizers to show the birefringence of the gel. S. Favette et al.; Chem. Commun., 2003, 2664-2665.

A slightly more recent example, from Prof. Marcella Bonchio and coll., reported the case of self-assembled gel system with a fibrillar nanostructure.[18] The POM here is a chiral aminophosphonate pentamolybdate, $[(RPO_3)_2Mo_5O_{15}]^{2-}$; the idea being to

protonate the amino groups ending the organic arms to form a network of hydrogen bonds leading to a rodlike structure. In an EtOH/H_2O (90/10) solution it turns into a gel with an internal structure of entangled fibers. This hierarchical architecture was observed by electron microscopy (*Fig.* 21), measuring the homogeneous fibers with a diameter between 20 and 40 nm and a maximum length of 5 μm.

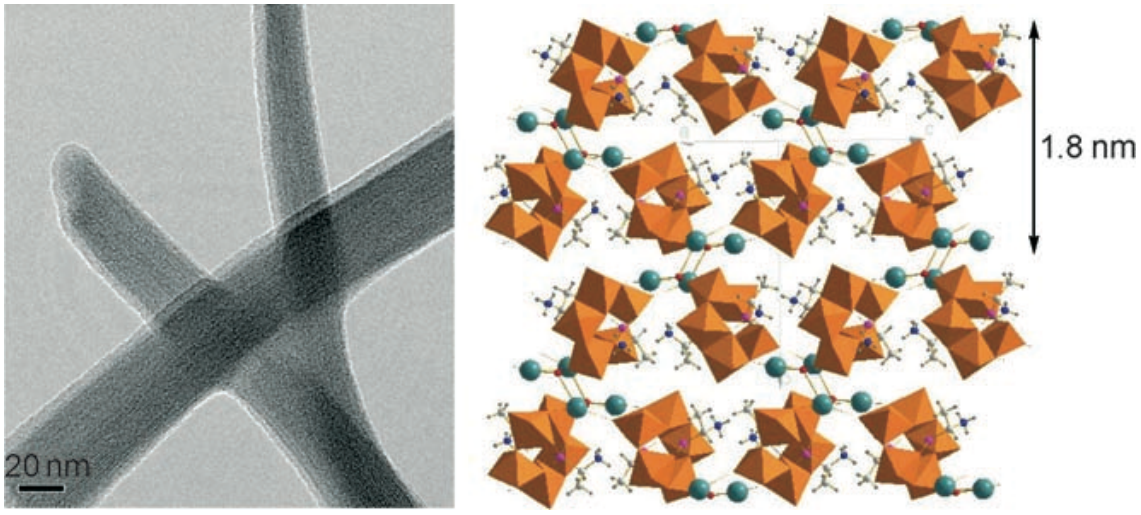

Figure 30 – Left: TEM analysis of entangled fibers network. Right: crystal packing diagram for POMs arrangement.

3.2. AUTO-ASSEMBLY FORMATION: SAXS AND NMR ANALYSIS

Terpyridine ligands are known for their abilities to form linear arrangement with various divalent and trivalent metal cations. In the way to form dumbbell-like POM-based dimers, we then grafted terpyridine units to monotopic organotin derivatives of POMs (in the Keggin and Dawson series). The resulting hybrids, respectively named K_{Sn}[tpy] and D_{Sn}[tpy] were obtained through a classical Sonogashira cross-coupling reaction from the parents iodo aryl terminated hybrids. In presence of $[Co(H_2O)_6](NO_3)_2$, paramagnetic Co(II) terpyridine complexes immediately formed. This phenomenon is clearly visible by NMR analysis (*Fig.* 22) since paramagnetic character induced an easily identifiable broadening of the ^1H peaks in the vicinity of the metal center. The conversion is total after the addition of 0.5 equivalent of metal complex per POM, indicating a 2:1 stoichiometry.

To switch from Co(II) to Co(III) complex, tetrabutyl ammonium tribromide ($TBABr_3$) was added (0.5 equivalent) and the solution went from an orange tint to an intense yellow.

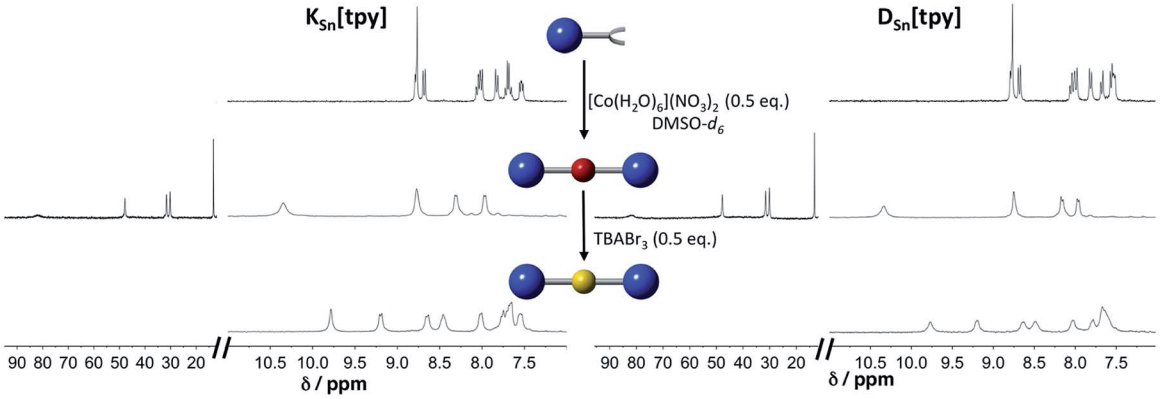

Figure 31 – ^{1}H NMR (300 MHz) in DMSO-d_6 solution containing K_{Sn}[tpy] (2mM, top left) and D_{Sn}[tpy] (top right) in the presence of 0.5 equiv. of $[Co(H_2O)_6](NO_3)_2$ (middle); after oxidation of the Co(II) with 0.5 equiv. $TBABr_3$ (down). M. S. Centallas et al.; Chem. Sci., 2020, 11, 11072-11080.

The final discrete species has a dumbbell-like structure. It was analyzed by SAXS and the obtained patterns confirmed this architecture by its positive comparison with the theoretical one computed by CRYSOL software (*Fig.* 23). Computational calculated model was developed by Prof. Carles Bo and his team, by density-functional theory method.

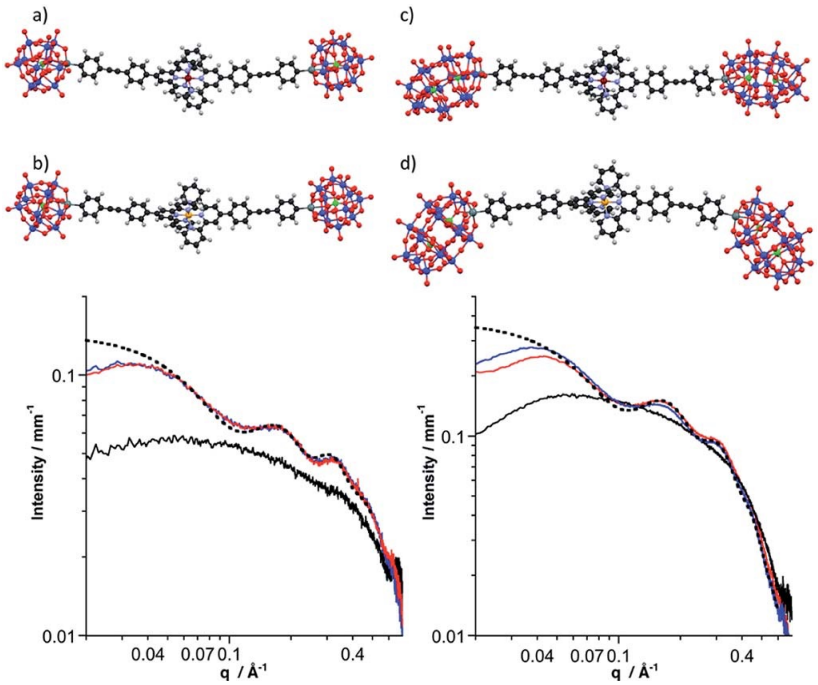

Figure 32 – Top: energy-minimized structures of the dumbbell-like species (a) K_{Sn}[tpy].Co^{II}, (b) K_{Sn}[tpy].Co^{III}, (c) D_{Sn}[tpy].Co^{II}, (d) D_{Sn}[tpy].Co^{III}. Bottom: SAXS pattern of a 1 mmol solution of the molecular building-units K_{Sn}[tpy] (left, black curve) and D_{Sn}[tpy] (right, black curve) in DMSO-d_6 and therir resulting dumbbell-shaped Co(II) (red curves) and Co(III) blue curves complexes and the computed SAXS pattern (CRYSOL) of the optimized structures of K_{Sn}[tpy].Co^{III} and D_{Sn}[tpy].Co^{III} (dotted black). M. S. Centallas et al.; Chem. Sci., 2020, 11, 11072-11080.

3.3. AGGREGATION AND GEL FORMATION

In the correct solvent (water or acetonitrile) the linear dimer assemblies tend to aggregate. SAXS analysis (*Fig.* 24) showed that the characteristic oscillations observed earlier disappeared and new ones were observed, at q mid-values (around 0.4 $Å^{-1}$), corresponding to new POM-POM interactions from a dimer to another, within the aggregate. SAXS patterns also revealed that increasing the charge of the metal center lead to bigger aggregates and shorter POM-POM distances (indicated by higher q values) since the change from Co(II) to Co(III) induces stronger electrostatic interactions. Same mechanism is observed between Keggin and Dawson, indicating that when the charge of the POM is closer to the Co one, the aggregate will be gain in stacking.

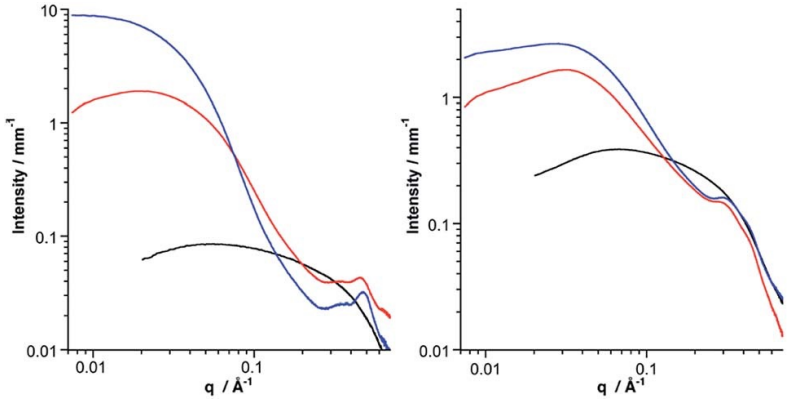

Compound	Nber dimers	q_1/Å^{-1}	d_1/Å	q_2/Å^{-1}	d_2/Å
K_{Sn}[tpy].Co^{II}	10–12	0.344	18.3	**0.464**	**13.5**
K_{Sn}[tpy].Co^{III}	50–60	0.350	18.0	**0.481**	**13.1**
D_{Sn}[tpy].Co^{II}	2–3	**0.311**	**20.2**	0.426	14.8
D_{Sn}[tpy].Co^{III}	3–4	**0.323**	**19.5**	0.426	14.8

Figure 33 – Top: SAXS pattern of a 1 mmol solution of the molecular building-unit K_{Sn}[tpy] (left, black curve) and D_{Sn}[tpy] (right, black curve) and the resulting aggregates POM.Co^{II} (red curves) and POM.Co^{III} (blue curves) assemblies in CD_3CN. Bottom: data extracted from the SAXS curves of K_{Sn}[tpy].Co^{II}, K_{Sn}[tpy].Co^{III}, D_{Sn}[tpy].Co^{II} and D_{Sn}[tpy].Co^{III} in CD_3CN solution, d = 2π/q; values in bold correspond to the main peak. M. S. Centallas et al.; Chem. Sci., 2020, 11, 11072-11080.

It was observed that when dropped in ethanol, the discrete dumbbells formed an organogel. This gel was washed in pure ethanol and then analyzed by thermogravimetric analysis (TGA), resulting in the information that it was constituted at around 7% by dimers, the rest being solvent molecules. When this gel is dropped in water, solvent molecules are exchanged and a hydrogel is observed (clearly distinguished by the slow sinking of the aggregate while molecules are exchanged), TGA indicating this time 5% of dimer (*Fig. 25*).

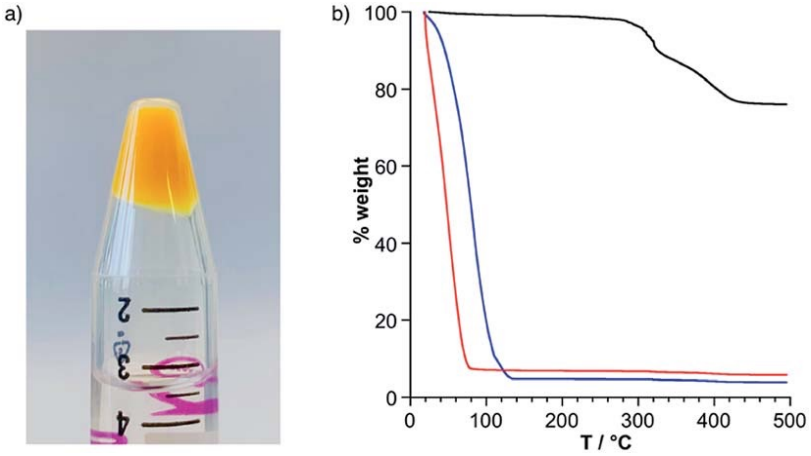

Figure 34 – (a) Ethanol organogel of K_{Sn}[tpy].Co^{III}. (b) TGA of K_{Sn}[tpy] (black) and K_{Sn}[tpy].Co^{III} as an ethanol organogel (red) and hydrogel (blue). M. S. Centallas et al.; Chem. Sci., 2020, 11, 11072-11080.

Finally, SAXS analysis were run to gain information on gel structure (*Fig. 26*). First information came from the peak observed between 0.2 and 0.7 $Å^{-1}$ indicating that a nanostructure organization is still existent. SAXS pattern also confirmed that previously identified trends were also present here, meaning that Keggin systems are more stacked than Dawson ones and Co^{III} than Co^{II} (higher q values, indicating shorter POM-POM distances).

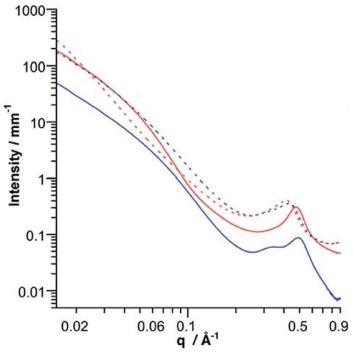

Compound	Scan	q_1/Å^{-1}	d_1/Å	q_2/Å^{-1}	d_2/Å
K_{Sn}[tpy].Co^{II}	1st	0.369	17.0	**0.477**	**13.2**
K_{Sn}[tpy].Co^{III}	1st	0.354	17.7	**0.492**	**12.8**
	5th	0.364	17.2	**0.486**	**12.9**
D_{Sn}[tpy].Co^{II}	1st	0.332	18.9	**0.417**	**15.1**
D_{Sn}[tpy].Co^{III}	1st	0.344	18.3	**0.437**	**14.4**
	5th	0.343	18.3	**0.433**	**14.5**

Figure 35 – Left: SAXS pattern of the POM.Co^n organogels: K_{Sn}[tpy].Co^{III} (plain blue), K_{Sn}[tpy].Co^{II} (plain red), D_{Sn}[pty].Co^{III} (dotted blue) and D_{Sn}.Co^{III} (dotted red). Right: data extracted from the SAXS curves of K_{Sn}[tpy].Co^{II}, K_{Sn}[tpy].Co^{III}, D_{Sn}[tpy].Co^{II} and D_{Sn}[tpy].Co^{III} as organogels, d = 2π/q; values in bold correspond to the main peak. M. S. Centallas et al.; Chem. Sci., 2020, 11, 11072-11080.

3.4. SUMMARY

The work presented here was detailed in a paper published in early 2020.[19] From this article, only the results obtained as part of this thesis were detailed here, but a large work has also been done on the computational part, feel free to refer to it if interested.

Discrete dumbbell-like species were synthesized from auto-assembly of POMs (both Dawson and Keggin) hybrids and Co complex in DMSO. When dispersed in acetonitrile the discrete species reacted to form larger nano-assemblies, while in ethanol an organogel was obtained. In both cases, electrostatic interactions ruled the formation. Next logical step from here would be to obtain more information about mechanical properties of the gel.

4. CONCLUSION AND PERSPECTIVES

Polyoxometalates hybrids are greatly promising for self-assembly structures owing to their charged and chaotropic nature. In this part, two examples of those were detailed. In the first one, a unique discrete supramolecular species was obtained, while in most cases mixtures of species of different nuclearities were formed. To do so, a new metallic complex with rigid organic arms was used to obtain only square-shaped discrete species. Aggregation of this species in different solvents (acetonitrile and water) was studied. Large structures (*i.e.* vesicles and elongated cherry-branches) were formed and characterized by combination of SAXS and TEM. A possible application for these systems could be in semiconductor devices for neuromorphic systems. The presence of a cavity-topology, similar to those developed by Fujita redox-active cages-like supramolecular species, could also be considered.[20]

In the second case, organogel and hydrogel were obtained from self-assembled POM dimers around a cobalt center. Due to the original character of such a system, a complete physico-chemical study is required, mechanical characteristics of the gels should be investigated and a detailed rheological study seems necessary before thinking about applications. Then, another interesting work should concern the impact of POMs and metallic center variation and see what impact it can have on gel properties.

5. BIBLIOGRAPHY

(1) Fujita, M.; Yazaki, J.; Ogura, K. Preparation of a Macrocyclic Polynuclear Complex, [(En)Pd(4,4'-Bpy)]4(N03)8,1Which Recognizes an Organic Molecule in Aqueous Media. 3.
(2) Jansze, S. M.; Cecot, G.; Wise, M. D.; Zhurov, K. O.; Ronson, T. K.; Castilla, A. M.; Finelli, A.; Pattison, P.; Solari, E.; Scopelliti, R.; Zelinskii, G. E.; Vologzhanina, A. V.; Voloshin, Y. Z.; Nitschke, J. R.; Severin, K. Ligand Aspect Ratio as a Decisive Factor for the Self-Assembly of Coordination Cages. *J. Am. Chem. Soc.* **2016**, *138* (6), 2046–2054. https://doi.org/10.1021/jacs.5b13190.
(3) Zhang, J.; Li, W.; Wu, C.; Li, B.; Zhang, J.; Wu, L. Redox-Controlled Helical Self-Assembly of a Polyoxometalate Complex. *Chem. - Eur. J.* **2013**, *19* (25), 8129–8135. https://doi.org/10.1002/chem.201300309.
(4) Yue, L.; Ai, H.; Yang, Y.; Lu, W.; Wu, L. Chiral Self-Assembly and Reversible Light Modulation of a Polyoxometalate Complex via Host–Guest Recognition. *Chem. Commun.* **2013**, *49* (84), 9770. https://doi.org/10.1039/c3cc45848b.
(5) Yin, P.; Li, T.; Forgan, R. S.; Lydon, C.; Zuo, X.; Zheng, Z. N.; Lee, B.; Long, D.; Cronin, L.; Liu, T. Exploring the Programmable Assembly of a Polyoxometalate–Organic Hybrid via Metal Ion Coordination. *J. Am. Chem. Soc.* **2013**, *135* (36), 13425–13432. https://doi.org/10.1021/ja404777g.
(6) Santoni, M.-P.; Pal, A. K.; Hanan, G. S.; Tang, M.-C.; Venne, K.; Furtos, A.; Ménard-Tremblay, P.; Malveau, C.; Hasenknopf, B. Coordination-Driven Self-Assembly of Polyoxometalates into Discrete Supramolecular Triangles. *Chem Commun* **2012**, *48* (2), 200–202. https://doi.org/10.1039/C1CC16155E.
(7) Favette, S.; Hasenknopf, B.; Vaissermann, J.; Gouzerh, P.; Roux, C. Assembly of a Polyoxometalate into an Anisotropic Gel. *Chem. Commun.* **2003**, No. 21, 2664. https://doi.org/10.1039/b308889h.
(8) Li, H.; Jia, Y.; Wang, A.; Cui, W.; Ma, H.; Feng, X.; Li, J. Self-Assembly of Hierarchical Nanostructures from Dopamine and Polyoxometalate for Oral Drug Delivery. *Chem. - Eur. J.* **2014**, *20* (2), 499–504. https://doi.org/10.1002/chem.201302660.
(9) Kutz, A.; Mariani, G.; Schweins, R.; Streb, C.; Gröhn, F. Self-Assembled Polyoxometalate–Dendrimer Structures for Selective Photocatalysis. *Nanoscale* **2018**, *10* (3), 914–920. https://doi.org/10.1039/C7NR07097G.
(10) Di, A.; Schmitt, J.; da Silva, M. A.; Hossain, K. M. Z.; Mahmoudi, N.; Errington, R. J.; Edler, K. J. Self-Assembly of Amphiphilic Polyoxometalates for the Preparation of Mesoporous Polyoxometalate-Titania Catalysts. *Nanoscale* **2020**, *12* (43), 22245–22257. https://doi.org/10.1039/D0NR05967F.
(11) Tong, L.; Wang, Z.; Xia, C.; Yang, Y.; Yuan, S.; Sun, D.; Xin, X. Self-Assembly of Peptide-Polyoxometalate Hybrid Sub-Micrometer Spheres for Photocatalytic Degradation of Methylene Blue. *J. Phys. Chem. B* **2017**, *121* (46), 10566–10573. https://doi.org/10.1021/acs.jpcb.7b07100.
(12) Izzet, G.; Macdonell, A.; Rinfray, C.; Piot, M.; Renaudineau, S.; Derat, E.; Abécassis, B.; Afonso, C.; Proust, A. Metal-Directed Self-Assembly of a Polyoxometalate-Based Molecular Triangle: Using Powerful Analytical Tools to Probe the Chemical Structure of Complex Supramolecular Assemblies. *Chem. – Eur. J.* **2015**, *21* (52), 19010–19015. https://doi.org/10.1002/chem.201503363.
(13) Izzet, G.; Abécassis, B.; Brouri, D.; Piot, M.; Matt, B.; Serapian, S. A.; Bo, C.;

Proust, A. Hierarchical Self-Assembly of Polyoxometalate-Based Hybrids Driven by Metal Coordination and Electrostatic Interactions: From Discrete Supramolecular Species to Dense Monodisperse Nanoparticles. *J. Am. Chem. Soc.* **2016**, *138* (15), 5093–5099. https://doi.org/10.1021/jacs.6b00972.
(14) Piot, M.; Hupin, S.; Lavanant, H.; Afonso, C.; Bouteiller, L.; Proust, A.; Izzet, G. Charge Effect on the Formation of Polyoxometalate-Based Supramolecular Polygons Driven by Metal Coordination. *Inorg. Chem.* **2017**, *56* (14), 8490–8496. https://doi.org/10.1021/acs.inorgchem.7b01187.
(15) Piot, M.; Abécassis, B.; Brouri, D.; Troufflard, C.; Proust, A.; Izzet, G. Control of the Hierarchical Self-Assembly of Polyoxometalate-Based Metallomacrocycles by Redox Trigger and Solvent Composition. *Proc. Natl. Acad. Sci.* **2018**, *115* (36), 8895–8900. https://doi.org/10.1073/pnas.1808445115.
(16) Salles, R.; Abécassis, B.; Derat, E.; Brouri, D.; Bernard, A.; Zhang, Q.; Proust, A.; Desmarets, C.; Izzet, G. Hierarchical Self-Assembly of Polyoxometalate-Based Organo Palladium(II) Metallomacrocycles via Electrostatic Interactions. *Inorg. Chem.* **2020**, *59* (4), 2458–2463. https://doi.org/10.1021/acs.inorgchem.9b03333.
(17) Yolanda Alesanco; Ana Viñuales; Javier Rodriguez; Ramón Tena-Zaera. All-in-One Gel-Based Electrochromic Devices: Strengths and Recent Developments. *Materials* **2018**, *11* (3), 414. https://doi.org/10.3390/ma11030414.
(18) Carraro, M.; Sartorel, A.; Scorrano, G.; Maccato, C.; Dickman, M. H.; Kortz, U.; Bonchio, M. Chiral Strandberg-Type Molybdates $[(RPO_3)_2Mo_5O_{15}]^{2-}$ as Molecular Gelators: Self-Assembled Fibrillar Nanostructures with Enhanced Optical Activity. *Angew. Chem. Int. Ed.* **2008**, *47* (38), 7275–7279. https://doi.org/10.1002/anie.200801629.
(19) Centellas, M. S.; Piot, M.; Salles, R.; Proust, A.; Tortech, L.; Brouri, D.; Hupin, S.; Abécassis, B.; Landy, D.; Bo, C.; Izzet, G. Exploring the Self-Assembly of Dumbbell-Shaped Polyoxometalate Hybrids, from Molecular Building Units to Nanostructured Soft Materials. *Chem. Sci.* **2020**, *11* (40), 11072–11080. https://doi.org/10.1039/D0SC03243C.
(20) Yoshizawa, M. Diels-Alder in Aqueous Molecular Hosts: Unusual Regioselectivity and Efficient Catalysis. *Science* **2006**, *312* (5771), 251–254. https://doi.org/10.1126/science.1124985.

PART III - ANILINE, DIAZONIUM, GRAFTING AND MEMORY EFFECTS

1. INTRODUCTION

1.1. POM/SUBSTRATE INTERACTION

1.1.1. MOTIVATION

The great structure versality presented by polyoxometalates, offering a multitude of potential properties in many different fields, makes them highly relevant candidates for applications in a wide variety of domains, such as memory devices as it will be detailed later; however, it is quite often mandatory to immobilize them first on a substrate.

To obtain a system where the POM is deposited on a surface, many ways are possible: drop casting / spin-coating, ionic interactions (negatively charged polyoxometalates with positively charged counter species), MOF / COF / polymer embedment, covalent grafting… While layer-by-layer (LBL) systems, relying on opposite charges interactions, are mainly used widely, this thesis will focus on covalent grafting.

Regarding substrates selection with conductive nature, the most common choices are gold, ITO, silicon, HOPG and glassy carbon. One will be favored over the others according to the deposition method and the final application aimed or characterization techniques used.

1.1.2. LAYER-BY-LAYER: SELECTED EXAMPLES

Among the most commonly used paths for polyoxometalate deposition on surface is the layer-by-layer (LBL) method and there are two main reasons for that. First, it allows a step-by-step control of the thickness of the deposited system. Second, generally, on POM-based LBL systems, polyoxometalate layers are separated by layers of positively charged organic molecules, offering possibility to tune the system by introducing new properties.

The construction of a LBL system is well summarize in a review published by Prof. Dirk G. Kurth and coll. in 2003[1] about polyoxometalates integration in larger system for technological applications by electrostatic layer-by-layers self-assembly method (called ELSA). The process is quite simple, it relies on the alternation of dipping a non-neutral (electronically speaking) substrate in solution of negatively charged POMs or cations (*Fig.* 1).

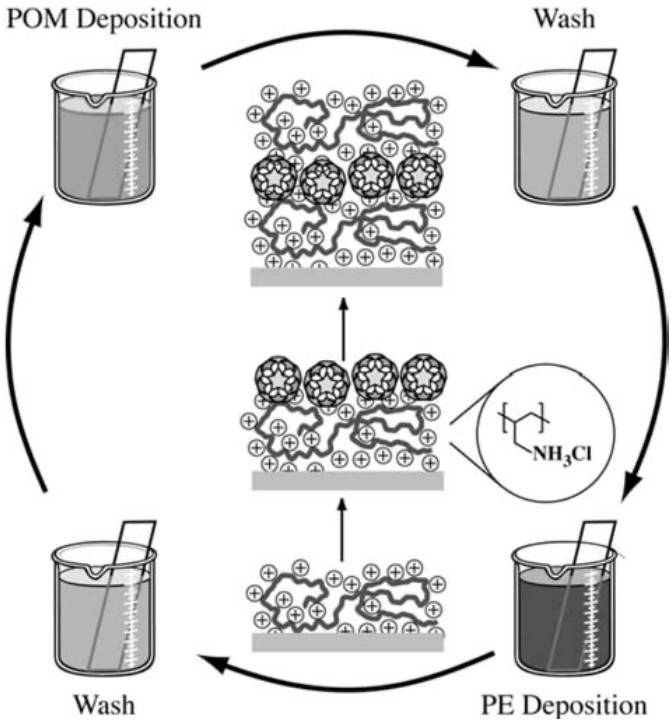

Figure 36 – ELSA deposition example scheme (PE = Polyelectrolyte, many PE/POM combinations, here PE is poly(allylamine hydrochloride) and POM $[Na(H_2O)P_5W_{30}O_{110}]^{14-}$). S. Liu et al.; Journal of Cluster Science, 2003, 14, 3, 405-419

In a paper from 2011, Prof. Christoph Bubeck and coll. presented a system where $H_3PW_{12}O_{40}$ POMs were assembled with graphene oxide according to the LBL method.[2] Aiming for the photocatalytic property of POM to allow the reduction of the graphene oxide (GO) under UV irradiation, the idea is to implement it in a field-effect transistor (FET) device to tune its performance. Since the photoreduction was confirmed by a color swap (*Fig.* 2), they created a FET device based on it and successfully shown the impact of the system thickness (the number of deposited layers) on its performance (on/off ratio and charge carrier mobility).

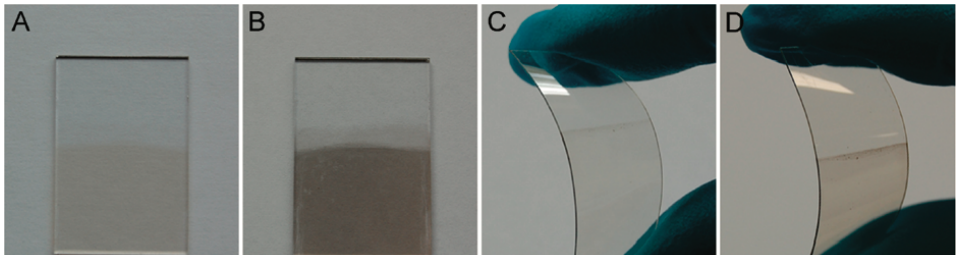

Figure 38 – Optical images of a LBL POM-GO based multilayer film prepared on a quartz substrate before (A) and after (B) 6 h of UV photoreduction and on a flexible PET substrate before (C) and after (D) 6 h of UV photoreduction. Both substrates are coated first by a PET/POM precursor film. H. Li et al.; J. Am. Chem. Soc., 2011, 133, 24, 9423-9429

In the global ecological crisis that we are living, it is primordial for scientists to participate in the general effort, thus it is interesting to observe how polyoxometalates are used in this area. Artificial photosynthesis being one of the hottest topics of our time, it is not a huge surprise that some researchers thought about polyoxometalates in this domain too. This is the case of Prof. Jungki Ryu and coll. who reported in 2017 a photoelectrochemical device enhanced by POMs incorporation.[3] A photoanode for solar water oxidation was ornamented by a LBL deposited topping of POMs (*Fig.* 3) in the idea of improvement regarding stability and photocatalytic properties. Once again, the degree of improvement is depending on the thickness of the system.

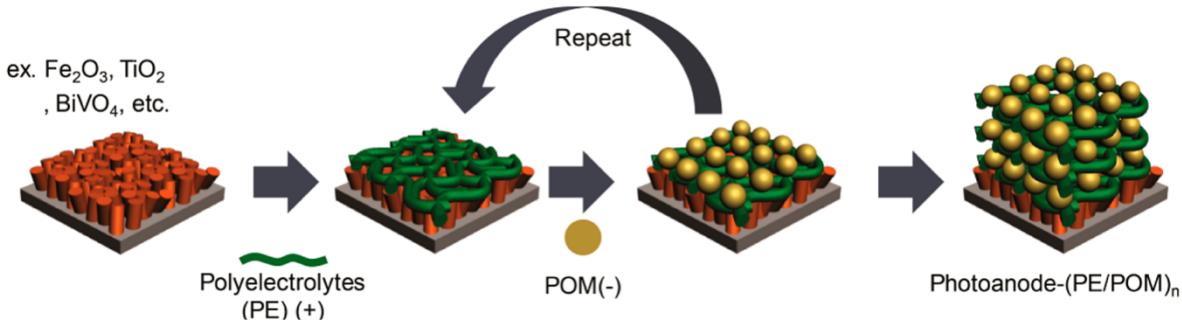

Figure 37 – Scheme of LBL assembly of a photoelectrochemical device. D. Jeon et al.; ACS Appl. Mater. Interfaces, 2017, 9, 40151-40161

Another example of potential ecological application was reported by Prof. Timothy McCormac and coll. last year.[4] Phosphate excess provoked by mankind existence leads, by an eutrophication process, to an oxygen impoverishment of the seabed and the death of aquatic ecosystems. The Dawson-based POM / Cu-phthalocyanine (Cu(PC)) LBL system presented here is aiming to help phosphate detection and quantitative estimation in water sample analysis. To do so, the device was tested by cyclic voltammetry: waves presence and evolution were compared while

adding phosphate in the solution (*Fig.* 4). The system has shown his efficiency and hopefully more and more papers will be published in the future regarding this topic.

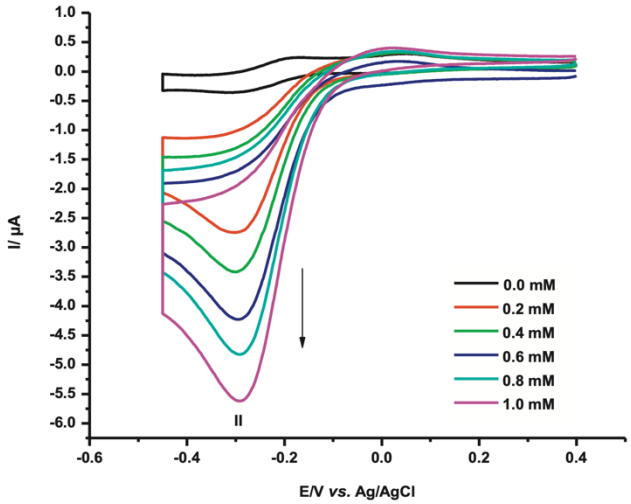

Figure 39 – Cyclic voltammogram of a multilayer assembly of Cu(PC)/PSS comprised of 4 bilayers in the presence and absence of various concentration of phosphate in pH 7.0 buffer solution (Tris-ammonium + maleic anhydride + NaCl) at a scan rate 10 mV.s^{-1}. B. Ali et al.; J. Elec. Chem., 2020, 858, 113170

1.2. COVALENT GRAFTING

1.2.1. PREVIOUS WORK AND SELECTED EXAMPLES

In comparison to the LBL method, where the POM doesn't need modification to be immobilized since it's already negatively charged, it is true that covalent grafting can first seems as an overcomplication in the way of immobilizing POM on a surface. Indeed, to be able to covalently graft a polyoxometalate it is necessary to add a connecting moiety and then to modify our species (lacunary POM, functionalization, Sonogashira post-functionalization…). However, whereas LBL relies on electrostatic interactions obtained by a reversible reaction, a covalent bond means stronger interaction, hence stability of the final device and a diminution of denaturation risk. Moreover, by simplifying the final device (elimination of the cationic intermediary species) there is more control on the POM – substrate interaction.

Covalent grafting can actually be achieved by two paths: one-step (direct) or two-steps (indirect). In this thesis only direct grafting, where the linking moiety is already attached to the POM, will be used, but it is important to mention that indirect grafting has also been explored, a two steps reaction where a monolayer of reactive moiety is grafted on the surface before POM hybrid bonds to it.

One of the examples of POMs covalently immobilized on surfaces is from 2005, when Prof. John Errington and coll. reported a system where POMs were grafted in two steps.[5] In this paper, silicon surface is covered by alkyl chains terminated by alcohol moieties, then a Lindqvist-based POM hybrid, $[TiW_5O_{18}(MeO)]^{3-}$, is grafted through an alcoholysis reaction to form covalent alkoxide bonds (*Fig.* 5).

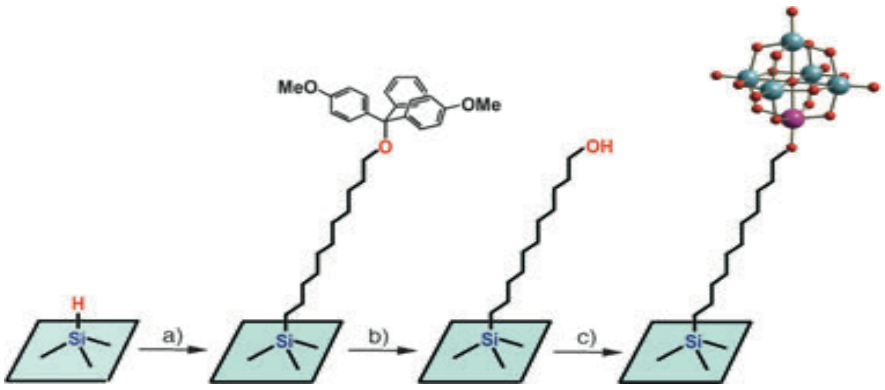

Figure 40 - Two-steps POM grafting process on hydrogenated Si surface. R. J. Errington et al.; Angew. Chem. Int. Ed., 2005, 44, 1254-1257.

Few years later, Prof. Leroy Cronin and coll. reported the case of a covalent SAM of Anderson-type POM hybrids asymetrically grafted.[6] The idea is to exploit the affinity between human fibroblast cells and pyrene platform, polyoxometalates were designed to have a pyrene moiety on one side and an amino on the other side : $[MnMo_6O_{24}(C_4H_8N)(C_{20}H_{18}N)]^{3-}$. 16-mercaptohexadecanoic acid is first deposited on a gold surface to allow the subsequent covalent bonding with the amino moiety. Since the SAM is deposited according a micropattern, they confirmed by microscopy that the cells respected POM-location (*Fig.* 6). Moreover, variation tests revealed that with two amino moieties, or without the POM, cells didn't respect any location pattern, indicating that if the pyrene platform is essential, it is also true for the polyoxometalate.

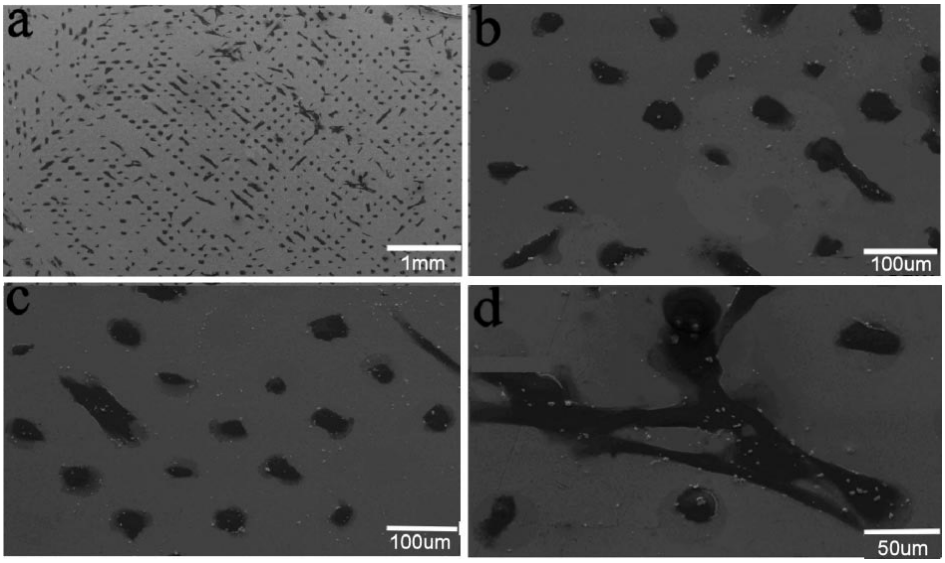

Figure 41 - SEM images of the interactions between hTERT cells and the pyrene group modified Anderson cluster linked to the SAMs. Cell locate themselves exclusively on the patterned areas: (a) full overview on the surface; (b-d) enlarged images. Y.-F. Song et al.; JACS, 2009, 131, 1340-1341.

On the direct grafting side, many papers have been published by our group. In 2018, Dr. Maxime Laurans *et al.* reported a study about the identification of the POM ($TBA_3[PW_{11}O_{39}\{Sn(C_6H_4)C{\equiv}C(C_6H_4)N_2\}]$) molecular signature after grafting to an hydrogenated Si surface.[7] By varying the constitutive metal (W/Mo) they showed that solid-state grafted POMs follow the trend of free POMs in solution (the Mo-based one is easier to reduce) by running I-V curves, on silicon-molecules-metal (SMM) junctions by applying a mercury drop as top electrode (*Fig.* 7), which disclosed tunneling barrier heigths. This work also revealed a primordial aspect of grafted POM: the electronic coupling between the POM and the substrate is weak, meaning a long data retention time, which is favorable for memory application.

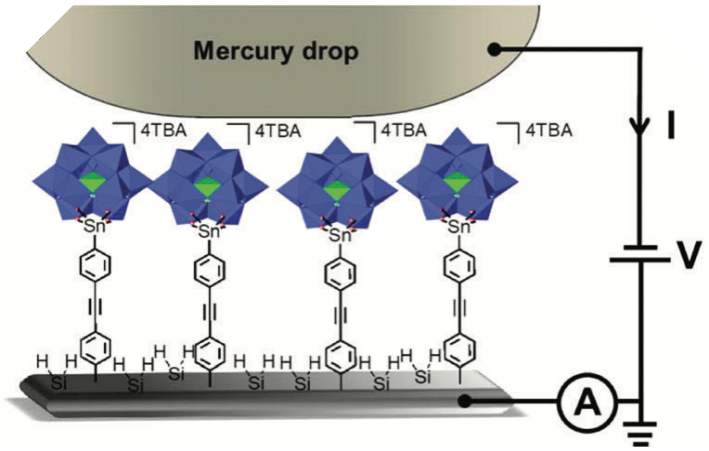

Figure 42 - Scheme of the molecular layer grafted on a Si substrate and the SMM junction Si-POM-//Hg. M. Laurans et al.; Nanoscale, 2018, 10, 17156-17165.

It is worth noticing that not only metal variation has been investigated but also nearly all the major fundamentals aspects of the POM/substrate interaction, not only they have been characterized (by electrochemistry, XPS, IRRAS…) but the charge transfer kinetics between POM and substrate has also been studied on different surfaces (graphene, Si, Au…); impact of variables such as organic arm length and grafting method were also reported.[8–10]

When it comes to grafting, our group used to synthesize a POM hybrid with an organic arm ending by a triazene moiety (N_3Et_2) by Sonogashira cross-coupling. Aiming for a diazonium ending moiety, the POM hybrid was dissolved in acetonitrile and 3 equivalents of HCl were added (*Fig.* 8). After precipitation, the final POM hybrid was stored in the freezer and was stable for some weeks.

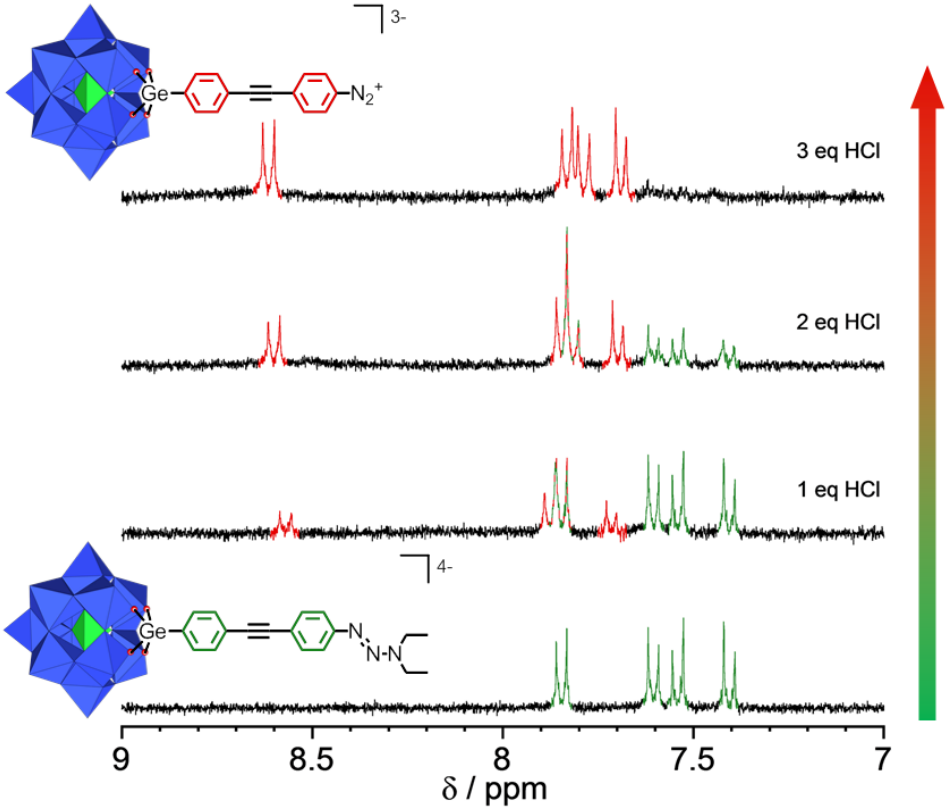

Figure 43 – ^{1}H NMR monitoring of $K_{Ge}[N_2^+]$ formation from $K_{Ge}[N_3Et_2]$ by addition of HCl in CD_3CN. C. Rinfray, thesis, Université Pierre et Marie Curie, 2014.

The grafting itself is realized by cyclic voltammetry. The first step is the reduction of the diazonium moiety, it leads to the releasing of dinitrogen and the formation of highly reactive radical aryl which will immediately covalently bonds to the substrate (*Fig.* 9).[9] It is worth noticing that the activation is unnecessary on silicon-hydrogenated or graphene substrates since the grafting occurs spontaneously.

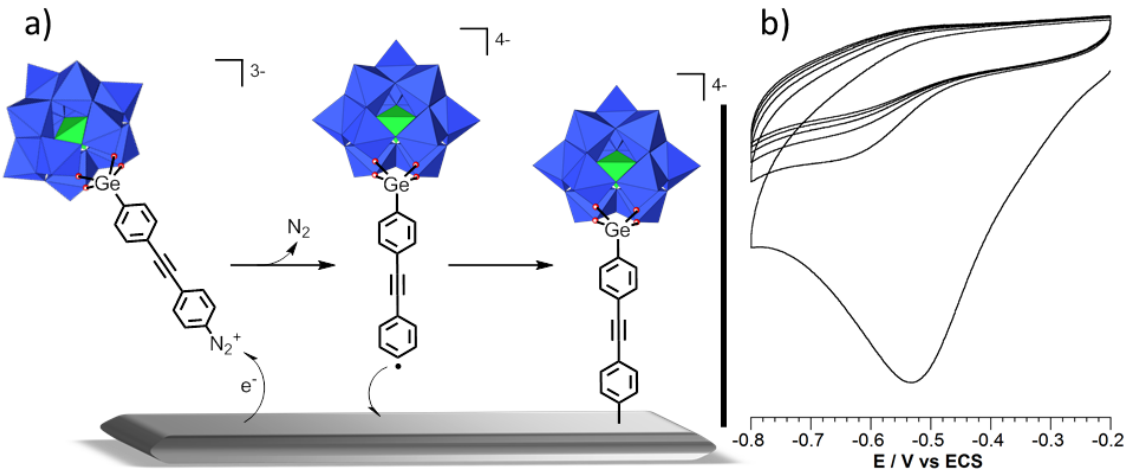

Figure 44 – Mechanism (a) and cyclic voltammogram (b) of electroreduction grafting of the diazonium $K_{Ge}[N_2^+]$. C. Rinfray, thesis, Université Pierre et Marie Curie, 2014.

1.2.2. DIAZONIUM *IN SITU* FORMATION

The previous synthesis path presented an issue that leads to the research of a new way to form N_2^+ termination. Indeed, the acid introduction in the last step, formation of diazonium by HCl addition, induced a partial counter-ions swap (H^+ instead of TBA^+) which modifies and complicates the interpretation of the peaks obtained in cyclic voltammetry. This problem was solved by an in-situ formation of the diazonium without proton addition in the solution.

Prof. J.C. Lacroix and his team reported an acid-free path for R-N_2^+ formation from R-NH_2, relying on *tert*-butyl nitrite (tBuO-NO) addition in large excess (15 equivalents).[11,12] While the mechanism itself is still under investigation, the diazonium formation was confirmed by evidences on absorption spectra and cyclic voltammetry characteristic wave (*Fig.*10).

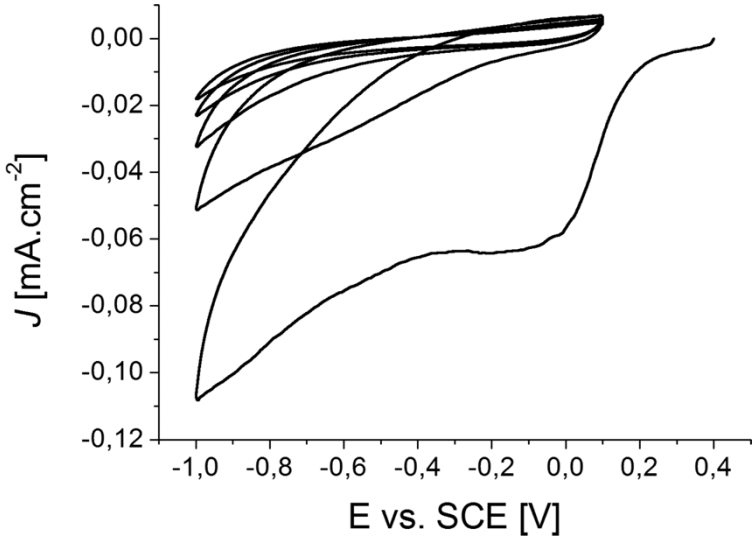

Figure 45 -Cyclic voltammogram of, in-situ formed, diazonium salt reduction (5 x 10^{-4} M in acetonitrile with Bu_4NBF_4 0.1 M) on GC electrode: 1st cycle to 5th cycle. Scan rate 0.1 V/s.V. Stockhausen, G. Trippé-Allard, N. Van Quynh, J. Ghilane, J.-C. Lacroix; J. Phys. Chem. C, 2015, 119, 19218-19227.

1.3. MOLECULAR MEMORY

1.3.1. INTRODUCTION

Dynamic random-access memory (DRAM) is currently the leading memory device in industrial applications, it is based on the combination of a transistor for reading and writing steps, and a capacitor for information storage. However, it has structural defaults such as an intrinsic volatility. Thereby, other memories devices are under vigorous research. Among them, resistive random-access memory (RRAM) is carefully observed with high expectations. RRAMs have a simple metal-insulator-metal structure and many advantages such as their nonvolatility.

According to the set-up, what is called “memory effect” can be represented by different aspects such as mechanic or magnetic, however in RRAM it corresponds to electric resistance switches. In this kind of device, the application of a determined voltage leads to a lowering of the resistance switching the device from an insulating state to a conductive state through the apparition of a conduction path.[13]

WORM (Write-Once-Read-Many) and flash are two types of RRAMs that can be obtained from the fabrication of memory devices. While both are non-volatile, which is mandatory to outperform DRAMs, they have different characteristics. WORM, as indicated by its name, offers a high stability, both time and electrically speaking. As indicated by its name, when an information is stored in a WORM device, it can be read as many times as desired but it cannot be erased. On the other hand, flash offers the possibility to erase and re-write over and over.

In this emerging domain, the utilization of a molecule as the molecular memory layer is even more emerging area and that will be the focus of this part with POM-based hybrids deposited between two metal electrodes.

1.3.2. SELECTED EXAMPLES

Among the most studied molecules for molecular memory are ferrocene and porphyrin.[14–16] Porphyrins present multilevel potential, because of the different charge states in which they present high stability (at ambient temperature and pression): neutral, monocationic and dicationic. When it comes to porphyrin, information storage means removing an electron, leaving a hole and forming a π-cation radical). Thus, writing means charge storing and reading means measurement of the stored charges.

Since DRAMs volatility, due to leakage from transistor (millisecond scale), requests frequent refreshment, presenting a higher charge retention time could be a way to outperform the old DRAMs. In a paper from 2000, Prof. Werner G. Kuhr and coll. reported a system where four different porphyrins were tested.[17] Porphyrin-derivates were obtained by attaching a thiol-ending organic arm, allowing a self-assemble monolayer film to be formed on a gold microelectrode. They tested the charge retention time of their system and the impact of the length of the organic arm on it. They conclude that elongating the arm led to higher retention time, up to 885 seconds and a multiplication superior to seven times when the longest arm is compared to the smallest. Few years later, Prof. Jonathan S. Lindsey and Prof. David F. Bocian went a step further and synthesized, in collaboration with the industrial sector, a prototypical test chip.[18]

Another example of memory device newly developed is the one presented by Prof. Pooi See Lee in 2016.[19] In this article a RRAM flexible device is fabricated. Hexagonal boron nitride (hBN) is deposited on Cu foil / PET substrate and recovered by Ag plots as top electrodes (*Fig.* 11). After memory property is disclosed (*Fig.* 12) by analyzing switching mechanism and retention time of hBN, they confirmed that the Cu foil (partially oxidized) did not interfere on its performance by testing another substrate (ITO) and top electrodes (Au). The system presented highly performant retention time, writing-erase cycles and, furthermore, bending capacity.

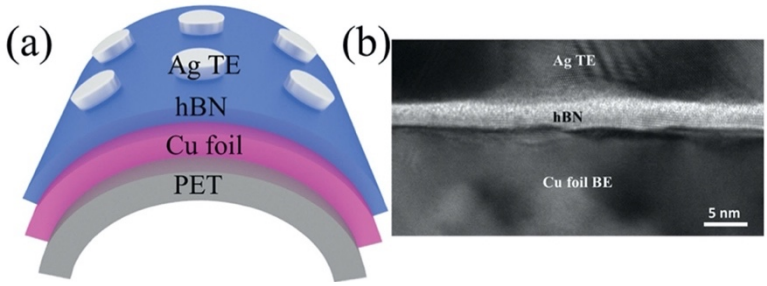

Figure 47 – (a) Schematic of the Ag/hBN/Cu foil on PET substrate device array. (b) Cross-section TEM image of the Ag/hBN/Cu foil memory cell, and the thickness of hBN is about ≈ 3 nm. K. Qian et al.; Adv. Funct. Mater., 2016, 26, 2176-2184.

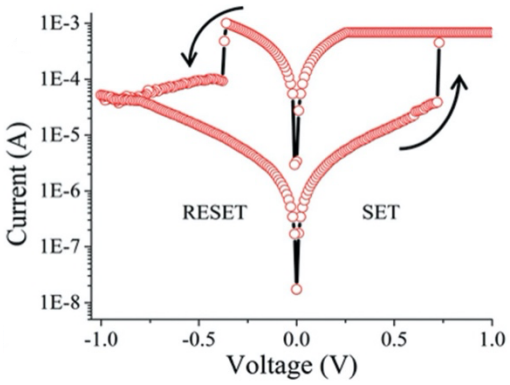

Figure 46 – The switching characteristics for the hBN memory device after electroforming process. K. Qian et al.; Adv. Funct. Mater., 2016, 26, 2176-2184.

1.3.3. POM IN MEMORY DEVICES

As previously explained, molecules that can have multi-redox stable stages are highly interesting for memory devices since it means multi-level storage property and

thus downsizing possibility (density increase). In this context POMs, considering their properties, are logically contemplated to integrate this kind of system.[20]

Transition metal oxide (TMO)-based memory devices aim for fabrication of non-volatile resistive random-access memories (RRAM). In this kind of device, the memory property is governed by resistive switching. This mechanism corresponds to a resistance modification in the TMO induced by the application of a determined voltage.

In view of gaining understanding on the precise role of the POM in the memory device and the underlying mechanisms, Prof S.-T. Han reported studies investigating the resistive switching and the role of the redox property, characterizing polyoxometalates, in the formation of the conductive path.[21,22]

Prof. Qichun Zhang, Prof. Pooi See Lee and coll. published in 2014 a paper where the multi-redox property of POMs was used to obtain a highly performant RRAM device.[23] In this example, Anderson-based hybrid POM ($[N(C_4H_9)_4]_3[MnMo_6O_{18}\{(OCH_2)_3\text{-}CNH_2\}_2]$) (*Fig.* 13) is embedded in a polymer for its processability.

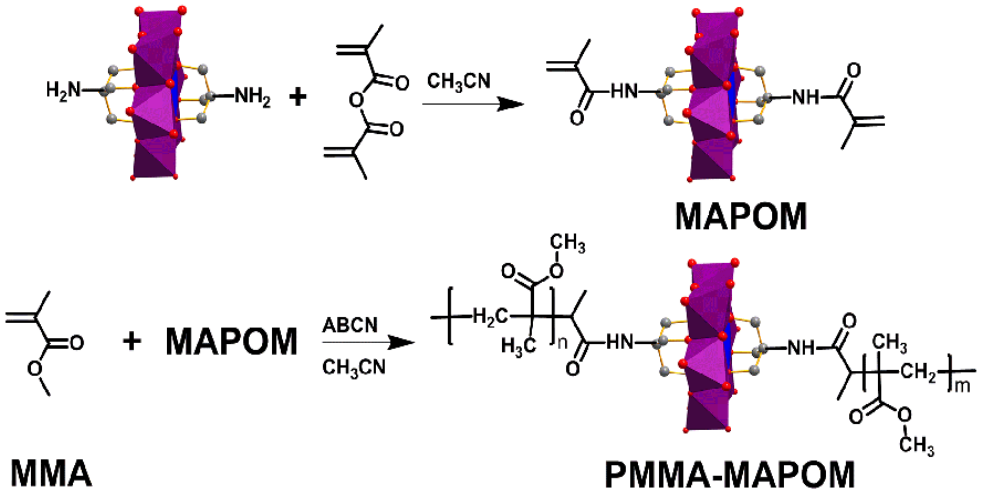

Figure 48 - The synthesis of the POM hybrid polymer. B. Hu et al.; Chem. Sci., 2013, 00, 1-5

The obtained system presents a ternary memory property (*Fig.* 14), corresponding to 3 reduction states of the POM (Mn (+IV), Mn (+III) and Mn (+II)). To switch from one to another, a precise voltage needs to be applied:

- - 2 V, OFF (or high resistance state) to ON (low resistance state): Mn (+IV) is reduced to Mn (+II).

- + 1 V, ON to intermediary state: Mn (+II) oxidized to Mn (+III).
- +1.5 V, intermediary to OFF: Mn (+III) oxidized to Mn (+IV).

They successfully synthesized a highly performant multilevel rewritable memory device based on polyoxometalate hybrids.

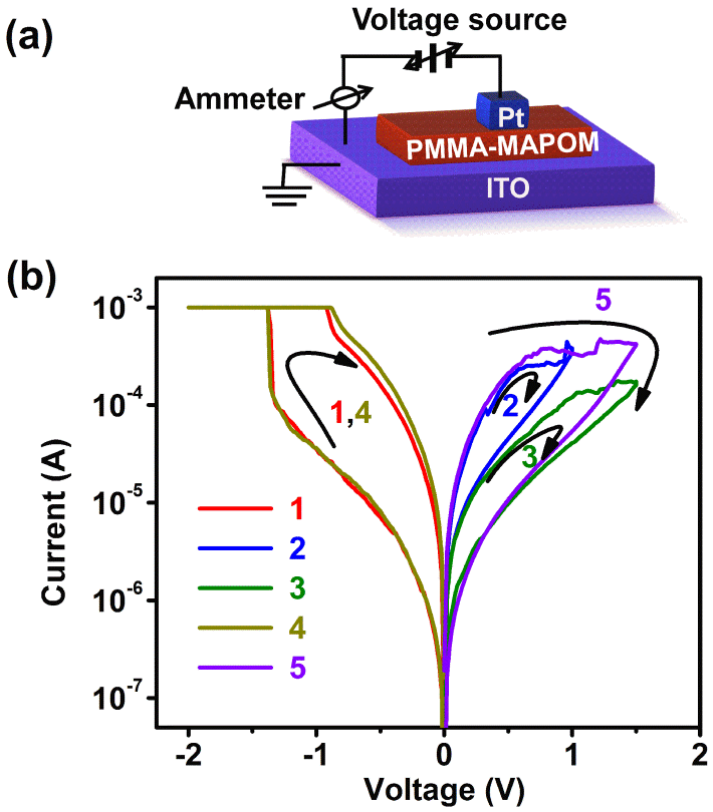

Figure 49 – (a) Schematic illustration and (b) the I-V characteristics of the memory device based on the POM hybrid polymer. B. Hu, C. Wang, J. Wang, J. Gao, K. Wang, J. Wu, G. Zhang, W. Cheng, B. Venkateswarlu, M. Wang, P. S. Lee, Q. Zhang; Chem. Sci., 2013, 00, 1-5

More recently, Prof. Zhi-Rong Chen and his group reported the case of Keggin-type POMs ($[GeW_{12}O_{40}]^{4-}$) embedded in a metalloviologen ($[Co_2(bpdo)_4(H_2O)_6]_n^{4n+}$) metal-organic framework (MOF).[24] The idea is that POMs will form hydrogen bonds in MOF cavities, and thus form a stable non-volatile memory device (*Fig.* 15 (a-b)). A big expected asset for it concerned its thermal resistency. To confirm it, endurance was tested at both room temperature and at 150°C (*Fig.* 15 (c-d)). Heating revealed a structural compression but no loss in performance, opening the door for potential usage in harsh environments.

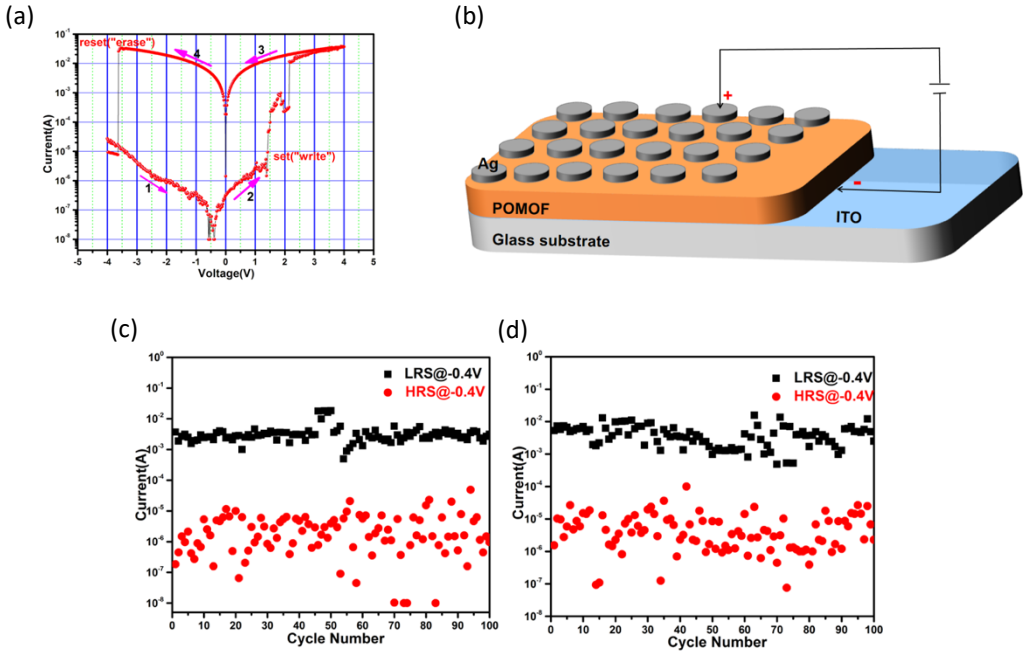

Figure 50 – POM here is $[GeW_{12}O_{40}]^{4-}$. (a) I-V curves of the ITO/POMOF/Ag device with one cycle; (b) Schematic illustration of the ITO/POMOF/Ag memory device; (c) cycle endurance of the ITO/POMOF/Ag device at room temperature; (d) cycle endurance of the device treated by heating at 150°C. B. Chen et al.; Chem. Mater., 2021, 33, 2178-2186.

The examples here were selected in the idea of showing that POMs are promising candidates for taking the role of insulator in the classic metal-insulator-metal structure of RRAMs. That is why in the following of this part, the case of a grafted thick and robust layer of polyoxometalates on ITO, developed between NTU and SU, will be presented.

2. DEVELOPMENT OF THE METHOD

Aiming to continue to explore the potential of POMs in electronic molecular domain, the idea in this thesis was to develop a covalent bond with the substrate, thanks to the activation of a diazonium moiety, generated *in situ*. Logically the first step was then to obtain a POM hybrid with amino ending.

2.1. POMS SYNTHESIS

Selection of the right POM-based hybrid, to obtain multilayers of good quality, has been the first subject of discussion for this thesis. Both Keggin and Dawson-type POMs were considered (*Fig.* 16) because of their outstanding redox potential as detailed in introduction. POM hybridization (especially addition of tin and bis-silyl organic arms) is quite well mastered in our laboratory in the form of a reaction between nucleophilic oxygens of the lacunary POM and presynthesized organo-tin or -silyl ($SnCl_3C_6H_4I$ or $RSi(OH)_3$). For the counter-ion, tetrabutylammonium (TBA, $N(C_4H_9)_4^+$) was chosen, since it allows to solubilize the POM in organic solvents.

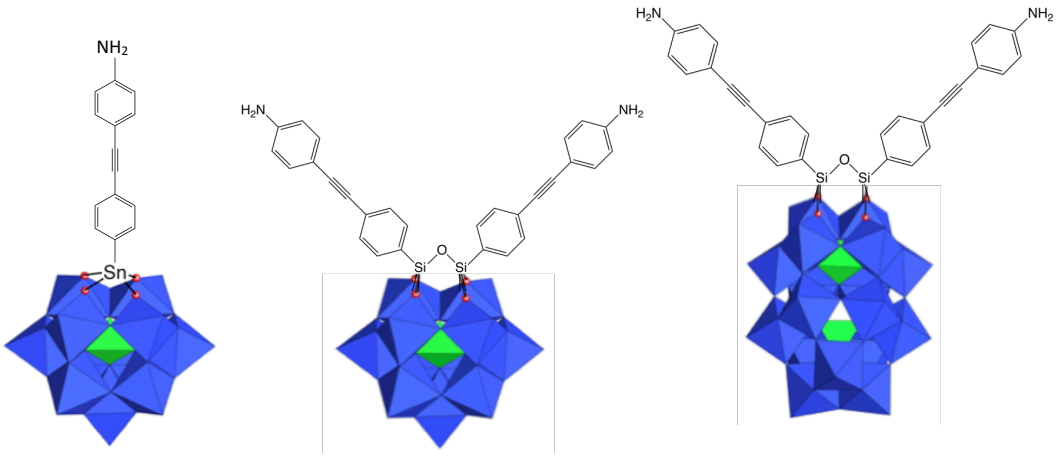

Figure 51 – for all, TBA counter-ions are not represented for clarity; (left) $K_{Sn}[ArNH_2]$; (center) $K_{Si}[ArNH_2]$; (right) $D_{Si}[ArNH_2]$.

$[N(C_4H_9)_4]_4[PW_{11}O_{39}\{Sn(C_{14}H_{10}N)\}]$ ($K_{Sn}[ArNH_2]$) was obtained from Sonogashira cross-coupling of the hybrid POM $[N(C_4H_9)]_4[PW_{11}O_{39}\{Sn(C_6H_4I)\}]$ ($K_{Sn}[I]$) with 4-ethylaniline, catalyzed by bis(triphenylphosphine)palladium(II) dichloride ($PdCl_2(PPh_3)_2$) and copper(I) iodide (CuI) in DMF; same goes for

$[N(C_4H_9)_4]_3[PW_{11}O_{39}\{Si_2O(C_{14}H_{10}N)_2\}]$ ($K_{Si}[ArNH_2]$) from $[N(C_4H_9)_4]_3[PW_{11}O_{39}\{Si_2O(C_6H_4I)_2\}]$ ($K_{Si}[I]$) and $([N(C_4H_9)_4]_6[P_2W_{17}O_{61}\{Si_2O(C_{14}H_{10}N)_2\}])$ ($D_{Si}[ArNH_2]$) from $[N(C_4H_9)]_6[P_2W_{17}O_{61}\{Si_2O(C_6H_4I)_2\}]$ ($D_{Si}[I]$) (*Fig.* 16).

To confirm the successful synthesis and after a washing process (precipitated in ether, addition of CH_2Cl_2, washed in water and reprecipitated in ether), they were characterized by ^1H (^{31}P in annex) NMR (*Fig.* 17) and electrochemistry (*Fig.* 19). Peaks of the newly elongated organic arm ending by an amino group were undoubtedly observed. Even if they are not present on *Fig.* 17, TBA peaks are present on ^1H NMR spectra (3.14, multiplet, 32H, N-CH_2-CH_2-CH_2-CH_3; 1.65, multiplet, 32H, N-CH_2-CH_2-CH_2-CH_3; 1.43, sextuplet, $J_{H,H}$ = 7.5 Hz, 32H, N-CH_2-CH_2-CH_2-CH_3; 1.00, triplet, $J_{H,H}$ = 7.5 Hz, 48H, N-CH_2-CH_2-CH_2-CH_3). The particular doublet of doublet peaks observable in the case of K_{Sn} (for instance: *Fig.* 17 (a, top)) is due to J-coupling between H and Sn ($J_{Sn,H}$ = 15.32 Hz and $J_{Sn,H}$ = 47,44 Hz).

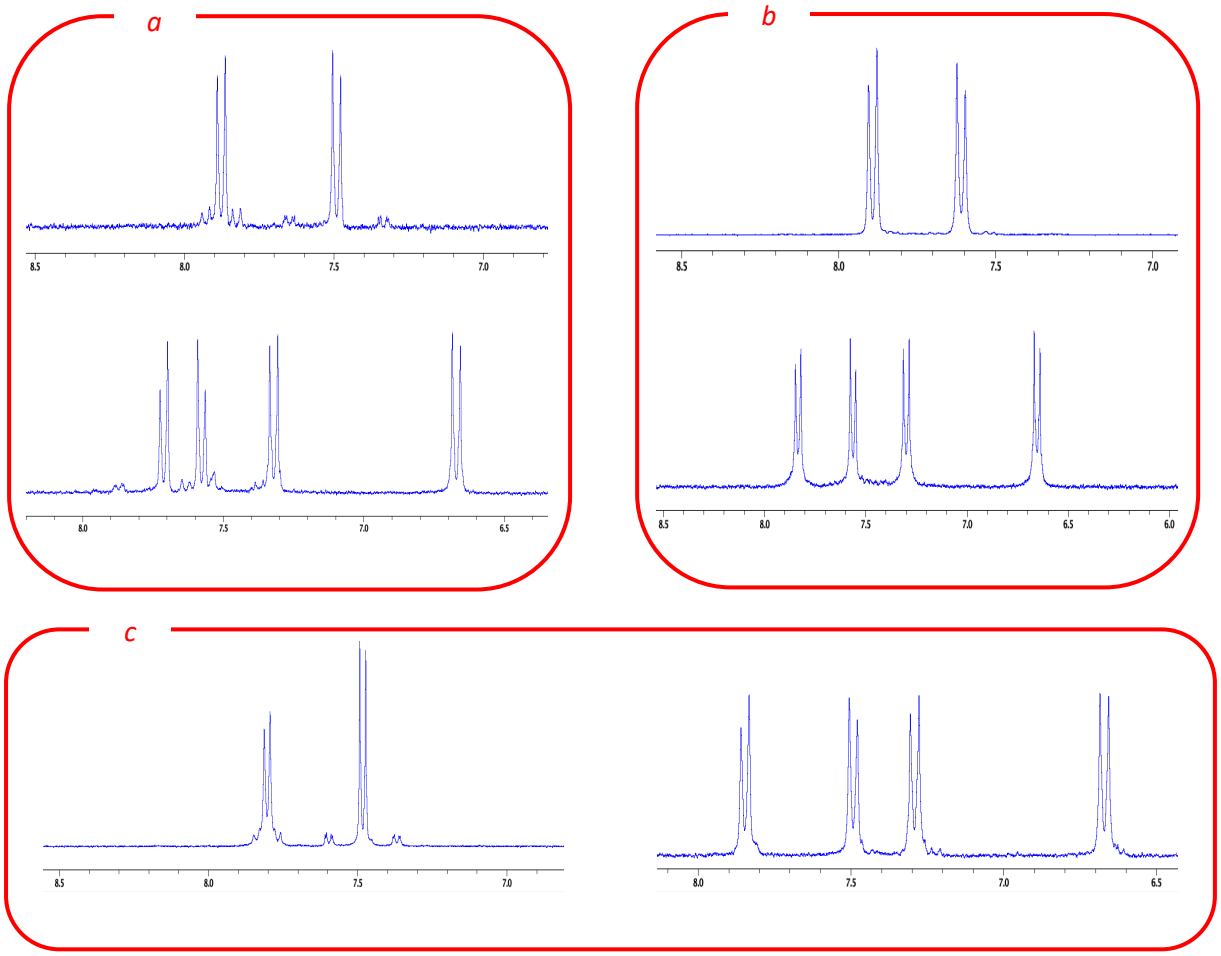

Figure 52 – part of ^1H NMR spectra in CD_3CN of (a) $K_{Sn}[I]$ top and $K_{Sn}[ArNH_2]$ bottom; (b) $K_{Si}[I]$ top and $K_{Si}[ArNH_2]$ bottom; (c) $D_{Si}[I]$ left and $D_{Si}[ArNH_2]$ right.

About choosing the right POM, research started with $K_{Sn}[ArNH_2]$ since it was the best known by the team. However, to obtain a bi-functionalized POM was thought to be more interesting than a mono-functionalized one. Indeed, the expectation was for one arm to form a covalent bond with the substrate and for the second to bond with an arm from another POM, allowing the possibility to form thicker film (*Fig.* 18).

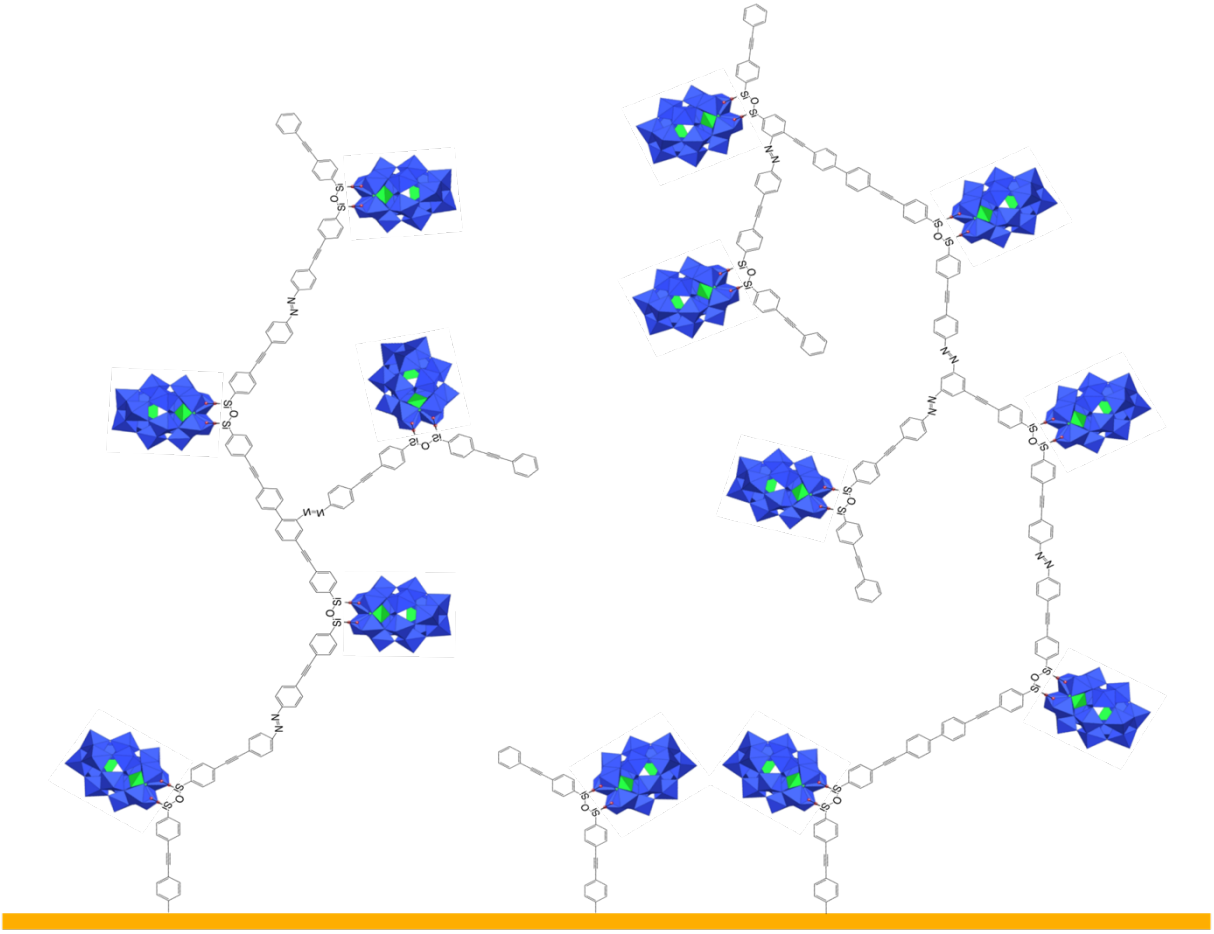

Figure 53 - Scheme representation of the expected chaotic grafting of Dawson POM with two silyl arms. Inspired by V. Derycke (Y.-P. Lin et al.; Sci. Rep., 2016, 6, 1, 31932.

Thus, $K_{Si}[ArNH_2]$ was studied. Yet, since Berzelius' yellow precipitate, POM solubility is an issue. This new hybrid being negatively charged only three times, it was not surrounded by enough TBA to allow a good solubilization in acetonitrile (especially with $[N_2]^+$ moieties). A highly charged POM with two arms was necessary, then $D_{Si}[ArNH_2]$ appeared to be the best choice.

In *Fig.* 19, CV of $K_{Sn}[ArNH_2]$, $K_{Si}[ArNH_2]$ and $D_{Si}[ArNH_2]$ are represented with ITO as working electrode and glassy carbon (for $K_{Sn}[ArNH_2]$ and $D_{Si}[ArNH_2]$). When the electron transfer to the mono-functionalized POM seems reversible, it appears to

be not so clear for the bi-functionalized one. It is also worth noticing that the working electrode has a real impact on the spectrum quality since the ones ran with glassy carbon are way more precise than those realized with ITO ($K_{Sn}[ArNH_2]$ example is displayed in *Fig*. 19). The glassy carbon example reveals the reversibility of the redox property of the hybrid (first reduction peak: -1.04 V, first re-oxidation peak: -0.96 V, gap: 80 mV, V vs ECS).

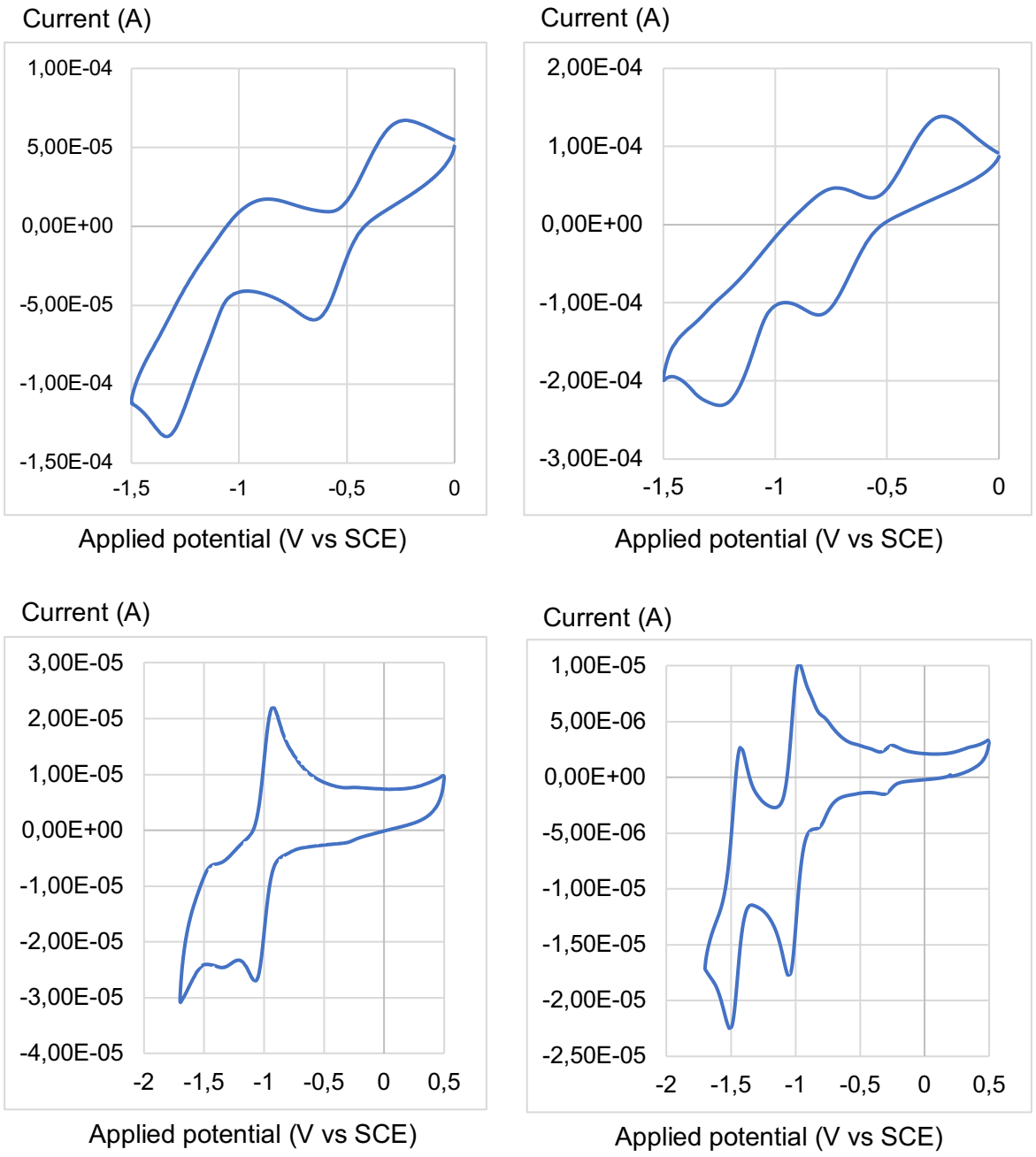

Figure 54 - CV of (top left) $D_{Si}[ArNH_2]$ on ITO; (top right) $K_{Si}[ArNH_2]$ on ITO; (bottom left) $K_{Sn}[ArNH_2]$ on ITO, (bottom right) $K_{Sn}[ArNH_2]$ on glassy carbon. 1mM. 0.3 $V.s^{-1}$. In acetonitrile, with $TBAPF_6$ (0.1 M).

2.2. *IN SITU* DIAZONIUM FORMATION

2.2.1. NMR MONITORING

Since the mechanism of the *in situ* diazonium formation by addition of tBuO-NO is still under investigation, it is only known that a large excess of it is needed, it was necessary to determine the exact number of equivalents by monitoring the formation of the diazonium function formation with NMR. *Fig.* 20 represents this follow-up for $K_{Sn}[ArNH_2]$ and $D_{Si}[ArNH_2]$. 15 equivalents appeared to be the minimum necessary amount. Increasing of this number was tested but revealed to having no impact. In the case of $K_{Sn}[ArNH_2]$ NMR monitoring indicated that after five equivalents, new peaks appeared but the resulting spectra was highly chaotic and rough-hewn. It required

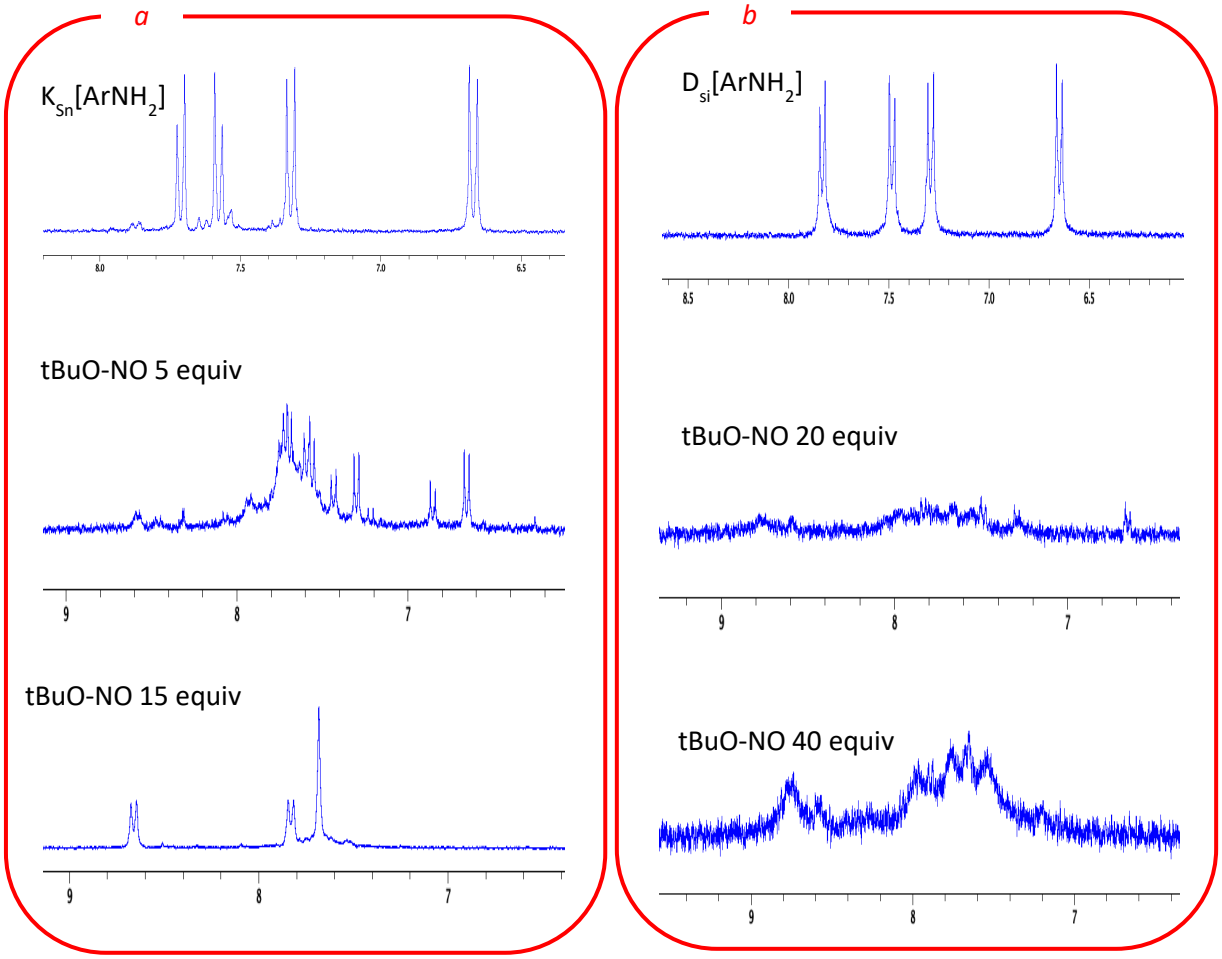

Figure 55 – ^1H NMR spectra in CD_3CN of (a) $K_{Sn}[ArNH_2]$ on top, after the addition of 5 equivalents of tBuO-NO in the middle, after the addition of 15 equivalents at the bottom; (b) $D_{Si}[ArNH_2]$ on top, after the addition of 20 equivalents of tBuO-NO in the middle, after the addition of 40 equivalents at the bottom.

fifteen equivalents to get it clear and distinct. In the other hand, for $D_{Si}[ArNH_2]$, addition

of tBuO-NO only lead to an impasto, or an extreme broadening depending on the side it is considered from, where more than precise peaks, only lumps can be distinguished. The most likely explanation for this phenomena is that Dawson anions present higher charge than Keggin anions, favorizing species aggregation, electrostatic interactions being induced by the apparition of positive charges at the end of the organic arms.

From this point it was decided that 15 equivalents of tBuO-NO were sufficient to perform a full synthesis, this being used for the rest of the work detailed later in this thesis, unless contrary is indicated.

2.2.2. COMPLEMENTARY TESTS WITH $NOBF_4$

For comparison, synthesis of the diazonium derivatives was tried with $NOBF_4$, a way to obtain and isolate diazonium moieties. To do so, six equivalents of $NOBF_4$ (for each amino moiety) are added to a solution of $D_{Si}[ArNH_2]$ in acetonitrile at -20°C. The number of equivalents was decided thanks to previous work from Dr. Rinfray, as he explained in his thesis that 2 or 4 equivalents were not sufficient. After five minutes, the obtained POM hybrids (after precipitation in ether and filtration) are analyzed. However, as revealed by NMR (*Fig.* 21), the resulting precipitation seems to have more distinguishable peaks (this being explained by the fact that large agglomerates are eliminated during the washing process and resolubilization) and as it will be detailed later, post-grafting analysis did not reveal any real improvement.

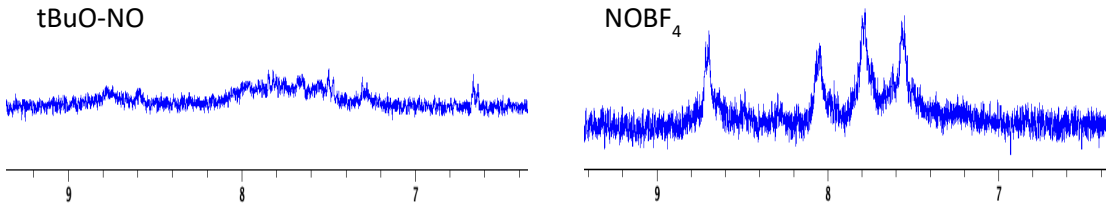

Figure 56 – ^1H NMR spectra in CD_3CN of (left) $D_{Si}[ArN_2^+]$ obtained via tBuO-NO (20 equivalents); (right) $D_{Si}[ArN_2^+]$ obtained via $NOBF_4$ (6 equivalents).

2.3. GRAFTING PROCESS INVESTIGATION

2.3.1. GRAFTING METHODOLOGY

The grafting itself takes place in a three-electrode electrochemical cell (*Fig.* 22). POM[$ArNH_2$] is solubilized (1 mM), under nitrogen atmosphere, in a solution of $TBAPF_6$ (as electrolyte) 0.1 M in acetonitrile. ITO was chosen as substrate, it can perfectly plays the role of bottom electrode in the final system, it is not so expensive price and is interesting in view of applications and the groups, both in NTU and SU, had already developed a savoir faire towards it.

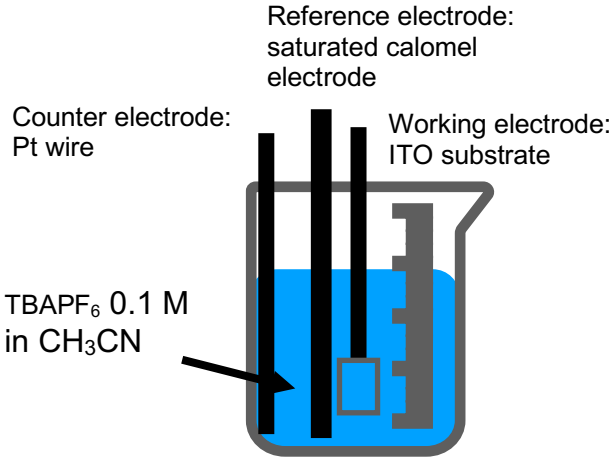

Figure 57 – Scheme representation of the electrochemical cell three-electrode set-up

When tBuO-NO is added to the solution, formation of a small precipitate can be observed. As it is considered undesirable in the close vicinity of the substrate, a waiting time of five minutes is added to the process, allowing the precipitate to reach the bottom of the cell.

Standard procedure corresponds to a POM concentration of 1 mM and 10 successive grafting cycles between 0 and -1 V. After grafting, substrate is washed (with CH_3CN and DMSO) and put back in the cell containing only the supporting electrolyte. CV are then run to confirm the presence of immobilized POMs on the substrate (*Fig.* 23). Post-grafting cyclovoltammograms indicated high reversibility in the redox process as shown by waves values and gap (for K_{Sn}, first reduction peak: -1.053 V, first re-

oxydation peak: -1.028 V, gap: 25 mV; for K_{Si}, first reduction peak: -0.365 V, first re-oxydation peak: -0.349 V, gap: 16 mV; for D_{Sn}, first reduction peak: -0.637 V, first re-oxydation peak: -0.559 V, gap: 78 mV).

A voltage sweeping rate study was performed to confirm the strengh of the bonding between the POM and the substrate. The obtained data of the intensity of the first reduction peak as a function of voltage sweep-rates or speed (from 0.1 V/s to 5 V/s) were plotted and the coefficient of determination close enough to 1 to assurate the linearity of the plot and thus that POMs is successfully immobilized on the substrate.

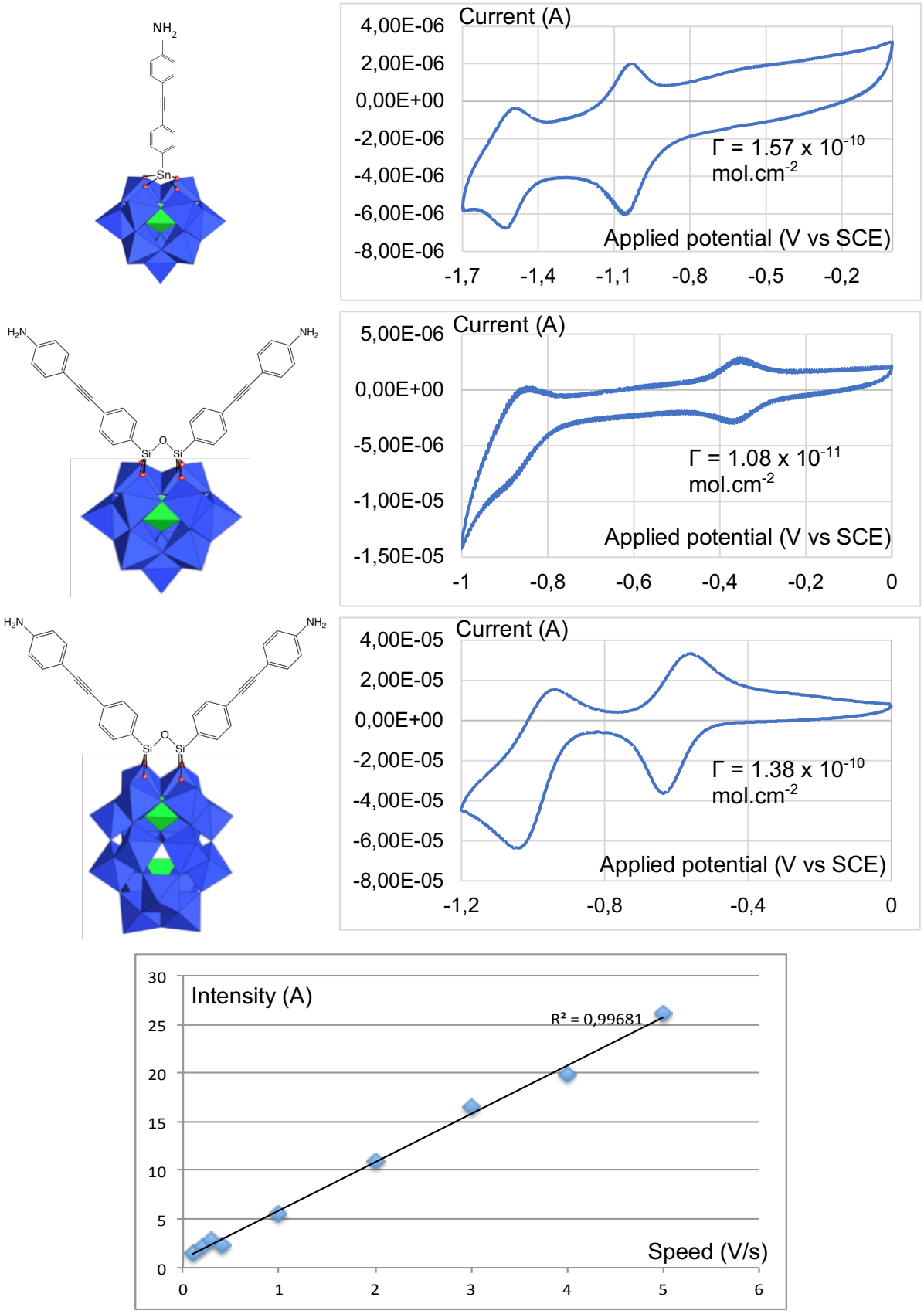

Figure 58 - CV of grafted POMs on ITO. (top) Keggin with Sn arm; (center) Keggin with Si arms; (bottom) Dawson with Si arms. 0.3 V.s^{-1}. (Graph) first reduction peak relative maximum intensity (A) evolution with speed (V/s)

2.3.2. METHODOLOGY REFINEMENT

2.3.2.1. SUBSTRATE COVERAGE

Quickest way to determine the substrate coverage, and thus to judge the grafting efficiency, relies on surface coverage or gamma calculation (equation 1).

(eq. 1) $\Gamma = Q / FA$ [mol.cm^{-2}]

Where Γ is the surface coverage in mole per square centimeters, Q is the redox charge in Coulombs, F the Faraday constant (96 485 C.mol^{-1}) and A the surface area (in cm^2). The key point to reach gamma is the integration of the reduction peak that will offer the Q value. Thanks to that coverage, estimation of the surface is available. For instance in *Fig.* 23, it indicates that $K_{Si}[ArNH_2]$ leads to a very low coverage, 1.08 x 10^{-11} mol.cm^{-2}, in comparison with $K_{Sn}[ArNH_2]$ and $D_{Si}[ArNH_2]$, 1.57 x 10^{-10} mol.cm^{-2} and 1.38 x 10^{-10} mol.cm^{-2} respectively.

According to Dr. Corentin Rinfray calculations (*cf*. C. Rinfray, thesis, Université Pierre et Marie Curie, 2014), a fully packed POM-hybrids monolayer corresponds to a gamma value of 9.2 x 10^{-11} mol.cm^{-2}. This is calculated in the case of the Keggin, since Dawson is mostly used in this thesis, and the aim being multilayers, this value gives a pretty relevant worst-case estimation for our grafting structure determination.

Gamma value gave information about the impact of any changes during the grafting process. It allows to monitor the effects of several parameters such as **potential range and number of cycles** confirming that they had no impact on the coverage. The idea to check a possible impact of the potential range on grafting came from a paper published by Prof. Kim Daasbjerg and coll. where they reported the case of anthraquinone (AQ) moieties electrografted by diazonium activation on gold substrate.[25] In this article they detailed that according to the potential range during electrografting, the thickness of the layer was controllable (thicker layer when the reduction peak of AQ is included in the potential window for grafting, thinner when only

diazonium activation peak is). In the case of this thesis, while the two first reduction waves of Dawson and Keggin-type POMs are included between 0 and -1.5 V, the reduction one of the diazonium on the other hand lies between -0.3 V and -0.5 V. Investigation on the potential impact of POM reduction waves on the grafting was then realized by comparing grafting when including the two waves, just one and finally only the diazonium reduction (*Fig.* 24), but it revealed to be none (*Fig.* 25). Same goes for the study about cycling repetition, increasing of this number up to 75 was tested but it didn't reveal to have any real impact

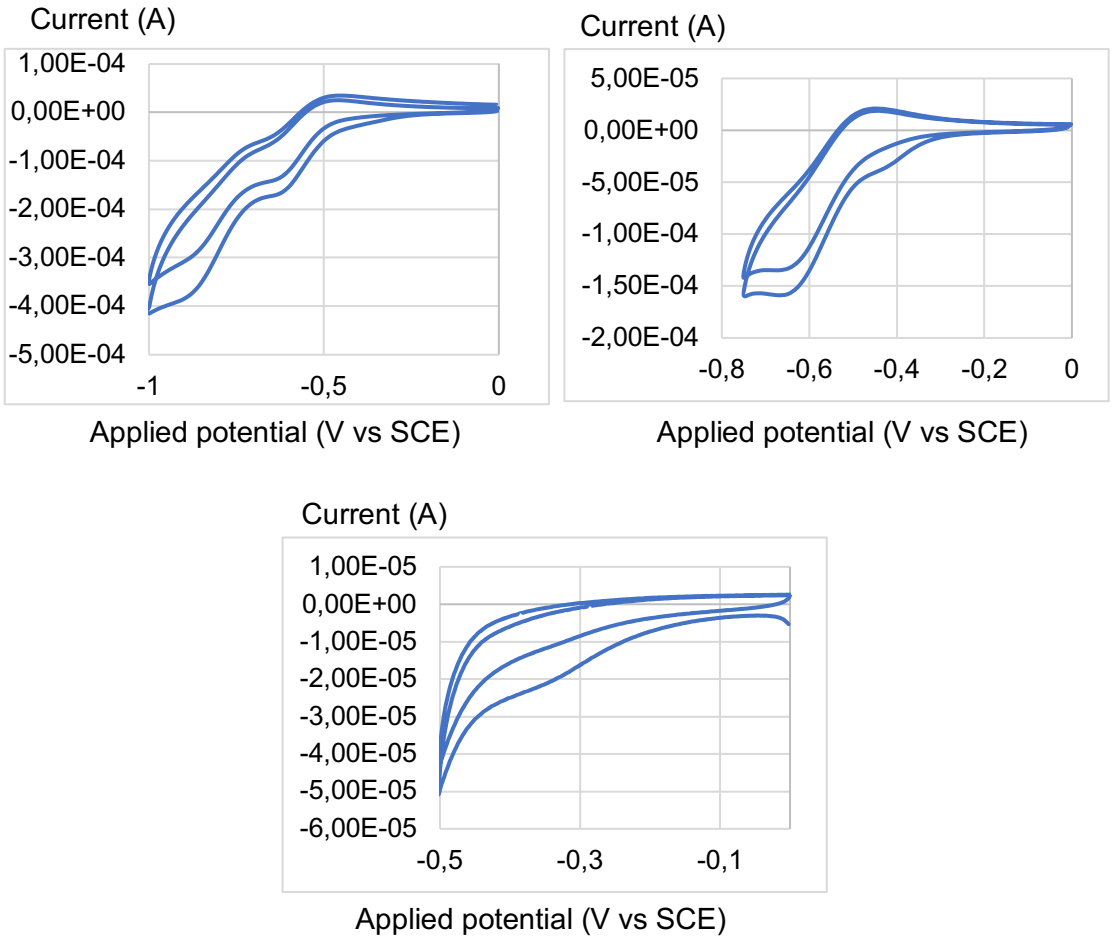

Figure 59 – CV of $D_{Si}[N_2^+]$ (top left) between 0 and -1 V; (top right) between 0 and -0.75V; (bottom) between 0 and -0.5 V. 0.3 V.s^{-1}.

Gamma variation indicates that most of the time, a second grafting process (from a new solution) increases the amount of grafted POMs (gamma increases), leading the double grafted substrates to be categorized as the basic substrates for further characterizations. After that, it is harder to find a general rule, but on some occasions a gamma increase during multiple grafting (up to six) was successfully

obtained - notably the case of three substrates grafted successively from the same hybrid batch and with the same method, the first one being double grafted (Γ = 1.35 x 10^{-10} mol.cm^{-2}), the second quadruple grafted (Γ = 3.51 x 10^{-10} mol.cm^{-2}) and the third sixfold grafted (Γ = 6.60 x 10^{-10} mol.cm^{-2}).

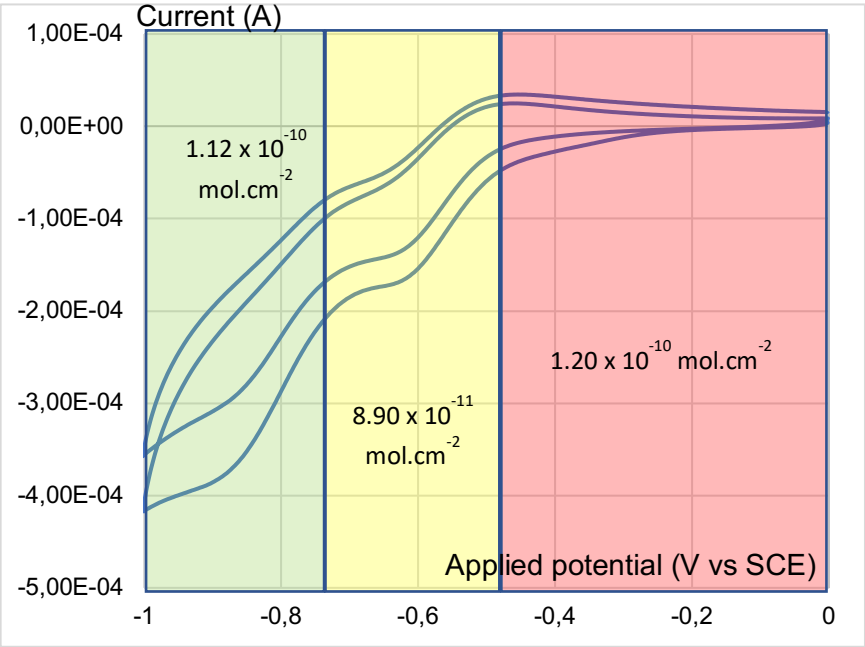

Figure 60 - Different average gamma values according to where grafting cycles are stopped.

Other modifications than potential range were also tested to check a potential impact on the grafting performance. **POM concentration variations** seemed to reveal that a plateau was reach at 1 mM, under this value lower gamma were obtained, but higher value didn't show any improvement (Table 1). Waiting time after the addition of tBuO-NO was studied too but without revealing any gamma impact.

POM concentration (mM)	0.2	0.5	1	2
Γ (mol.cm^{-2})	2.23 x 10^{-11}	9.64 x 10^{-11}	1.38 x 10^{-10}	1.18 x 10^{-10}

Table 1 - Gamma values of grafted $D_{Si}[ArNH_2]$ on ITO. Variation of the POM concentration Following standard grafting procedure except on concentration. All realized in the same conditions with the same batch.

Then, **chronoamperometry (CA)** was considered, to check if stabilizing the potential at a determined value (-0.5 V so it includes the diazonium activation peak) could improve grafting performances. However, it didn't reveal any gamma value enhancement as shown by *Fig.* 26.

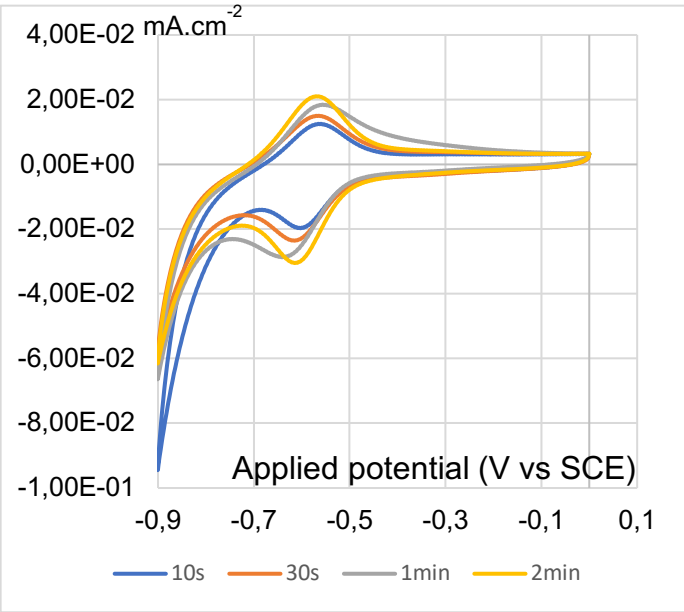

Grafting time	10 s	30 s	1 min	2 min	2 h
Γ (mol.cm^{-2})	2.94 x 10^{-11}	3.71 x 10^{-11}	4.83 x 10^{-11}	6.12 x 10^{-11}	2.51 x 10^{-11}

Figure 61 - (top) CV of complete substrates with POM layers grafted by chronoamperometry with different grafting times (10 s in blue, 30s in orange, 1 min in grey and 2 min in yellow). (bottom) Table of gamma values of the grafted layer after CA.

Before concluding this subpart, it is important to precise one last thing about **reproducibility**. If frequently the gamma ends in the expected range, situations with a very low gamma (under 5 x 10^{-11} mol.cm^{-2} for a double grafted D_{Si} layer that should lands around 2 x 10^{-10} mol.cm^{-2}) were sometimes encounter. Most logical explanation being a lower quality POM batch, but it is not clearly determined yet. Thus, it is safe to say that in around 80% of the cases, no problem was encountered.

2.3.2.2. AFM CHARACTERIZATION & SWISS-CHEESE STRUCTURE

After repeated grafting completion, average gamma estimation was in a range between 1.2 x 10^{-10} mol.cm^{-2} to 2 x 10^{-10} mol.cm^{-2} (for monografting), meaning that grafting was successful but further characterization was necessary, to get an idea of the surface uniformity. To do so, the substrate was analyzed by AFM.

Topographic microscopy revealed surprising results. Indeed, what was expected to be a thin film (our POM size being estimated under 3 nm), luckily uniform,

turned out to be a thick holey film that could grow up to 1 um. The three different POMs were tested to confirm our results (*Fig.* 27).

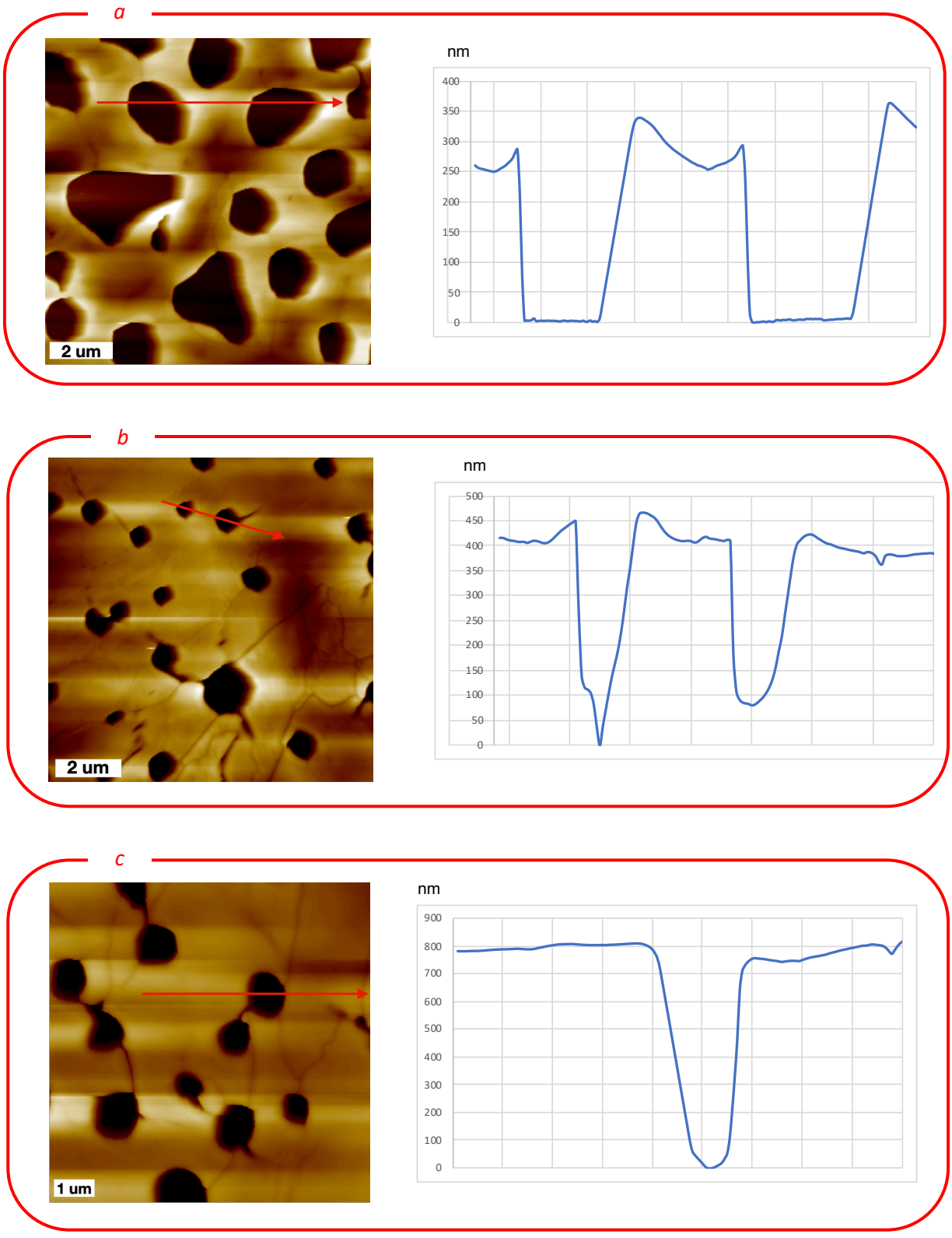

Figure 62 – AFM images of monografted layers on ITO and corresponding height profile. (a) $K_{Sn}[ArNH_2]$; (b) $K_{Si}[ArNH_2]$; (c) $D_{Si}[ArNH_2]$.

These images being in total contradiction with the gamma value (all estimated under 2 x 10^{-10} mol.cm^{-2}) even a very optimistic mind would find this thickness suspicious for this system. However, it was repeated again and again, and a very thick layer was obtained every time. Elemental analysis was the solution found to understand this phenomenon. Scanning Electron Microscopy coupled with Energy-dispersive X-ray spectroscopy (SEM-EDX) analysis were run both at the surface of the film and inside the holes.

Results presented in *Fig.* 28 solved this squaring the circle-problem: if POM can be observed at the bottom of the holes, the thick layer on top is essentially composed of $TBAPF_6$, the electrolyte used during grafting. If the reason for its immobilization on top of the substrate - strong enough to survive to repeated acetonitrile and dimethyl sulfoxide washing - is still a mystery, the way to eliminate it was found in ultrasonication of the substrate in pure acetonitrile for approximately ten minutes (*Fig.* 29).

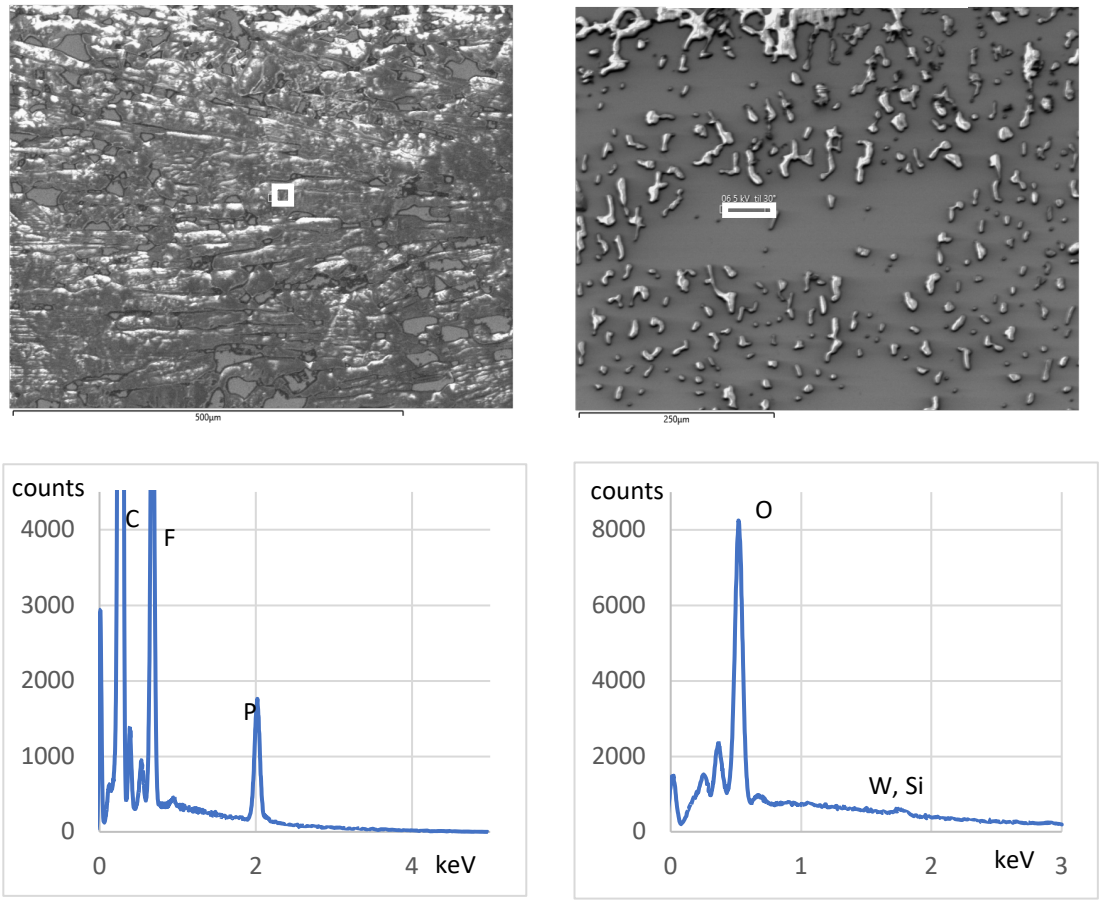

Figure 63 – SEM and corresponding EDX spectra of grafted layer on ITO. (left) at the surface of the layer; (right) in the bottom of the holes.

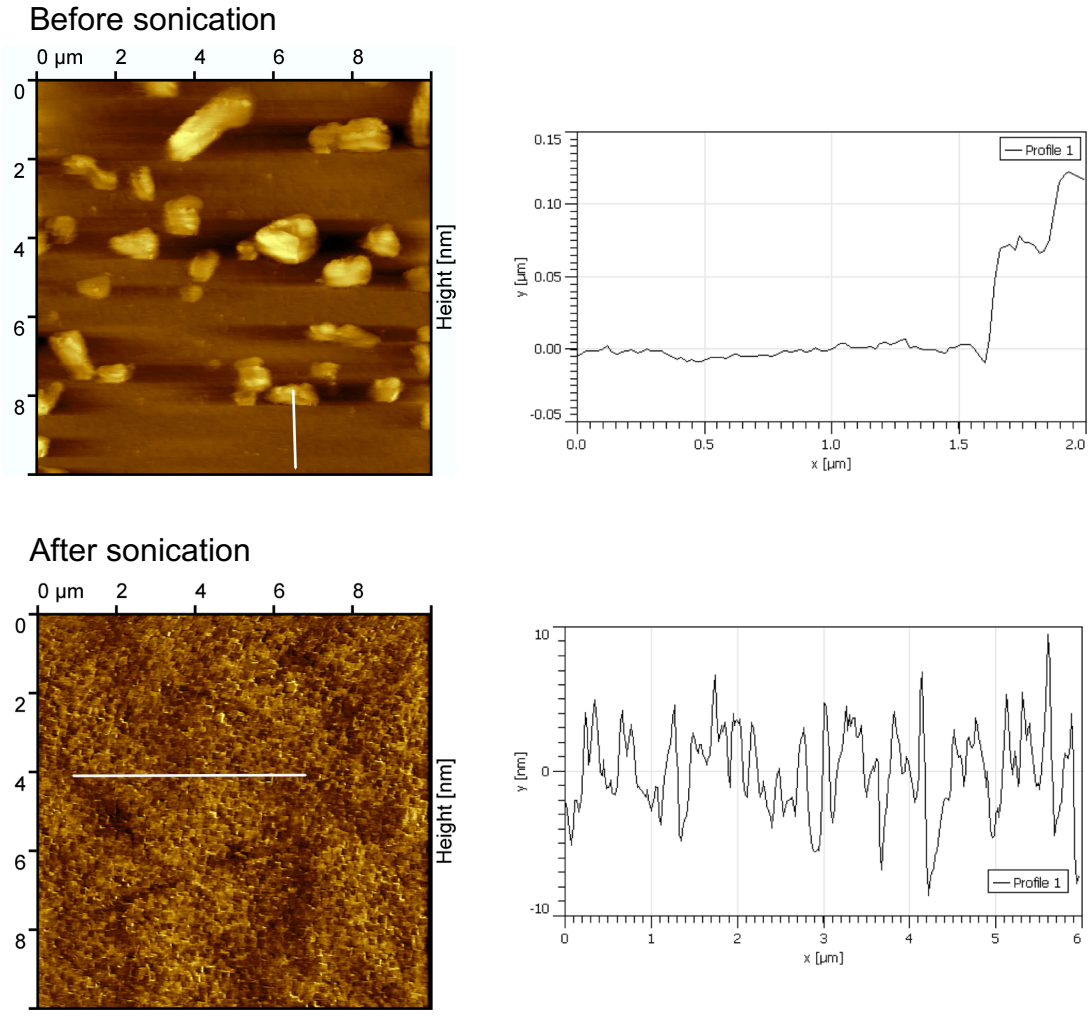

Figure 64 – AFM images and corresponding topographic profiles of a same $D_{Si}[ArNH_2]$ double grafted substrate before (top) and after (bottom) sonication in CH_3CN for 10 min.

A complementary test was run, trying to understand if the thick layer of TBA deposition was caused by the POM presence underneath. However, with only 4-iodoaniline grafting, same issue was encountered.

2.3.3. FINAL PROCESS DESCRIPTION

After all these wonderings, a from head to toe-process was obtained and will be detailed here.

1. A 5 mL solution of $TBAPF_6$ (0.1 M) in acetonitrile is poured in a electrochemical cell under nitrogen atmosphere.
2. ITO substrate is cut and washed in ultrasonicate baths of acetone and ethanol. Typical aimed grafting area being 1 cm^2.

3. A three-electrode system is set-up, with ITO as working electrode.
4. POM[$ArNH_2$] is added to the solution (1 mM).
5. CV is run, 3 cycles between 0 and -1.2 V to confirm the POM presence and quality
6. tBuO-NO is added (15 equiv.), 5 minutes are waited.
7. CV is run, 10 cycles between 0 and -1 V.
8. Electrochemical cell is emptied and washed.
9. Substrate is washed in acetonitrile and DMSO, then ultrasonicate for 10 min in an acetonitrile bath.
10. A new solution of $TBAPF_6$ (0.1 M) in acetonitrile is poured under nitrogen atmosphere in the cell, newly grafted ITO is used as working electrode.
11. CV is run to observe the waves of grafted POM hybrids, varying the voltage range according.
12. Substrate is washed in acetonitrile and DMSO, then ultrasonicate for 10 min in an acetonitrile bath.

Since a multilayer film is the aim, multi-grafting was tested to see if it allows to graft more POM on the surface. In this case, steps 4, 6, 7, 8 and 9 are repeated as many times as desired. Firstly, multi-grafting was considered as a possible way to solve the holey structure issue, desiring to see if the newly grafted POMs would fill the holes. After the revelation of the $TBAPF_6$ constitution of the thick layer and its elimination by sonication, multi-grafting was considered as a way to increase the gamma value of the thin yet uniform layers. However, the gamma – thickness relation was finally found to be less direct than expected, as it will discussed later.

3. MONO AND MULTIGRAFTING

3.1. THICKNESS DETERMINATION

3.1.1. AFM & ETCHING

Now that the grafting process was clearly determined and the $TBAPF_6$ excess eliminated, AFM images confirmed that the coverage was uniform, with a rugosity always measured between 2 and 3nm (which corresponds to the rugosity of the raw ITO used in this set-up) on large image (50 µm x 50 µm), as presented in *Fig.* 30 where the average roughness value (R_A) is 1.357 nm, while average roughness of these ITO substrates was measured around 3 nm. It seems that, similarly as a carpet on gravels, the uniform POM film tends to smooth the irregularities of the substrate.

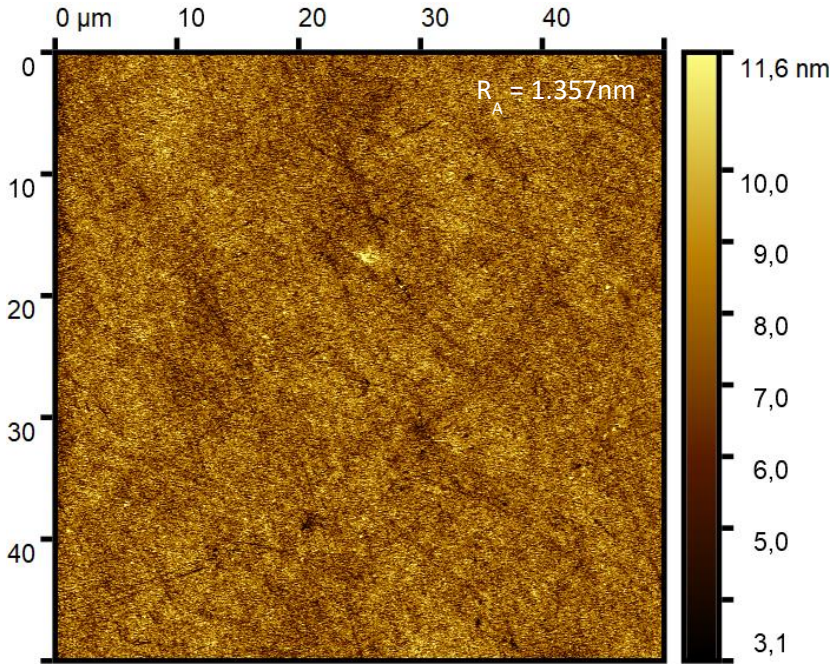

Figure 65 – AFM image of grafted double layers originated from $D_{Si}[ArNH_2]$ on ITO.

Next step being to determine with precision the thickness of the film, etching technique has been suggested. The substrate used in this set-up is composed of glass with an ITO layer of 150 nm on top of it. The idea of the etching was to eliminate ITO

in the middle of the substrate. This new design would allow to only graft on one side of the substrate, and thus to obtain the thickness value by comparing the height of the raw ITO side with the grafted one. To do so, the area where ITO is preserved are covered by tape, then the substrate is covered by Zn powder and highly concentrated HCl is poured. Then, acid is neutralized by a large amount of water and the tape is withdrawn (*Fig.* 31).

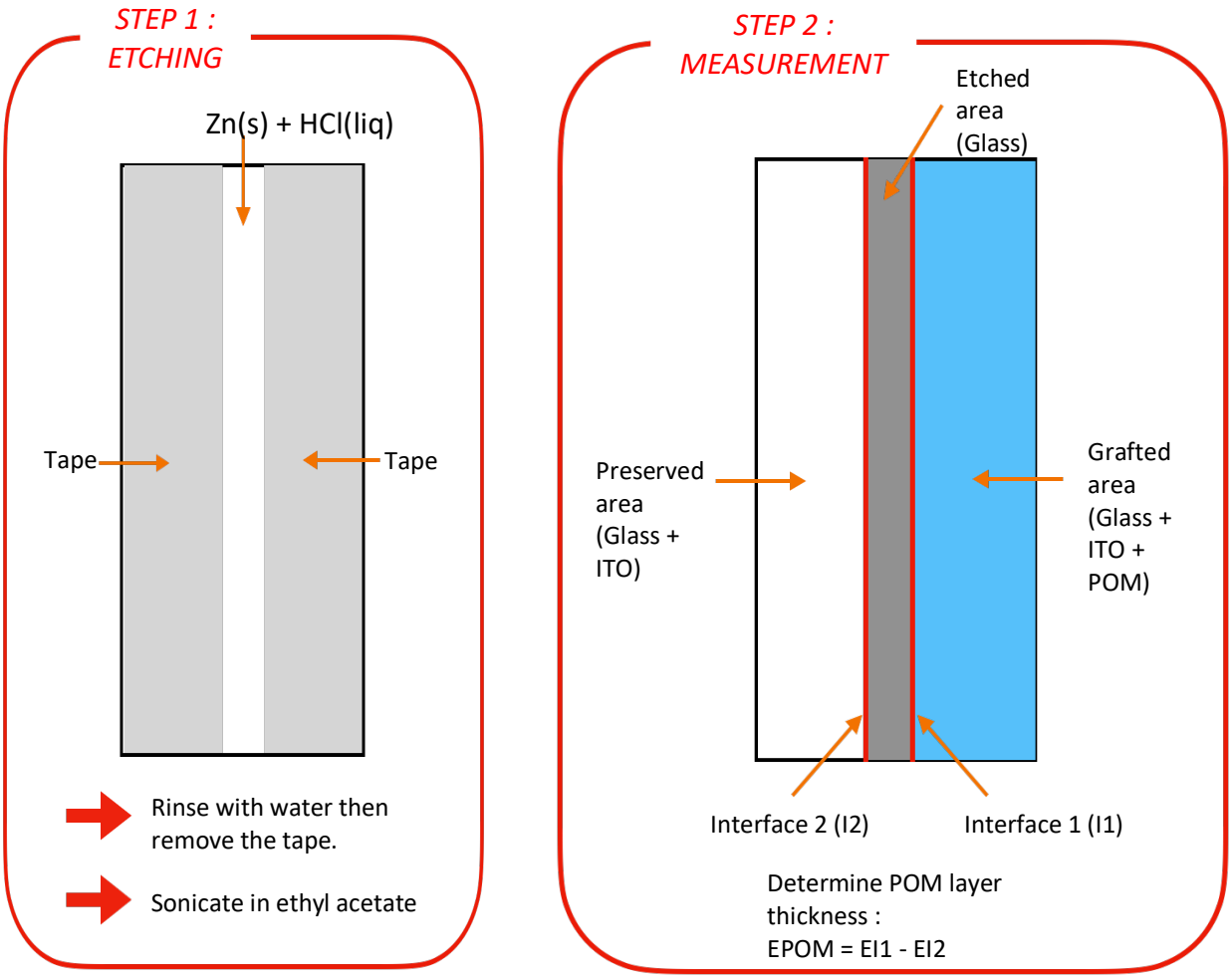

Figure 66 – Scheme representation of the etching method.

However, this technique revealed poor results for this system. Height measure had a very large variation, reproducibility of the values was close to none and it even happened that raw ITO was measured higher than grafted ITO (*Fig.* 32).

	1 (nm)	2 (nm)	3 (nm)	4 (nm)	5 (nm)	6 (nm)	Average (nm)
ITO	98	97	122	134			112.75
ITO + POM	142	190	190	157	134	191	167.33

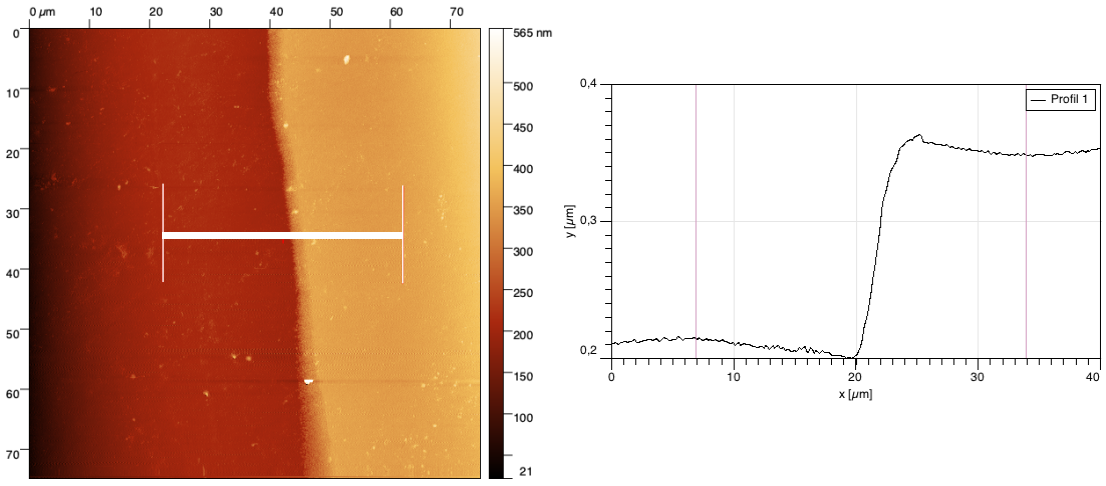

Figure 67 – (top) Measured height (in nm) of the two interfaces on 6 different POMs double grafted substrates. (bottom) AFM image and corresponding topographic profile of etched ITO substrate after $D_{Si}[ArNH_2]$ double grafting, at the interface between glass (red, left) and ITO + POM (orange, right) areas.

An explanation could be that the tape did not preserved the ITO as well as expected. However, the clean and frank obtained edges observed is not indicating in this way. Maybe the etching method was not complete or was inhomogeneous. More investigation would be necessary to clearly determine the reason of this failure, but a new method of thickness determination was quickly found.

3.1.2. SEM-FEG

Once again, solution came from SEM. A slice view of the substrate by electron microscopy allowed to observe and measured each layer of our system: glass, ITO, POM hybrids, and potential $TBAPF_6$ on top. Results indicated a POM layer with an average thickness always superior to 10 nm in case of double grafted substrates (*Fig.* 33).

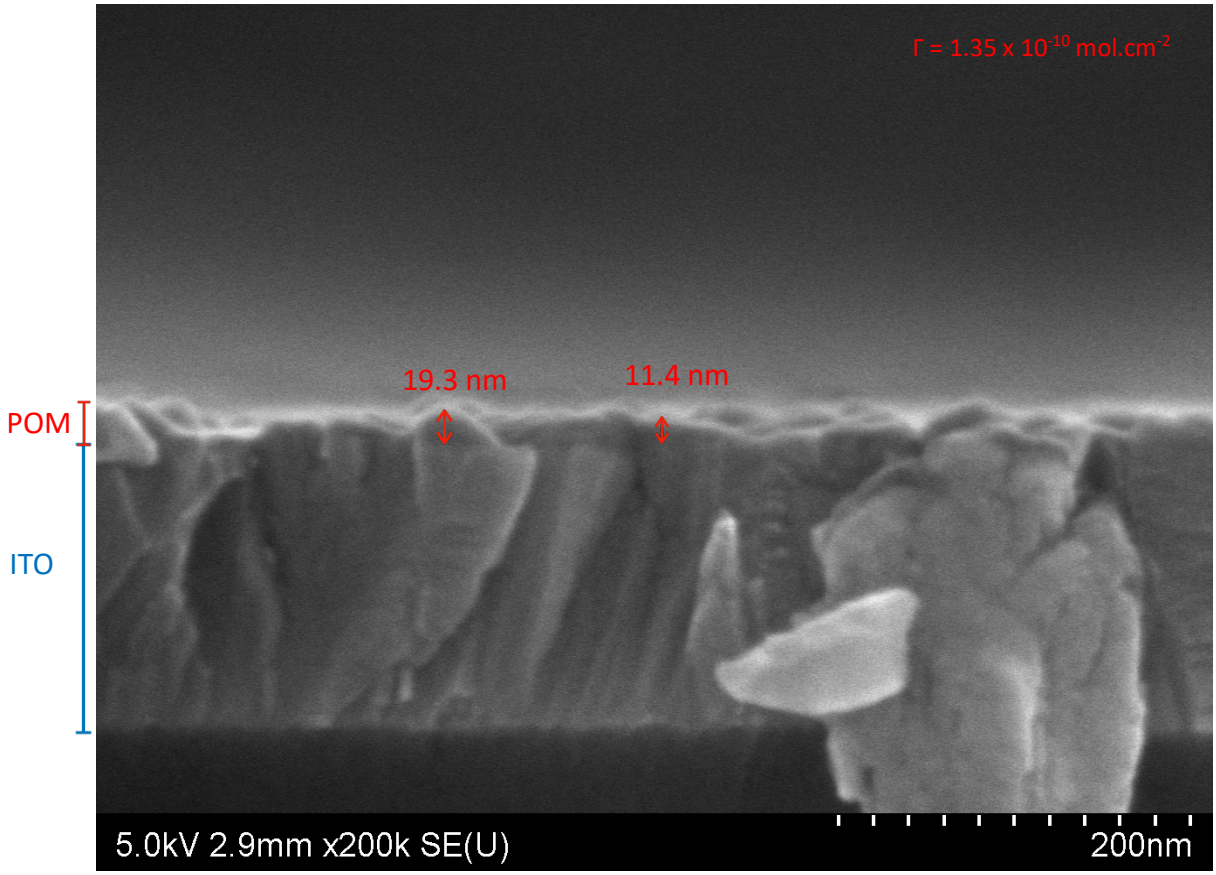

Figure 68 – SEM slice vision of a double grafted layer (originated from $D_{Si}[ArNH_2]$) on ITO.

These measurements appear to be clear, reproducible and pretty positive according to the fact that multi-layer was aimed. However, a uniform film of 15 nm does not match with the gamma value, which barely indicates 2 x 10^{-10} mol.cm^{-2} (corresponding to a bit more than 2 layers, so less than 10 nm). This gap between the SEM value and the gamma value leads to an interrogation about the effective meaning, precision and relevance of the gamma, since the SEM value seems indisputable. Gamma appears to be more an indicator of tendency, a way to know if the grafting is successful or not, than a way to determine the exact amount of grafted POMs. Indeed, a situation was encountered were a very small gamma (inferior to 5 x 10^{-11} mol.cm^{-2}) after two grafting (which happens time to time when one of the variabilities of the grafting goes wrong, a poor-quality POMs hybrids batch for instance) revealed under SEM analysis a non-uniform layer, with thick areas, and others with nearly no POMs. This is due to the chaotic aggregation of grafted POMs, which is smoothed when enough polyoxometalates are grafted. However, the highest values obtained (superior to 20 nm) were always measured on high-gamma substrates (*Fig.* 34).

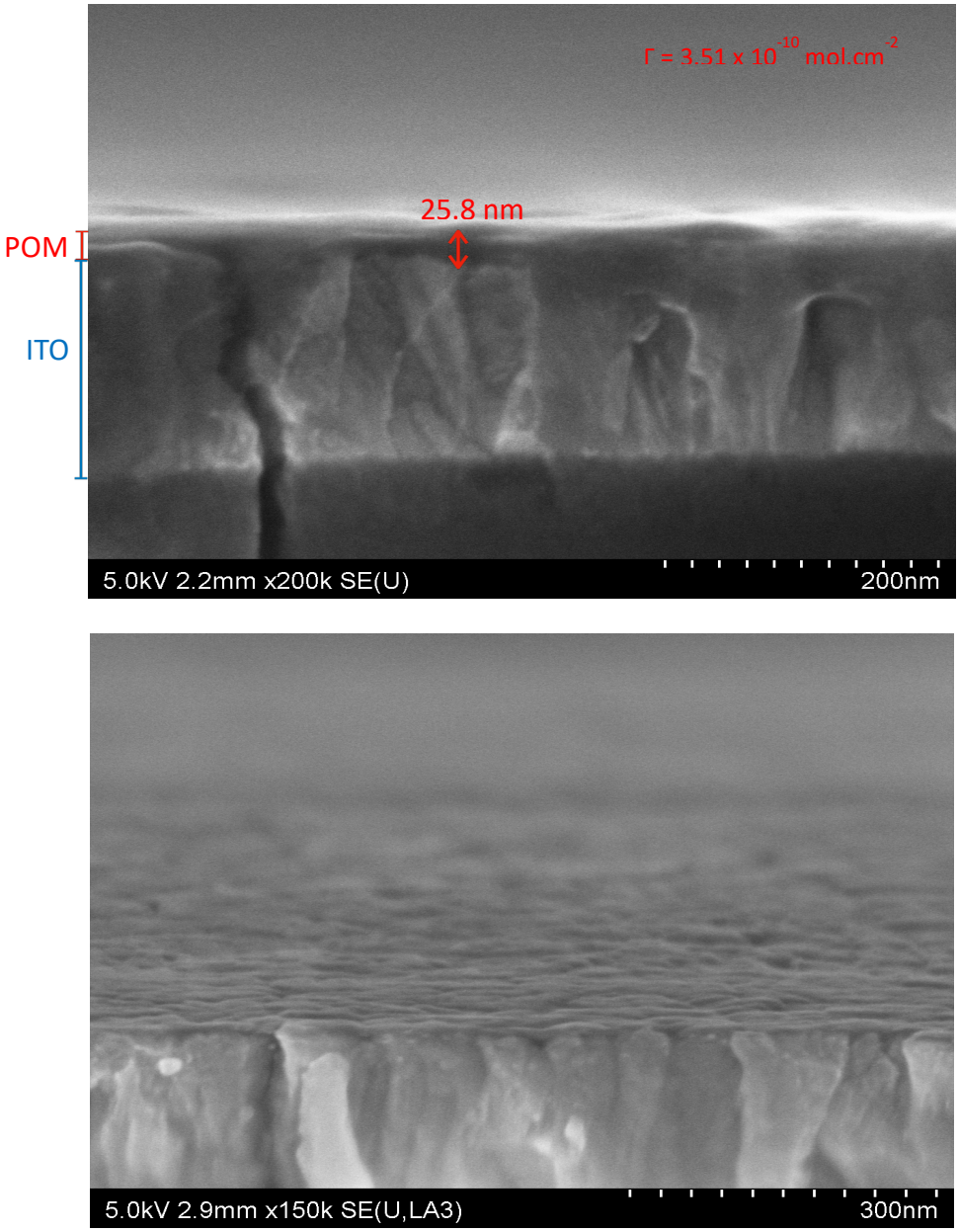

Figure 69 – (top) SEM slice vision of a quadruple grafted layer (originated from $D_{Si}[ArNH_2]$) on ITO with a particularly high gamme value. (bottom) Tilted picture showing uniformity.

A possible explanation for the under estimation of the gamma, is the electrolyte size, indeed a too dense layer would block the path of a too big electrolyte, leading in reducing the apparent conductivity in cyclic voltammetry. This hypothesis is powered by a complementary test where $TBAPF_6$ is replaced by $LiBF_4$, a smaller electrolyte. In this experiment, $LiBF_4$ was use as electrolyte in both the grafting and post-grafting analysis. Then, another post-grafting was run with $TBAPF_6$ in CH_3CN. In comparison, a four times higher gamma value is obtained with the smaller electrolyte (3.92×10^{-10} mol.cm^{-2} with $LiBF_4$ *versus* 1.02×10^{-10} mol.cm^{-2} with $TBAPF_6$).

Interestingly, when SEM was ran on double grafted $K_{Sn}[ArNH_2]$ layers, we obtained layer thinner than with the Dawson but thicker than the expected monolayer, around 10 nm. However, when the same experiment was tried with $K_{Sn}[ArN_2^+]$ isolated as described in part 1.2.1., not generated *in situ*, no layer was visible, even if the POM presence was confirmed by CV and XPS, indicating that the grafted film was thinner than 5 nm and corresponds to a monolayer (*Fig.* 35).

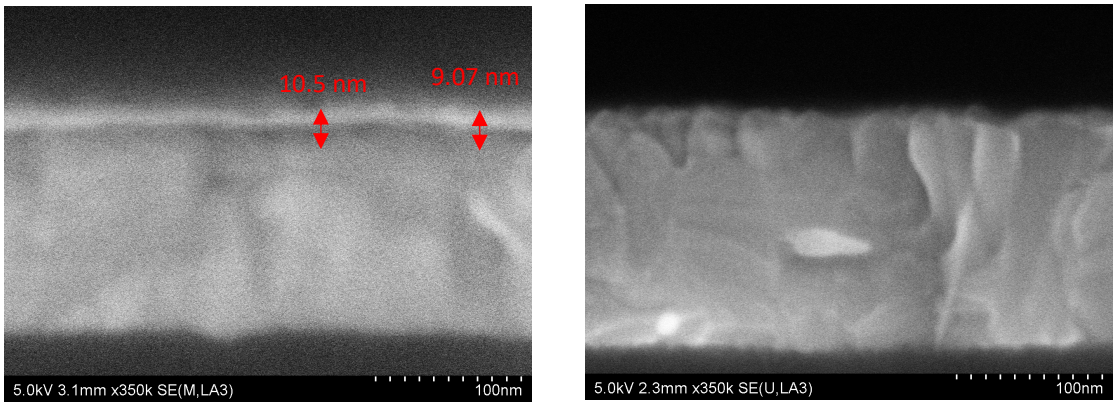

Figure 70 – SEM images of (left) mono grafted K_{Sn}, obtained from diazonium formed in situ, on ITO; (right) mono grafted K_{Sn}, obtained from diazonium isolated previously, on ITO.

3.1.3. XPS analysis

X-ray photoelectron spectrometry (XPS) was used to gain information about the internal structure of the layer. In particular, as shown by *Fig.* 36, the case of nitrogen revealed that a secondary peak (399.91 eV), next to the large one representing the N in the tetrabutylammonium counterion (402.32 eV), indicates that another type of nitrogen is still present in the layer, forming a strong bonding with another organic arm, resulting from the, initially formed, radical evolution. Tungsten characteristic doublet (4f 7/2 and 4f 5/2, respectively 35.70 eV and 37.85 eV)confirmed the presence of POM-based hybrids at the surface.

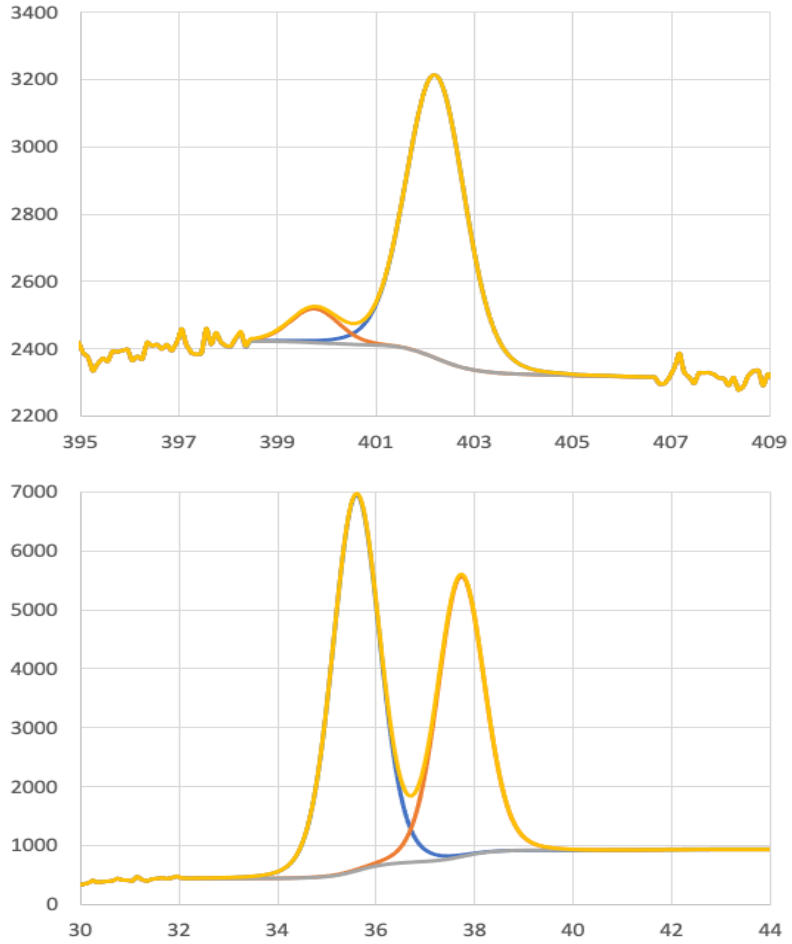

Figure 71 – XPS spectra of nitrogen (top) and tungsten (bottom) in a sixfold grafted layer (originated from $D_{Si}[ArNH_2]$) on ITO. Baseline (grey), fitted line (yellow), participation peaks (blue and orange).

The XPS study was also used to obtain an estimation of the thickness of the tested layers, via a method based on mean free path calculus. Three substrates were tested but the gamma – calculated thickness relation was found contradictory (respectively Γ = 1.35 x 10^{-10} mol.cm^{-2}, Γ = 3.51 x 10^{-10} mol.cm^{-2} and Γ = 6.60 x 10^{-10} mol.cm^{-2} for calculated thickness of 8.8 nm, 10,2 nm and 7.2 nm) and thus a third method (SEM) was find necessary, to confirm which one was right. The set of three substrates presented earlier was analyzed by SEM, XPS and gamma estimation, leading to Table 1, revealing the differences between the techniques.

Number of grafting	Gamma value (mol.cm^{-2})	Thickness estimated by SEM (nm)	Thickness estimated by XPS (nm)
2	1.35 x 10^{-10}	12.0	8.8
4	3.51 x 10^{-10}	21.3	10.2
6	6.60 x 10^{-10}	24.3	7.2

Table 2 – Comparison of thickness or coverage estimations by different techniques (gamma, XPS and SEM), varying the number of grafting.

3.2. FUNDAMENTAL ELECTRONIC PROPERTIES CHARACTERISATION

Electrical surface characterizations of the substrate were realized via atomic force microscopy using the conductive mode scanning spread resistance microscopy (SSRM). Since the POM are non-conductive species, the aim was to investigate on the gamma – thickness connection. Indeed, a thicker layer should be indicated by a lower current. Thus, if the substrates with a larger gamma would be the one with the higher resistance, a link could be established between gamma and thickness. However, it turned out to be unsuccessful. To show that, a representative selection of data is presented in Table 3, revealing that while gamma increases, it is hard to find similar or opposite trend in resistance and in current. This is even more clear when the data are plotted. *Fig.* 37 shows that if there is a resistance variation it is too small to be observed out of the background noise.

Γ (mol.cm^{-2})	Resistance (TΩ)	Courant (pA)
2.29 x 10^{-11}	0.179	-2.13
3.87 x 10^{-11}	0.477	-3.5
4.06 x 10^{-11}	0.479	-0.927
5.66 x 10^{-11}	0.086	-3.422
6.46 x 10^{-11}	0.604	-0.643
6.82 x 10^{-11}	0.477	-0.946
6.88 x 10^{-11}	0.455	-1.155
1.02 x 10^{-10}	0.525	-0.887
1.18 x 10^{-10}	0.309	-1.096
1.31 x 10^{-10}	0.527	-0.834
1.36 x 10^{-10}	0.410	-1.223
1.52 x 10^{-10}	0.522	-0.758
1.73 x 10^{-10}	0.451	-0.664

Table 3 - Representative selection of gamma, resistance, and current values, measured on double grafted ITO substrates with D_{Si}.

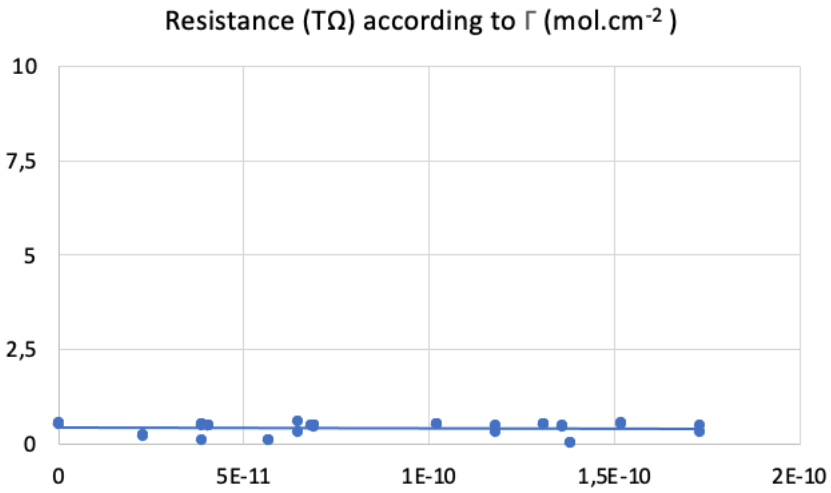

Figure 72 – Resistance plotted according to gamma variations. Measured on double grafted ITO with D_{Si}.

Nevertheless, it is worth noticing that these experiments gave interesting results on other aspects: uniformity and work function. Images confirmed the uniformity of the substrate both in conductivity (picoampere scale) and resistance (teraohm scale) as shown by *Fig*. 38 (a).

SSRM is a technique relying on the measurement of resistivity, the current being calculated from the combination of the applied bias and the measured resistance (c-AFM). It provides information on the surface potential, such as the work function (Kelvin Probe Force Microscopy, KPFM). Variations observed on the obtained work function maps revealed a gap of approximately 200 meV (correlation from Volt to eV is direct) on the surface. It is highlighting the thickness variation, since the denser the layer is, less the ITO will impact the POM work function and more it is related to the other POMs surrounding it, diminishing the influence of the substrate. As shown by *Fig.* 38 (b) a gap of 90 meV can be observed between a representative “up” position and a representative “low” position. Highest positions (which corresponds to where the layer should be thickest) present a weaker work function. It is important to mention that KPFM requires calibration to obtain absolute values, without that (problems were encountered during calibration), the measurement are relatives one to another.

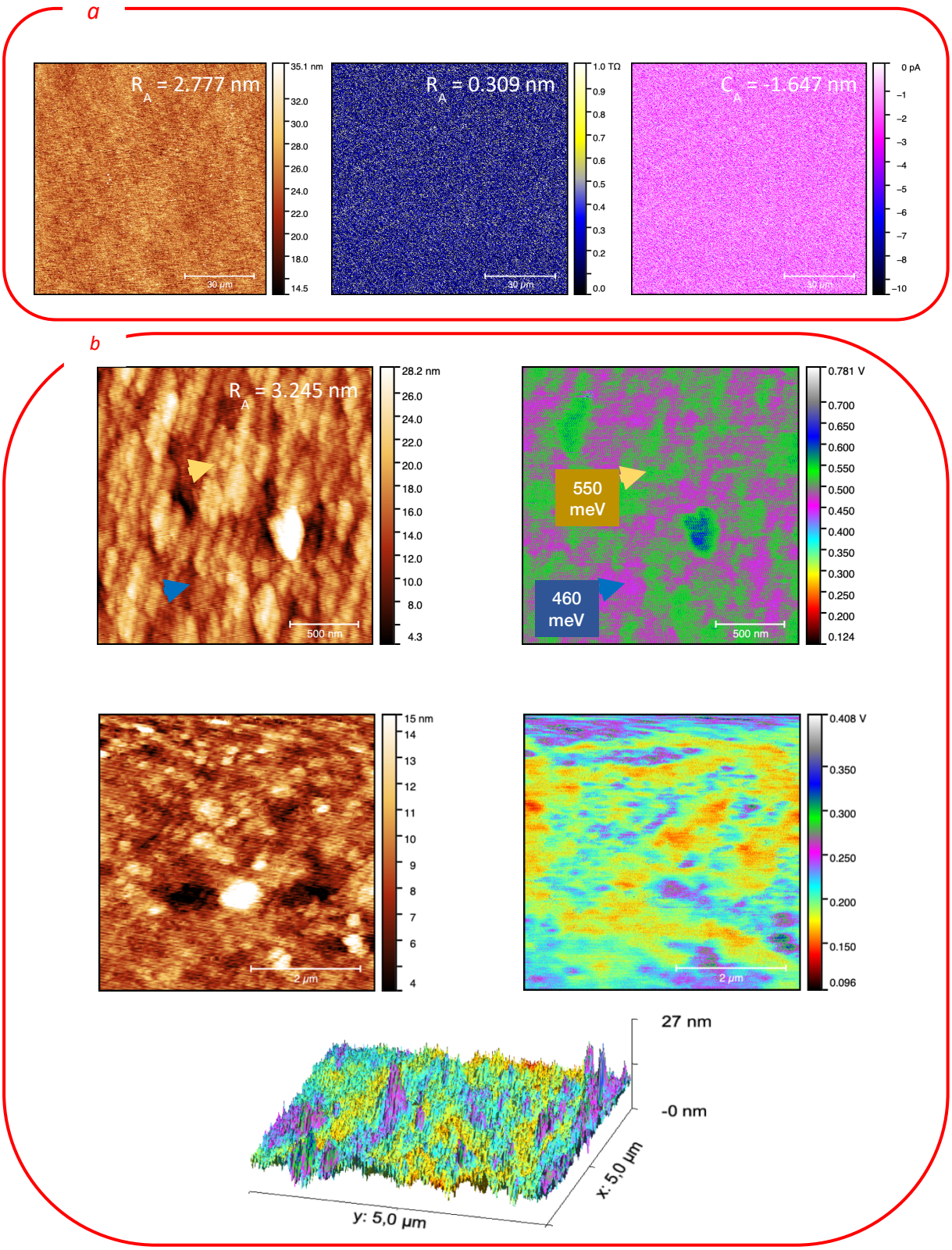

Figure 73 – (a) c-AFM images of the same double grafted layer (originated from $D_{Si}[ArNH_2]$) (left) topography, (center) resistance, (right) current. (b) KPFM images of (top) the same substrate as (a) topography and work function map; (bottom) topography, work function map and 3D view of a similar substrate

4. MEMORY TESTS

4.1. PROCESS DESCRIPTION

To perform resistive memory test on the system, it was necessary to get top electrodes on the device. To do so, gold plots are formed and deposited by chemical vaporization. After that, I-V curves are obtained by applying a voltage on the top electrode and measuring the exit value to observe potential resistive switch in the POM hybrids film (*Fig.* 38*)*.

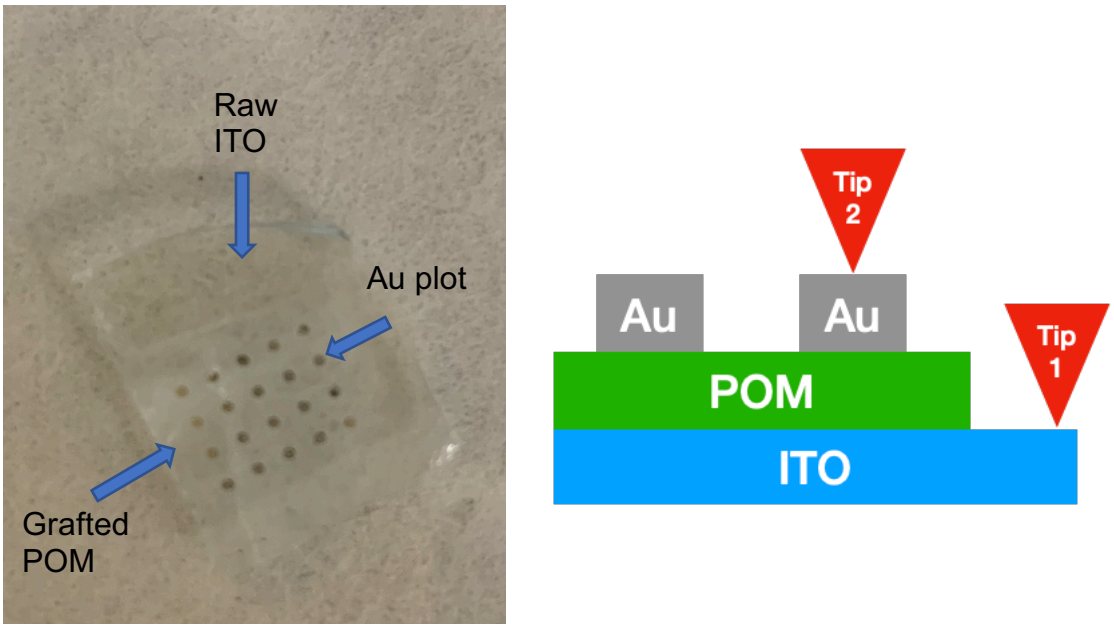

Figure 74 - (left) Photo a complete system with top electrode. (right) Scheme representation of a complete system and the tip (point-of-contact) positioning for memory effect measurement.

4.2. RESULTS AND DISCUSSION

More than one hundred devices were tested on multiple substrates, with 40% of the devices successfully detected with memory effect. Over these positive responses, 95% of them corresponded to WORM memory and 5% to flash memory (*Fig.* 39 (a)).

As detailed in the introduction part, flash memory is characterized by its erasability property. In *Fig.* 39 (a, left) the step that can be seen between 1 and 2 (or 5 and 6) corresponds to the resistance switch from OFF to ON states, when the step between 3 and 4 (or 7 and 8) represents the resistance switch from ON to OFF states. Similarly, the WORM memory presented in *Fig.* 39 (a, right) shows the resistance switch from OFF to ON states at -1.2 V and the persistence of the ON mode up to 5 V.

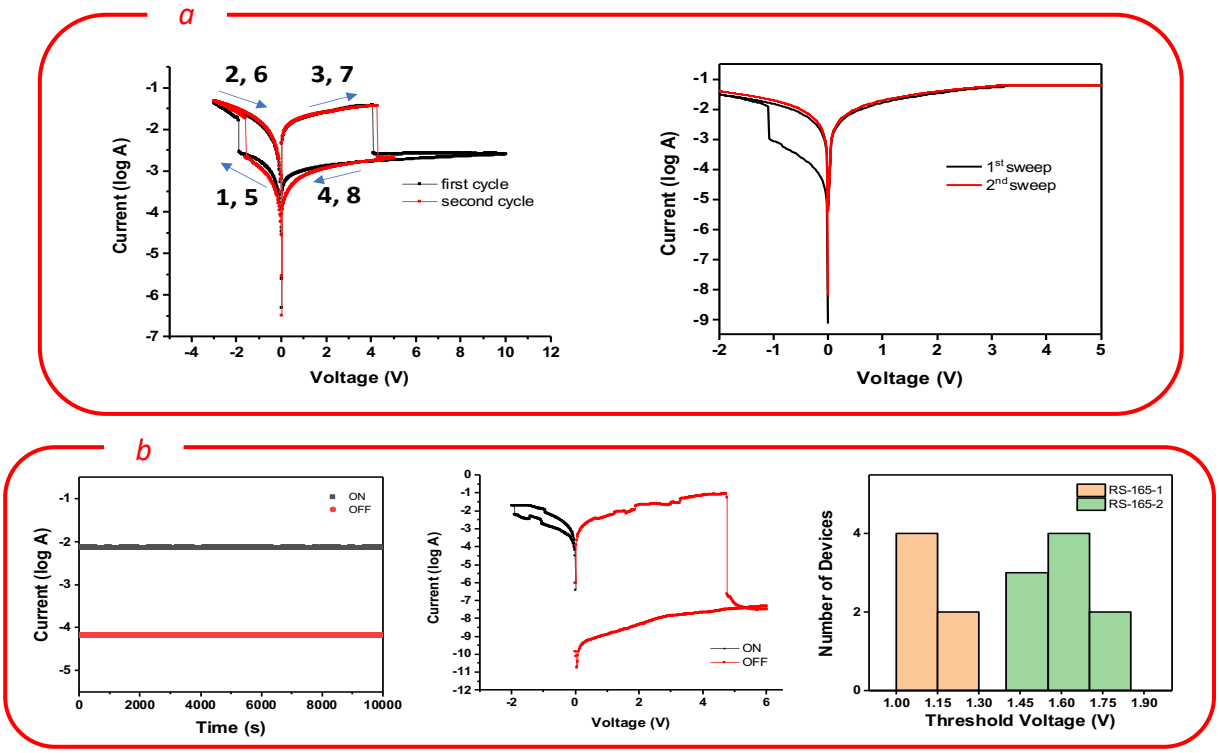

Figure 75 - (a) Graph representatives of Flash memory (left) and WORM memory (right). (b) (left) Graph representation of the stability of the current over time; (center) WORM forced reset scenario; (right) chart of the threshold activation voltage for two representatives substrates (double grafted layer originated from $D_{Si}[ArNH_2]$).

The non-volatility of the system and its high stability were characterized by current measurement over time when the device is on mode ON. As shown in *Fig.* 39 (b), trying to force to erase a WORM memory leads to a destruction of the memory effect. Interestingly if the threshold voltage (voltage value to switch from OFF to ON states) is pretty narrow when different positions are tested on the same substrate, it varies between a substrate and another. Since the same POM is grafted ($D_{Si}[ArNH_2]$) in all the tested systems, a possible explanation of the threshold variation could be that it is caused by thickness and density variations. Indeed, in a paper from 2017, T. Venkatesan and coll., discussed the role of counterions in the non-volatile memory device.[26] Their system is based on a ruthenium molecular film (*mer*-[Ru(2(phenylazo)pyridine)$_3$](PF_6)$_2$), while testing different counterions they noted that

they had an impact of the hysteresis and they concluded that counterions size, and thus mobility, where related to the hysteresis. In the case of this thesis, the counterion is not changing (except one $LiBF_4$ try), but from one sample to another, the thickness and the density of the film vary, and so does the mobility of the $TBAPF_6$. It could explain the variation in the Vset values.

Finally, a capacitance measurement was realized. The OFF state to ON state transition was analyzed, *Fig.* 41 (a), and it revealed that the capacitance was multiply by four after the resistance switch (1.2 V), from ~ 0.2 nF (OFF) to ~ 0.8 (ON), indicating a higher energy storage capacity in ON state. Then, after being turned ON, 0 to 2 V domain was tested. The stability and uniformity of the capacitance values obtained over this potential area confirmed the WORM character of the memory device and thus its intrinsic unerasable property.

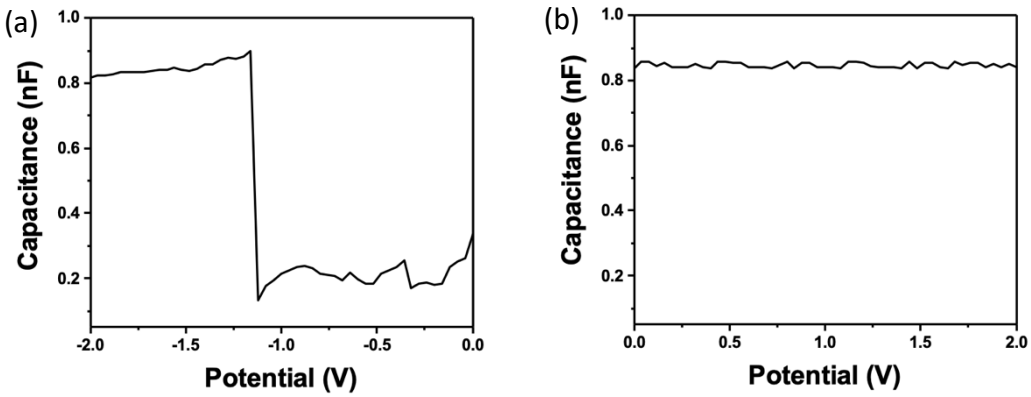

Figure 76 – Capacitance measurements, realized on ITO substrate covered by double grafted D_{Si} film. (a) OFF to ON states transition; (b) ON state stability over large potential range.

In the case of polyoxometalates, the resistive switch corresponds to the reduction of the POM. From that point, the electron needs to reach the bottom electrode and thus two main scenarios are possible for it. One presenting an electron hopping from one hybrid to another, the other where the conductive filament are formed by oxygen vacancies. The second hypothesis is the most referenced, explored and thus, likely.[21] According to this scenario, oxygen vacancies are formed, and randomly distributed, when the redox reaction occurs. Then, they will migrate at the bottom electrode and after enough accumulation, they will form conductive filaments, switching the resistance from OFF to ON. Finally, the last information we can get from the capacitance is obtained via equation 2:

(eq. 2) $Q = C \times U$ [C]

With Q, the stocked charge (in C), C the capacitance (in F) and U the voltage (in V). From that, it is easy to obtain the number of elementary charges stocked and to compare it with the estimation of grafted POMs (obtained via Γ). When comparing the numbers, it turned out that around 1 on 1000 POM is actually reduced, indicating that the system is far from exploring its whole potential.

5. CONCLUSION

Firstly, different POMs were synthesized and post-functionalized to obtain aniline-ending organic arms ($K_{Sn}[ArNH_2]$, $K_{Si}[ArNH_2]$, $D_{Si}[ArNH_2]$). Then all the different characteristics of the diazonium synthesis and the activation/grafting process were studied and tweaked (number of cycles, voltage range…).

After a successful clean grafting of polyoxometalate, the layer was confirmed to be uniform and thick by different characterization techniques (AFM, CV, SEM-EDX). For the device fabrication aiming for memory system application, top electrodes were deposit and I-V curves were measured to determine its characteristics. The final device with its relatively thick layer corresponds to a WORM-type device, a non-volatile and unerasable memory system that presents the advantage of a high stability in data storage.

6. FUTURE WORK

A certain level of thickness mastering of the polyoxometalate layer was achieved, but it has to be increased to analyze its impact on memory properties. The ideal goal would be to gain the ability to determine two synthesis paths, one for the WORM and one for the flash, as it has been successfully described by others, like Prof. Wai-Yeung Wong and coll. who reported the case of ferrocene-base polymer, with the possibility to form either WORM or flash-type memory according to the organic arm add by Sonogashira cross-coupling to the ferrocene.[27] A similar process was reported by Prof. Qichun Zhang and coll., with an unique starting molecule and different pathways to reach either flash or WORM memory-types.[28] Reaching this kind of system allow the researcher to choose between systems according to what is needed. Moreover, considering the capacitance results and the estimation of 0.1% of POMs reduced, two paths could be considered: diminishing the number of grafted POMs since most of it is not reduced, or finding a way to enhance the percentage of reduced POMs while keeping the same amount of grafted POMs.

7. REFERENCES

(1) Liu, S.; Volkmer, D.; Kurth, D. G. Functional Polyoxometalate Thin Films via Electrostatic Layer-by-Layer Self-Assembly. *J. Clust. Sci.* **2003**, *14* (3), 405–419. https://doi.org/10.1023/B:JOCL.0000005072.28928.96.
(2) Li, H.; Pang, S.; Wu, S.; Feng, X.; Müllen, K.; Bubeck, C. Layer-by-Layer Assembly and UV Photoreduction of Graphene–Polyoxometalate Composite Films for Electronics. *J. Am. Chem. Soc.* **2011**, *133* (24), 9423–9429. https://doi.org/10.1021/ja201594k.
(3) Jeon, D.; Kim, H.; Lee, C.; Han, Y.; Gu, M.; Kim, B.-S.; Ryu, J. Layer-by-Layer Assembly of Polyoxometalates for Photoelectrochemical (PEC) Water Splitting: Toward Modular PEC Devices. *ACS Appl. Mater. Interfaces* **2017**, *9* (46), 40151–40161. https://doi.org/10.1021/acsami.7b09416.
(4) Ali, B.; McCormac, T.; Maccato, C.; Barreca, D.; Carraro, G. Multilayer Assemblies of a Cu-Phthalocyanine with Dawson Type Polyoxometalates (POMs) for the Electrocatalytic Reduction of Phosphate. *J. Electroanal. Chem.* **2020**, *858*, 113770. https://doi.org/10.1016/j.jelechem.2019.113770.
(5) Errington, R. J.; Petkar, S. S.; Horrocks, B. R.; Houlton, A.; Lie, L. H.; Patole, S. N. Covalent Immobilization of a TiW5 Polyoxometalate on Derivatized Silicon Surfaces. *Angew. Chem. Int. Ed.* **2005**, *44* (8), 1254–1257. https://doi.org/10.1002/anie.200461065.
(6) Song, Y.-F.; McMillan, N.; Long, D.-L.; Kane, S.; Malm, J.; Riehle, M. O.; Pradeep, C. P.; Gadegaard, N.; Cronin, L. Micropatterned Surfaces with Covalently Grafted Unsymmetrical Polyoxometalate-Hybrid Clusters Lead to Selective Cell Adhesion. *J. Am. Chem. Soc.* **2009**, *131* (4), 1340–1341. https://doi.org/10.1021/ja807091v.
(7) Laurans, M.; Dalla Francesca, K.; Volatron, F.; Izzet, G.; Guerin, D.; Vuillaume, D.; Lenfant, S.; Proust, A. Molecular Signature of Polyoxometalates in Electron Transport of Silicon-Based Molecular Junctions. *Nanoscale* **2018**, *10* (36), 17156–17165. https://doi.org/10.1039/C8NR04946G.
(8) Gam Derouich, S.; Rinfray, C.; Izzet, G.; Pinson, J.; Gallet, J.-J.; Kanoufi, F.; Proust, A.; Combellas, C. Control of the Grafting of Hybrid Polyoxometalates on Metal and Carbon Surfaces: Toward Submonolayers. *Langmuir* **2014**, *30* (8), 2287–2296. https://doi.org/10.1021/la500067e.
(9) Rinfray, C.; Izzet, G.; Pinson, J.; Gam Derouich, S.; Ganem, J.-J.; Combellas, C.; Kanoufi, F.; Proust, A. Electrografting of Diazonium-Functionalized Polyoxometalates: Synthesis, Immobilisation and Electron-Transfer Characterisation from Glassy Carbon. *Chem. - Eur. J.* **2013**, *19* (41), 13838–13846. https://doi.org/10.1002/chem.201302304.
(10) Huder, L.; Rinfray, C.; Rouchon, D.; Benayad, A.; Baraket, M.; Izzet, G.; Lipp-Bregolin, F.; Lapertot, G.; Dubois, L.; Proust, A.; Jansen, L.; Duclairoir, F. Evidence for Charge Transfer at the Interface between Hybrid Phosphomolybdate and Epitaxial Graphene. *Langmuir* **2016**, *32* (19), 4774–4783. https://doi.org/10.1021/acs.langmuir.6b00870.
(11) Stockhausen, V.; Trippé-Allard, G.; Van Quynh, N.; Ghilane, J.; Lacroix, J.-C. Grafting π-Conjugated Oligomers Incorporating 3,4-Ethylenedioxythiophene (EDOT) and Thiophene Units on Surfaces by Diazonium Electroreduction. *J. Phys. Chem. C* **2015**, *119* (33), 19218–19227. https://doi.org/10.1021/acs.jpcc.5b05456.
(12) Nguyen, V. Q.; Sun, X.; Lafolet, F.; Audibert, J.-F.; Miomandre, F.; Lemercier, G.; Loiseau, F.; Lacroix, J.-C. Unprecedented Self-Organized Monolayer of a Ru(II) Complex by Diazonium Electroreduction. *J. Am. Chem. Soc.* **2016**, *138* (30), 9381–9384. https://doi.org/10.1021/jacs.6b04827.
(13) Williams, R. S. How We Found the Missing Memristor. *IEEE Spectr.* **2008**, 28–35.
(14) Fabre, B. Ferrocene-Terminated Monolayers Covalently Bound to Hydrogen-Terminated Silicon Surfaces. Toward the Development of Charge Storage and

Communication Devices. *Acc. Chem. Res.* **2010**, *43* (12), 1509–1518. https://doi.org/10.1021/ar100085q.
(15) Kuhr, W. G.; Gallo, A. R.; Manning, R. W.; Rhodine, C. W. Molecular Memories Based on a CMOS Platform. *MRS Bull.* **2004**, *29* (11), 838–842. https://doi.org/10.1557/mrs2004.238.
(16) Jurow, M.; Schuckman, A. E.; Batteas, J. D.; Drain, C. M. Porphyrins as Molecular Electronic Components of Functional Devices. *Coord. Chem. Rev.* **2010**, *254* (19–20), 2297–2310. https://doi.org/10.1016/j.ccr.2010.05.014.
(17) Roth, K. M.; Dontha, N.; Dabke, R. B.; Gryko, D. T.; Clausen, C.; Lindsey, J. S.; Bocian, D. F.; Kuhr, W. G. Molecular Approach toward Information Storage Based on the Redox Properties of Porphyrins in Self-Assembled Monolayers. *J. Vac. Sci. Technol. B Microelectron. Nanometer Struct.* **2000**, *18* (5), 2359. https://doi.org/10.1116/1.1310657.
(18) Lindsey, J. S.; Bocian, D. F. Molecules for Charge-Based Information Storage. *Acc. Chem. Res.* **2011**, *44* (8), 638–650. https://doi.org/10.1021/ar200107x.
(19) Qian, K.; Tay, R. Y.; Nguyen, V. C.; Wang, J.; Cai, G.; Chen, T.; Teo, E. H. T.; Lee, P. S. Hexagonal Boron Nitride Thin Film for Flexible Resistive Memory Applications. *Adv. Funct. Mater.* **2016**, *26* (13), 2176–2184. https://doi.org/10.1002/adfm.201504771.
(20) Busche, C.; Vilà-Nadal, L.; Yan, J.; Miras, H. N.; Long, D.-L.; Georgiev, V. P.; Asenov, A.; Pedersen, R. H.; Gadegaard, N.; Mirza, M. M.; Paul, D. J.; Poblet, J. M.; Cronin, L. Design and Fabrication of Memory Devices Based on Nanoscale Polyoxometalate Clusters. *Nature* **2014**, *515* (7528), 545–549. https://doi.org/10.1038/nature13951.
(21) Chen, X.; Huang, P.; Zhu, X.; Zhuang, S.; Zhu, H.; Fu, J.; Nissimagoudar, A. S.; Li, W.; Zhang, X.; Zhou, L.; Wang, Y.; Lv, Z.; Zhou, Y.; Han, S.-T. Keggin-Type Polyoxometalate Cluster as an Active Component for Redox-Based Nonvolatile Memory. *Nanoscale Horiz.* **2019**, *4* (3), 697–704. https://doi.org/10.1039/C8NH00366A.
(22) Chen, X.; Zhou, Y.; Roy, V. A. L.; Han, S. Evolutionary Metal Oxide Clusters for Novel Applications: Toward High-Density Data Storage in Nonvolatile Memories. *Adv. Mater.* **2018**, *30* (3), 1703950. https://doi.org/10.1002/adma.201703950.
(23) Hu, B.; Wang, C.; Wang, J.; Gao, J.; Wang, K.; Wu, J.; Zhang, G.; Cheng, W.; Venkateswarlu, B.; Wang, M.; Lee, P. S.; Zhang, Q. Inorganic–Organic Hybrid Polymer with Multiple Redox for High-Density Data Storage. *Chem Sci* **2014**, *5* (9), 3404–3408. https://doi.org/10.1039/C4SC00823E.
(24) Chen, B.; Huang, Y.-R.; Song, K.-Y.; Lin, X.-L.; Li, H.-H.; Chen, Z.-R. Molecular Nonvolatile Memory Based on $[\alpha\text{-}GeW_{12}O_{40}]^{4-}$ /Metalloviologen Hybrids Can Work at High Temperature Monitored by Chromism. *Chem. Mater.* **2021**, *33* (6), 2178–2186. https://doi.org/10.1021/acs.chemmater.1c00090.
(25) Bousquet, A.; Ceccato, M.; Hinge, M.; Pedersen, S. U.; Daasbjerg, K. Redox Grafting of Diazotated Anthraquinone as a Means of Forming Thick Conducting Organic Films. *Langmuir* **2012**, *28* (2), 1267–1275. https://doi.org/10.1021/la203657n.
(26) Goswami, S.; Matula, A. J.; Rath, S. P.; Hedström, S.; Saha, S.; Annamalai, M.; Sengupta, D.; Patra, A.; Ghosh, S.; Jani, H.; Sarkar, S.; Motapothula, M. R.; Nijhuis, C. A.; Martin, J.; Goswami, S.; Batista, V. S.; Venkatesan, T. Robust Resistive Memory Devices Using Solution-Processable Metal-Coordinated Azo Aromatics. *Nat. Mater.* **2017**, *16* (12), 1216–1224. https://doi.org/10.1038/nmat5009.
(27) Xiang, J.; Wang, T.-K.; Zhao, Q.; Huang, W.; Ho, C.-L.; Wong, W.-Y. Ferrocene-Containing Poly(Fluorenylethynylene)s for Nonvolatile Resistive Memory Devices. *J. Mater. Chem. C* **2016**, *4* (5), 921–928. https://doi.org/10.1039/C5TC03042K.
(28) Li, Y.; Wang, Z.; Zhang, C.; Gu, P.; Chen, W.; Li, H.; Lu, J.; Zhang, Q. Thiadizoloquinoxaline-Based N-Heteroacenes as Active Elements for High-Density Data-Storage Device. *ACS Appl. Mater. Interfaces* **2018**, *10* (18), 15971–15979.

https://doi.org/10.1021/acsami.8b05178.

PART IV - GENERAL CONCLUSION

This thesis tried to reveal the promising potential of polyoxometalate-based hybrids as platforms for future applications, by initiating a synergy between E-POM laboratory at Sorbonne Université and Prof. Lee's laboratory at the Nanyang Technological University. To do so, the focus was put on two areas: self-assembly and covalent grafting for resistive random-access memory.

Post-functionalization via Sonogashira cross-coupling is an ideal tool for a precise designing of the desired platforms. In this work, the first example concerns the addition of pyridyl moieties to an organosilyl hybridized polyoxometalate. To solve a previous issue of mixture between squares and triangles, resulting of a balanced competition between enthalpy and entropy, a new metallic center was imagined and synthesized, $[Pd(en)(MeCN)_2](BF_4)_2$, allowing to eliminate triangles from the equation after the self-assembly process, thanks to the rigidity of the connecting arms. This new discrete species, isolated in DMSO, was described and analyzed by a combination of theoric computational study, ^1H and DOSY NMR and SAXS technique.

It was found that varying the solution composition by mixing solvents could lead to the aggregation of the squares in different architectural macrostructures. TEM analysis revealed that, in presence of D_2O vesicles were formed while cherry-branches were observed in presence of CD_3CN. Structure variations are due to solvation and hydrophobic properties.

Another POM-based platform for auto-assembly was synthesized, K_{Sn}[tpy], forming dimer structure around a cobalt metallic center. This discrete species formation was followed by ^1H NMR and SAXS. The idea behind these dimers was the formation of a POM-based organogel or hydrogel. SAXS analysis confirmed that a nanostructure organization was present inside the gel. Tests variation were run on Dawson instead of Keggin and Co^{III} instead of Co^{II}, revealing that it was possible to have an impact on the POM-POM distance, thus the POM density, of the gel. The novel character of this compound induces the necessity of physico-chemical studies, in rheological domain for instance.

In part III of this thesis, POM-based hybrids were designed to be covalently bonded to an ITO substrate. To do so, a new method was developed, adapted from literature, where the diazonium moieties ending the organic arms of the hybrids were

formed *in situ*, and not previously isolated, avoiding a potential protonation issue. To define the right grafting method, repetitions and variations were necessary, testing every parameters one by one: the hybrid itself (Keggin or Dawson, mono-functionalized or bi-functionalized), potential range, cycling number, grafting repetition… When the correct methodology was defined, analysis of the layer became the new objective. If AFM and XPS were not satisfactory, SEM, EDX, c-AFM and SSRM allowed to get some understanding of the immobilized film on ITO, its presence, its thickness (around 15 to 25 nm) and its uniformity. Finally, gold top electrodes were deposited to perform resistive memory tests, revealing the WORM character of the final devices. A memory based on resistance switching of the compound, allowing a non-volatile and unerasable storage of information. The future of this system should rely on the synthesis of a second device, presenting a property of erasability, increasing the application field to both flash and WORM resistive memories, but working on increasing the estimated percentage of reduced POMs should also be considered.

In this work, the synergy of the two labs revealed its full potential since the laboratory in Paris mastered the synthesis and the grafting parts while the laboratory in Singapore brought its expertise on the memory application side. This new connection created between these two laboratories will hopefully be strong enough to survive and grow over time.

APPENDIX

APPENDIX A: EXPERIMENTAL PARTS

1. Materials & methods

1.1. Chemicals

Every reagent and solvent issued from commercial sources were bought from Alfa-Aesar, Aldrich, Acros, Fisher and VWR-Prolabo and used directly.

1.2. Characterisations

1.2.1. NMR Spectroscopy

^{1}H and ^{31}P NMR spectra were obtain from Bruker spectrometer (Avance III 300 MHz, Avance III 400 MHz and Avance III 600 MHz, with BBFO probes). ^{1}H spectra are referenced according to tetramethylsilane. Solvent signal is used as internal reference. ^{31}P spectra are referenced according to phosphoric acid at 85%.

1.2.2. Electrochemistry

Cyclovoltammetry and chronoamperometry were performed on an Autolab PGSTAT 100 (Metrohm). The set-up is a classic three-electrodes set-up, with Pt wire as counter-electrode and saturated calomel electrode (SCE) as reference electrode. Glassy carbon or ITO were used for the working electrode.

1.2.3. Elemental analysis

Elemental analysis were realize by the Institut des Sciences Analytiques at Villeurbanne (France).

1.2.4. SEM-FEG/EDX

SEM-FEG and EDX analysis were performed by David Montero from the Institut des Matériaux de Paris Centre, on respectively a Hitachi SU-70 and an Oxford X-Max 50 mm2.

1.2.5. AFM

AFM measurements were realized under the supervision of Dr Ludovic Tortech at the Comissariat à l'Energie Atomique (Saclay, France), on a Nano-Observer from Scientec. Electrical measurements are performed through a "resiscope", a set-up developed by the Génie Electrique et Electronique de Paris to perform SSRM-like measurements over a dynamic range of 10^{10} Ω. The surface potential, KPFM, is performed using a dual lock-in set-up, decoupling the vibrational signal of topography from the alternative bias applied to the tip.

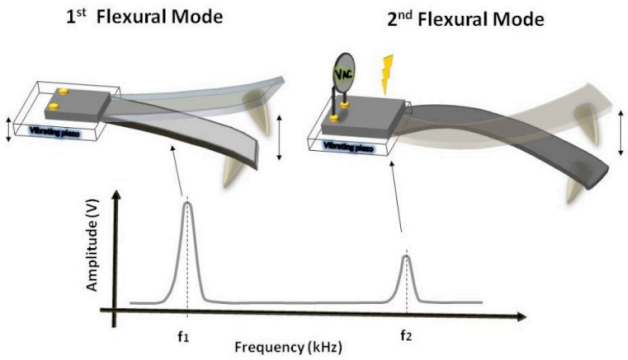

Figure 77 – Schematic representation of the vibrational mode in KPFM

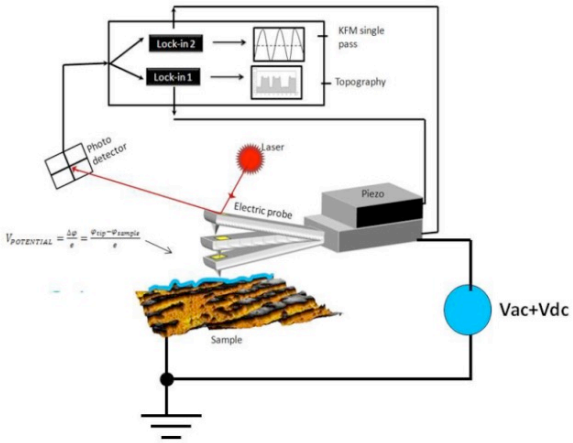

Figure 2 – Global schematic of the working mode KPFM

Tips used are 240 AC-PP from μmasch for the overall characterization. Conduction is ensure by a Pt/Ir coating. Stiffness is given at 2 N/m (v = 70 kHz). For fine measurements, PPP-NCLPt from nanosensor are used, with a stiffness given at 48 N/m (v = 190 kHz). In both cases, tips radius is of 20 nm, and height of 15 μm.

1.2.6. SAXS

SAXS measurements were perform at the Source Optimisée de Lumière d'Energie Intermédiaire du LURE, a synchrotron based at Saint-Aubin (France).

1-iodo-4-(trichlorostannane)benzene

$C_6H_4ICl_3Sn$

367.91 $g.mol^{-1}$

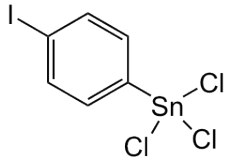

1-iodo-4-(trimethylstannane)benzene (6.0 g, 16.3 mmol, 1 equiv.) and tin chloride (15.4 mL, 131 mmol, 8 equiv.) are introduced in a micro-wave and heated for 70 min at 120°C. Then, at ambient temperature, crude products are evaporated at 75°C to obtain the final product.

^{1}H NMR (CD_3CN): δ 7.96 (d, 2H, J_{H-H} = 8 Hz, J_{Sn-H} = 42 Hz), 7.37 (d, 2H, J_{H-H} = 8 Hz, J_{Sn-H} = 112 Hz).

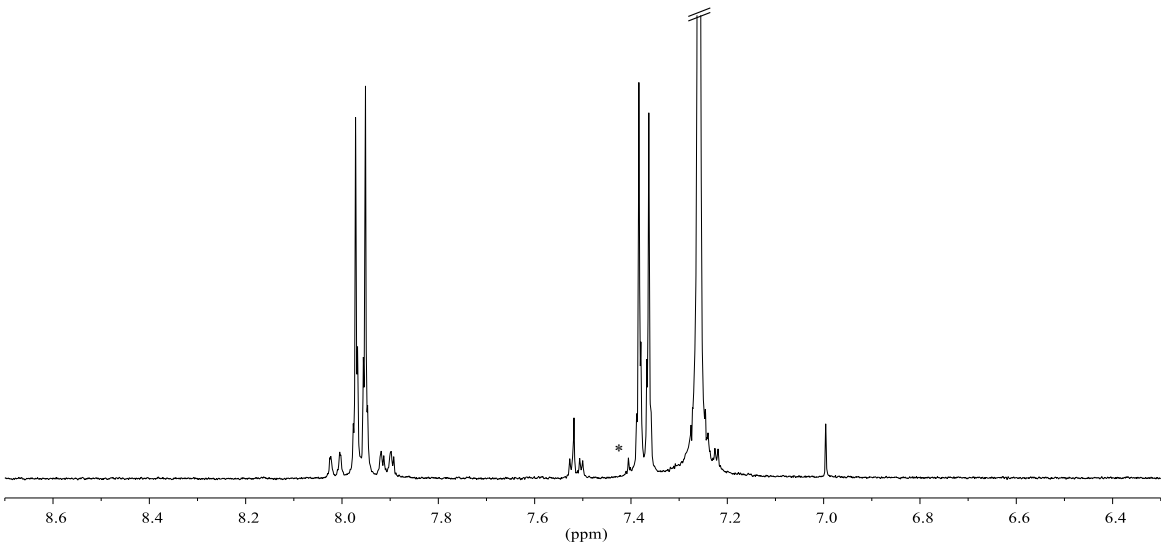

^{1}H NMR spectra of $C_6H_4ICl_3Sn$ in CD_3CN.

1-iodo-4-(triethoxysilyl)benzene

$C_{12}H_{19}ISi$

367.91 $g.mol^{-1}$

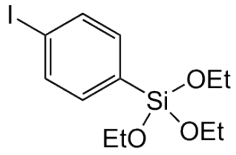

Under Ar atmosphere, *i*-PrMgCl (15.5 mL, 2 M in THF, 31 mmol, 1 equiv.) is added dropwisely in a 1,4-diiodobenzene solution (10 g, 30 mmol in 76 mL of THF, 1 equiv.) at -30°C. The obtained yellowish solution is stirred for 5h30 and added to a tetraethoxysilane solution (40.5 mL, 182 mmol in 60 mL of THF, 6 equiv.) still at -30°C. After one hour, the solution is launch for 2 days at ambien temperature, still under vigorous stirring. The obtained precipitate is filtered and distilled. The second product is the 1-iodo-4-(triethoxysilyl)benzene.

^{1}H NMR (CD_3CN): δ 7.80 (d, J = 8.10 Hz, 2H), 7.42 (d, J = 8.10 Hz, 2H), 3.86 (q, J = 7.15 Hz, 6H), 1.20 (t, J = 7.15 Hz, 9H).

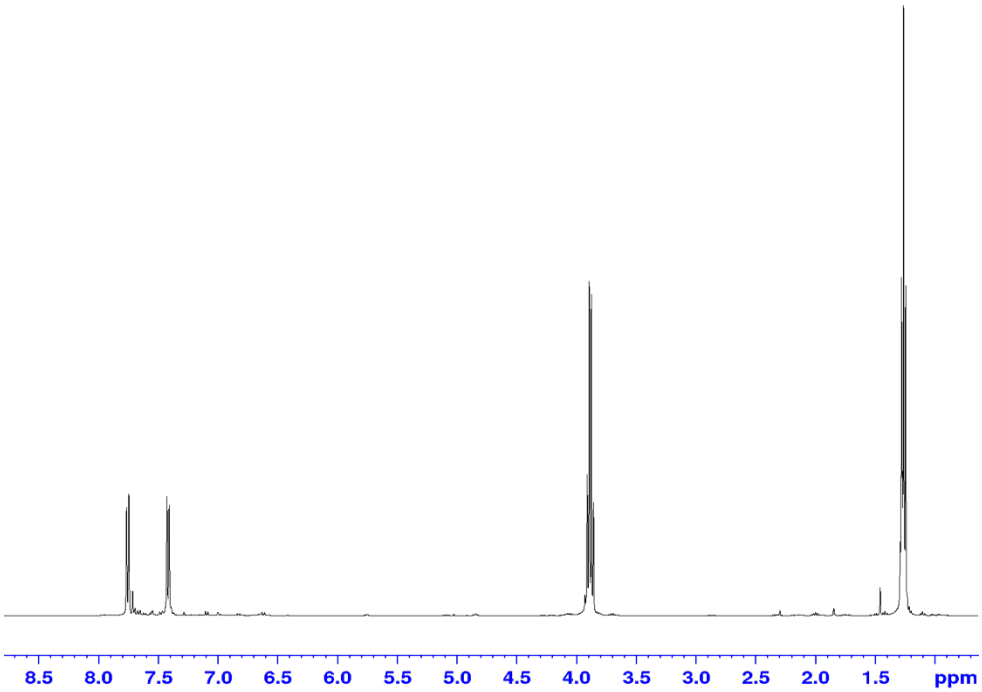

^{1}H NMR of $C_{12}H_{19}ISi$ in CD_3CN

$(TBA)_4[PW_{11}O_{39}\{Sn(C_6H_4I)\}]$ $K_{Sn}[I]$

$PW_{11}O_{39}SnC_{70}H_{148}IN_4$

3968.77 $g.mol^{-1}$

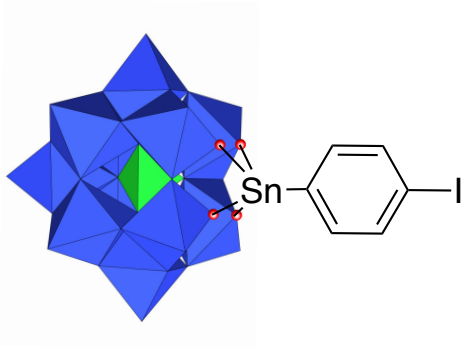

$K_7[PW_{11}O_{39}]$ (2.5 g, 2953 $g.mol^{-1}$, 0.85 mmol) is dropped in water (25 mL) and Cl_3ArPhI is added (0.5 g, 428 $g.mol^{-1}$, 1.17 mmol). pH is set at 3.1 by addition of KOH (1 M). After 15 min of stirring, solution is centrifugated. Under vigorous stirring, TBABr (2 g, 323 $g.mol^{-1}$, 6.2 mmol) in 2 mL of water is added. After another centrifugation, white precipitate is isolated and washed by ethanol and ether.

Elemental analysis: (Cal %) C 21.17, H 3.73, N 1.41 (Exp %) C 20.73, H 3.65, N 1.37.

IR (KBr, cm^{-1}): 2962 (s), 2935 (s), 2874 (s), 1629 (l), 1483 (s), 1474 (s), 1070 (s), 963 (s), 885 (s), 814 (s), 711 (l), 662 (l), 514 (m), 381 (s).

^{1}H NMR (CD_3CN): δ 77.85 ppm (d, 2H, J_{H-H} = 8.08 Hz, J_{Sn-H} = 31.15 Hz), 7.46 ppm (d, 2H, J_{H-H} = 8.08 Hz, J_{Sn-H} = 95 Hz), 3.12 ppm (m, 36H), 1.62 (m, 36H), 1.38 (m, 36H), 0.98 (m, 54H).

^{31}P NMR (CD_3CN): δ -10.76 ppm (s, J_{Sn-P} = 24.4 Hz)

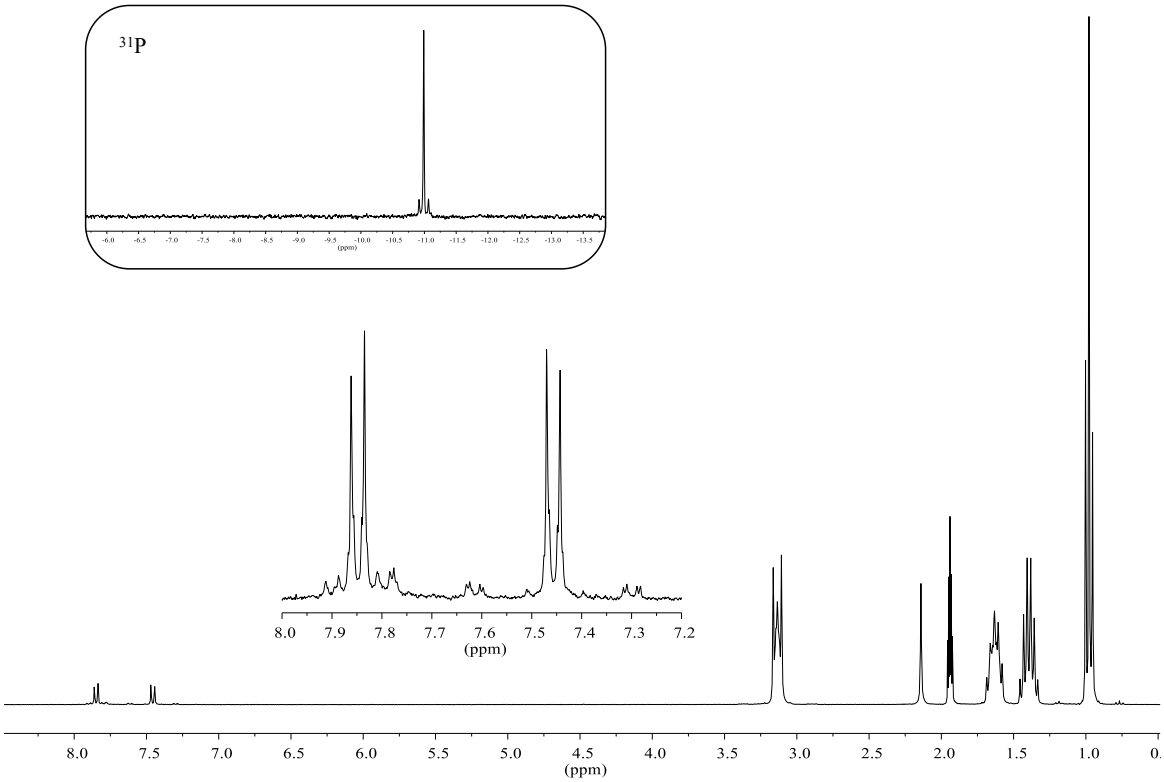

^{1}H and ^{31}P NMR spectra of $K_{Sn}[I]$ in CD_3CN.

$(TBA)_4[PW_{11}O_{39}\{Sn(C_{29}H_{18}N_3\}]$ $K_{Sn}[tpy]$

$PW_{11}O_{39}SnC_{93}H_{162}N_7$

4174.253 $g.mol^{-1}$

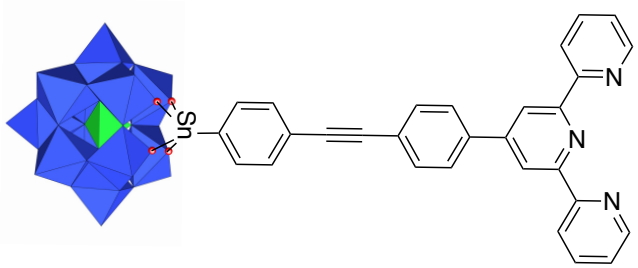

A mixture of K_{Sn}[I] (300 mg, 0.076 mmol), 4'-(4-ethynylphenyl)-2,2':6',2''-terpyridine (51 mg, 0.153 mmol, 2 equiv.), CuI (2.3 mg, 0.012 mmol, 0.16 equiv.) and $[PdCl_2(PPh_3)_2]$ (6.4 mg, 9.1 x 10^{-3} mmol, 0.12 equiv.) in 4 mL of dry DMF was prepared in a Schlenk tube under Ar atmosphere. After careful degassing with argon for 10 minutes, freshly distilled TEA (200 uL, 1.43 mmol, 19 equiv.) was added. The mixture was stirred overnight at room temperature. Upon completion of the reaction (monitored by ^{1}H NMR), the product was then precipitated by the addition of an excess of diethyl ether. The residue is then redissolved in the minimum amount of DMF and diluted into 30 mL of DCM containing TBABr (500 mg, 1.55 mmol, 20 equiv.). Some insoluble impurities are then discarded, solution is concentrated to 5 mL and precipitated upon the addition of an excess of ethanol. The almost colorless solid was then redissolved in ca. 4 mL of MeCN and added to ca. 8 mL of ethyl acetate. A slight brown precipitate was removed from the colorless supernatant that precipitates by the addition of a large excess of diethyl ether, yielding a colorless powder.

Elemental analysis: (Cal %) C 26.76, H 3.91, N 2.35 (Exp %) C 27.08, H 4.11, N 2.23.

IR (KBr, cm^{-1}): 2960 (s), 2935 (s), 2873 (s), 2233 (s), 1629 (l), 1483 (s), 1474 (s), 1381 (l), 1348 (s), 1069 (s), 962 (s), 885 (s), 811 (s), 711 (l), 662 (l), 514 (m), 381 (s).

^{1}H NMR (CD_3CN): δ 8.79 (s, 2H), 8.76 (ddd, J = 0.9 Hz, 1.8 Hz, 4.7 Hz, 2H), 8.72 (dt, J_t = 1.0 Hz, J_d = 7.9 Hz, 2H), 7.99 (td, J_d = 1.8 Hz, J_t = 7.7 Hz, 2H), 7.96 (d, J = 8.4 Hz, 2H), 7.79 (d, J = 8.4 Hz, 2H), 7.77 (d, J_{HH} = 8.1 Hz, J_{SnH} = 88 Hz, 2H), 7.69 (d+dd, J_{HH} = 8.1 Hz, J_{SnH} = 40 Hz, 2H), 7.47 (ddd, J = 1.0 Hz, 4.7 Hz, 7.5 Hz, 2H), 3.12 (m, 32H), 1.63 (m, 32H), 1.39 (h, J = 7.3 Hz, 32H), 0.99 (t, J = 7.3 Hz, 48H).

^{31}P NMR (CD_3CN): δ -10.66 (s+d, J_{SnP} = 24.0 Hz)

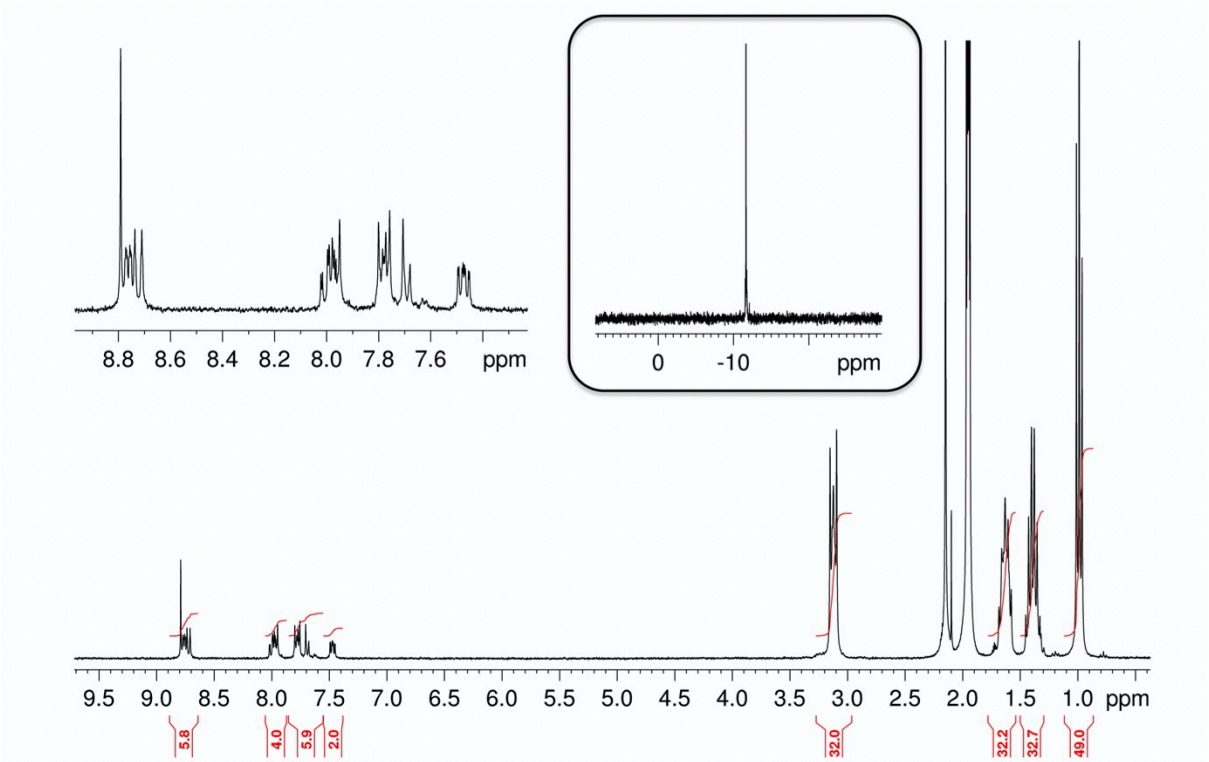

^{1}H and ^{31}P NMR spectra of K_{Sn}[tpy] in CD_3CN.

$(TBA)_4[PW_{11}O_{39}\{Sn(C_6H_4)C{\equiv}C(C_6H_4)NH_2\}]$ $K_{Sn}[ArNH_2]$

$PW_{11}O_{39}SnC_{78}H_{154}N_5$

3958.61 $g.mol^{-1}$

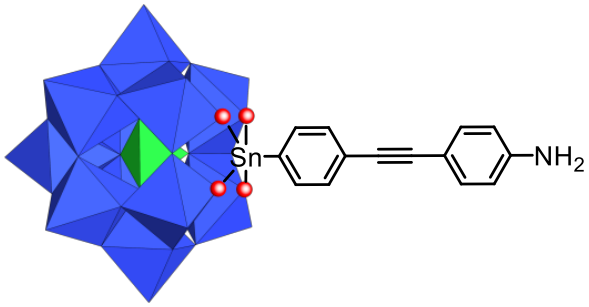

K_{Sn}[I] (390 mg, 0.098 mmol), 4-ethynylaniline (30.9 mg, 0.264 mmol, 2.69 equiv.), $[PdCl_2(PPh_3)_2]$ (11.8 mg, 0.017 mmol, 0.17 equiv.) and CuI (3.9 mg, 0.020 mmol, 0.20 equiv.) are added in dried Schlenk under Ar atmosphere with 5 mL of dried DMF and distillated TEA (270 uL, 1.96 mmol, 20 equiv.). The solution is stirred overnight at ambient temperature and precipitated in ether. After centrifugation, the obtained solid is dissolved in a minimum of acetonitrile with TBABr (300 mg, 0.931 mmol, 9.5 equiv.). The solution is precipitated in ethanol, centrifugated and washed in ethanol and in ether.

Elemental analysis: (Cal %) C 23.67, H 3.92, N 1.78 (Exp %) C 23.52, H 3.80, N 1.66.

IR (KBr, cm^{-1}): 2960 (m), 2933 (m), 2873 (m), 1483 (m), 1380 (f), 1069 (F), 962 (F), 886 (F), 813 (F), 515 (f), 380 (m).

^{1}H NMR (CD_3CN): δ 7,67 (d+dd, $^3J_{H-H}$=8,18Hz, $^3J_{Sn-H}$=95,36Hz, 2H, Ar-*H*), δ=7,54 (d+dd, $^3J_{H-H}$=8,18Hz, $^4J_{Sn-H}$=34,16Hz, 2H, Ar-*H*), δ=7,28 (d, $^3J_{H-H}$=8,68Hz, 2H, Ar-*H*), δ=6,63 (d, $^3J_{H-H}$=8,71Hz, 2H, Ar-*H*), δ=4,46 (s, 2H, Ar-N*H*$_2$), δ=3,12 (m, 32H, N-C*H*$_2$-CH_2-CH_2-CH_3), δ=1,63 (m, 32H, N-CH_2-C*H*$_2$-CH_2-CH_3), δ=1,39 (sex, $^3J_{H-H}$=7,44Hz, 32H, N-CH_2-CH_2-C*H*$_2$-CH_3), δ=0,98 (t, $^3J_{H-H}$=7,40Hz, 48H, N-CH_2-CH_2-CH_2-C*H*$_3$).

^{31}P NMR (CD_3CN): δ -10.98 ppm (s+d, J_{Sn-P} = 23.14 Hz)

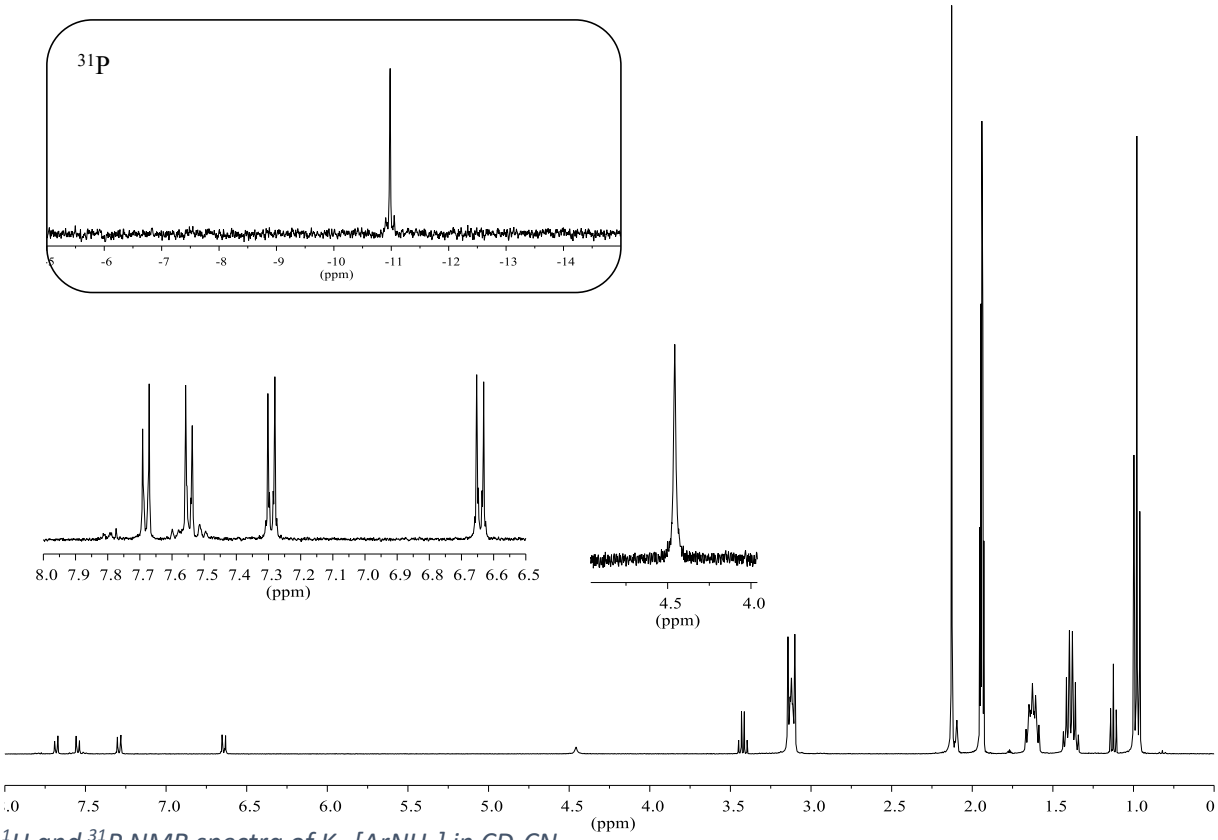

^{1}H and ^{31}P NMR spectra of $K_{Sn}[ArNH_2]$ in CD_3CN.

$(TBA)_3[PW_{11}O_{40}\{Si(C_6H_4I_2)\}_2]$ $K_{Si}[I]$

$PW_{11}O_{40}Si_2C_{12}H_8I_2$

3882.06 $g.mol^{-1}$

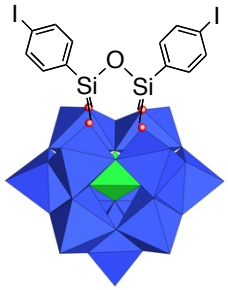

$K_7[PW_{11}O_{39}].14H_2O$ (4g, 1.25 mmol, 1 equiv.) and 1-iodo-4-(triethoxysilyl)benzene (2.74g, 7.5 mmol, 6 equiv.) are dissolved in a H_2O/CD_3CN (1/1) solution. In an ice bath, pH is set at 2.0 by addition of HCl (1 M). Solution is stirred at ambient temperature overnight. Precipitation is obtained by the addition of TBABr (1.21 g, 3.75 mmol, 3 equiv.). The solution is filtered and the precipitate washed by water, ethanol, chloroform and ether.

Elemental analysis: (Cal %) C 18.56, H 3.01, N 1.08 (Exp %) C 19.74, H 3.24, N, 1.25.

IR (KBr, cm^{-1}): 2962 (s), 2933 (s), 2873 (s), 1572 (m), 1780 (m), 1377 (m), 1111 (s), 1067 (s), 996 (s), 964 (vs), 872 (vs), 824 (s), 767 (s), 721 (s).

^{1}H NMR (DMSO-d_6): δ 87.85 (d, J = 8.1 Hz, 4H), 7.67 (d, J = 8.1 Hz, 4H), 3.45 (m, 24H), 1.85 (m, 24H), 1.45 (sextuplet, J = 7.74 Hz, 24H), 0.99 (t, J = 7.4 Hz, 36H).

^{31}P NMR (CD_3CN): δ -13.3 (s).

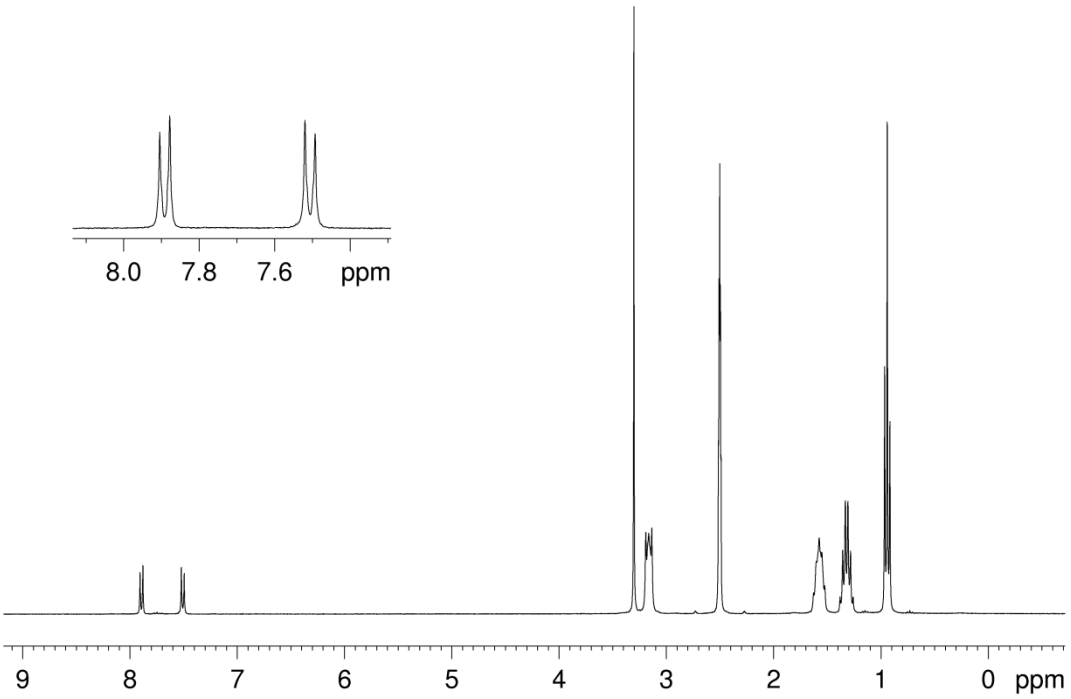

^{1}H NMR spectra of D_{Sn}[tpy] in CD_3CN.

$(TBA)_3[PW_{11}O_{39}\{O(SiC_6H_4I_2)_2\}]$ $K_{Si}[pyr]$

$PW_{11}O_{40}Si_2C_{74}H_{52}N_5$

4112.49 $g.mol^{-1}$

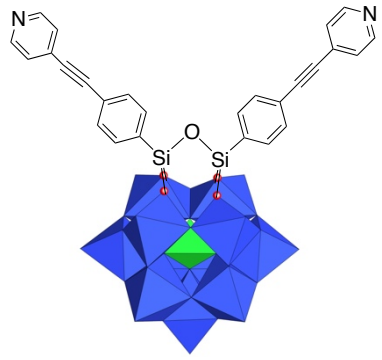

$K_{Si}[I]$ (442 mg, 0.114 mmol), 4-ethynylpyrydine hydrochloride (100 mg, 0.72 mmol, 6.32 equiv.), CuI (2.1 mg, 0.011 mmol, 0.10 equiv.) and $[PdCl_2(PPh_3)_2]$ (13.4 mg, 0.019 mmol, 0.17 equiv.) are added in a dried Schlenk under Ar atmosphere. 5 mL of dryed DMF are added with distillated TEA (0.32 mL, 2.30 mmol, 20 equiv.). The solution is heated at 80)C for 1 hour in a micro-wave. 0.7 g of TBABr are added and the solution is precipitated in a large volume of ether. The obtained green precipitate is dissolved in a minimum amount of acetonitrile and precipitated in ethanol. The obtained solid is centrifugated and washed in ether.

Elemental analysis: (Cal %) C 23.19; H 3.26; N 1.83; (Exp %) C 22.78; H 3.13; N 1.63.

IR (KBr, cm^{-1}): 2964 (s), 2875 (s), 2221 (w), 1632 (w), 1598 (m),1540 (w), 1482 (m), 1470 (m), 1384 (m), 1153 (w), 1110 (s), 1067 (s), 1040 (s), 965 (vs), 873 (vs), 824 (vs), 769 (s), 715 (s), 623 (m), 600 (m), 523 (m), 395 (s), 384 (s), 353 (m), 335 (m).

^{1}H NMR (CD_3CN): δ 8.61 (d, *J* = 6.0 Hz, 4H), 7.93 (d, *J* = 8.2 Hz, 4H), 7.70 (d, *J* = 8.2 Hz, 4H), 7.48 (d, *J* = 6.0 Hz, 4H), 3.12 (m, 24 H), 1.64 (m, 24 H), 1.40 (m, 24 H), 1.00 (t, *J* = 7.4 Hz 36 H)).

^{31}P NMR (CD_3CN): δ -12.02 (s).

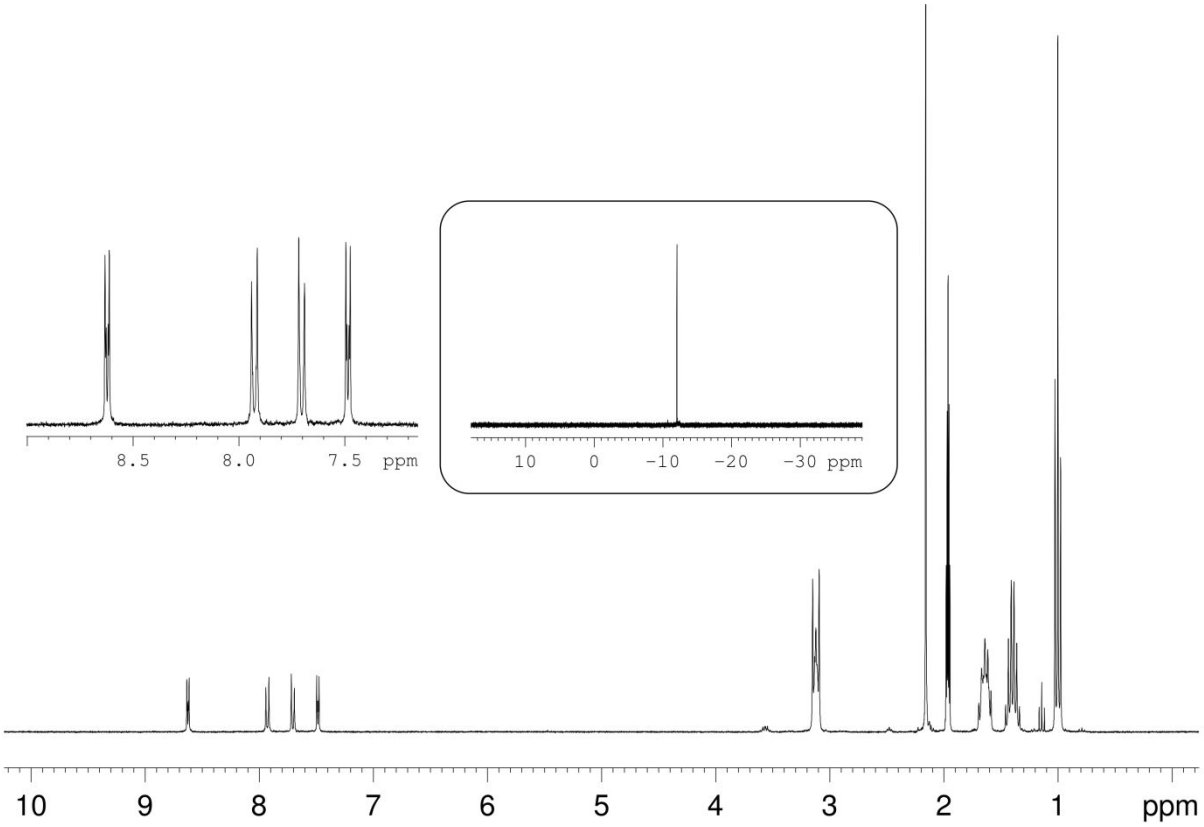

^{1}H and ^{31}P NMR spectra of K_{Si}[pyr] in CD_3CN.

$(TBA)_3[PW_{11}O_{40}\{Si(C_6H_4)C{\equiv}C(C_6H_4)NH_2\}_2]$ $K_{Si}[ArNH_2]$

$PW_{11}O_{40}Si_2C_{76}H_{128}N_5$

3859.386 $g.mol^{-1}$

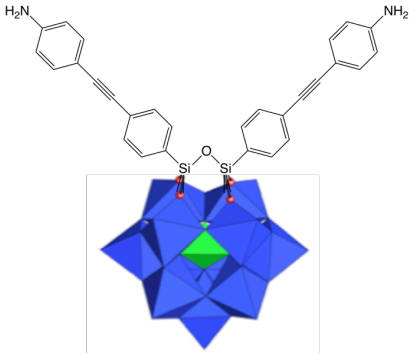

K_{Si}[I] (500 mg, 0.16 mmol), 4-ethynylaniline (93.72 mg, 0.80 mmol, 5 equiv.), $[PdCl_2(PPh_3)_2]$ (11.65 mg, 0.016 mmol, 0.15 equiv.) and CuI (4.58 mg, 0.024 mmol, 0.10 equiv.) are added in dried Schlenk under Ar atmosphere with 5 mL of dried DMF and distillated TEA (440 uL, 3.18 mmol, 20 equiv.). The solution is stirred overnight at ambient temperature and precipitated in ether. After centrifugation, the obtained solid is dissolved in a minimum of acetonitrile with TBABr (500 mg, 1.55 mmol, 9.7 equiv.). The solution is precipitated in ethanol, centrifugated and washed in ethanol and in ether.

Elemental analysis: (Cal %) C 23.63, H 3.31, N 1.81 (Exp %) C 25.98, H 4.25, N 2.05.

^{1}H NMR (CD_3CN): δ 7,84 (d, J = 4.7 Hz, 4H), 7.56 (d, J = 4.1 Hz, 4H), 7.30 (d, J = 4.4 Hz, 4H), 6.66 (d, J = 4.3 Hz, 4H), 4.48 (s, 4H), 3.10 (m, 28H), 1.63 (m, 28H), 1.38 (m, 28H), 0.99 (t, J = 7.3 Hz, 42H).

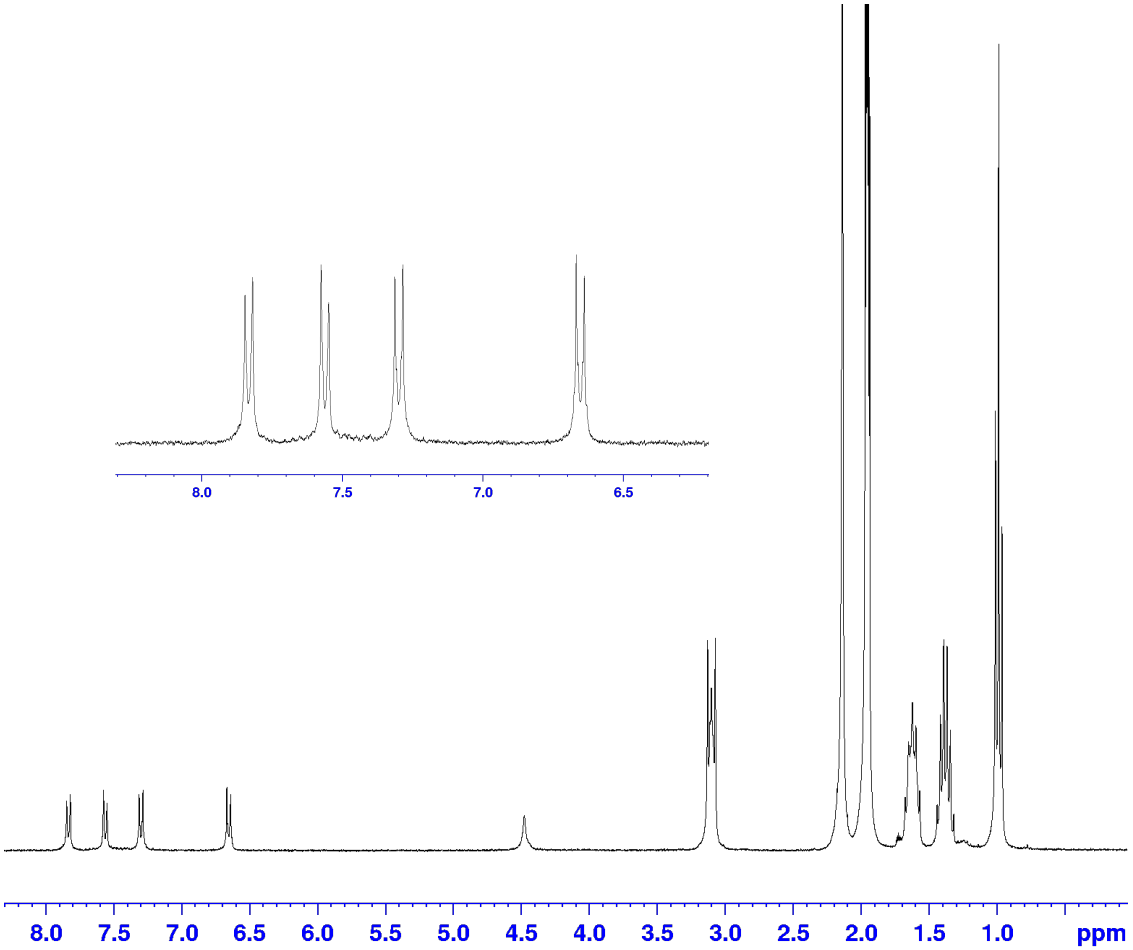

^{1}H NMR spectra of $K_{Si}[ArNH_2]$ in CD_3CN.

$(TBA)_7[P_2W_{17}O_{61}\{Sn(C_6H_4I)\}]$ $D_{Sn}[I]$

$P_2W_{17}O_{61}SnC_{118}H_{256}I$

6182.17 $g.mol^{-1}$

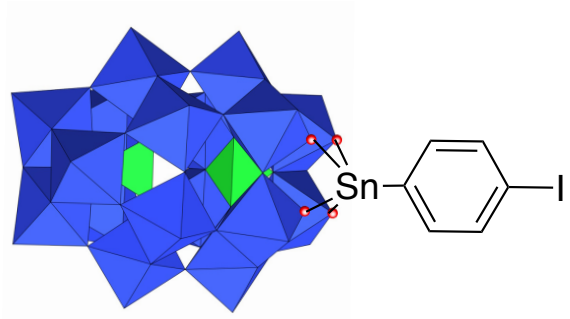

$K_{10}[P_2W_{17}O_{61}].20H_2O$ (3g, 4917 $g.mol^{-1}$, 0.61 mmol) is dropped in water (30 mL) and Cl_3ArPhI is added (0.47 g, 428 $g.mol^{-1}$, 1.1 mmol). pH is set at 3.2 by addition of KOH (1 M). After 15 min of stirring, solution is centrifugated. Under vigorous stirring, TBABr (2 g, 323 $g.mol^{-1}$, 6.2 mmol) in 2 mL of water is added. After another centrifugation, white precipitate is isolated and washed by ethanol and ether.

Elemental analysis: (Cal %) C 24.36, H 4.22, N 1.82 (Exp %) C 23.91, H 4.15, N 1.82.

IR (KBr, cm^{-1}): 2960 (l), 2934 (l), 2872 (l), 1484 (m), 1089 (s), 954 (m), 911 (s), 780 (s), 526 (m), 362 (s), 330 (m).

^{1}H NMR (CD_3CN): δ 7.8 (d, 2H, J_{H-H} = 8 Hz, J_{Sn-H} = 27 Hz), 7.5 (d, 2H, J_{H-H} = 81 Hz, J_{Sn-H} = 91 Hz), 3.15 (m, 40H), 1.64 (m, 10H), 1.4 (m, 40H), 0.98 (m, 60H).

^{31}P NMR (CD_3CN): δ -10.6 (s, 1P, J_{Sn-P} = 27 Hz), -13.7 (s, 1P)

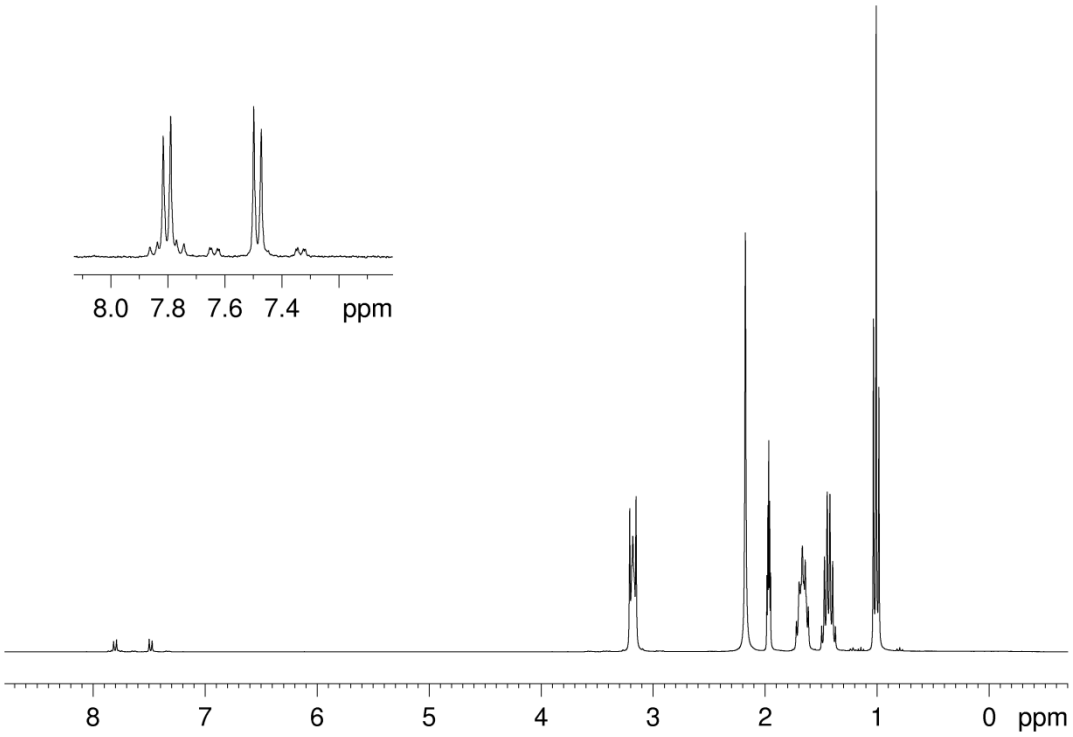

^{1}H NMR spectra of D_{Sn}[I] in CD_3CN.

$(TBA)_6[P_2W_{17}O_{61}\{Sn(C_{29}H_{18}N_3\}]$ $D_{Sn}[tpy]$

$P_2W_{17}O_{61}SnC_{125}H_{234}N_9$

6387.27 $g.mol^{-1}$

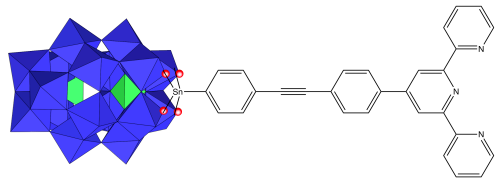

A mixture of $D_{Sn}[I]$ (200 mg, 0.032 mmol), 4'-(4-ethynylphenyl)-2,2':6',2''-terpyridine (21 mg, 0.064 mmol, 2 equiv.), CuI (1.0 mg, 5.1 x 10^{-3} mmol, 0.16 equiv.) and $[PdCl_2(PPh_3)_2]$ (2.7 mg, 3.8 x 10^{-3} mmol, 0.12 equiv.) in 4 mL of dry DMF was prepared in a Schlenk tube under Ar atmosphere. After careful degassing with argon for 10 minutes, freshly distilled TEA (134 uL, 0.96 mmol, 30 equiv.) was added. The mixture was stirred overnight at room temperature. Upon completion of the reaction (monitored by ^1H NMR), the product was then precipitated by the addition of an excess of diethyl ether. The residue is then redissolved in the minimum amount of DMF and diluted into 30 mL of DCM containing TBABr (300 mg, 1.24 mmol, 39 equiv.). Some insoluble impurities are then discarded, and the solution is washed 4 times with water. The organic layer was collected and concentrated up to *ca.* 5 mL, precipitated as a colorless solid by addition of diethyl ether (122 mg, 59%).

Elemental analysis: (Cal %) C 26.51, H 4.26, N 2.19(Exp %) C 25.93, H 4.12, N 2.01.

IR (KBr, cm^{-1}): 2961 (s), 2932 (m), 2872 (m), 2206 (w), 1633 (w), 1540 (s), 1472 (s), 1383 (m), 1321 (m), 1264 (w), 1195 (s), 1124 (w), 1070 (s), 963 (vs), 886 (s), 813 (vs), 801 (vs), 717 (w), 705 (w), 661 (w), 515 (w), 381 (s).

^1H NMR (CD_3CN): δ 8.79 (s, 2H), 8.76 (ddd, J = 1.0 Hz, 1.8 Hz, 4.7 Hz, 2H), 8.72 (dt, J_t = 1.0 Hz, J_d = 7.9 Hz, 2H), 7.99 (td, J_d = 1.8 Hz, J_t = 7.7 Hz, 2H), 7.95 (d, J = 8.4 Hz, 2H), 7.79 (d, J = 8.3 Hz, 2H), 7.77 (m, 4H), 7.62 (d, J = 8.0 Hz), 7.47 (ddd, J = 1.0 Hz, 4.7 Hz, 7.5 Hz, 2H), 3.17 (m, 32H), 1.65 (m, 56H), 1.42 (h, J = 7.3 Hz, 56H), 0.99 (t, J = 7.3 Hz, 84H).

^{31}P NMR (CD_3CN): δ -10.49 (s+d, J_{SnP} = 31.0 Hz), -13.54 (s).

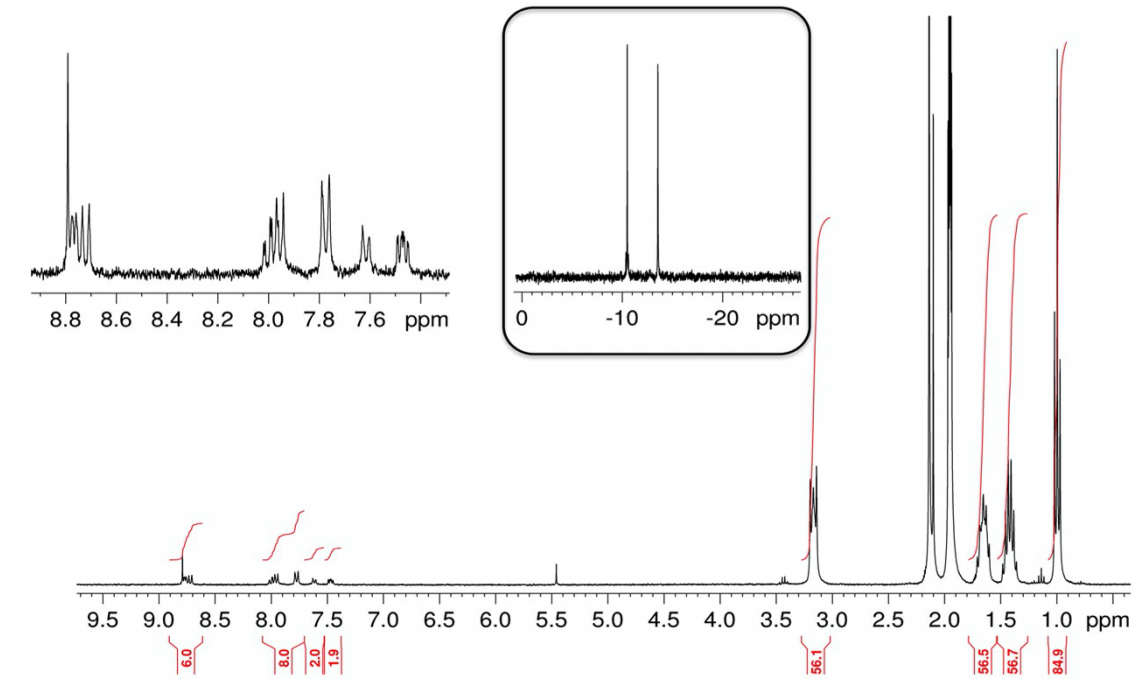

^{1}H and ^{31}P NMR spectra of D_{Sn}[tpy] in CD_3CN.

$(TBA)_6[P_2W_{17}O_{62}\{O(Si(C_6H_4)I)_2\}]$ $D_{Si}[I]$

$P_2W_{17}O_{62}Si_2I_2C_{108}H_{224}N_6$

6096.33 $g.mol^{-1}$

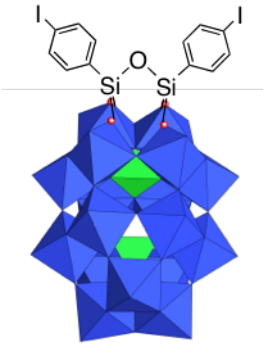

$K_{10}[\alpha_2\text{-}P_2W_{17}O_{61}].20H_2O$ (2 g, 0.407 mmol, 1 equiv.) is dropped in a 20 mL H_2O/CH_3CN (1/1) solution. At low temperature (iced bath), pH is set at 2.0 by a dropwise addition of HCl solution (1 M). 1-Iodo-4-(triethoxysilyl)benzene (600 mg, 1.628 mmol, 4 equiv.) is then added under vigorous stirring. After overnight stirring at ambient temperature, precipitation is obtained by the addition of TBABr (920 mg, 2.86 mmol, 7 equiv.). Centrifugation is used to separate the precipitate from the solvent. Then, the solid is dissolved in a minimal amount of CH_3CN, precipitated in ethanol, centrifugated, washed with ether, centrifugated again and finally dried.

Elemental analysis: (Cal %) C 21.28, H 3.70, N 1.38 (Exp %) C 21.17, H 3.67, N 1.38.

IR (KBr, cm^{-1}) : ν 2962 (s), 2935 (s), 2874 (s), 1570 (m), 1483 (s), 1378 (m), 1151 (m), 1124 (s), 1089 (s), 1042 (s), 988 (m), 955 (s), 916 (s), 813 (s), 767 (s), 722 (sh), 598 (m), 562 (m), 529 (s), 389 (s), 353 (s), 330 (s).

^{1}H NMR (CD_3CN): δ 7.76 (d, J = 8.1 Hz, 4H), 7.58 (d, J = 8.1 Hz, 4H), 3.15 (m, 48H), 1.64 (m, 48H), 1.41 (sextuplet, 7.2 Hz, 48H), 0.99 (t, J = 7.2 Hz, 72H).

^{31}P NMR (CD_3CN): δ 9.22 (s, 1P), 12.19 (s, 1P).

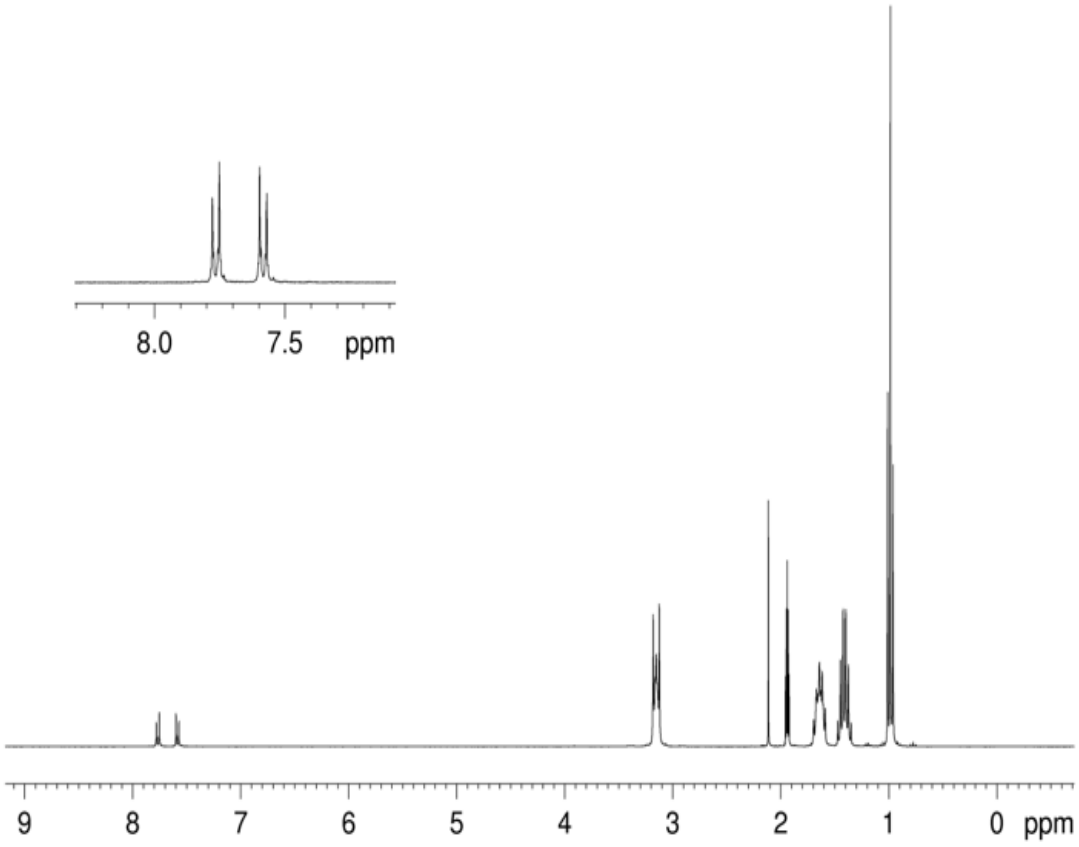

^{1}H NMR spectra of D_{Sn}[tpy] in CD_3CN

$(TBA)_6[P_2W_{17}O_{62}\{Si(C_6H_4)C{\equiv}C(C_6H_4)NH_2\}_2]$ $D_{Si}[ArNH_2]$

$P_2W_{17}O_{62}Si_2C_{124}H_{236}N_8$

6074.40 $g.mol^{-1}$

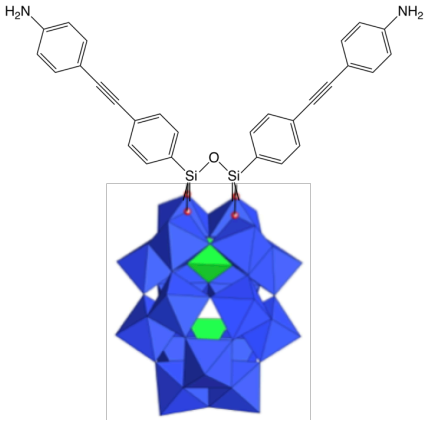

$D_{Si}[I]$ (1.1 g, 0.18 mmol), 4-ethynylaniline (110 mg, 0.94 mmol, 5.2 equiv.), $[PdCl_2(PPh_3)_2]$ (13.22 mg, 0.018 mmol, 0.10 equiv.) and CuI (5.2 mg, 0.027 mmol, 0.15 equiv.) are added in dried Schlenk under Ar atmosphere with 5 mL of dried DMF and distillated TEA (540 uL, 3.90 mmol, 21.7 equiv.). The solution is stirred overnight at ambient temperature and precipitated in ether. After centrifugation, the obtained solid is dissolved in CH_2Cl_2 (40 mL) with TBABr (500 mg, 1.55 mmol, 8.6 equiv.) and washed with water three times. The solution is then concentrated and precipitated in ether.

Elemental analysis: (Cal %) C 24.51, H 3.89, N 1.84 (Exp %) C 27.71, H 4.40, N 2.31.

^{1}H NMR (CD_3CN): δ 7,83 (d, J = 4.8 Hz, 4H), 7.48 (d, J = 4.4 Hz, 4H), 7.29 (d, J = 5.0 Hz, 4H), 6.65 (d, J = 5.1 Hz, 4H), 4.48 (s, 4H), 3.14 (m, 72H), 1.64 (m, 72H), 1.40 (m, 72H), 0.99 (t, J = 7.4 Hz, 108H).

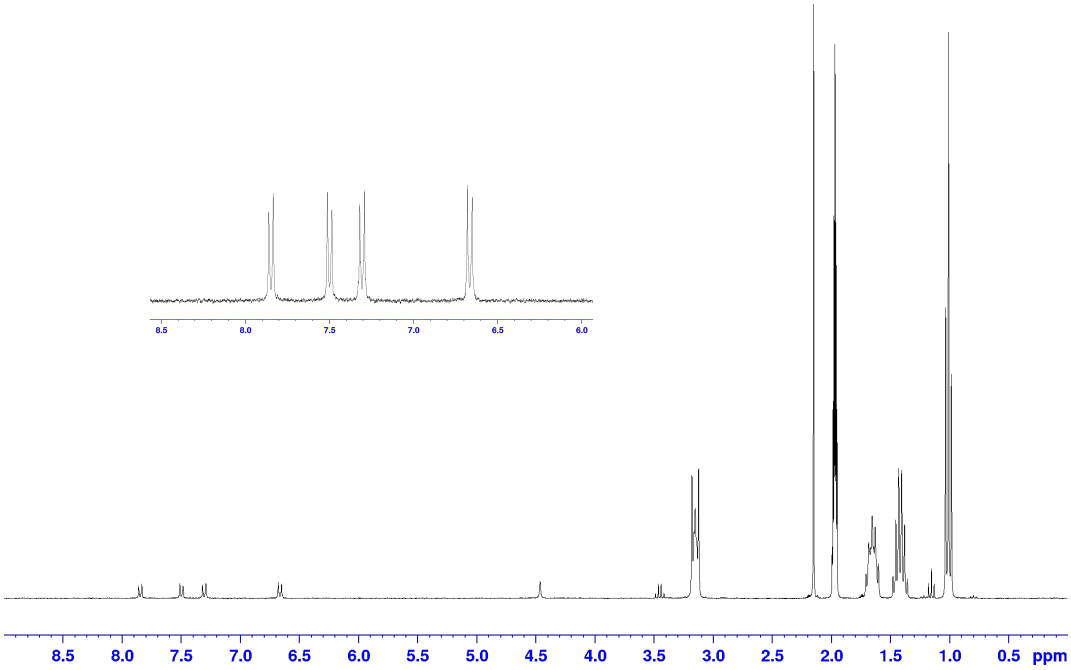

^{1}H NMR spectra of $D_{Si}[ArNH_2]$ in CD_3CN.

ARTICLES

Chemical Science

ROYAL SOCIETY OF CHEMISTRY

EDGE ARTICLE

View Article Online
View Journal | View Issue

Check for updates

Cite this: *Chem. Sci.*, 2020, **11**, 11072

All publication charges for this article have been paid for by the Royal Society of Chemistry

Exploring the self-assembly of dumbbell-shaped polyoxometalate hybrids, from molecular building units to nanostructured soft materials†

Mireia Segado Centellas,[a] Madeleine Piot,[b] Raphaël Salles,[b] Anna Proust,[b] Ludovic Tortech,[bc] Dalil Brouri,[d] Sébastien Hupin,[e] Benjamin Abécassis,[f] David Landy,[g] Carles Bo *[ah] and Guillaume Izzet *[b]

Received 10th June 2020
Accepted 10th September 2020

DOI: 10.1039/d0sc03243c

rsc.li/chemical-science

The formation of hierarchical nanostructures using preformed dumbbell-like species made of covalent organic–inorganic polyoxometalate (POM)-based hybrids is herein described. In this system, the presence of charged subunits (POM, metal linkers, and counter ions) in the complex molecular architecture can drive their aggregation, which results from a competition between the solvation energy of the discrete species and intermolecular electrostatic interactions. We show that the nature of the POM and the charge of the metal linker are key parameters for the hierarchical nanoorganization. The experimental findings were corroborated with a computational investigation combining DFT and molecular dynamics simulation methods, which outlines the importance of solvation of the counter ion and POM/counter ion association in the aggregation process. The dumbbell-like species can also form gels, in the presence of a poorer solvent, displaying similar nanoorganization of the aggregates. We show that starting from the designed molecular building units whose internal charges can be controlled by redox trigger we can achieve their implementation into soft nanostructured materials through the control of their supramolecular organization.

Introduction

The development of nanostructured soft materials through hierarchical self-assembly is drawing growing attention of scientists inspired by the structural complexity of natural systems.[1–3] These compounds involve a variety of interaction combinations that can lead to the emergence of innovative structures or even functionalities.[4] Classical synthetic strategies of such artificial assemblies with multiple levels of organization rely on the use of molecular building units displaying orthogonal and switchable interactions (*e.g.* metal coordination, electrostatic and hydrophobic effects…).[5–7] In this context we recently described the hierarchical self-assembly of organic/inorganic polyoxometalate (POM)-based hybrids in which the POM is covalently bonded to remote binding sites.[8–10] POMs are nanosized polyanionic molecular metal-oxo clusters that constitute original building units for the elaboration of multifunctional materials[11–17] owing to their multiple properties (such as electron reservoirs)[18] and sensitiveness to different interactions.[19–22] As they are polyanionic species they establish strong electrostatic interactions with cationic species. Furthermore, owing to their large size and their delocalized charges they display chaotropic behavior[23,24] and may give rise to self-assemblies with large association constants, albeit resulting from very weak interactions.[25] In our reported system, the coordination-driven self-assembly of a ditopic hybrid (displaying two remote terpyridine binding sites) in the presence of a cationic metal linker (Fe^{2+}, Co^{2+} or Co^{3+}) provided different supramolecular organizations (discrete metallomacrocycles, dense nanoparticles, and 1D worm-like nanoobjects), according to the solvent composition or the redox state of the metal ion. We concluded that the aggregation of the discrete metallomacrocycles combining negatively charged POMs and cationic metal linkers, resulted from a competition between the

[a]*Institut Català d'Investigació Química (ICIQ), The Barcelona Institute of Science and Technology, Av. Països Catalans, 17, Tarragona 43007, Spain. E-mail: cbo@iciq.cat*

[b]*Institut Parisien de Chimie Moléculaire, CNRS UMR 8232, Sorbonne Université, F-75005 Paris, France. E-mail: guillaume.izzet@sorbonne-universite.fr*

[c]*LICSEN, NIMBE, CEA, CNRS, Université Paris-Saclay, CEA Saclay, 91191 Gif-sur-Yvette Cedex, France*

[d]*Laboratoire de Réactivité de Surface, CNRS UMR 7179, Sorbonne Université, F-75005 Paris, France*

[e]*Normandie Univ, UNIROUEN, INSA Rouen, CNRS, COBRA, 76000 Rouen, France*

[f]*Laboratoire de Chimie, Ecole Normale Supérieure de Lyon, CNRS, UMR 5182, Université Claude Bernard, Université de Lyon, 69007 Lyon, France*

[g]*Unité de Chimie Environnementale et Interactions sur le Vivant (UCEIV, UR 4492), SFR Condorcet FR CNRS 3417, Université du Littoral Côte d'Opale, 59140 Dunkerque, France*

[h]*Departament de Química Física i Inorgànica, Universitat Rovirai Virgili, Carrer Marcel í Domingo s/n, Tarragona 43007, Spain*

† Electronic supplementary information (ESI) available: general methods, synthetic protocols, NMR spectra, ESI MS spectra, SAXS fits, TEM micrographs and MD simulation setups. See DOI: 10.1039/d0sc03243c

solvation energy of the discrete species with the electrostatic interactions between the charged units. In order to understand the thermodynamics of the formation of the discrete metallomacrocycles, we also compared the metal coordination behavior of two analogue ditopic building units differing by the nature (and hence the charge) of the POM (*i.e.* Keggin-*versus* Dawson-types).[26] This study outlined the decisive effect of the charge of the POM disfavouring the formation of large assemblies probably due to an important entropic contribution. This was confirmed by an isothermal titration calorimetry (ITC) experiment that confirmed the stronger association in the case of the Keggin hybrids. However, the analysis of the previous system was particularly intricate since mixtures of molecular triangles and squares were observed, which limited the interpretation. In order to simplify the system, we decided to investigate the self-assembly behavior of monotopic hybrids either in the Keggin or the Dawson series. We herein describe the formation of molecular dimers with dumbbell structures from these hybrids. We also show that these supramolecular systems are prone to aggregation according to the solvent composition and demonstrate that the difference in the nature of the POM, the charge of the metal linker or the solvent composition considerably affects the supramolecular organization, which in some cases lead to the formation of molecular gels retaining the initial nanostructuration. Since in previous studies some of us and other authors have shown that molecular dynamics (MD) simulations provided unique insight into the origin of POMs/counter-cation interactions,[27–32] we show here that the solvent plays a key role by modulating ion-pairing and thus self-assembly.

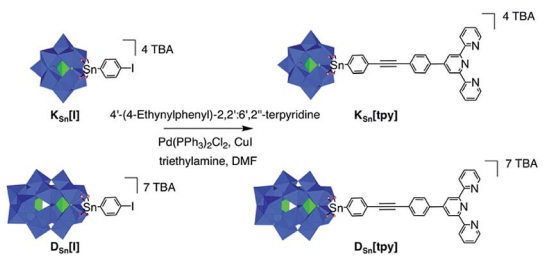

Scheme 1 Synthetic route to K_{Sn}[tpy] and D_{Sn}[tpy] (in the polyhedral representation, the WO_6 octahedra are depicted with oxygen atoms at the vertices and metal cations buried inside). Color code: WO_6 octahedra, blue; PO_4 tetrahedra, green.

Results and discussion

Synthesis of the POM-based molecular units

The POM-based building units $[PW_{11}O_{39}\{SnC_{29}H_{18}N_3\}]^{4-}$ and $[P_2W_{17}O_{61}\{SnC_{29}H_{18}N_3\}]^{7-}$ respectively denoted as **K_{Sn}[tpy]** and **D_{Sn}[tpy]**‡ contain one terpyridine (tpy) unit connected to the mono-lacunary site of a Keggin-($[PW_{11}O_{39}]^{7-}$) and Dawson-(α_2-$[P_2W_{17}O_{61}]^{10-}$) type polyoxotungstate. Their synthesis is performed in one step from the iodo-aryl terminated POM-based platforms **K_{Sn}[I]** and **D_{Sn}[I]** by adapting our reported procedure involving a Sonogashira cross-coupling reaction (Scheme 1).[33] The hybrid POMs are isolated as tetrabutyl ammonium (TBA) salts and characterized by ^{1}H and ^{31}P NMR spectroscopy, mass spectrometry, elemental analyses and FTIR spectroscopy (Fig. S1–S4†).

Formation and characterization of discrete molecular dumbbells

Terpyridine ligands produce a linear arrangement when coordinated to a metal center such as Co(II). The addition of $[Co(H_2O)_6](NO_3)_2$ to a solution of **K_{Sn}[tpy]** or **D_{Sn}[tpy]** (2 mM) in DMSO-d_6 instantly leads to the appearance of a single set of signals in the ^{1}H low-field region (above 10 ppm) attributed to the formation of paramagnetic Co(II) terpyridine complexes (Fig. 1). The reaction is complete after the addition of 0.5 equiv. of Co per POM hybrid, in agreement with the formation of a supramolecular species displaying a 2 : 1 stoichiometry between the POM and the metal linker. The ^{1}H signals of the supramolecular species (especially those of protons located at the vicinity of the metal centre) are considerably broadened compared to those of the parent hybrid **K_{Sn}[tpy]** or **D_{Sn}[tpy]** as a result of the paramagnetism of the Co(II) center. However, their linewidths are similar to those of a reference Co(II) bis-terpyridine complex (Fig. S5†), suggesting that the POM-based

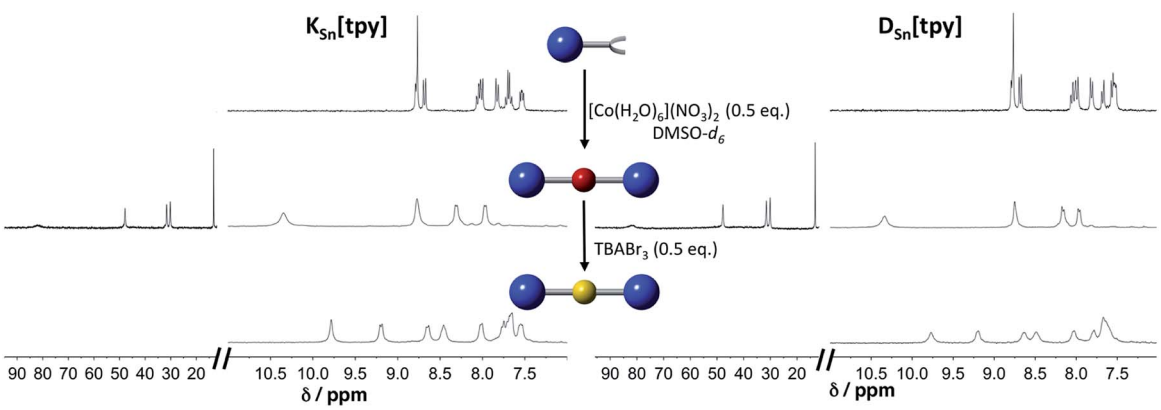

Fig. 1 ^{1}H NMR (300 MHz) in DMSO-d_6 solution containing K_{Sn}[tpy] (2 mM, top left) and D_{Sn}[tpy] (top right) in the presence of 0.5 equiv. of $[Co(H_2O)_6](NO_3)_2$ (middle); after oxidation of the Co(II) with 0.5 equiv. $TBABr_3$ (down).

supramolecular compounds are discrete species in DMSO-d_6. The addition of tetrabutyl ammonium tribromide (0.5 equiv., 20 mM in DMSO-d_6) into a DMSO-d_6 solution containing **K_{Sn}[tpy]** or **D_{Sn}[tpy]** in the presence of 0.5 equiv. of $[Co(H_2O)_6](NO_3)_2$ leads to a rapid fading of the solution colour from bright orange to the characteristic yellow colour of the low-spin Co(III) bis(terpyridine) complex, the process being complete in a few minutes.

The ^{1}H NMR spectra of the resulting species display well-resolved ^{1}H NMR signals, yet broader than those of the parent hybrid since transverse relaxation T_2 is faster for large molecules. No signal is observed above 10 ppm, indicating the absence of paramagnetic species. These studies suggest that in DMSO-d_6, all **POM.Co^N** complexes (in the following, **POM.M^N** stands for the supramolecular species displaying a 2 : 1 stoichiometry between the POM hybrid and the metal linker at the oxidation state N) behave as discrete species. Computational studies confirm the stability of the 2 : 1 supramolecular structures. The optimized DFT structures of **K_{Sn}[tpy].Co^{II}**, **D_{Sn}[tpy].Co^{II}**, **K_{Sn}[tpy].Co^{III}** and **D_{Sn}[tpy].Co^{III}** show an octahedral coordination of central cobalt (Fig. 2 and S6†). The most stable electronic and spin configuration for both Co(II) complexes is a paramagnetic doublet state with one unpaired electron in a orbital of sigma character, in which the d metal orbital and equatorial nitrogen atom lone pairs are involved. For Co(III) systems, the ground-state is a singlet low-spin. This difference in electronic configuration gives significant differences in Co–N distances, which are enlarged from 1.96 to 2.19 when going from **K_{Sn}[tpy].Co^{III}** to **K_{Sn}[tpy].Co^{II}**. While the energy-minimized structures of the dumbbell-like species **K_{Sn}[tpy].Co^{II}** and **K_{Sn}[tpy].Co^{III}** are almost identical (d_{P-P} = 4.29 nm for both structures), we observe a slight discrepancy in the structures of **D_{Sn}[tpy].Co^{II}** and **D_{Sn}[tpy].Co^{III}**. Keggin systems show more linear structures, than the corresponding Dawson complexes. Indeed, as **D_{Sn}[tpy]** lacks the additional pseudo symmetry plane found in **K_{Sn}[tpy]**,[26] various conformers differing by the relative orientation between the Dawson units exist with **D_{Sn}[tpy].Co^N**. The conformational difference between the energy minimized structures of **D_{Sn}[tpy].Co^{II}** and **D_{Sn}[tpy].Co^{III}** (d_{P1-P1} = 4.19 and 4.16 nm, d_{P2-P2} = 4.94 and 4.65 nm for **D_{Sn}[tpy].Co^{II}** and **D_{Sn}[tpy].Co^{III}** respectively) does not correspond to a specific structural modification upon the change of the Co centre charge but mostly reflects the structural diversity of the Dawson-based dumbbell-like species **D_{Sn}[tpy].Co^N**.

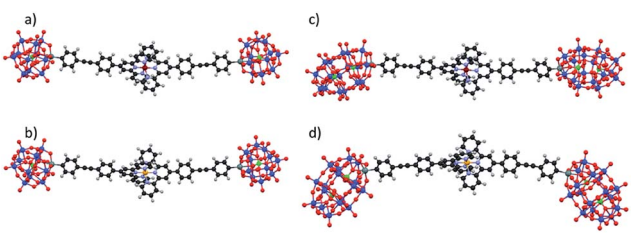

Fig. 2 Energy-minimized structures of the dumbbell-like species K_{Sn}[tpy].Co^{II} (a), K_{Sn}[tpy].Co^{III} (b), D_{Sn}[tpy].Co^{II} (c) and D_{Sn}[tpy].Co^{III} (d).

We performed small-angle X-ray scattering (SAXS) to complete the characterization of the dumbbell-like species in DMSO-d_6.

SAXS is a powerful technique to characterize the structures of large synthetic molecules, molecular assemblies, nanoparticles[34] and aggregates with sizes ranging from 1 to 100 nm.[35,36] With regard to POM chemistry, we and others have shown that this technique is particularly well-suited to characterize nanosized metal-oxo cluster assemblies.[8,9,37–41] A significant SAXS signal is visible for both molecular building units, consistent with well-dispersed nanometric objects (Fig. 3). Electrostatic interactions between the POMs result in a small decrease in intensity at small wave vectors, which prevents the observation of the Guinier regime as previously observed.[8–10,41] The SAXS diagrams of all dumbbell-like Co(II) and Co(III) complexes display oscillations as we have observed in other supramolecular systems.[8,9] These oscillations reveal characteristic distances larger than the POM dimension and have, in the low q region, a higher intensity than the starting building units, as a consequence of larger structures. Interestingly, for both hybrids, the SAXS pattern of the Co(II) and Co(III) complexes is almost identical, even in the low q region, which indicates that neither the structure nor the dispersion of the supramolecular systems is altered by the change in the redox state of the metal linker. To confirm the structure of the dumbbell-shaped species, theoretical SAXS patterns of the energy-minimized structures of the POM-based building units and molecular dimers have been computed using the program CRYSOL[42] without any adjustment of free parameters (Fig. 3 and S7†). For both dumbbells, the theoretical intensity is very similar to the experimental that in the SAXS patterns. In particular, the two oscillations and the intensity at small q values (neglecting the decrease in intensity below 0.04 Å^{-1} caused by the electrostatic interactions) are nicely reproduced, which further supports the structure and the discrete character of the dumbbell-like species in DMSO-d_6. It should be noted that despite the slight discrepancy between the energy-minimized structures of **D_{Sn}[tpy].Co^{II}** and **D_{Sn}[tpy].Co^{III}**, their computed SAXS patterns are very similar (Fig. S7†).

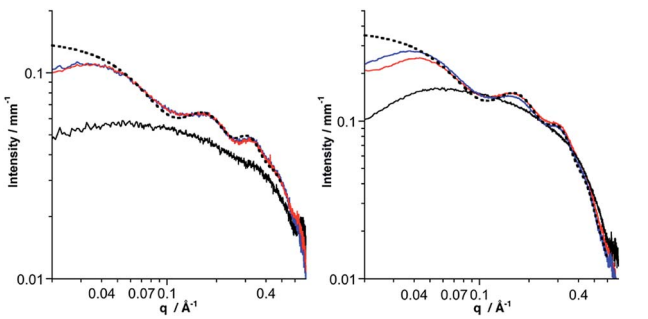

Fig. 3 SAXS pattern of a 1 mmol solution of the molecular building-units K_{Sn}[tpy] (left, black curve) and D_{Sn}[tpy] (right, black curve) in DMSO-d_6, and their resulting dumbbell-shaped Co(II) (red curves) and Co(III) (blue curves) complexes and the computed SAXS pattern (CRYSOL) of the optimized structures of K_{Sn}[tpy].Co^{III} and D_{Sn}[tpy].Co^{III} (dotted black). The solvent and the capillary were subtracted to obtain these patterns.

Comparison of the complexation energy between the Keggin-type and Dawson-type POM-based hybrids

In order to probe the thermodynamics of the formation of these complexes, an isothermal titration calorimetry (ITC) experiment was performed. A solution of $[Co(H_2O)_6](NO_3)_2$ in DMSO (2.2 mM) was incrementally injected into a solution of **K$_{Sn}$[tpy]**, **D$_{Sn}$[tpy]** or 4′-(4-ethynylphenyl)-2,2′:6′,2″-terpyridine (a terpyridine reference) in DMSO. The resulting isotherms are displayed in Fig. 4. For all compounds, the exothermal heat effects show an inflection point at a molar ratio of 0.5, which implies that the stoichiometry of the assembly is 2 : 1. Therefore, calorimetric data were fitted according to a model considering the formation of the 2 : 1 assembly directly from the free species. To perform such analysis, the sequential binding site model was used with the number of sites equal to 2, but with a formation constant of the 1 : 1 assembly fixed to 1. The values of fitted parameters are summarized in Table 1. For the terpyridine reference compound, the strong affinity results from a strong enthalpy stabilization (70.1 kJ.mol^{-1}) that is compensated by a weak entropic destabilization (−10.7 J.K^{-1}.mol^{-1}). Indeed, the overall reaction leads to the removal of the molecules previously coordinated to the Co(II) centre, which lowers the entropic cost. The complexation of **K$_{Sn}$[tpy]** and **D$_{Sn}$[tpy]** follows a similar trend but with different association constants. The enthalpic stabilization is more important with the POM-based hybrids and especially with **K$_{Sn}$[tpy]**. This is attributed to the coulombic interactions related to the intramolecular POM–Co and POM–POM interactions. If we neglect the overall contributions of the TBA cations in the electrostatic interactions, the coulombic work term associated with the complexation of the Co(II) centre is a balance between the attractive POM–Co and repulsive POM–POM interactions.

$$w_{el} = \frac{2Nq_{POM}q_{Co}}{4\pi\varepsilon_0\varepsilon_s R_{POM-Co}} - \frac{Nq_{POM}{}^2}{4\pi\varepsilon_0\varepsilon_s R_{POM-POM}}$$

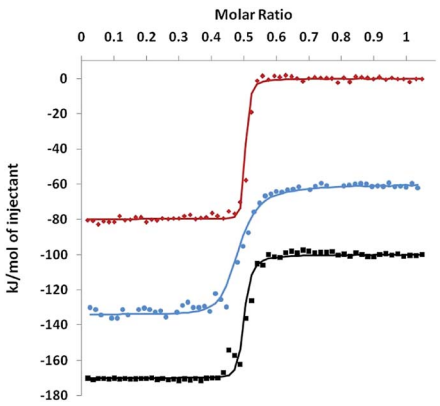

Fig. 4 ITC isotherm obtained by injecting a $[Co(H_2O)_6](NO_3)_2$ solution in DMSO (2.2 mM) into a K$_{Sn}$[tpy] (red), D$_{Sn}$[tpy] (blue, with a vertical shift of −60 kJ.mol^{-1}) or 4′-(4-ethynylphenyl)-2,2′:6′,2″-terpyridine (black, with a vertical shift of −100 kJ.mol^{-1}) solution in DMSO (0.385, 0.150 and 0.385 mM, respectively) at 25 °C. The lines correspond to fits according to a model considering a direct formation of the 2 : 1 assembly.

Table 1 Thermodynamic parameters for the binding of the POM-based hybrids and the terpyridine reference compound to $[Co(H_2O)_6](NO_3)_2$

Ligand	K/M^{-2}	ΔH/kJ mol^{-1}	ΔS/J K^{-1} mol^{-1}
K$_{Sn}$[tpy]	3.48×10^{12}	−79.7	−27.4
D$_{Sn}$[tpy]	1.10×10^{11}	−74.1	−37.0
4′-(4-Ethynylphenyl)-2,2′:6′,2″-terpyridine	5.28×10^{11}	−70.1	−10.7

According to the energy minimized structures $R_{POM-Co} = 2.2$ nm and 2.3 nm and $R_{POM-POM} = 4.3$ nm and 4.6 nm, (the centre of the POM is estimated to be the P atom for **K$_{Sn}$[tpy]** and the midway point between the two P atoms for **D$_{Sn}$[tpy]**) for **K$_{Sn}$[tpy].Co^{II}** and **D$_{Sn}$[tpy].Co^{II}** respectively.

The calculated electrostatic stabilization energies are 10.6 kJ mol^{-1} (**K$_{Sn}$[tpy]**) and 4.5 kJ mol^{-1} (**D$_{Sn}$[tpy]**) in excellent agreement with the enthalpic differences observed between the POM-based hybrids and the terpyridine reference. Simple calculations thus show that an optimum electrostatic interaction occurs when $q_{POM} = 2q_{Co}$ *i.e.* for **K$_{Sn}$[tpy]**. The comparison of the entropy of the complexation of all systems shows that it is significantly higher for the POM-based hybrids than for the terpyridine reference. Furthermore, **D$_{Sn}$[tpy]** has a higher entropic destabilization, than **K$_{Sn}$[tpy]** as previously suggested for the complexation of ditopic POM-based hybrids.[26]

Aggregation of the molecular dumbbells

The coordination of **K$_{Sn}$[tpy]** and **D$_{Sn}$[tpy]** by $[Co(H_2O)_6](NO_3)_2$ in CD_3CN, leads to the appearance of broad and ill-defined signals in the ^{1}H low-field region (Fig. S8 and S9†) characteristic of colloidal systems while the solutions remain homogeneous and instantly displays the characteristic reddish orange coloration of Co(II) bis-terpyridine complexes. Similarly, the addition of CD_3CN or D_2O to a solution of the discrete dumbbell-shaped species in DMSO-d_6, leads to the drastic broadening of the ^{1}H signals. The aggregation of the dumbbell-shaped species was investigated by SAXS. We evaluated with this modular system the effect of the nature of the POM (**K$_{Sn}$[tpy]** *versus* **D$_{Sn}$[tpy]**) and the charge of the metal linker (Co^{2+} *versus* Co^{3+}) on the size and nano-organization of the aggregates. As expected, the SAXS patterns of the aggregates display an increase of the intensity in the low q region compared to the starting POM-based hybrid in solution at a similar concentration. Considering that the intensity in the low q region is proportional to the molar mass of the molecular system, the evaluation of the intensity allows us to estimate the number of POMs and hence of dumbbell-shaped species per aggregate. We observe that some POM-based assemblies display a decrease in intensity at small wave vectors.

This effect, attributed to the electrostatic interactions between the POM assemblies, is more pronounced with the Co^{2+} linker and with Dawson-type POMs. As all solutions contain the same initial concentration of hybrid POMs, large

Table 2 Data extracted from the SAXS curves of K_{Sn}[tpy].Co^{II}, K_{Sn}[tpy].Co^{III}, D_{Sn}[tpy].Co^{II}, and D_{Sn}[tpy].Co^{III} in CD_3CN solution, $d = 2\pi/q$. The value noted in bold corresponds to the main peak

Compound	Nber dimers	q_1/Å^{-1}	d_1/Å	q_2/Å^{-1}	d_2/Å
K_{Sn}[tpy].Co^{II}	10–12	0.344	18.3	**0.464**	**13.5**
K_{Sn}[tpy].Co^{III}	50–60	0.350	18.0	**0.481**	**13.1**
D_{Sn}[tpy].Co^{II}	2–3	**0.311**	**20.2**	0.426	14.8
D_{Sn}[tpy].Co^{III}	3–4	**0.323**	**19.5**	0.426	14.8

aggregates have lower concentrations. The amplitude of the decrease at low q is in agreement with the concentration (and hence the size) of the aggregate (Table 2). Finally, for all SAXS patterns, the oscillations corresponding to the discrete species, displayed in Fig. 3, are not observed anymore. However, each SAXS pattern exhibits two new peaks at intermediate q values (0.3 Å^{-1} < q < 0.5 Å^{-1}) denoted as q_1 and q_2, which were not present for the discrete dumbbell-like species in DMSO-d_6. These peaks, which were also observed in previous POM-based aggregates,[9,10] arise from the nanostructured features of the aggregates and correspond to POM–POM correlations within the aggregates (Fig. 5 and S10–S13†). The data extracted from the SAXS analysis are listed in Table 2. Typically, the aggregates made of **K_{Sn}[tpy]** contain much more POM building units than those of **D_{Sn}[tpy]**. Furthermore, the q_1 and q_2 peaks are more intense for the Keggin system than for the Dawson one, probably as a consequence of the lower nuclearity of the Dawson aggregates (and hence the less important numbers of POM–POM interactions within these aggregates). Finally, one can observe that increasing the charge of the metal linker leads to the formation of bigger aggregates with shorter POM–POM distances (*e.g.* higher q_1 and q_2 values) owing to increased electrostatic interactions between the POMs and the Co complexes. These results indicate that the aggregation is favoured (bigger aggregates with shorter POM–POM distances) when the charge of the metal linker approaches that of the POM.

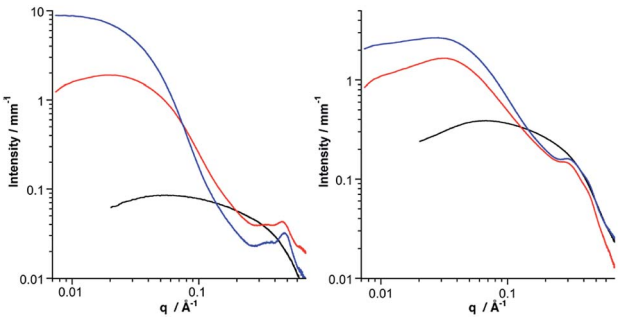

Fig. 5 SAXS pattern of a 1 mmol solution of the molecular building-unit K_{Sn}[tpy] (left, black curve) and D_{Sn}[tpy] (right, black curve) and the resulting aggregates POM.Co^{II} (red curves) and POM.Co^{III} (blue curves) assemblies in CD_3CN (respectively obtained upon the addition of 0.5 equiv. $[Co(H_2O)_6](NO_3)_2$ and further oxidation of the Co(II) with 0.5 equiv. $TBABr_3$). The solvent and the capillary were subtracted to obtain these patterns.

Transmission electron microscopy (TEM) of the aggregates **K_{Sn}[tpy].Co^{II}** and **K_{Sn}[tpy].Co^{III}** in MeCN was performed after the deposition of few drops of solutions containing the supramolecular assemblies dispersed in MeCN on a Cu grid covered with an amorphous carbon film. The resulting micrographs of **K_{Sn}[tpy].Co^{II}** and **K_{Sn}[tpy].Co^{III}** only show ill-defined aggregates of few nanometers (5 to 20 nm) probably due to the removal of the solvent (imposed by the high vacuum conditions), while the solvent certainly plays a key role in maintaining the structuration of the aggregates. Nevertheless we observe that the aggregates of **K_{Sn}[tpy].Co^{III}** are slightly bigger than those of **K_{Sn}[tpy].Co^{II}**, in agreement with SAXS (Fig. S14†).

Molecular dynamics simulation

The electrostatic potential maps in Fig. 6 illustrate the charge distribution of **K_{Sn}[tpy].Co^{III}** that identifies two regions of opposite charge within the molecular system: the POM region, which shows a high negative charge, and the Co(III) region that shows a relatively high positive charge. This opens the possibility of intermolecular aggregation by means of complementary coulombic electrostatic interactions. Due to the high negative charge of POMs, aggregation is expected to strongly depend also on the competitive interactions with the counter-cations and the solvent. Thus, explicit treatment of solvent and cations (TBA) is needed to describe the behaviour of dumbbell-type hybrid POMs in solution (DMSO and water). It should be noted that SAXS studies conducted in DMSO/water mixtures also indicated the formation of aggregates (Fig. S15†). Through MD simulations we investigated the aggregation phenomena and the factors on which they depend. Our analysis connects the intermolecular hybrid POM aggregate formation with the solvent dependence of the POM/TBA interactions. We analysed each phenomenon separately. First, we present the results of the structural features of **K_{Sn}[tpy].Co^{III}** anion-pairs formed spontaneously during MD simulations, and secondly the key role of TBA cations and the solvent in the aggregation process. Simulations starting from a model constructed by randomly distributed **K_{Sn}[tpy].Co^{III}** units in the simulation box led to the spontaneous formation of aggregates, pairs and even a trimer, in water but not in DMSO.

The distance distribution function ($g(r)$) between a POM (P atom) of one **K_{Sn}[tpy].Co^{III}** unit and the Co atom of the other unit, computed from the whole trajectories, permits analyzing the dynamical structure of the solution. We performed this analysis for the two solvents as shown in Fig. 7 and S16.† In water, $g(r)$ reveals high and well defined peaks at short distances

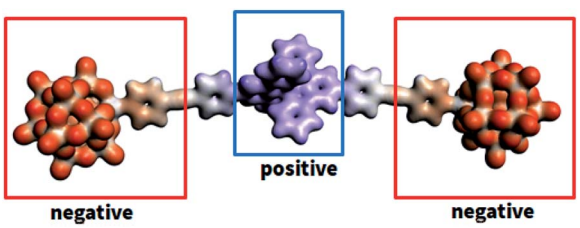

Fig. 6 Computed electrostatic potential map of K_{Sn}[tpy].Co^{III}.

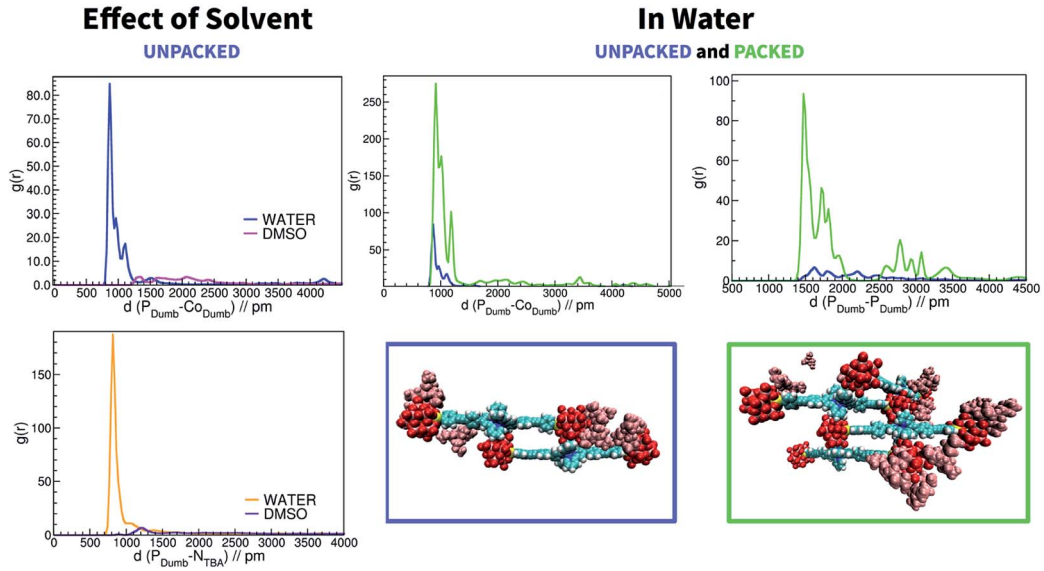

Fig. 7 Top left: distance distribution functions ($g(r)$) between a POM (P atom) of one K_{Sn}[tpy].Co^{III} unit and the Co atom of the other unit for the UNPACKED setup in water (blue) and in DMSO (pink). Middle: $g(r)$ between POM (P atom) of one K_{Sn}[tpy].Co^{III} unit and the Co atom of the other unit for initial setups UNPACKED (blue) and PACKED (green) in water. Right: $g(r)$ between two POMs (P atom) of different K_{Sn}[tpy].Co^{III} units for initial setups UNPACKED (blue) and PACKED (green) in water. Bottom left: distance distribution functions $g(r)$ between POM and TBA for the UNPACKED setup in water (orange) and DMSO (purple). Snapshots: spontaneously formed dimer in the UNPACKED setup (blue), and tetramer in the PACKED setup (green). TBA ions colored pinkish; POM oxygens colored red; organic chains colored blue.

(~9 Å) indicating close contacts between different units. In contrast, no peaks exist at short distances for DMSO. Visual inspection of the trajectory showed formation of **K_{Sn}[tpy].Co^{III}** pairs by means of the expected electrostatic interactions between the two distinctly charged regions of the hybrid POM, that led to a dimer structure depicted in Fig. 7. It should be noted that when we started the simulation from a pre-organized PACKED setup, the peaks in Fig. 7 (right side) totally match those of the UNPACKED setup (see the description of the MD simulation setup in the ESI† file), in position but not in intensity due to the presence of the pre-organized tetramer. Therefore, this confirms that the coulombic aggregation patterns are maintained in assemblies of different building units in water. Interestingly, by computing $g(r)$ between the two POMs (P atom) of different forms of **K_{Sn}[tpy].Co^{III}** units, we can observe at a close distance (below 2 nm) a peak at 14.7 Å and a broader set of peaks between 17.0 and 18.5 Å (Fig. 7 and S17†2). These values are in very good agreement with SAXS that indicates two preferential POM–POM short distances within the aggregates. We simulated the scattering data of six snapshots of tetramer aggregates (Fig. S18†). Each simulated SAXS pattern displays two broad peaks at *ca.* 0.35 $Å^{-1}$ and 0.45 $Å^{-1}$ in perfect agreement with the experimental SAXS data. Going from DMSO to water we observed an increase in the number of **K_{Sn}[tpy].Co^{III}** pairs, and realized that the number of TBA cations around the anions also seemed to increase. Aimed at analysing whether TBA played some role in the aggregation process, we computed $g(r)$ between the negative region of POM (P atom) and TBA cations. Indeed, the results in Fig. 7 show intense peaks in water and not in DMSO. Hence, though TBA molecules are strongly associated with dumbbells in water solution, they are much more labile in DMSO. Actually, the distance distribution function between TBA cations also reveals strong differences in the behaviour of TBA in the different solvents (Fig. S19†). TBA cations partly aggregate in water, but they are very well solvated in DMSO. Thus, there is a strong correlation between aggregation and TBA association, the higher the POM/TBA association, the higher the aggregation.

We observed the different steps that led to the formation of a **K_{Sn}[tpy].Co^{III}** dimeric pair for the UNPACKED setup in water (Fig. 8). The most important feature that can be extracted is that TBA counter cations assist the formation of the dimers. The first step is a POM–POM anchorage mediated by TBA cations. Two TBA cations, which are associated with each POM, interact excluding water between them, by forming a supramolecular POM–TBA–TBA–POM assembly. Then, in the second step organic chain–TBA interactions come into play. TBA maintains the contact with the organic chain, and triggered by POM–Co(III) coulombic driving force, a kind of **K_{Sn}[tpy].Co^{III}** walking along the chain was recorded. In this movement TBA cations help to avoid POM–POM repulsion. Subsequently, in the last step of this walking, the first Co(III)–POM contact is rather stable. Afterwards, in step four, like in a Ferris wheel, both dumbbells units rotate around the POM–Co axis until reaching the second POM–Co(III) interaction, which leads to the formation of the anion–anion dimeric pair, the pattern of aggregation of assemblies of different subunits. Also in this case TBA helps to avoid POM–POM repulsion. This marvellous sequence of movements assisted by TBA leads to the formation of aggregates in water. In contrast, as no TBA cations are associated with POM in DMSO, dimeric pair formation is not favoured.

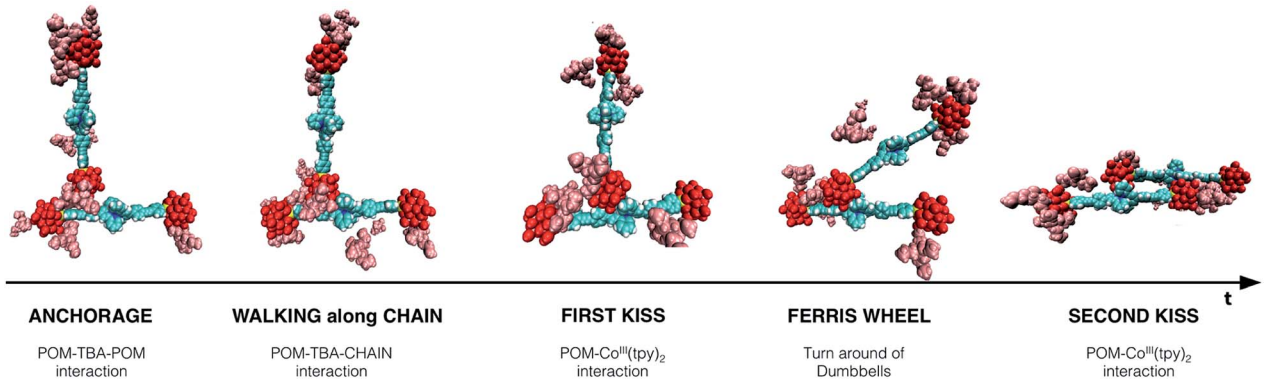

Fig. 8 Time-evolution snapshots of dumbbell–dumbbell dimer assisted by TBA counter cations.

Formation of nanostructured gels

With the aim of isolating the different dumbbell species, we observed that the solutions of **K$_{Sn}$[tpy].Co^{III}** and **D$_{Sn}$[tpy].Co^{III}** in DMSO-d_6, quickly precipitate in the presence of an excess of ethanol or ethanol/diethyl ether (2/1) for **K$_{Sn}$[tpy].Co^{III}** and **D$_{Sn}$[tpy].Co^{III}**, respectively. After washing with pure ethanol, the resulting precipitates appear as a gel containing *ca.* 7% of the hybrids (Fig. 9a), according to thermogravimetric analysis (TGA). When the resulting organogels are dipped into aqueous solution they initially float, owing to the lower density of ethanol compared to water. After a few minutes they start to sink into the aqueous solution suggesting the exchange of ethanol molecules by water. The formation of a hydrogel was confirmed by TGA, which shows that the resulting systems contain *ca.* 5% of the hybrid POMs and lose the solvent molecules at higher temperature, in agreement with the difference of volatility between ethanol and water (Fig. 9b and S20†). The organogels of **K$_{Sn}$[tpy].Co^{II}** and **D$_{Sn}$[tpy].Co^{II}** can also form upon the addition of an excess of ethanol/diethyl ether (2/1) to solutions of the dumbbell species in DMSO-d_6 solution, followed by washing with ethanol. SAXS analysis of all organogels was performed to complete their characterization (Fig. 10a). All SAXS curves display a rather intense peak at q values between 0.2 and 0.7 Å^{-1} (similar to previously observed values in CD_3CN) suggesting that some nano-organization is maintained in the organogels. Similarly, the trends previously described for q_1 and q_2 for the aggregates in CD_3CN are also observed for the organogels (Table 3 and Fig. S21–S24†).

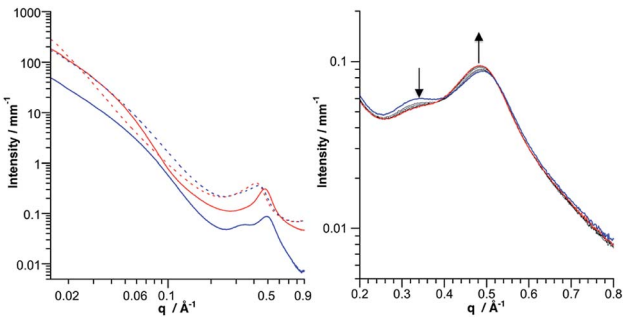

Fig. 10 (Left) SAXS pattern the **POM.Co^n** organogels: K$_{Sn}$[tpy].Co^{III} (plain blue), K$_{Sn}$[tpy].Co^{II} (plain red), D$_{Sn}$[tpy].Co^{III} (dotted blue) and D$_{Sn}$[tpy].Co^{III} (dotted red). (Right) Evolution of the SAXS pattern of K$_{Sn}$[tpy].Co^{III} under successive acquisitions; the bold blue and red lines correspond to the first and last scans respectively. The solvent and the capillary were subtracted to obtain these patterns.

For instance, q_1 and q_2 values are higher in the Keggin systems than in the Dawson ones and the gels with the Co(III) metal linker display higher q_1 and q_2 values than the **POM.Co^{II}** gels. For all compounds, the SAXS intensity keeps increasing for $q \rightarrow 0$ with a slope of *ca.* q^{-2}, which suggests that the gels have a lamellar organization (Fig. S25†). Interestingly the **POM.Co^{III}** systems evolve under the X-ray beam during successive SAXS acquisition at the synchrotron (Fig. 10b and S26†), which was evidenced by a local colour change (from orange to red) after

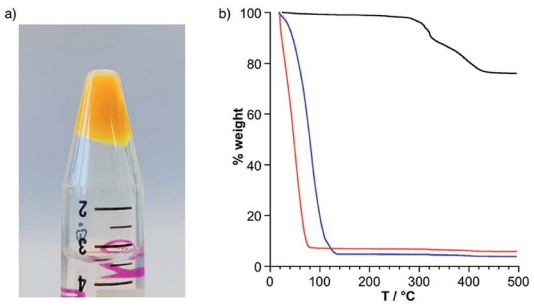

Fig. 9 (a) Ethanol organogel of K$_{Sn}$[tpy].Co^{III}. (b) Thermogravimetric analysis of K$_{Sn}$[tpy] (black) and K$_{Sn}$[tpy].Co^{III} as an ethanol organogel (red) and hydrogel (blue).

Table 3 Data extracted from the SAXS curves of K$_{Sn}$[tpy].Co^{II}, K$_{Sn}$[tpy].Co^{III}, D$_{Sn}$[tpy].Co^{II}, and D$_{Sn}$[tpy].Co^{III} as organogels, $d = 2\pi/q$. The value noted in bold correspond to the main absorption peak

Compound	Scan	q_1/Å^{-1}	d_1/Å	q_2/Å^{-1}	d_2/Å
K$_{Sn}$[tpy].Co^{II}	1st	0.369	17.0	**0.477**	**13.2**
K$_{Sn}$[tpy].Co^{III}	1st	0.354	17.7	**0.492**	**12.8**
	5th	0.364	17.2	**0.486**	**12.9**
D$_{Sn}$[tpy].Co^{II}	1st	0.332	18.9	**0.417**	**15.1**
D$_{Sn}$[tpy].Co^{III}	1st	0.344	18.3	**0.437**	**14.4**
	5th	0.343	18.3	**0.433**	**14.5**

beam exposure. We performed 5 successive acquisitions separately and noticed that the peaks at *ca.* 0.4–0.5 $Å^{-1}$ continuously shift towards smaller q values in agreement with the partial formation of **POM.Co^{II}** (Table 3), the effect being more pronounced for the Keggin than the Dawson-based system. It seems likely that the gel formation arises from the nano-organization of the POM-based dumbbells that is imposed by the electrostatic interactions between the charged moieties. These interactions maintain the POMs at a controlled distance in the aggregates. This leaves some void, which is filled with the solvent molecules. When the solvent molecules evaporate the gel irreversibly collapses in order to fill the voids. The intermolecular interactions between the dumbbells species are thus, in this system, at the basis of the formation of the gels. Smart materials with controllable properties can be obtained when the interplay between the intermolecular interactions within the molecular material is properly understood.[43] The properties and performance of these materials notably depend on the spatial organization and the distances between the components.[44] In the present system, the redox state of the metal linker of the gels can be photoswitched resulting in the modification of the POM–POM distances. These soft nanostructured materials thus have potential applications as redox-responsive smart materials.

Conclusions

We reported the formation of a series of discrete dumbbell-like POM-based hybrids displaying positive and negative charges. These complex molecular architectures, that differ by the nature of the POM (Keggin *versus* Dawson) and the charge of the cobalt linker (2+ and 3+) are able to further self-assemble into different hierarchical species (aggregates of different size, nanostructured gels) owing to a competition between the solvation energy of the discrete species and intermolecular electrostatic interactions. In DMSO, a strongly dissociating solvent, the systems behave as discrete species and were thoroughly characterized by combination of ^{1}H NMR spectroscopy, SAXS and DFT calculations. The formation of the dumbbell-like species in DMSO was also studied by ITC. These measurements showed that the metal coordination to the POM-based building unit was reinforced by coulombic interactions between the POMs and the metal linker and counter balanced by an entropic cost associated with the POM (the Dawson entropic contribution being more important than that of the Keggin). When lowering the dissociating character of the solvent or in the presence of a protic solvent the aggregation of the species occurred. In MeCN, we observed by SAXS the formation of nanostructured aggregates of different sizes according to the nature of the POM and the charge of the cobalt linker. We concluded that aggregation is favoured (bigger size and shorter POM–POM distances) when the charge of the metal linker approaches that of the POM. Molecular dynamics simulations, in combination with DFT calculations, corroborated that the dumbbell-like species are discrete in DMSO and that they aggregate in H_2O. Interestingly, the computational results outlined the non-innocent role of the TBA counter ions in the aggregation process. Typically, the aggregation occurs when some TBA cations are strongly associated with the POMs and assist the interaction between the molecular dumbbells. Finally, we observed the formation of gels in the presence of ethanol. In this case the solvation energy of the aggregate becomes too low and promotes precipitation. SAXS analysis of the gel indicated that the gel retained some nanostructural features of the aggregates. We thus showed that starting from the designed molecular building units of controlled size and topologies we can achieve their implementation into soft nanostructured materials through the control of their supramolecular organization.

Conflicts of interest

There are no conflicts to declare.

Acknowledgements

We thank Carlos Afonso and Hélène Lavanant for assistance in mass spectrometry measurments. We also thank Javiez Perez and Thomas Bizien for assistance in using beamline SWING. SOLEIL Synchrotron is acknowledged for providing beamtime and synchrotron radiation facilities. This work was supported by the French National Research Agency (EXPAND Project Grant ANR 14-CE08-0002). The authors thank the ICIQ Foundation, CERCA Program and AGAUR (grant 2017SGR00290) of the Generalitat de Catalunya, and the Spanish Ministerio de Ciencia, Innovacion y Universidades through project CTQ2017-88777-R for financial support.

Notes and references

‡ Acronyms used for the hybrid POMs: K and D refer to the Keggin- and Dawson-type anions respectively, Sn as a subscript relates to the primary functionalization and the term in brackets corresponds to the remote organic moieties.

1 G. M. Whitesides, J. K. Kriebel and B. T. Mayers, *Self-Assembly and Nanostructured Materials*, Springer, Berlin, 2005.
2 A. Babloyantz, *Molecules, Dynamics, and Life: An Introduction to Self-Organization of Matter*, John Wiley & Sons, New York, 1986.
3 Y. Sun, C. Y. Chen and P. J. Stang, *Acc. Chem. Res.*, 2019, **52**, 802.
4 P. Luisi, *Found. Chem.*, 2002, **4**, 183.
5 S. Datta, M. L. Saha and P. J. Stang, *Acc. Chem. Res.*, 2018, **51**, 2047.
6 C. Rest, R. Kandanelli and G. Fernandez, *Chem. Soc. Rev.*, 2015, **44**, 2543.
7 Y. Yan and J. B. Huang, *Coord. Chem. Rev.*, 2010, **254**, 1072.
8 G. Izzet, B. Abécassis, D. Brouri, M. Piot, B. Matt, S. A. Serapian, C. Bo and A. Proust, *J. Am. Chem. Soc.*, 2016, **138**, 5093.
9 M. Piot, B. Abécassis, D. Brouri, C. Troufflard, A. Proust and G. Izzet, *Proc. Natl. Acad. Sci. U. S. A.*, 2018, **115**, 8895.

10 R. Salles, B. Abécassis, E. Derat, D. Brouri, A. Bernard, Q. C. Zhang, A. Proust, C. Desmarets and G. Izzet, *Inorg. Chem.*, 2020, **59**, 2458.
11 Y. F. Song and R. Tsunashima, *Chem. Soc. Rev.*, 2012, **41**, 7384.
12 A. Proust, B. Matt, R. Villanneau, G. Guillemot, P. Gouzerh and G. Izzet, *Chem. Soc. Rev.*, 2012, **41**, 7605.
13 M. P. Santoni, G. S. Hanan and B. Hasenknopf, *Coord. Chem. Rev.*, 2014, **281**, 64.
14 G. Izzet, F. Volatron and A. Proust, *Chem. Rec.*, 2017, **17**, 250.
15 M. Stuckart and K. Y. Monakhov, *Chem. Sci.*, 2019, **10**, 4364.
16 A. V. Anyushin, A. Kondinski and T. N. Parac-Vogt, *Chem. Soc. Rev.*, 2020, **49**, 382.
17 L. J. Ren, H. K. Liu, H. Wu, M. B. Hu and W. Wang, *Adv. Mater.*, 2020, 32.
18 M. Sadakane and E. Steckhan, *Chem. Rev.*, 1998, **98**, 219.
19 B. Li, W. Li, H. L. Li and L. X. Wu, *Acc. Chem. Res.*, 2017, **50**, 1391.
20 A. Misra, K. Kozma, C. Streb and M. Nyman, *Angew. Chem., Int. Ed.*, 2020, **59**, 596.
21 H. N. Miras, J. Yan, D. L. Long and L. Cronin, *Chem. Soc. Rev.*, 2012, **41**, 7403.
22 P. C. Yin, D. Li and T. B. Liu, *Chem. Soc. Rev.*, 2012, **41**, 7368.
23 K. I. Assaf and W. M. Nau, *Angew. Chem., Int. Ed.*, 2018, **57**, 13968.
24 T. Buchecker, P. Schmid, S. Renaudineau, O. Diat, A. Proust, A. Pfitzner and P. Bauduin, *Chem. Commun.*, 2018, **54**, 1833.
25 M. A. Moussawi, N. Leclerc-Laronze, S. Floquet, P. A. Abramov, M. N. Sokolov, S. Cordier, A. Ponchel, E. Monflier, H. Bricout, D. Landy, M. Haouas, J. Marrot and E. Cadot, *J. Am. Chem. Soc.*, 2017, **139**, 12793.
26 M. Piot, S. Hupin, H. Lavanan, C. Afonso, L. Bouteiller, A. Proust and G. Izzet, *Inorg. Chem.*, 2017, **56**, 8490.
27 M. K. Bera, B. F. Qiao, S. Seifert, B. P. Burton-Pye, M. O. de la Cruz and M. R. Antonio, *J. Phys. Chem. C*, 2016, **120**, 1317.
28 Y. Mei, W. Huang, Z. Yang, J. Wang and X. N. Yang, *Fluid Phase Equilib.*, 2016, **425**, 31.
29 S. A. Serapian and C. Bo, *J. Phys. Chem. B*, 2016, **120**, 12959.
30 D. Sures, M. Segado, C. Bo and M. Nyman, *J. Am. Chem. Soc.*, 2018, **140**, 10803.
31 M. Segado, M. Nyman and C. Bo, *J. Phys. Chem. B*, 2019, **123**, 10505.
32 A. Sole-Daura, A. Notario-Estevez, J. J. Carbo, J. M. Poblet, C. de Graaf, K. Y. Monakhov and X. Lopez, *Inorg. Chem.*, 2019, **58**, 3881.
33 V. Duffort, R. Thouvenot, C. Afonso, G. Izzet and A. Proust, *Chem. Commun.*, 2009, 6062.
34 J. Maes, N. Castro, K. De Nolf, W. Walravens, B. Abecassis and Z. Hens, *Chem. Mater.*, 2018, **30**, 3952.
35 A. Guinier and G. Fournet, *Small Angle Scaterring of X-Rays.*, Wiley, New York, 1955.
36 J. Als-Nielsen and D. McMorrow, *Elements of Modern X-ray Physics*, Wiley, New York, 2001.
37 M. Li, W. Y. Wang and P. C. Yin, *Chem.–Eur. J.*, 2018, **24**, 6639.
38 M. Nyman, *Coord. Chem. Rev.*, 2017, **352**, 461.
39 Y. L. Wu, R. F. Shi, Y. L. Wu, J. M. Holcroft, Z. C. Liu, M. Frasconi, M. R. Wasielewski, H. Li and J. F. Stoddart, *J. Am. Chem. Soc.*, 2015, **137**, 4111.
40 V. Jallet, G. Guillemot, J. Lai, P. Bauduin, V. Nardello-Rataj and A. Proust, *Chem. Commun.*, 2014, **50**, 6610.
41 G. Izzet, A. Macdonell, C. Rinfray, M. Piot, S. Renaudineau, E. Derat, B. Abécassis, C. Afonso and A. Proust, *Chem.–Eur. J.*, 2015, **21**, 19010.
42 D. Svergun, C. Barberato and M. H. J. Koch, *J. Appl. Crystallogr.*, 1995, **28**, 768.
43 A. Priimagi, G. Cavallo, P. Metrangolo and G. Resnati, *Acc. Chem. Res.*, 2013, **46**, 2686.
44 A. R. Hirst, B. Escuder, J. F. Miravet and D. K. Smith, *Angew. Chem., Int. Ed.*, 2008, **47**, 8002.

Inorganic Chemistry

pubs.acs.org/IC

Article

Hierarchical Self-Assembly of Polyoxometalate-Based Organo Palladium(II) Metallomacrocycles via Electrostatic Interactions

Raphaël Salles, Benjamin Abécassis, Etienne Derat, Dalil Brouri, Aurélie Bernard, Qichun Zhang, Anna Proust, Christophe Desmarets,* and Guillaume Izzet*

Cite This: *Inorg. Chem.* 2020, 59, 2458−2463

Read Online

ACCESS | Metrics & More | Article Recommendations | Supporting Information

ABSTRACT: The design and synthesis of a supramolecular square composed of polyoxometalate-based hybrid donors and ethylenediamine palladium(II) nodes are reported. The structure of the metallomacrocycle scaffold was inferred by diffusion NMR, small-angle X-ray scattering (SAXS), and molecular modeling. The metallomacrocycle scaffold that contains negatively and positively charged subunits can further self-assemble owing to a competition between the solvation energy of the discrete species and intermolecular electrostatic interactions. When the dissociating character of the solvent was lowered or when in the presence of a protic solvent, different types of multiscale organizations (vesicles and pseudo-1D structures) were selectively formed and were characterized by SAXS and transmission electron microscopy.

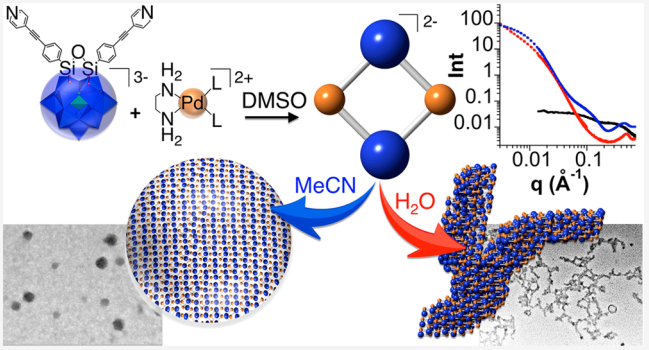

INTRODUCTION

Individual molecular building blocks that can self-assemble into different complex molecular architectures with proper molecular organization are currently drawing vigorous attention from the scientific community.[1−8] Indeed, the path that goes from discrete molecules to nanostructured macro- or mesoscopic assemblies is a cutting-edge challenge for present and future chemistry.[9−11] The way has already been partially paved by research on coordination-driven self-assembly,[12,13] albeit supramolecular architectures regulated by redox-active building units have been much less investigated.[14−16] Polyoxometalates (POMs) are anionic oxo-clusters that display unique redox properties and are thoroughly investigated for their promising technological applications.[17−19] They can be functionalized into organic−inorganic hybrids through the covalent grafting of organometallic fragments onto the POM framework.[20−22] Thanks to their nanoscale size, their tunable redox properties, and their sensitivity to various types of interactions, hybrid POMs are promising building blocks for the elaboration of complex nanostructured supramolecular architectures. For instance, hybrid POMs displaying remote coordination sites can self-assemble in metallomacrocycles upon metal coordination, where positive and negative charges can further be associated. We previously developed such an approach by connecting ditopic Keggin-types and Dawson-type hybrid donors to linear metal acceptors.[23,24] Yet, this system afforded mixtures of triangle- and square-shaped secondary building units, leading to defects in the stacking of the metallomacrocycles. Pd(II) metal centers, especially those derived from *cis*-blocked Pd(II) precursors, are widely used as acceptors to devise finite 2D and 3D architectures.[25,26] This drove us to investigate the self-assembly of a similar hybrid POM ditopic donor with a 90° Pd(II) acceptor, since a unique type of square-shaped metallomacrocycle (containing two hybrid POMs and two Pd nodes) should be formed using this strategy. We herein report the self-assembly of bis-silylated Keggin-based building units in the presence of $[Pd(en)(MeCN)_2](BF_4)_2$, a well-known metal acceptor that displays two orthogonal accessible coordination sites imposed by the ethylenediamine (en) ligand. We show that in a highly dissociating solvent these hybrid POMs self-assemble into a unique discrete supramolecular architecture that can further self-aggregate into different hierarchical assemblies according to the solvent composition.

EXPERIMENTAL SECTION

Triethylamine was distilled from CaH_2. Dimethylformamide was purchased stored under argon over a molecular sieve. $[PdCl_2(PPh_3)_2]$,[27] $[Pd(en)_2(CH_3CN)_2](BF_4)_2$,[28,29] and the iodo aryl terminated hybrid platform $K_{Si}[I]$[30] were prepared according to published procedures. All other reagents were used as supplied. Reactions were carried out under dry argon by using Schlenk-tube techniques. Microwave-assisted syntheses were performed in an

Received: November 13, 2019
Published: January 24, 2020

https://dx.doi.org/10.1021/acs.inorgchem.9b03333
Inorg. Chem. 2020, 59, 2458−2463

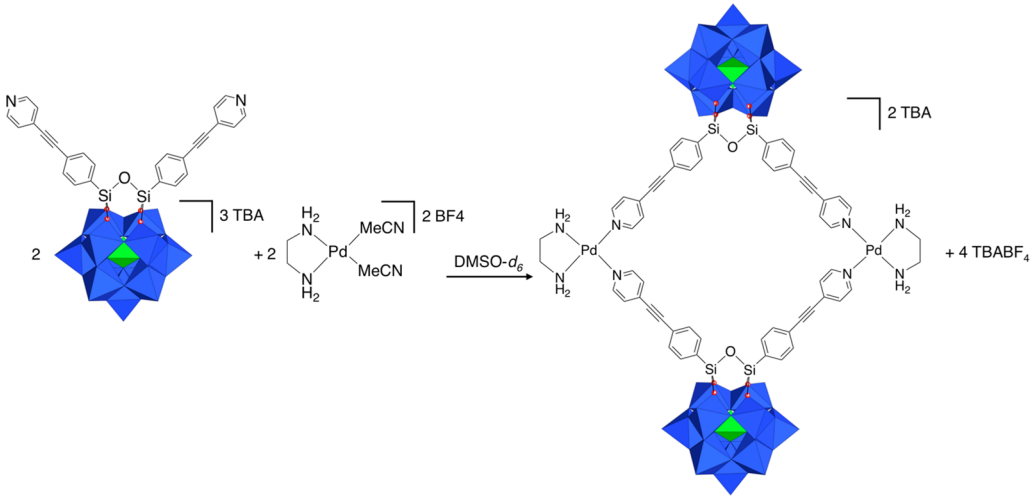

Figure 1. Metal-driven formation of the molecular square from the POM hybrid $\mathbf{K_{Si}[pyr]}$.

ambient pressured reactor (Milestone Start S) equipped with a temperature control unit. The IR spectrum was recorded from KBr pellets on a Jasco FT/IR 4100 spectrometer. NMR spectra were recorded on a Bruker Avance II 300 spectrometer equipped with a QNP probe head or a Bruker Avance III 600 spectrometer equipped with a BBFO probe head. ^{1}H chemical shifts are quoted as parts per million [ppm] relative to tetramethylsilane by using the solvent signals as a secondary standard (s = singlet, d = doublet, t = triplet, m = multiplet), and coupling constants (J) are quoted in hertz [Hz]. ^{31}P chemical shifts are quoted relative to 85% H_3PO_4.

The ^{1}H DOSY spectra were acquired by using the pulse sequence ledbpgp2s. The gradient strength G was varied in 16 or 32 linear steps from 1.00 to 48.8 G cm^{-1} to ensure at least 90% signal attenuation. The spectra were processed by using the fitting routine integrated in the TopSpin 4.0 package.

The small-angle X-ray scattering data were acquired on the SWING beamline at synchrotron SOLEIL (Saint Aubin, France). The nanocrystal dispersions were loaded in glass capillaries with an outside diameter between 1 and 1.5 mm and glass walls of 0.01 mm (WJM-Glas, Germany). The energy of the X-ray beam was 12 keV. The scattered X-rays were detected using an EIGER 4 M detector situated at 6.231 or 0.517 m distance from the sample. Ten images were taken with a typical acquisition time of 250 ms and were averaged to increase the signal-to-noise ratio. The SAXS intensity was normalized using beamline-specific procedures and radially averaged using FOXTROT 3.4.1.

TEM was carried out at the Plateforme de l'Institut des Matériaux de Paris Centre, Sorbonne Université, using a JEM 2011 LaB6 Jeol electron microscope operating at a 200 kV accelerating voltage with a 1.8 Å resolution. Micrographs were recorded after deposition of a few drops of solutions of $\mathbf{K_{Si}[pyr]_2{\cdot}[Pd(en)]_2}$ (c_{POM} = 25 μM) on a Cu grid covered with an amorphous carbon film and several rinses with the appropriate solvent (water for DMSO-d_6/D_2O mixtures and acetonitrile for DMSO-d_6/CD_3CN). The 25 μM solutions were prepared by quickly diluting solutions of the POM−Pd supramolecular assembly (c_{POM} = 0.5 mM) in DMSO-d_6/D_2O = 1/1 and DMSO-d_6/CD_3CN = 1/4 with the appropriate solvent (water or acetonitrile) before deposition on the Cu grid.

Optimization of geometries of the square-shaped supramolecular species was performed by energy minimization with a DFTB method. We built the putative $\mathbf{K_{Si}[pyr]_2{\cdot}[Pd(en)]_2}$ system, and its geometries were optimized using the XTB program developed by Grimme et al.[31] using the last generation of semiempirical tight-binding method, namely, GFN2-xTB.[32] To ensure that the geometry found was a stable conformer, simulated annealing was performed after a first geometry optimization, and then the most stable conformer was reoptimized.

Synthesis of K_{Si}[pyr]. First, 442 mg of K_{Si}[I] (0.114 mmol), 100 mg of 4-ethynylpyrydine hydrochloride (0.72 mmol), 2.1 mg of CuI (1.1×10^{-2} mmol), and 13.4 mg of [$PdCl_2(PPh_3)_2$] (1.90×10^{-2} mmol) were combined in a Schlenk tube under Ar atmosphere. Next, 5 mL of dry DMF was added under argon atmosphere. After careful degassing with argon for 5 min, 0.32 mL (2.30 mmol) of freshly distilled TEA was added. The mixture was stirred at 80 °C for 1 h, under microwawe irradiation. Next, 0.7 g of tetrabutyl ammonium bromide was then added to the solution, which was subsequently precipitated in an excess of diethyl ether. A dark green gel was recovered by filtration. It was then redissolved in the minimal amount of acetonitrile and precipitated by addition of absolute ethanol. A colorless solid was obtained after filtration and was washed with ethanol and diethyl ether.

Yield: 339 mg, 78%. ^{1}H NMR (CD_3CN): δ 8.61 (d, J = 6.0 Hz, 4H), 7.93 (d, J = 8.2 Hz, 4H), 7.70 (d, J = 8.2 Hz, 4H), 7.48 (d, J = 6.0 Hz, 4H), 3.12 (m, 24 H), 1.64 (m, 24 H), 1.40 (m, 24 H), 1.00 (t, J = 7.4 Hz 36 H). ^{31}P NMR (CD_3CN): δ −12.02 (s). IR (KBr, cm^{-1}): ν 2964 (s), 2875 (s), 2221 (w), 1632 (w), 1598 (m), 1540 (w), 1482 (m), 1470 (m), 1384 (m), 1153 (w), 1110 (s), 1067 (s), 1040 (s), 965 (vs), 873 (vs), 824 (vs), 769 (s), 715 (s), 623 (m), 600 (m), 523 (m), 395 (s), 384 (s), 353 (m), 335 (m). Elemental analysis for $PSi_2W_{11}O_{40}C_{74}H_{124}N_5$ (%): calcd C 23.19, H 3.26, N 1.83; found C 22.78, H 3.13, N 1.63.

RESULTS AND DISCUSSION

Design and Synthesis of the POM-Based Building Unit and the Discrete Supramolecular Assembly. We have previously shown that the metal-driven self-assembly of Keggin-type hybrids led to more stable supramolecular species than Dawson-type analogues, probably owing to a lower charge and, hence, a lower entropy contribution of the self-assembly.[33,34] Furthermore, Keggin-type POMs display a pseudo-axial symmetry (not present in the Dawson analogues) that should lead to the formation of a unique pseudo-D_{2h} supramolecular assembly upon metal coordination in which the aromatic rings of the organic linker should be chemically equivalent and, therefore, give a single set of NMR signals. Therefore, we focused on the Keggin-type POM-based hybrid $[PW_{11}O_{39}\{O(SiC_{13}H_8N)_2\}]^{3-}$, isolated as a tetrabutyl ammonium (TBA) salt, named $\mathbf{K_{Si}[pyr]}$, that contains two pyridine functions connected to a bis-siloxane organic tether grafted on the lacunary site of the monovacant POM $[PW_{11}O_{39}]^{7-}$ (Figures 1 and S1). A Sonogashira cross-coupling reaction, as previously developed in the group,[30] was used to attach the

https://dx.doi.org/10.1021/acs.inorgchem.9b03333
Inorg. Chem. 2020, 59, 2458−2463

pyridine function to the parent hybrid platform containing two iodo-aryl groups.

The addition of $[Pd(en)(MeCN)_2](BF_4)_2$ to a solution of $\mathbf{K_{Si}[pyr]}$ (5 mM) in DMSO-d_6 was followed by ^{1}H NMR spectroscopy. The monitored reaction results show the progressive formation of a unique set of new signals and the concomitant disappearance of those of the starting POM-based building block. The reaction is complete after the addition of 1.2 equiv of Pd(II) (Figures 2, S2, and S3), which suggests that

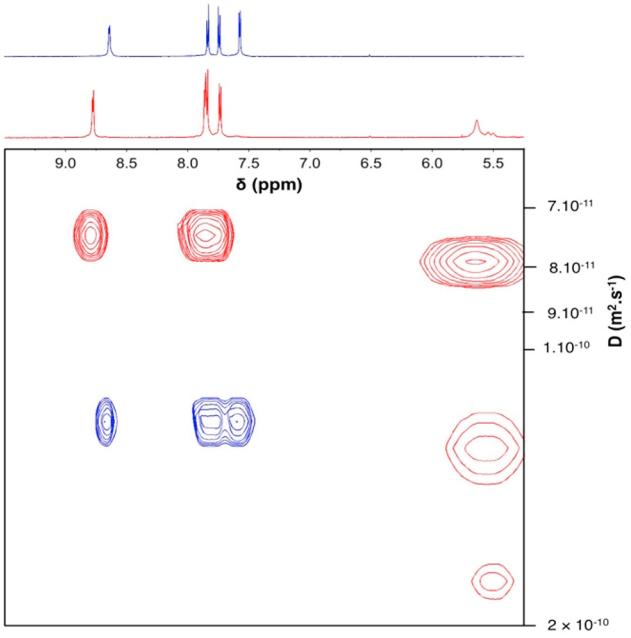

Figure 2. ^{1}H NMR (600 MHz, DMSO-d_6) with corresponding DOSY ^{1}H NMR of $\mathbf{K_{Si}[pyr]}$ (5 mM, blue) and its resulting supramolecular assembly in the presence of 1.2 equiv of $[Pd(en)(MeCN)_2](BF_4)_2$ (red).

the resulting species presents a 1:1 stoichiometry between the POM and the Pd(II) units while a minor excess of Pd(II) species, observed at ca. 5.5 ppm, is necessary to complete the reaction of $\mathbf{K_{Si}[pyr]}$. We performed DOSY NMR to evaluate the diffusion coefficients of the starting hybrid POM before and after the addition of 1.2 equiv of $[Pd(en)(MeCN)_2](BF_4)_2$. In both cases the aromatic signals of the hybrid POM decay similarly, according to the pulsed-field gradient strengths with a unique diffusion coefficient: $D_1 = 1.2 \times 10^{-10}$ m^2 s^{-1} for the starting hybrid and $D_2 = 7.7 \times 10^{-11}$ m^2 s^{-1} for the supramolecular species (Figures 2, S4, and S5). Furthermore, in the last case, the major peak at 5.6 ppm, corresponding to the ethylenediamine ligand, displays a diffusion coefficient close to that of D_2, suggesting the participation of the Pd(en) moieties in the supramolecular assembly (note that the slight discrepancy in the diffusion coefficient of the aromatic signals and those of the ethylenediamine moieties probably arises from some exchange of the Pd(en) moieties in the supramolecular assembly and in the minor unbounded forms at the time scale of the DOSY experiment). By contrast, the minor peaks at 5.50 and 5.55 ppm display a considerably higher diffusion coefficient that cannot be properly evaluated with a unique diffusion coefficient (Figure S6) and are attributed to unbounded Pd(en) species in equilibrium with the supramolecular assembly.

We previously evaluated the ratio in the diffusion coefficient between a given assembly and the starting POM hybrid platform on a series of hybrid POM assemblies of different nuclearities (dimer, trimer, and tetramer). We found that the diffusion coefficient ratio between the starting hybrid POM and a dimer was about 1.7, a value that is rather close to $D_1/D_2 = 1.6$, which suggests the formation of a dimeric macrocyclic species.

Structural Characterization of the Metallomacrocycle: Molecular Modeling and SAXS Analysis. To gain insight into the structure of the cyclic oligomer, the optimization of geometries of the square-shaped supramolecular species was performed by energy minimization with a DFTB method owing to the large size of the system (Figure 3). More specifically, we built the putative $\mathbf{K_{Si}[pyr]_2}$·$\mathbf{[Pd(en)]_2}$ system, and its geometry was optimized with the XTB program developed by Grimme et al.[31] This computational structure can be seen in Figure 3. One can notice its relative flatness since the dihedral angle between the four units (defined by the two Pd atoms and the two oxygens of bridging the silicon atoms) is 1.97° (Table S1). The two POM units are separated by a distance of 14.7 Å, while the distance between the two Pd atoms is 24.0 Å. The two Pd−POM−Pd angles are found to be 116.9° and 117.3°.

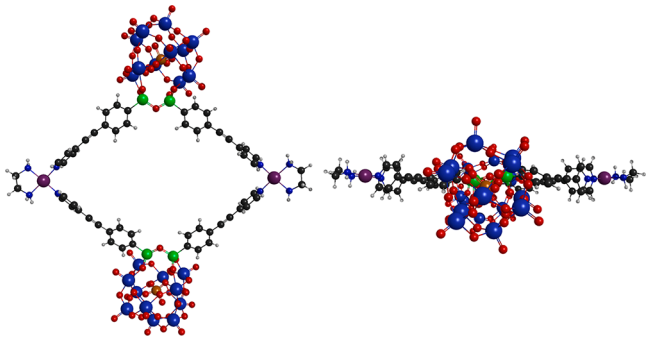

Figure 3. Optimized structure (left: top view; right: side view) of $\mathbf{K_{Si}[pyr]_2}$·$\mathbf{[Pd(en)]_2}$.

We also performed SAXS to complete the analysis of the supramolecular system. This technique is indeed well suited to characterize the structure of molecular assemblies and aggregates with sizes that range from 1 to 100 nm that we and others have successfully used to characterize the formation of POM-based self-assemblies.[35−37] A significant SAXS signal is visible for the molecular building block $\mathbf{K_{Si}[pyr]}$ in DMSO-d_6 solution, consistent with well-dispersed nanometric objects. As previously observed with hybrid POMs, electrostatic repulsion between the charged species results in a small decrease in intensity at small wave vectors. The SAXS diagram of the supramolecular assemblies displays oscillations in intensity that are the characteristic of a distance larger than the POM dimension (Figure 4). We also observed that in DMSO-d_6 the POM−Pd supramolecular systems evolved under the beam, preventing scan accumulation. If we ignore the decrease in intensity caused by the electrostatic interactions, we can notice that the maximum intensity increases by a factor of ca. 2 between the POM−Pd supramolecular assembly and the parent $\mathbf{K_{Si}[pyr]}$ building unit, in agreement with the formation of a molecular dimer. To further consolidate this, the theoretical SAXS pattern of the optimized structure of $\mathbf{K_{Si}[pyr]_2}$·$\mathbf{[Pd(en)]_2}$ was computed

https://dx.doi.org/10.1021/acs.inorgchem.9b03333
Inorg. Chem. 2020, 59, 2458−2463

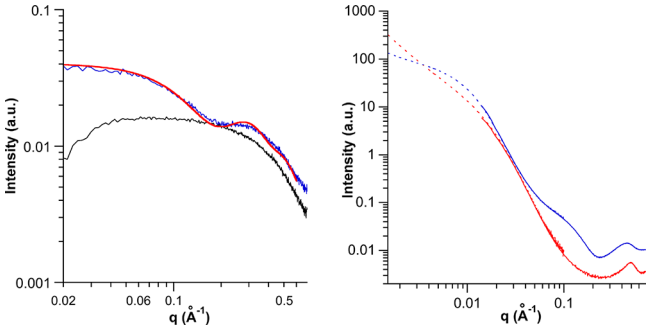

Figure 4. (Left) Experimental SAXS pattern of a solution of $\mathbf{K_{Si}[pyr]}$ (0.5 mM in DMSO-d_6, black) and the resulting supramolecular assembly in the presence of 1.2 equiv of $[Pd(en)(MeCN)_2](BF_4)_2$ (blue) and the computed SAXS pattern (CRYSOL) of the optimized structure of $\mathbf{K_{Si}[pyr]_2.[Pd(en)]_2}$ (red). (Right) Experimental SAXS pattern of a solution of the POM−Pd supramolecular assembly in (c_{POM} = 0.5 mM) in DMSO-d_6/D_2O: 1/1 (red) and DMSO-d_6/CD_3CN: 1/4 (blue).

using the program CRYSOL[38] from the atomic coordinates of the optimized structure. We observe that the intensity at small q values and the first oscillation are very well reproduced, which fully support the macrocyclic structure.

Aggregation Induced by the Addition of CD_3CN and D_2O. We have previously shown that in the presence of a less dissociating solvent than DMSO (such as acetonitrile) or a protic solvent, POM-based metallomacrocycles that contain positive and negative charges can aggregate through electrostatic interactions between the charged subunits.[23,24] Here, in the presence of CD_3CN or D_2O, the ^1H NMR spectrum of the POM−Pd supramolecular system drastically broadens. Note that the final concentration should not exceed c_{POM} = 0.5 mM in order to avoid partial precipitation of the solution. The two mixtures (DMSO-d_6/CD_3CN: 1/4; DMSO-d_6/D_2O: 1/1, c_{POM} = 0.5 mM) were analyzed by SAXS (Figure 4) and electron microscopy (Figure 5) to characterize the overall structure of

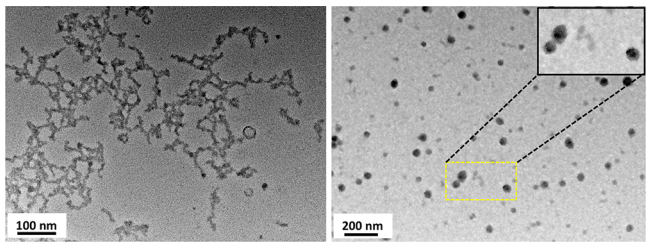

Figure 5. TEM micrograph of the POM−Pd assemblies in DMSO/D_2O 1:1 (left) and DMSO-d_6/CD_3CN 1:4 (right, magnification of three vesicles in the right corner) mixtures.

these new supramolecular architectures. In the SAXS patterns, we observe in both DMSO-d_6/CD_3CN and DMSO-d_6/D_2O mixtures the presence of a new peak, at large q values (q = 0.35−0.5 Å^{-1}), which is not present in the SAXS pattern of the discrete species in DMSO-d_6. These peaks correspond to specific POM−POM distances within the aggregates and indicate that they are both nanostructured. While in DMSO-d_6/CD_3CN, the peak can be deconvoluted by a single component centered at q = 0.436 Å^{-1} (corresponding to a distance d = 1.44 nm), and two components are necessary to accurately fit the peak in the case of the DMSO−D_2O mixture (q_1 = 0.376 Å^{-1}, q_2 = 0.490 Å^{-1} corresponding to distances d_1 = 1.67 nm and d_2 = 1.28 nm, respectively, Figure S7). This shows that the main POM−POM distance is significantly shorter in the presence of water. In DMSO-d_6/D_2O (1/1) solution, at small wavevectors the intensity keeps increasing for $q \rightarrow 0$, with a slope between q^{-1} and q^{-2}, suggesting that the aggregates are anisotropic and contain (at least) one preferential orientation. Among the various models tested to fit the data, the SAXS patterns were best reproduced by using a model of almost infinite flexible cylinders of 5.4 nm in radius (50% polydispersity) and a Kuhn length (i.e., average segment length of the flexible cylinder) of 15 nm (Figure S8). Note that the exact evaluation of the length of the cylinder (above hundreds of nanometers) is not possible with $q > 2 \times 10^{-3}$ Å^{-1}.

These results were confirmed by TEM analysis (Figure 5), which shows that the aggregates appear, once deposited on the surface, to be ramified flexible cylinders with cherry-branch structures with a section of 8−10 nm (slightly less than the values obtained by SAXS). The difference in the evaluation of the section between SAXS and TEM may arise from the SAXS model not accounting for the branched character that the aggregates probably have in solution. In the case of DMSO-d_6/CD_3CN mixture, the slope at low q is much lower, but the Guinier regime is never reached. TEM micrographs of the aggregates obtained by the deposition of the same sample on a grid after further dilution in acetonitrile shows the formation of isotropic polydisperse assemblies (Figure 5) with a diameter in the range of 15−55 nm (Figure S9).

Guided by these results, we tried to fit the SAXS pattern with various models such as homogeneous spheres with constant electron density or a vesicle model with a layer of POMS separating an interior and an exterior part filled with solvent molecules. Both modes do not reproduce well the SAXS intensity. The faint oscillation at ca. q = 0.08 Å^{-1} together with the slowly increasing intensity at lower q suggest an inhomogeneous electron density inside a closed shape. A multishell vesicle model (n = 1.5, i.e., mixture of single-layer vesicles and two-shell vesicles of 2.3 nm thickness) indeed reproduces the oscillation at q = 0.08 Å^{-1}, yet the polydispersity of the compound is probably too important to obtain a satisfactory fit, especially in the low q region (Figure S10). Actually, a close inspection of many big aggregates (>30 nm) shows that they display a higher density core which is in agreement with the formation of multiple layer vesicles as suggested by SAXS.

We previously observed that different types of hierarchical self-assemblies can be selectively formed according to the solvent composition as a consequence of different aggregation modes of the metallomacrocycles. In the previous study, the size of the aggregates (dense nanoparticles and pseudo-1D structures) were much smaller than those of the current study, probably as a consequence of stronger electrostatic interactions in the current POM−Pd metallomacrocycles. The difference in the aggregation mode between DMSO/CD_3CN and DMSO/D_2O mixtures probably arises from the solvation of the charged species and hydrophobic effects. Indeed, from SAXS, as the vesicle layers are rather thin (evaluated to 2.3 nm, i.e., bilayer of the metallomacrocycle), the surface-to-volume ratio is considerably increased in these assemblies compared to that in the elongated structures. Consequently, in the vesicles the number of POMs (and Pd(II) nodes) pointing toward the solvent is higher than in the elongated nanostructures that are formed in the presence of water, a solvent in which POMs (as

https://dx.doi.org/10.1021/acs.inorgchem.9b03333
Inorg. Chem. 2020, 59, 2458−2463

TBA salts) and Pd(en) complexes are insoluble. Owing to improved packing in the elongated structures, the POM−POM distances are shorter than in the vesicles where the POMs are more solvated.

CONCLUSIONS

Here, we elaborated a new POM-based metallomacrocycle using a ditopic hybrid POM donor and a 90° metal acceptor. Using this synthetic strategy, a single discrete supramolecular square species was obtained. Moreover, we observed that this new supramolecular species is able to further self-assemble into different types of nanostructured hierarchical species (vesicles and pseudo-1D structures) according to the solvent composition. These complex molecular assemblies display bigger structures than the previously reported systems owing to improved electrostatic interactions. The large cherry-branched structures display a large size, and the close POM−POM distances hold great promise as semiconducting materials for the elaboration of neuromorphic networks.

ASSOCIATED CONTENT

Supporting Information

The Supporting Information is available free of charge at https://pubs.acs.org/doi/10.1021/acs.inorgchem.9b03333.

NMR spectra, SAXS fits, size histogram from TEM analysis, and Cartesian coordinates of the energy-optimized structure (PDF)

AUTHOR INFORMATION

Corresponding Authors

Christophe Desmarets − *Institut Parisien de Chimie Moléculaire, CNRS UMR 8232, Sorbonne Université, F-75005 Paris, France*; Email: christophe.desmarets@sorbonne-universite.fr

Guillaume Izzet − *Institut Parisien de Chimie Moléculaire, CNRS UMR 8232, Sorbonne Université, F-75005 Paris, France*; orcid.org/0000-0002-9849-4939; Email: guillaume.izzet@sorbonne-universite.fr

Authors

Raphaël Salles − *Institut Parisien de Chimie Moléculaire, CNRS UMR 8232, Sorbonne Université, F-75005 Paris, France; School of Materials Science & Engineering, Nanyang Technological University, Singapore 639678 Singapore*

Benjamin Abécassis − *Laboratoire de Chimie, Ecole Normale Supérieure de Lyon, CNRS, UMR 5182, Université Claude Bernard, Université de Lyon, 69007 Lyon, France*; orcid.org/0000-0002-1629-9671

Etienne Derat − *Institut Parisien de Chimie Moléculaire, CNRS UMR 8232, Sorbonne Université, F-75005 Paris, France*; orcid.org/0000-0002-8637-2707

Dalil Brouri − *Laboratoire de Réactivité de Surface, CNRS UMR 7179, Sorbonne Université, F-75005 Paris, France*

Aurélie Bernard − *Institut Parisien de Chimie Moléculaire, CNRS UMR 8232, Sorbonne Université, F-75005 Paris, France*

Qichun Zhang − *School of Materials Science & Engineering, Nanyang Technological University, Singapore 639678 Singapore*; orcid.org/0000-0003-1854-8659

Anna Proust − *Institut Parisien de Chimie Moléculaire, CNRS UMR 8232, Sorbonne Université, F-75005 Paris, France*; orcid.org/0000-0002-0903-6507

Complete contact information is available at: https://pubs.acs.org/10.1021/acs.inorgchem.9b03333

Author Contributions

The manuscript was written through contributions of all authors. All authors have given approval to the final version of the manuscript.

Notes

The authors declare no competing financial interest.

ACKNOWLEDGMENTS

Stéphane Baudron is acknowledged for fruitful discussions. We thank Javiez Perez and Thomas Bizien for assistance in using beamline SWING. SOLEIL Synchrotron is acknowledged for providing beamtime and synchrotron radiation facilities. This work was supported by the French National Research Agency (EXPAND project, ANR 14-CE08-0002). This work benefited from the use of the SasView application, originally developed under NSF award DMR-0520547. SasView contains code developed with funding from the European Union's Horizon 2020 research and innovation program under the SINE2020 project, grant agreement 654000. R.S. acknowledges Sorbonne University for a Ph.D. grant under the dual program with Nanyang Technological University.

REFERENCES

(1) Robinson, M. E.; Nazemi, A.; Lunn, D. J.; Hayward, D. W.; Boott, C. E.; Hsiao, M. S.; Harniman, R. L.; Davis, S. A.; Whittell, G. R.; Richardson, R. M.; De Cola, L.; Manners, I. Dimensional Control and Morphological Transformations of Supramolecular Polymeric Nanofibers Based on Cofacially-Stacked Planar Amphiphilic Platinum(II) Complexes. *ACS Nano* **2017**, *11*, 9162−9175.

(2) Lescop, C. Coordination-Driven Syntheses of Compact Supramolecular Metallacycles toward Extended Metallo-organic Stacked Supramolecular Assemblies. *Acc. Chem. Res.* **2017**, *50*, 885−894.

(3) Chan, M. H. Y.; Ng, M.; Leung, S. Y. L.; Lam, W. H.; Yam, V. W. W. Synthesis of Luminescent Platinum(II) 2,6-Bis-(N-dodecylbenzimidazol-2 '-yl)pyridine Foldamers and Their Supramolecular Assembly and Metallogel Formation. *J. Am. Chem. Soc.* **2017**, *139*, 8639−8645.

(4) Jiang, H. J.; Zhang, L.; Chen, J.; Liu, M. H. Hierarchical Self-Assembly of a Porphyrin into Chiral Macroscopic Flowers with Superhydrophobic and Enantioselective Property. *ACS Nano* **2017**, *11*, 12453−12460.

(5) Rest, C.; Kandanelli, R.; Fernandez, G. Strategies to create hierarchical self-assembled structures via cooperative non-covalent interactions. *Chem. Soc. Rev.* **2015**, *44*, 2543−2572.

(6) Mariani, G.; Moldenhauer, D.; Schweins, R.; Gröhn, F. Elucidating Electrostatic Self-Assembly: Molecular Parameters as Key to Thermodynamics and Nanoparticle Shape. *J. Am. Chem. Soc.* **2016**, *138*, 1280−1293.

(7) Kim, Y.; Li, W.; Shin, S.; Lee, M. Development of Toroidal Nanostructures by Self-Assembly: Rational Designs and Applications. *Acc. Chem. Res.* **2013**, *46*, 2888−2897.

(8) Yu, G. C.; Jie, K. C.; Huang, F. H. Supramolecular Amphiphiles Based on Host-Guest Molecular Recognition Motifs. *Chem. Rev.* **2015**, *115*, 7240−7303.

(9) Sun, Y.; Chen, C. Y.; Stang, P. J. Soft Materials with Diverse Suprastructures via the Self-Assembly of Metal-Organic Complexes. *Acc. Chem. Res.* **2019**, *52*, 802−817.

(10) Yan, Y.; Huang, J. B. Hierarchical assemblies of coordination supramolecules. *Coord. Chem. Rev.* **2010**, *254*, 1072−1080.

(11) Yamada, T.; Otsubo, K.; Makiura, R.; Kitagawa, H. Designer coordination polymers: dimensional crossover architectures and proton conduction. *Chem. Soc. Rev.* **2013**, *42*, 6655−6669.

(12) Chakrabarty, R.; Mukherjee, P. S.; Stang, P. J. Supramolecular Coordination: Self-Assembly of Finite Two- and Three-Dimensional Ensembles. *Chem. Rev.* **2011**, *111*, 6810−6918.
(13) Schmidt, A.; Casini, A.; Kühn, F. E. Self-assembled M2L4 coordination cages: Synthesis and potential applications. *Coord. Chem. Rev.* **2014**, *275*, 19−36.
(14) Herasymchuk, K.; Miller, J. J.; MacNeil, G. A.; Sergeenko, A. S.; McKearney, D.; Goeb, S.; Salle, M.; Leznoff, D. B.; Storr, T. Coordination-driven assembly of a supramolecular square and oxidation to a tetra-ligand radical species. *Chem. Commun.* **2019**, *55*, 6082−6085.
(15) Bivaud, S.; Balandier, J. Y.; Chas, M.; Allain, M.; Goeb, S.; Salle, M. A Metal-Directed Self-Assembled Electroactive Cage with Bis(pyrrolo)tetrathiafulvalene (BPTTF) Side Walls. *J. Am. Chem. Soc.* **2012**, *134*, 11968−11970.
(16) Tominaga, M.; Suzuki, K.; Kawano, M.; Kusukawa, T.; Ozeki, T.; Sakamoto, S.; Yamaguchi, K.; Fujita, M. Finite, spherical coordination networks that self-organize from 36 small components. *Angew. Chem., Int. Ed.* **2004**, *43*, 5621−5625.
(17) Ji, Y. C.; Huang, L. J.; Hu, J.; Streb, C.; Song, Y. F. Polyoxometalate-functionalized nanocarbon materials for energy conversion, energy storage and sensor systems. *Energy Environ. Sci.* **2015**, *8*, 776−789.
(18) Miras, H. N.; Yan, J.; Long, D. L.; Cronin, L. Engineering polyoxometalates with emergent properties. *Chem. Soc. Rev.* **2012**, *41*, 7403−7430.
(19) Li, B.; Li, W.; Li, H. L.; Wu, L. X. Ionic Complexes of Metal Oxide Clusters for Versatile Self Assemblies. *Acc. Chem. Res.* **2017**, *50*, 1391−1399.
(20) Izzet, G.; Volatron, F.; Proust, A. Tailor-made Covalent Organic-Inorganic Polyoxometalate Hybrids: Versatile Platforms for the Elaboration of Functional Molecular Architectures. *Chem. Rec.* **2017**, *17*, 250−266.
(21) Proust, A.; Matt, B.; Villanneau, R.; Guillemot, G.; Gouzerh, P.; Izzet, G. Functionalization and post-functionalization: a step towards polyoxometalate-based materials. *Chem. Soc. Rev.* **2012**, *41*, 7605−7622.
(22) Hampson, E.; Cameron, J. M.; Amin, S.; Kyo, J.; Watts, J. A.; Oshio, H.; Newton, G. N. Asymmetric Hybrid Polyoxometalates: A Platform for Multifunctional Redox-Active Nanomaterials. *Angew. Chem., Int. Ed.* **2019**, *58*, 18281.
(23) Piot, M.; Abécassis, B.; Brouri, D.; Troufflard, C.; Proust, A.; Izzet, G. Control of the hierarchical self-assembly of polyoxometalate-based metallomacrocycles by redox trigger and solvent composition. *Proc. Natl. Acad. Sci. U. S. A.* **2018**, *115*, 8895−8900.
(24) Izzet, G.; Abécassis, B.; Brouri, D.; Piot, M.; Matt, B.; Serapian, S. A.; Bo, C.; Proust, A. Hierarchical Self-Assembly of Polyoxometalate-Based Hybrids Driven by Metal Coordination and Electrostatic Interactions: From Discrete Supramolecular Species to Dense Monodisperse Nanoparticles. *J. Am. Chem. Soc.* **2016**, *138*, 5093−5099.
(25) Fujita, M.; Tominaga, M.; Hori, A.; Therrien, B. Coordination assemblies from a Pd(II)-cornered square complex. *Acc. Chem. Res.* **2005**, *38*, 369−378.
(26) Bardhan, D.; Chand, D. K. Palladium(II)-Based Self-Assembled Heteroleptic Coordination Architectures: A Growing Family. *Chem. - Eur. J.* **2019**, *25*, 12241−12269.
(27) Dangles, O.; Guibe, F.; Balavoine, G.; Lavielle, S.; Marquet, A. Selective Cleavage of the Allyl and Allyloxcarbonyl Groups through Palladium-Catalyzed Hydrostannolysis with Tributyltin Hydride - Application to the Selective Protection-Deprotection of Amino-Acid Derivatives and in Peptide-Synthesis. *J. Org. Chem.* **1987**, *52*, 4984−4993.
(28) Khalaf Alla, P. A.; Shoukry, M. M.; van Eldik, R. Amine-bridged binuclear complexes involving [Pd(ethylenediamine)(H2O)(2)](2+), 4,4 '-bipiperidine and DNA constituents. *J. Coord. Chem.* **2015**, *68*, 2041−2053.
(29) Tambara, K.; Pantos, G. D. Conversion of aldoximes into nitriles and amides under mild conditions. *Org. Biomol. Chem.* **2013**, *11*, 2466−2472.
(30) Duffort, V.; Thouvenot, R.; Afonso, C.; Izzet, G.; Proust, A. Straightforward synthesis of new polyoxometalate-based hybrids exemplified by the covalent bonding of a polypyridyl ligand. *Chem. Commun.* **2009**, 6062−6064.
(31) Grimme, S.; Bannwarth, C.; Shushkov, P. A Robust and Accurate Tight-Binding Quantum Chemical Method for Structures, Vibrational Frequencies, and Noncovalent Interactions of Large Molecular Systems Parametrized for All spd-Block Elements (Z = 1−86). *J. Chem. Theory Comput.* **2017**, *13*, 1989−2009.
(32) Bannwarth, C.; Ehlert, S.; Grimme, S. GFN2-xTB-An Accurate and Broadly Parametrized Self-Consistent Tight-Binding Quantum Chemical Method with Multipole Electrostatics and Density-Dependent Dispersion Contributions. *J. Chem. Theory Comput.* **2019**, *15*, 1652−1671.
(33) Izzet, G.; Macdonell, A.; Rinfray, C.; Piot, M.; Renaudineau, S.; Derat, E.; Abécassis, B.; Afonso, C.; Proust, A. Metal-Directed Self-Assembly of a Polyoxometalate-Based Molecular Triangle: Using Powerful Analytical Tools to Probe the Chemical Structure of Complex Supramolecular Assemblies. *Chem. - Eur. J.* **2015**, *21*, 19010−19015.
(34) Piot, M.; Hupin, S.; Lavanant, H.; Afonso, C.; Bouteiller, L.; Proust, A.; Izzet, G. Charge Effect on the Formation of Polyoxometalate-Based Supramolecular Polygons Driven by Metal Coordination. *Inorg. Chem.* **2017**, *56*, 8490−8496.
(35) Nyman, M. Small-angle X-ray scattering to determine solution speciation of metal-oxo clusters. *Coord. Chem. Rev.* **2017**, *352*, 461−472.
(36) Li, M.; Wang, W. Y.; Yin, P. C. A General Approach to Access Morphologies of Polyoxometalates in Solution by Using SAXS: An Ab Initio Modeling Protocol. *Chem. - Eur. J.* **2018**, *24*, 6639−6644.
(37) Wu, Y. L.; Shi, R. F.; Wu, Y. L.; Holcroft, J. M.; Liu, Z. C.; Frasconi, M.; Wasielewski, M. R.; Li, H.; Stoddart, J. F. Complexation of Polyoxometalates with Cyclodextrins. *J. Am. Chem. Soc.* **2015**, *137*, 4111−4118.
(38) Svergun, D.; Barberato, C.; Koch, M. H. J. CRYSOL - A program to evaluate x-ray solution scattering of biological macromolecules from atomic coordinates. *J. Appl. Crystallogr.* **1995**, *28*, 768−773.

https://dx.doi.org/10.1021/acs.inorgchem.9b03333
Inorg. Chem. 2020, 59, 2458−2463

ACKNOWLEDGEMENTS

It would be an understatement to say that this thesis would not have been the same without the help of many people. Thus, I'd like to thank them all for their support during these three years.

Obviously, I must start with Professor Anna Proust, for her comprehension and her kindness, for the discussion we had (and not only about chemistry) and for understanding me and the way I work. I also have a special thought for Dr. Guillaume Izzet, to be with me every day in the lab is not a sinecure but he always helped, advised and supervised me without losing his smile. Dr. Florence Volatron was also of huge help, I remember her patience during the hours and hours we spent at the AFM and all the relevant clues she gave me. Globally, I am grateful to all the E-POM team for the great work conditions allowed by everybody, the great scientific emulation resulting from the group meeting and their general kindness.

At NTU I'd like to thank Prof. Lee for accepting me in her lab when my situation was precarious and for her active participation in my work. All of her team was very warmhearted and offered spontaneous assistance. I would particularly like to thank Poh Wei Church for all the work he did and the time he spent helping me.

Getting to the end of this three years without losing my mind would not have been possible without my friends, so I am grateful to all of them: Kelly for all the giggles and also because she always accepted my extravaganza in the office, Alexandre for our not so successful cooking experiences, Agathe for her enthusiasm and her positiveness whatever the situation, Guillaume for the nights playing on the computer developing new addictions, Ingrid for following my reading recommendations while I constantly ignored hers, Thibaut for luring me out of my place to socialize, Taleen for the hours spent watching absurd movies without ever complaining, Lise for the unusual walks/talks and François for the time we spent pretending to understand art.

I also want to thank my friends who don't understand chemistry. Raphaël, Antoine, Hugo, Adrien, and Odile, for helping me keeping in my mind that there is an outside world, and Loc for listening to my complaints and pretending to be interested by the colors of my samples.

Finally, I am grateful to my family who supported me during these three years.

ABSTRACT:

Polyoxometalates (POMs) are nano-scaled metal-oxides, considered as promising candidates in many application fields thanks to their electron reservoir and redox properties. When turned into hybrids, by adding at least one organic arm, POMs can be used as platforms for the synthesis of larger devices. This thesis, realized in co-tutelle between Sorbonne Université and Nanyang Technological University, presents the results of this PhD work focusing on two aspects of POMs-based hybrids integration in large systems for different applications. Firstly, the formation of auto-assembled discrete species and their aggregation under specific solvent conditions was investigated. While on one hand a gel was obtained (organo- or hydro-), on the other hand square-shaped structure were obtained, leading to vesicles or elongated cherry-branches according to the solvent. Secondly, the covalent grafting of POM-based hybrids on ITO substrates for the formation of memory devices was studied. After confirmation of the thickness and the characteristics of the grafted layer via a panel of techniques (SEM, AFM, XPS…), a top electrode was deposited to measure the memory properties of the final system. It confirmed the resistive memory nature, the non-volatility of the device and the “write once read many” character, where an information can be stored but not erased.

RÉSUMÉ:

Les polyoxométallates (POMs) sont des oxydes métalliques considérés comme des candidats prometteurs dans de nombreux domaines d’application grâce à leur propriétés redox et de réservoir d’électrons. Dans leur forme hybridée, c’est-à-dire avec au moins un bras organique, les POMs peuvent être utilisés comme plateformes pour la synthèse de plus grands dispositifs. Cette thèse, réalisée en cotutelle entre Sorbonne Université et Nanyang Technological University, présente deux aspects de l’intégration d’hybrides à base de POMs dans de grands systèmes pour différentes applications. Premièrement, la formation d’espèces discrètes auto-assemblées et leur agrégation (en fonction des solvants) ont été étudiées. D’un côté un gel a été obtenu, de l’autre une structure de forme carrée a menée à des vésicules et des branches de cerisiers. Deuxièmement, le greffage covalent d’hybrides à base de POM sur des subtrats d’ITO pour la formation de dispositifs de mémoire a été étudié. Après confirmation de l’épaisseur et des caractéristiques de la couche greffée via un panel de techniques (SEM, AFM, XPS…), les propriétés mémoire du système final ont été mesurées, confirmant la nature résistive de la mémoire, ainsi que sa non-volatilité et sa propriété « write once read many » (WORM).